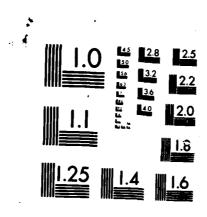
AD-A165 535 PROCEEDINGS OF THE 1983 ANTENNA APPLICATIONS SYMPOSIUM VOLUME 2(U) ROME AIR DEVELOPMENT CENTER GRIFFISS AFB MY DEC 85 RADC-TR-85-242-VOL-2 1/4 UNCLASSIFIED F/G 9/5 NL



The second second second

MICROCOPY RESOLUTION TEST CHART
STATIONAL RUPEBLY OF STANDARDS-1963-A

(2)

RADC-TR-85-242 Vol II (of two) In-House Report December 1985



PROCEEDINGS OF THE 1985 ANTENNA APPLICATIONS SYMPOSIUM

Sponsored by
ELECTROMAGNETIC SCIENCES DIVISION
ROME AIR DEVELOPMENT CENTER
HANSCOM AFB, BEDFORD MASS. 01731
AIR FORCE SYSTEMS COMMAND



APPROVED FOR PUBLIC RELEASE: DISTRIBUTION UNLIMITED

TE FILE COPY

ROME AIR DEVELOPMENT CENTER
Air Force Systems Command
Griffiss Air Force Base, NY 13441-5700

This report has been reviewed by the RADC Public Affairs Office (PA) and is releasable to the National Technical Information Service (NTIS). At NTIS it will be releasable to the general public, including foreign nations.

RADC-TR-85-242, Vol II (of two) has been reviewed and is approved for publication.

APPROVED:

PAUL H. CARR, Acting Chief Antennas & RF Components Branch Electromagnetic Sciences Division

part 1. Can

APPROVED: Wear Cother

ALLAN C. SCHELL

Chief, Electromagnetic Sciences Division

FOR THE COMMANDER:

JOHN A. RITZ Plans Office

DESTRUCTION NOTICE - For classified documents, follow the procedures in DOD 5200.22-M, Industrial Security Manual, Section II-19 or DOD 5200.1-R, Information Security Program Regulation, Chapter IX. For unclassified, limited documents, destroy by any method that will prevent disclosure of contents or reconstruction of the document.

If your address has changed or if you wish to be removed from the RADC mailing list, or if the addressee is no longer employed by your organization, please notify RADC (EEAA) Griffiss AFB NY 13441-5700. This will assist us in maintaining a current mailing list.

Do not return copies of this report unless contractual obligations or notices on a specific document requires that it be returned.

REPORT DOCUMENTATION PAGE					
1. REPORT SECURITY CLASSIFICATION Unclassified		1b. RESTRICTIVE MARKINGS			
26. SECURITY CLASSIFICATION AUTHORITY		3. DISTRIBUTION/AVAILABILITY OF REPORT			
20. DECLASSIFICATION/DOWNGRADING SCHED	\	Approved f	or public	relesse:	
28. DECEASSIFICATION/DOWNGRADING SCINCE	.000	Approved for public release; Distribution unlimited.			
4 PERFORMING ORGANIZATION REPORT NUM	BER(S)	5. MONITORING ORGANIZATION REPORT NUMBER(S)			
RADC-TR-85-242 (Volume II)					
6. NAME OF PERFORMING ORGANIZATION	6b. OFFICE SYMBOL (If applicable)	7a. NAME OF MONIT	TORING ORGAN	IZATION	
Rome Air Development Center	EEAA				
6c. ADDRESS (City. State and ZIP Code)		7b. ADDRESS (City,	State and ZIP Cod	ie)	
Hanscom AFB					
Massachusetts 01731					
1. NAME OF FUNDING/SPONSORING ORGANIZATION	8b. OFFICE SYMBOL (If applicable)	9. PROCUREMENT INSTRUMENT IDENTIFICATION NUMBER			UMBER
Rome Air Development Center	EEAA	<u></u>			
&c ADDRESS (City, State and ZIP Code)		10 SOURCE OF FUN	DING NOS.	·	
Hanscom AFB		PROGRAM ELEMENT NO.	PROJECT NO.	TASK NO.	WORK UNIT
Massachusetts 01731				}	1
11 TITLE (Include Security Classification) Proce	eedings of the	62702F	4600	14	01
1985 Antenna Applications Sym	mposium	L			
12. PERSONAL AUTHOR(S)					
13a TYPE OF REPORT 13b. TIME C	OVERED	14. DATE OF REPOR	AT (Yr , Mo., Day) 15. PAGE (OUNT
In-house FROM	то	1985 December		372	
16. SUPPLEMENTARY NOTATION Volume			330; Volu	me II consi	sts of pages
Banfel Te McGrath, Contract N	Monitor (RADC/EE	AA)			
17. COSATI CODES	18. SUBJECT TERMS (C.	ontinue on reverse if ne	cessary and ident	ify by block numbe	r)
FIELD GROUP SUB. GR.	Antennas ,	Microstrip Multibeam Antennas			
03 03	Satellite Ant	ennas, Refle	ector	Array Ante	nnas ,
19. ABSTRACT (Continue on reverse if necessary and	Broodband Antidentify by block number	STITLE O	AR JUNE,		7- -
·£					,
The Proceedings of the 1985	Antenna Applicat	ions Symposium	n is a coll	ection of	
state-of-the-art papers relat	ing to phased a	rray antennas,	, multibeam	antennas,	
satellite antennas, microstri various other antennas.	ip antennas, rer	lector antenna	as, Hr, VHF	, UHF and	
	,	1			
	, , , b	ب مام ره این			
,					
c					
20. DISTRIBUTION/AVAILABILITY OF ASSTRA	21. ABSTRACT SECURITY CLASSIFICATION				
UNCLASSIFIED/UNLIMITED SAME AS RPT. EX DTIC USERS UNCLASSIFIED					
22s. NAME OF RESPONSIBLE INDIVIDUAL		22b. TELEPHONE NI (Include Area Co		22c. OFFICE SYN	BOL
Daniel T. McGrath, Capt, USAI	<u> </u>	(617) 861-40)36	RADC/EEA	<u>A</u>

PREFACE

The Antenna Applications Symposium, held at the University of Illinois' Robert Allerton Park, was cosponsored by Rome Air Development Center's Electromagnetic Sciences Division (RADC/EEAA), Hanscom AFB, MA and the University of Illinois' Electromagnetic Laboratory under Contract F19628-85-M-0008. Professor Paul Mayes of UI was the symposium chairman. Capt. Daniel McGrath of RADC/EEA was the symposium manager for the Air Force.

Accesion	For		
NTIS DTIC Unanno Justifica	CRA&I TAB Wiced	8	
By			
Availability Codes			
Dist	Avail a Spe	nd for cial	
A-1			

Contents

Volume 1

Keynote: "Antenna Technology," R. C. Johnson

Wednesday, September 18, 1965

Session 1

Arrays

Chairman: P. R. Franchi, Rome Air Development Center

1.	"Antenna Elements for Integrated Phased Arrays," D. H. Schaubert, R. W. Jackson and D. M. Pozar	1
2.	"Cross Polarization Considerations for Microstrip Antenna Array Modules," M. L. Oberhart and Y. T. Lo	27
3.	"Ku-Band High-Gain Microstrip Planar Array for TDRSS," F. Lalezari and C. Gilbert	45
4.	"Diode Grids for Electronic Beam Steering and Frequency Multiplication," W. W. Lam, C. F. Jou, N. C. Luhmann, Jr., and D. B. Rutledge	67
5.	"Design of a Tilted Beam Waveguide Planar Array," J. M. Wachsman	73
6.	"Resonant Microstrip Dipole Arrays," J. Lane, N. Sa, and J. Toth	91

Session II

Broadband and Multiband Antennas

Chairman: P. E. Mayes, University of Illinois

7.	"Some Broadband, Low-Profile Antennas," P. Mayes, D. Tanner, R. Waller, J. Drewniak, T. Szmurlo, A. Boris and D. Kunkee	105	•
8.	"A Dual Feed Dual Polarized Log-Periodic HF Antenna System," D. V. Campbell, P. Dubowicz, B. Feigenbaum and K. Loffer	141	•
9.	"Coaxial Antennas for Duplex Operation," J. N. Hines and R. E. Myer		
10.	"A Dual Frequency Microstrip Antenna for Ka Band," R. Q. Lee and M. F. Baddour	165	
11.	"Traveling Wave Dipole Array for HF-VHF-UHF Tactical DF Systems," S. C. Kuo, H. Cook, and H. Hochman	189	
12.	"Broadband Size-Reduced Antennas for Spacecraft Applications," J. L. Wong and H.E. King		
13.	"Reduction of Coupling Between Cosited Antennas by Separation of Near Fields," D. V. Campbell, P. Dubowicz and R. Hoverter	205	
	Thursday, September 19, 1985		
	Session III		
	Reflectors, Lenses and Feeds		
	Chairman: Y. Rahmat-Samii, Jet Propulsion Laboratory, California Institute of Technology		
*14.	"Overview of Reflector Antenna Technology," Y. Rahmat-Samii		
15.	"K & S Band Feed System for an 18-Meter High-Efficiency Cassegrain Antenna," B. X. Nguyen, R. Rudolph, G. H. Schennum and C. H. Tsao	221	
16.	"Low-Loss Symmetric Off-Axis Feeds for Symmetric Dual Reflector Antennas," T. Veruttipong, V. Galindo-Israel and W. Imbriale	255	
17.	"Improving the Performance of a Small Reflector Antenna," M. Lewis, J. Toth, R. Kliger and W. Miccioli	313	3
		Volume	11
18.	"Reflector Pattern Control Using Variable Phase Plates."	331	

D. Jacavanco, Sr.

Contents

19.	"A Numerical Method for Approximating Antenna Surfaces Defined by Discrete Surface Points," R. Q. Lee and R. J. Acosta	351	
20.	"Experimental Transform Feed Antenna," D. T. McGrath	359	
21.	"High Efficiency Multibeam Antenna Design," P. G. Ingerson and C. A. Chen	377	
	Session IV		
	Analysis and Measurement I		
	Chairman: R. Mittra, University of Illinois		
22.	"On the Use of the Numerical Electromagnetics Code (NEC) to Solve for the Input Impedance and Radiative Efficiency of Loaded, Thin-Wire Antennas," B. M. Halpern and R. Mittra	405	
23.	"Electromagnetic Analysis of Dielectric Honeycomb Supports for Frequency Selective Surfaces," R. E. Jorgenson, R. Mittra, H. Ohta, K. C. Lang and T. K. Wu	435	
24.	"Application of Planar Near Field Measurement Techniques for Space Antennas," R. D. Ward and M. A. Shulz	459	
25.	"Evaluation of a VHF Satellite Antenna System," C. W. Thousand	475	
26.	"Automated Three-Antenna Polarization Measurements Using Digital Signal Processing," J. R. Jones and D. W. Hess	497	
27.	"Preliminary Evaluation of MMIC Array Antenna Performance," J. Smetana and R. J. Acosta		
28.	"Simple Expressions for the Phase Centers of Small Horn Antennas," P. R. Franchi	513	
29.	"Shaped Beam Earth Coverage Horn Antennas," J. C. Lee and W. Rotman	529	
	Friday, September 20, 1985		
	Session V		
Analysis and Measurement II			
	Chairman: R. Lampe, RCA Missile & Surface Radar Division		
30.	"Circular Array of Coaxially-Fed Monopole Elements in a Parallel Plate Waveguide," B. Tomasic	543	

31.	"VHF Satellite Antenna System," M. R. Matthew	581
32.	"A Simple Technique to Correct for Curvature Effects on Conformal Phased Arrays," J. Antonucci and P. Franchi	607
33.	"Optimization for Antenna Arrays in an Arbitrary Interference Environment," A. Y. Piatnicia and Y. T. Lo	631
34.	"Wideband Monopulse Antenna Design," D. L. Thomas	661

Contents

のの意味のいのいのは、「「これできない」「「これできない」「「「「」」

REFLECTOR PATTERN CONTROL USING VARIABLE PHASE PLATES

Daniel Jacavanco, Sr.

EM Technology Applications Section
EM Techniques Branch
Electromagnetic Sciences Division
Rome Air Development Center
Hanscom AFB, MA 01731

ABSTRACT

Results are presented for two applications of a novel technique for pattern control in reflector antenna systems. In the first, suppression of a high power mobile S-band source was accomplished while maintaining a continuous link with a desired low power signal, fixed in position. This resulted in the proper operation of a phase sensitive receiver to lock onto the desired signal, and not the stronger interfering signal during antenna experiments.

In the second application, a direct measure of the angular variation of ground clutter at the RADC antenna test facility was accomplished using the variable phase plate technique. This new measurement approach offers a significant improvement over the traditional 'field probe' method for characterizing the quiet zone of an antenna mount. By nulling out the direct ray and using a high gain paraboloid, local scattering centers have been identified with greater angular resolution than the field probe method. New scatterers have been identified that have the potential to seriously degrade low sidelobe pattern measurements in the vertical plane.

1. INTRODUCTION

Preliminary results of a new technique for pattern control in reflector systems have been reported by Jacavanco^{1,2}. Two AFIT Masters Theses have been written on the theoretical aspects of the problem - Havens³ and Rudisill⁴. The essence of the technique is depicted in Figure 1. Two small aluminum disks, attached to rods are held in place on the surface of a reflector by collet chucks. Pattern control is accomplished by adjusting the height of the disks above the surface, thereby modifying the amplitude and phase distribution in the aperture plane of the reflector.

Figure 2 shows the small effect the placement of two eight inch diameter disks flush with the surface of the reflector have upon the antenna pattern. Figure 3 shows a measured antenna pattern after a null has been created at nine degrees. The large dot is the original level of the antenna response at that angle before nulling. Cancellation of 20 dB is obtained with little degradation to the overall antenna performance.

The purpose of this paper is to describe two practical applications of this novel technique for pattern control.

2. JAMMED REFERENCE ANTENNA

In order to measure the RF performance of low sidelobe antennas, the RADC Electromagnetic Test Facility uses the Scientific Atlanta 2020 Antenna Measurement System. The heart of the S/A 2020 system is a phase-locked, narrow band, high dynamic

range receiver. This receiver is required when antennas are measured that possess very low sidelobes. In this case, the dynamic range of the receiver has to be much greater than the ratio of the main beam to average sidelobe level of the antenna under test in order to measure the depth of the pattern nulls. The phase reference for the receiver is obtained through a separate reference signal antenna.

The following problem exists when adaptive phased array antennas are tested: During the test of the adaptive performance, two signals are presented to the low gain reference antenna — the desired signal and the jammer signal. The signals come from two different sources separated in angle, but at the same frequency. However, the jammer signal power level is usually 50 dB greater than the desired signal. The receiver locks on to the stronger signal (the jammer), loses phase lock with the desired signal and becomes inoperable for measuring the amount of desired signal power received by the antenna under test.

The reflector-disk pattern control method provides the isolation required between the desired signal and the jammer at minimal cost, and in no way affects the operation of the system for the measurement of non-adaptive antennas. The horn antenna which receives the reference signal has been replaced by a high gain reflector antenna mounted on the roof of the measurement facility and pointed towards the transmitter building. Two small moveable

disks, mounted on the surface of the dish are adjusted in position until the jammer signal is cancelled. What follows is a description of how this was achieved manually with a description of the test results.

A six foot diameter S-band reflector, attached to a short section of a metal tower was mounted on the roof of the main building. The antenna, with a suitable feed horn, was pointed towards the transmitter building. An S-band link was established at 3.4 GHz. See Figure 4 for the plan view of the test range. A jammer-equipped truck was outfitted with an S-band signal source, TWT, six foot reflector and a/c generator. The truck was deployed on the road to the transmitter building at approximately the same depression angle used in earlier tests on an 80 element linear array adaptive antenna.

The first step was to measure the relative strength of the two signals reaching the main building. For this measurement they were separated slightly in frequency so that they could be viewed simultaneously by a spectrum analyzer. A small S-band horn with a main-beam wide enough to include the desired and interfering sources was placed at the same position as the S-band dish. Both signals were viewed with a Tektronix Spectrum Analyzer. A precision step attenuator, mounted in the coaxial line between the small horn and the spectrum analyzer was used to compare the two signals. It required 50 dB of attenuation to reduce the jammer signal level to the level the desired signal. See Figure 5.

The next step was to measure the relative stengths of the two signals when both are received by the six foot reflector antenna with the two aluminum disks mounted on the surface. Again the step attenuator was inserted in the coaxial line between the feed horn and the spectrum analyzer. The paraboloid was boresighted in order to be sure that the mainbeam and not a sidelobe intersected the transmitter building. Figure 6 shows the relative strengths of the signal and jammer when received by the dish. As expected, the -20 dB dB sidelobes of the dish reduced the strength of the jammer relative to the desired signal to -30 dB.

Finally, the two 8-inch diameter aluminum disks were adjusted until the jammer signal was cancelled. This was performed manually while viewing the output displayed on the spectrum analyzer. The first 30 dB of cancellation was not difficult to obtain - the proper position of the disks was found by carefully moving each one individually until the received power of the jammer was minimized. The fine tuning of the disk positions to obtain the last 10 dB of cancellation was more difficult. There was no effect noted upon the desired signal. Using the step attenuator, the amount of cancellation achieved by the final placement of the disks was measured to be 40 - 45 dB. See Figure 7. Thus it was was demonstrated that an unjammed reference signal (desired) was made available for the 2020 Antenna Measurement System.

Present plans include the installation of computer controlled

stepping motors to automatically control the position of the disks. When driven by a gradient search algorithm that minimizes the total power output of the reference antenna, antenna measurements over a broad range of frequencies will be possible.

For the purposes of display only, the jammer frequency was slightly offset from the desired signal. In practice, the two signals would be at the same frequency. In order to overcome the limitation of a minimum total power output algorithm (i.e. jammer power equals desired power), one could simply shut off the desired signal while the nulling of the jammer signal is accomplished.

3. QUIET ZONE MEASUREMENT

The traditional method of measuring the "quiet zone" of an antenna test mount is to plot the output of a modest sized probe antenna as it traverses a line perpendicular to the direction to the transmitting antenna in a far-field range. From the plot of the variation in amplitude with traverse distance, one can calculate the strength of reflected waves from the maxima and minima of the interference pattern of the trace. The direction of arrival of the strongest reflection is inferred from the periodicity of the pattern. The accuracy of this measurement of free space standing waves is usually limited to a few tenths of a dB variation, corresponding to a quiet zone of approximately -35 dB.

Figure 8 shows why reflections from the ground must be determined and eliminated (if possible) in an antenna test range. It

is a plot of the power received by a four foot diameter paraboloid taken in the vertical elevation plane at 3.1 GHz. The "sky side" of the plot is when the dish is pointed above the transmitter, while the "ground side" of the plot is when the dish looks into the ground. The disparity between the two halves is obviously due to ground reflections. For the purpose of this discussion, the pattern has been smoothed out by plotting the average of the trace over those angles where the ground reflection caused excessive pen fluctuation (-12 degrees to -24 degrees).

Figure 9 is a schematic diagram showing the relationship between the direct ray and reflected rays during an antenna pattern measurement. Typically the transmitting antenna has average sidelobes of -20 dB relative to the main beam. Also, for the terrain in question, the forward scatter of the ground bounce is in the -20 dB range also. This means that the reflected wave in Figure 9 is of the order of -40 dB relative to the main beam. Franchi and Poles⁵, have measured the quiet zone of the mount in question to be -35 dB over a 12 foot dimension.

For the following experiment, a four foot diameter paraboloid was equipped with the two-disk nulling device described by

Jacavancol and full vertical plane measurements of the pattern were made from +45 degrees above the horizon to -45 degrees below the local horizon. (Mount limitations prevented further movement).

When the antenna was pointed above the horizon, two jammers

were effectively present. However, since the direct ray is stronger than the reflected by 40 dB, it is considered the effective jammer. The cancellation achieved by the movement of the disks was limited only by the overall system noise level because both signals enter through the sidelobes. This is seen in Figure 10 as the series of dots at the bottom of the plot from +36 to +45 degrees. The nulling technique works well while the main beam is looking up because it seeks to minimize the total power received by the antenna, and only works in the sidelobe region. It may be called a manual version of the gradient search algorithm with a man in the loop.

The situation is entirely different when the antenna is pointed into the ground during a measurement. The direct ray becomes a sidelobe jammer, because it enters through the sidelobe as the dish is pointed down. Since the two disks are sized and positioned on the reflector surface to cancel only signals entering in the sidelobes, the direct ray is the only ray affected by the nulling technique. As the main beam scans the ground during the vertical movement, the energy received by the main beam is not affected by the nulling action of the disks. In fact, the cancellation achieved is limited by the amount of energy entering the main beam. That is to say, the disks are adjusted until minimum power is received by the dish. At this point, the antenna is receiving equal amounts of of direct energy through a null in the sidelobe and reflected energy by way of the main beam.

The highest return is at -36 degrees and corresponds to the grassy area in front of the antenna building. This reflection is -35 dB relative to the direct ray and agrees with a recent measurement by Franchi and Poles⁵.

The second highest return is at -24 degrees. The strength is -41 dB relative to the direct ray and is the reflection from the security fence.

The third highest return is in between -40 and -48 degrees. It corresponds to the flat grassy area next to the road that encircles the building.

The following argument is offered for the scatter in the achieved cancellation on the sky side, close to the main beam in Figure 10. At the Ipswich Facility, the town has located a large water tower across the street from the transmitter building. It is very tall and extends from +9 to +15 degrees in elevation. It is conceivable that the cancellation on the sky side was limited by reflections off this tower in a manner identical to the performance of the antenna looking into the ground. Further testing is needed to verify the reflection off the water tower. If this reflection is at -50dB relative to the direct ray, it could seriously limit the measurement of ultra-low sidelobe antennas at the RADC range.

4. CONCLUSION

A description of two applications of a novel technique for pattern control in reflector systems has been described. In the

first, an unjammed coherent reference signal has been provided for the proper operation of the Scientific/Atlanta 2020 Antenna Measurement System. This has been accomplished without the need for an expensive buried cable system, and works better (the full dynamic range of the receiver is assured) than other alternatives that were considered.

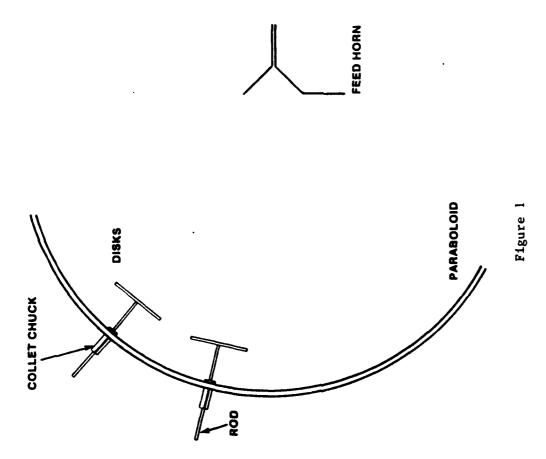
In the second, a direct measure of the angular variation of the ground clutter at the test range has been obtained. For the first time, the locations of the scattering centers that contribute to the reflected signals at the measurement site were identified.

5. ACKNOWLEDGEMENTS

The author is indebted to Mr. Raymond Schofield for help in the jammed reference antenna work and to SRA Blake R. Borsic, SRA Stephen P. Donahue, and AlC Gilbert L. Adkins for technical assistance in the ground clutter experiment.

6. REFERENCES

- 1. Jacavanco, D.J., "Controlled Pattern Distortion Effects", 1984 Antenna Applications Symposium, Allerton House, U. of IL.
- Jacavanco, D.J., "Nulling in a Reflector By Dynamic Surface Control", RADC-TR-85-125.
- 3. Havens, D. "Pattern Nulling By Reflector Shaping" AFIT TR-83D-26.
- Rudisill, M., "Null Generation Using Disks on a Reflector", AFIT TR-84D-55.
- 5. Peter Franchi and Livio Poles, Private Communication.



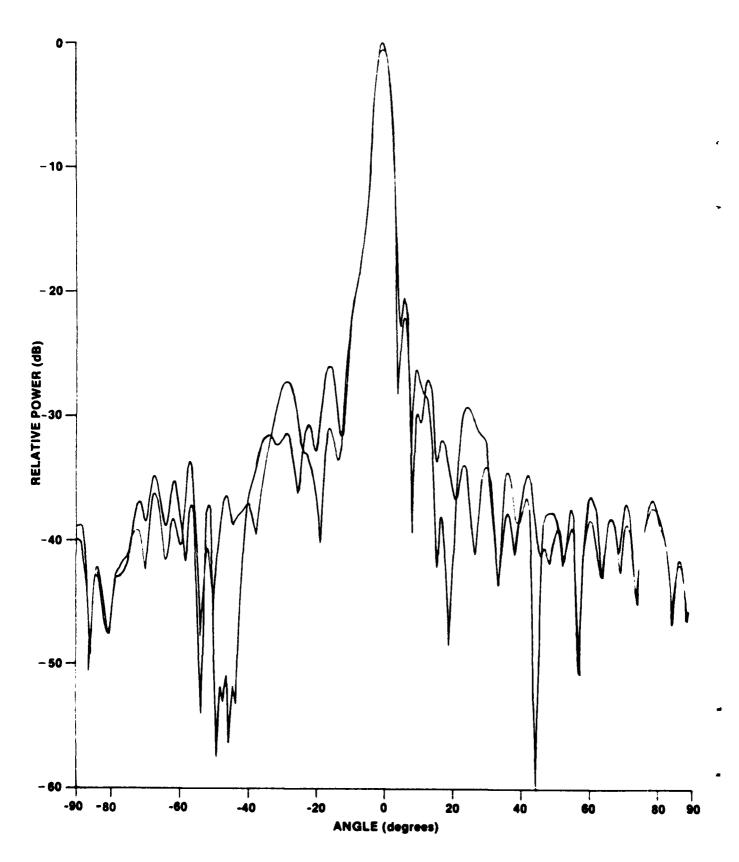
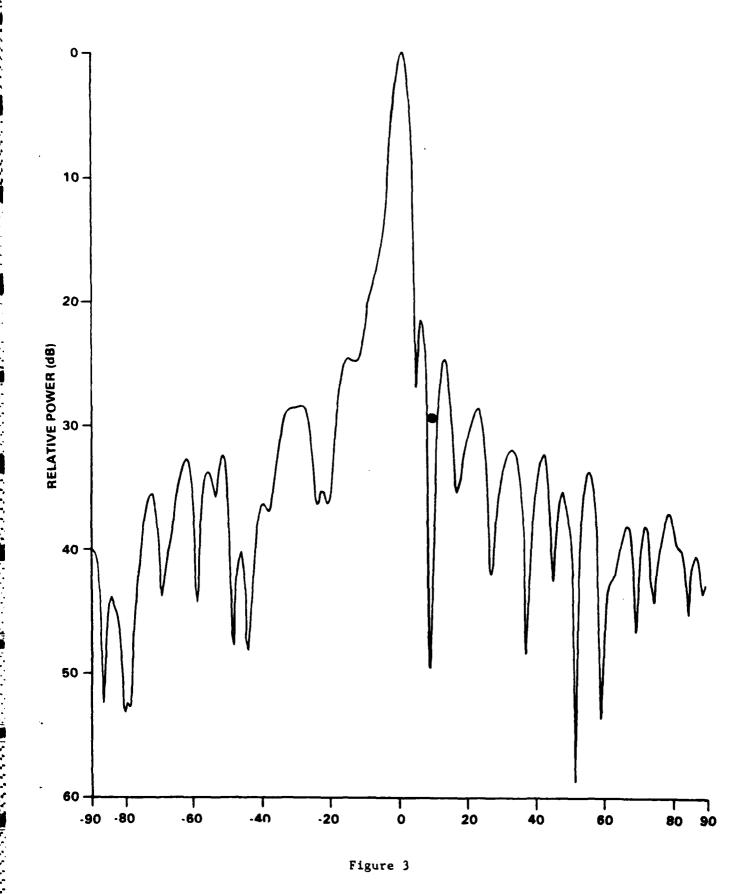
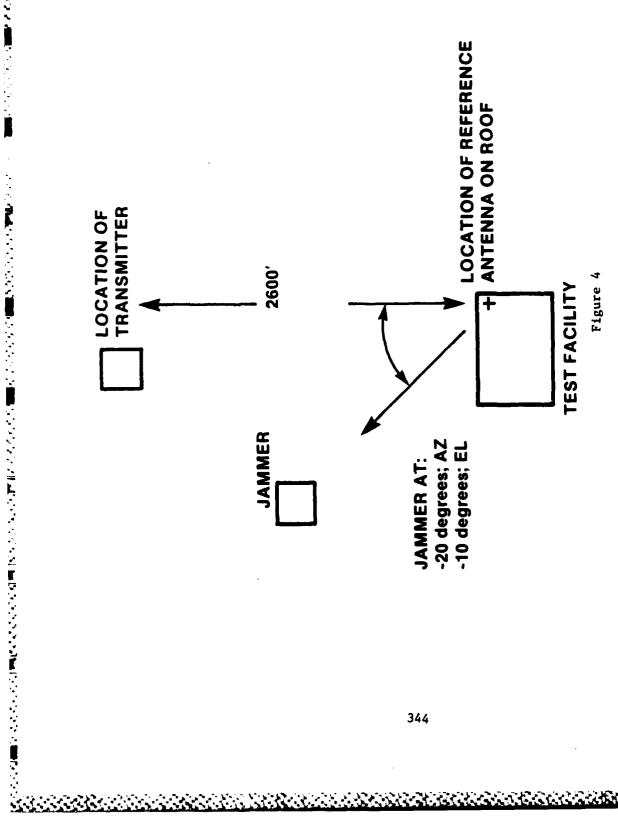


Figure 2





ジャンス 可能な かいしょう はいきゅう はいい マンド 大き 直げ こうごうけい はいき

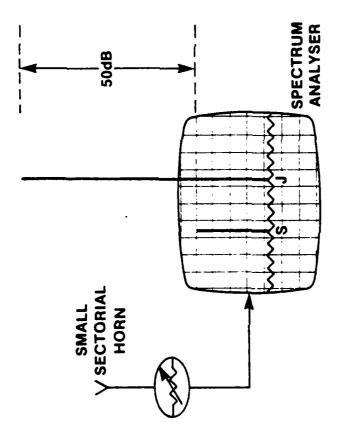
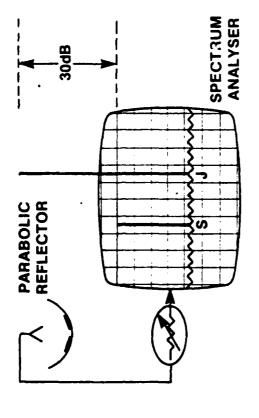


Figure 5

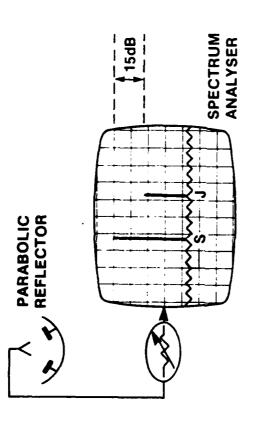
INITIAL CONDITIONS



このから 自己のののない 人間 日のないないない ない 自己の

BEFORE NULLING

Figure 6



AFTER NULLING

Figure 7

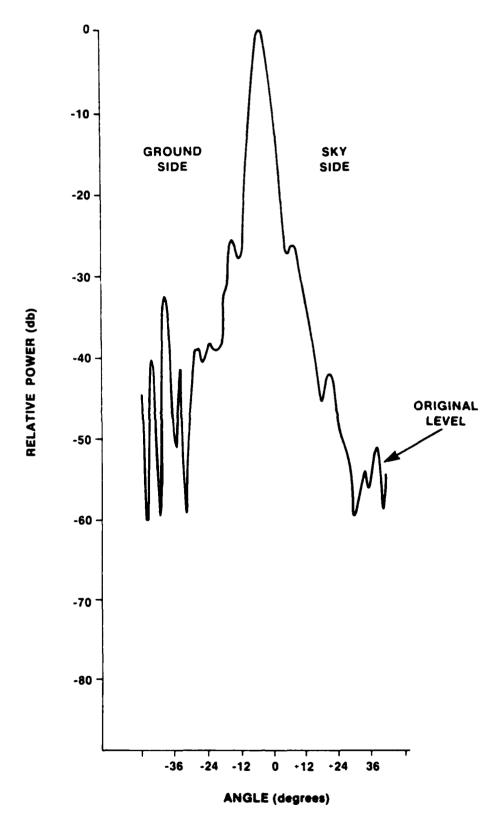


Figure 8

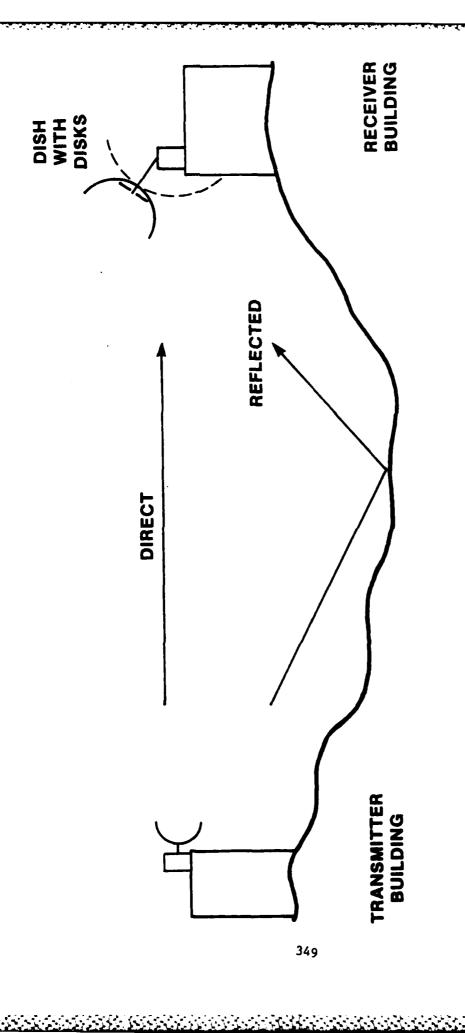


Figure 9

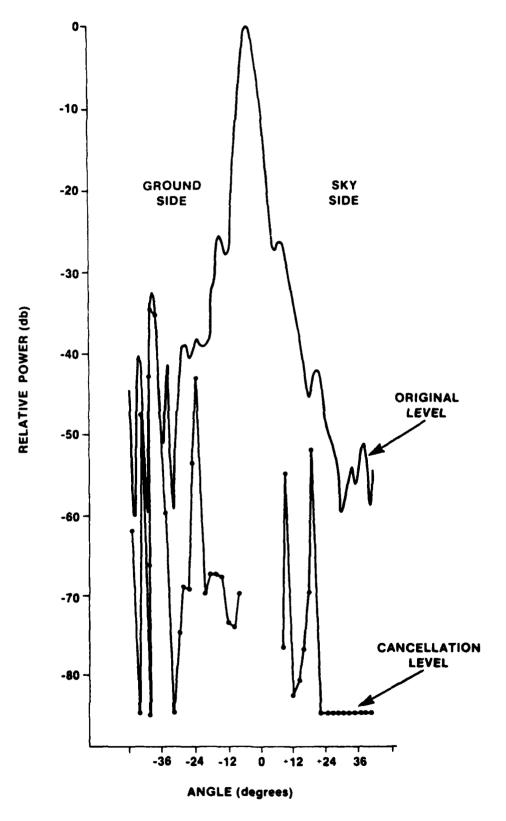


Figure 10

A NUMERICAL METHOD FOR APPROXIMATING ANTENNA SURFACES DEFINED BY DISCRETE SURFACE POINTS

Richard Q. Lee and Roberto Acosta National Aeronautics and Space Administration Lewis Research Center Cleveland, Ohio 44135

1. INTRODUCTION

Reflector antennas on earth orbiting spacecrafts generally cannot be described analytically. The reflector surface is subjected to large temperature fluctuation and gradients, and is thus warped from its true geometrical shape. Aside from distortion by thermal stresses, reflector surfaces are often purposely shaped to minimize phase aberations and scanning losses. To analyze distorted reflector antennas defined by discrete surface points, a numerical technique must be applied to compute an interpolatory surface passing through a grid of discrete points. Although numerical techniques for analyzing reflector surface distortions and doubly curved reflector surfaces have been reported in open literatures, 1-3 all these techniques are rather complicated and involve lengthy computations. In this paper, a simple numerical technique based on Taylor's expansion and finite differences approximation is presented. By applying the numerical technique to approximate the surface normals of a distorted reflector surface, the aperture field over a near-field plane is obtained using geometric

optics technique. The aperture integration method is then applied to find the radiation patterns.⁴

2. FORMULATION

The proposed numerical technique is a quadratic approximation of a distorted surface defined by a grid of nine points.

Let (x,y,z) be the coordinate of any point, P, on the surface which is described by

$$z = z(x,y)$$

The position vector of P is given by

$$\dot{\vec{r}} = x\hat{x} + y\hat{y} + z\hat{z}$$

To obtain an approximation for the surface z(x,y), the position vector is replaced by its Taylor's expansion around $\hat{r}_0(x_0, y_0, z_0)$, the closest point to the point of incidence. That is

$$\vec{r}(x,y,z) = \vec{r}_0(x_0, y_0, z_0) + (x - x_0) \frac{a\vec{r}}{ax} + (y - y_0) \frac{a\vec{r}}{ay}$$

$$+ \frac{1}{2} \left[(x - x_0)^2 \frac{a^2\vec{r}}{ax^2} + (y - y_0)^2 \frac{a^2\vec{r}}{ay^2} + 2(x - x_0)(y - y_0) \frac{a^2\vec{r}}{axay} \right] + 0(x^3, y^3)$$

where the partial derivatives of \vec{r} are evaluated at $\vec{r}_0(x_0, y_0, z_0)$. All terms higher than the quadratics of x and y have been neglected as indicated by $O(x^3, y^3)$. The surface may then be approximated by

$$z(x,y) = \hat{z} \cdot \hat{r} = z_0 + (x - x_0) \frac{\partial z}{\partial x} + (y - y_0) \frac{\partial z}{\partial y}$$

$$+ \frac{1}{2} \left[(x - x_0)^2 \frac{\partial^2 z}{\partial x^2} + 2(x - x_0)(y - y_0) \frac{\partial^2 z}{\partial x \partial y} + (y - y_0)^2 \frac{\partial^2 z}{\partial y z} \right] + 0(x^3, y^3)$$

All the partial derivatives of z are evaluated at $\dot{r}_0(x_0, y_0, z_0)$. The normals to the interpolatory surface can be found by taking the gradient of z(x,y) as follows:

$$\widehat{n} = \frac{\partial z}{\partial x} \widehat{x} + \frac{\partial z}{\partial y} \widehat{y} + \widehat{z}$$

$$n_{x} = \frac{\partial z}{\partial x} + (x - x_{0}) \frac{\partial^{2} z}{\partial x^{2}} + (y - y_{0}) \frac{\partial^{2} z}{\partial x \partial y} + O(x^{2}, y^{2})$$

$$n_{y} = \frac{\partial z}{\partial y} + (x - x_{0}) \frac{\partial^{2} z}{\partial x \partial y} + (y - y_{0}) \frac{\partial^{2} z}{\partial y^{2}} + O(x^{2}, y^{2})$$

$$n_{z} = -1$$

where (n_x, n_y, n_z) are the x, y, and z components of \widehat{n} with the normal pointing toward the source. Finite differences can be applied to approximate the partial derivatives. Since the partial derivatives are of second order, a grid of nine points is required.

The partial derivatives may be expressed as

$$\frac{a^{2}z}{ax^{2}} \sim \frac{\frac{(z_{4}-z_{0})}{(x_{4}-x_{0})} - \frac{(z_{0}-z_{5})}{(x_{0}-x_{5})}}{\frac{(x_{4}-x_{5})}{2}}$$

$$\frac{\partial z}{\partial x} \sim \frac{z_4 - z_5}{x_4 - x_5}$$

$$\frac{a^{2}z}{ay^{2}} \sim \frac{\frac{(z_{2}-z_{0})}{(y_{2}-y_{0})} - \frac{(z_{0}-z_{7})}{(y_{0}-y_{7})}}{\frac{(y_{2}-y_{7})}{2}}$$

$$\frac{\partial z}{\partial y} \sim \frac{z_2 - z_7}{y_2 - y_7}$$

$$\frac{a^2z}{axay} \sim \frac{(z_1 - z_3)}{(x_1 - x_3)} - \frac{(z_6 - z_8)}{(x_6 - x_8)}$$

where (x_1,y_1,z_1) , (x_2,y_2,z_2) ... (x_8,y_8z_8) are the coordinates of the points around the closest point (x_0,y_0,z_0) .

3. DISCUSSION AND RESULT

In applying the numerical technique to compute the surface normals, the nine closest points to the point of incidence are located by searching an array of discrete surface points defining the distorted antenna surface. Ray-tracing is then used to

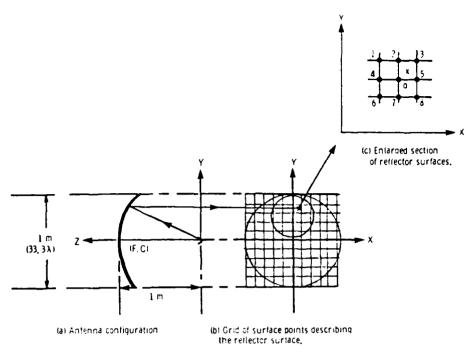
compute the reflected field from the approximated normals. The secondary far field patterns are obtained from the Fourier transformation of the aperture field distribution.

To illustrate the numerical technique, the numerical algorithm has been programmed and applied to the antenna configuration shown in figure 1. The surface grid points for an artificially "enlarged" parabolic surface are generated. Thus, the boundary points along the rim of the actual reflector surface can be included in the computation. The computed secondary far field patterns for the symmetric and the offset cases are shown in figures 2 and 3 respectively. In the figures, the E-plane radiation patterns computed from an analytic expression of a parabolic surface are drawn with solid lines, while that computed numerically are drawn with dots and broken lines. The E-plane radiation patterns computed numerically from a grid of 50x50 surface points of $\sim 0.7 \lambda$ spacing was found to compare exactly to that computed from an analytic expression. For the offset case, the aperture surface is described by fewer points; therefore, a higher density of target points is required to produce the same accuracy. With a scan step of $\lambda/3$ for the symmetric case and $\lambda/6$ for the offset case, the computer time required to compute the secondary radiation patterns numerically is 25 sec for the symmetric case and 17 sec for the offset case. respectively. For comparison purpose, the radiation pattern

for the offset case has been computed using spline function approximation.⁵ The computed E-plane pattern is shown in figure 3.

REFERENCES

- Agrawal, P.K., Kauffman, J.F., and Croswell, W.F., (1979) A
 Method for Pattern Calculation for Reflector Antennas Whose
 Geometry is Described by a Finite Number of Discrete Surface
 Points, in <u>IEEE International Symposium on Antennas and</u>
 Propagation, Vol. 1, IEEE, Piscataway, NJ, pp. 67-70.
- 2. Chan, K.K., and Raab, A.R., (1981) Surface-Current Analysis of Distorted Reflector Antenna, <u>IEE Proc.</u>, <u>Part H: Micro-waves</u>, Opt Antennas, 128:206-212.
- 3. Sletten, C.J., (1981) Ray Tracing Method for Doubly Curved Reflector Surfaces, Proc. IEEE, 69:743-744.
- 4. Lam, T.C., Lee, S.W., and Acosta, R., (1984) <u>Secondary Pattern Computation of an Arbitrarily Shaped Main Reflector</u>, UILU-ENG-84-2547. NASA Grant NAG3-419, Electromagnetics Laboratory Scientific Report No. 84-7, University of Illinois.
- Steinbach, R.E., and Winegar, S.R., (1985) Interdisciplinary Design Analysis of a Precision Spacecraft Antenna, in <u>Structures</u>, <u>Structural Dynamics</u>, and <u>Materials Conference</u>, <u>26th</u>, AIAA, New York, pp. 704-712.



現るなどと問題のなるなどの意思などのなどを見れるというとも必要ななななどのもの問題のなるとのと言葉なるとという言語を

Figure 1 - Antenna configuration used in the study,

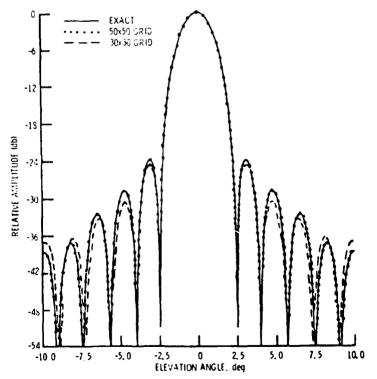


Figure 2, - E - plane pattern for the symmetric case.

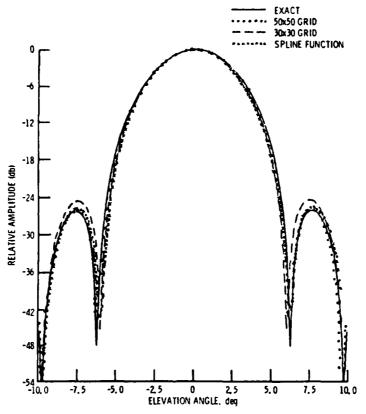


Figure 3. - E - plane pattern for the offset case.

EXPERIMENTAL TRANSFORM FEED ANTENNA

Daniel T. McGrath Rome Air Development Center Electromagnetic Sciences Division Hanscom AFB, MA 01731

Abstract

To verify the properties of transform feed antennas, Rome Air Development Center has built and tested an experimental model for azimuth-only scan. The 30-wavelength line source array is space fed by a cylindrical bootlace lens constructed of parallel plate waveguide with coaxial monopole elements. The transform feed is a parallel plate waveguide Rotman lens.

This antenna is shown to have 22% signal bandwidth at 57° scan when time delays are applied at the Rotman lens inputs. Low sidelobe patterns are achieved over the operating band and scan region. Low sidelobe difference patterns are obtained without the need for a separate feed network. With proper design, total antenna losses could be limited to less than 3 dB including element mismatch, spillover, waveguide and cable losses.

1. INTRODUCTION

Transform feed antennas have long been considered a solution to the inherent dispersion of phased arrays [1], [2]. Also known as "completely overlapped subarray" antennas, they combine the advantages of wide instantaneous bandwidth and pattern control [3]. The Rome Air Development Center (RADC) model, shown in Figs. 1-3, is an X-band, azimuth-only scan antenna, designed to demonstrate the properties of this generic architecture.

The key feature of the antenna is its nearly constant gain versus frequency at scan angles out to 55° from broadside: The 16 time delay steered subarrays correct for the natural squint of the phase-steered aperture array. In addition, amplitude tapering need only be applied at the subarrays to produce a tapered aperture illumination for low sidelobes. Reasonably good difference patterns are obtained without the need for a second feed network. Finally, the space-feed structure can result in a very efficient antenna.

This paper discusses the results obtained with the RADC model: Signal bandwidth is greater than 22% at the 55° scan angle: Peak and average sidelobes are below -20 dB and -30 dB, respectively, over the 8-10 GHz band, at both 0° and 55° scan, in both the sum and difference patterns. Losses due to element mismatch, spillover, waveguide and cables are less than 2.5 dB. Recommendations for improvements are also presented.

2. HARDWARE DESCRIPTION

There are three major components in the completely overlapped subarray antenna (COSA), shown in Fig. 3. The largest is the cylindrical objective lens, whose front face is the 60-element aperture array. A 16-beam Rotman lens feeds that objective lens through a 2-foot radius parallel-plate waveguide cavity. The Rotman lens linear output face is centered at the objective lens focal point. The amplitudes applied to the Rotman lens beam ports are set in the third major component, the corporate feed. Amplitude weighting is set with fixed, coaxial attenuators. The coaxial line stretchers shown are for phase trimming only: the time delays are in the coax cables joining them to the beam ports. The three power splitters shown in Fig. 3 are commercial stripline units. The small two-way splitter was later replaced with a "magic tee" hybrid for forming simultaneous sum and difference patterns.

2.1 Objective Lens

The purpose of the cylindrical lens is to focus an incident wave onto the Rotman lens feed. Because scanning is performed by phase shifters in the transmission lines joining the two faces, it need not be a wide angle lens.

A cylindrical lens was chosen for two reasons [4]: the line lengths are all the same; and it allows a very short focal length, resulting in a compact antenna. Usually, the back face elements are

located directly behind their corresponding front face elements [5], [6], which was our initial approach. Unfortunately, the resulting element spacings along the cylindrical face varied by more than 33%. Under that circumstance, impedance matching the entire back face with a single element design (probe length and ground plane spacing) was not possible.

The final design of the lens, as Fig. 3 shows, uses uniformly-spaced back face elements. As described in [7], that (carefully chosen) spacing does increase the scanning aberrations of the lens, but that only affects the antenna's performance at the extreme limits of scan angle and frequency.

To test the cylindrical lens independently of the rest of the antenna, we connected a 4-way power divider to the center 4 focal array elements. With the outside two ports weighted -10 dB relative to the center two, this simulates the ideal Rotman lens outputs for broadside scan. Measured E-plane patterns are shown in Fig. 4.

2.2 Rotman Lens

The essential structure of the Rotman lens is the same as the objective lens: All elements are coaxial monopole probes with their center conductors extending into parallel-plate guide. Each array of probes is backed by an aluminum spacer that forms an image plane (see inset of Fig. 3). In contrast to the cylindrical lens, the beamformer in the COSA has to be a wide-angle lens. Its outermost

beams illuminate the edges of the objective, which are at $\pm 45^{\circ}$ relative to the focal array's broadside.

Our design used g=1.137 [8], with perfect foci at ±30°. The coax cables are phase-trimmed to the proper lengths "w." A quadratic length is subtracted from w to correct for the shape of the focal array: Ideally it should be circular, with radius equal to the objective's focal length.

A major modification to the Rotman lens was the interleaving of terminated (dummy) elements with the 16 active beam ports. The required angles of the 16 beams dictated a spacing of about $.7\lambda_0$ (f₀=9 GHz). Tomasic and Hessel [9] have shown (Fig. 5) that the element pattern is severely narrowed for spacings greater than $.6\lambda$. The dummy beam ports decreased the spacing to $0.35\lambda_0$, greatly improving the illumination of the antenna ports, as illustrated in Fig. 6.

Unfortunately, those dummy ports absorb half the power incident on the beam port array, with a consequent 3 dB reduction in antenna gain. On the other hand it is certainly possible to sum those extra ports in a second corporate feed. Alternatively, a smaller Rotman lens might reduce the length of the beam port arc, with a consequent reduction in element spacing.

Element spacings of both the beam port and the antenna port arrays were nonuniform. However, unlike the cylindrical array, the variation in spacing was only about 10%. Impedance matching those arrays for the

average spacing has apparently worked quite well. Patterns of a few of the Rotman lens beams are Fig. 7.

2.3 Corporate Feed

The corporate feed, or variable power divider is designed to apply the proper amplitudes and phases to the Rotman lens inputs. Fixed co-axial attenuators set the amplitude weights. They are followed by co-axial line stretchers for minor phase adjustments. These were required because the near-in sidelobe levels are extremely sensitive to errors in the corporate feed.

We have two sets of cables to link the corporate feed outputs to the beam ports: one for broadside scan; the second for 55° scan. The first set is phase trimmed to correct for the shape of the beam port arc, whose center of curvature is not at the center of the antenna port array. These cable lengths equalize the electrical path lengths from the power divider outputs to the center of the antenna port arc. The second set includes this correction, but also implements the time delay steering.

The pattern of the Rotman lens feed, when driven from the 16-way power divider is Fig. 8. The dashed line of this figure is the ideal pattern. With the Rotman lens feed inserted into the waveguide cavity behind the cylindrical lens, this will be the shape of the aperture distribution. The variation between the desired and actual distribution is

due more to amplitude errors in the corporate feed than to any fault in the Rotman lens.

EXPERIMENTAL RESULTS

3.1 Broadside Scan Measurements

Measured sum and difference patterns are shown in Figs. 9 and 10.

Random errors are somewhat higher at 8.25 GHz than at other frequencies, accounting for the higher average sidelobe level as well as filling of the central null in the difference pattern.

Fig. 11 is an analysis of the antenna gain. The measured gain is the lowest curve, with encircled points. The other of the two lower curves is the predicted gain, found as follows: The theoretical maximum gain is that of the flared aperture, and is given by Schelkunoff & Friis [10] and is the top curve on the plot. The two crosshatched areas represent unavoidable losses. The first is the sum of mismatch losses of all five probe arrays, calculated from Tomasic's theory [9]. The second is the measured loss in the objective lens and Rotman lens cables, plus the calculated loss through the 2 'space-feed region. The next, unshaded region is the 3 dB lost to the dummy Rotman lens beam ports. The most significant loss in the system, however, is the 6-7 dB in the corporate feed, because we have used fixed attenuators for amplitude weighting. Use of directional couplers instead would reduce that loss substantially.

4.2 550 Scan Measurements

For 550 scan, the theoretical maximum gain is reduced by 2.4 dB due to cos 550 scanning loss. In addition, the aperture array has a much higher

active impedance. Except near 10 GHz, where the grating lobe begins to appear on the opposite side of the pattern, the predicted and actual gains agree to with 1.5 dB, indicating that all significant losses are accounted for. The reduction in antenna gain is apparent also in the higher average sidelobe levels in the patterns of Fig. 13.

The 9 GHz pattern has a prominent sidelobe at 27°. It is caused by multiple reflections between faces of the objective lens. The impedance mismatch of the aperture array, on transmit, reflects some power back toward the feed. The cylindrical array then re-reflects a portion of that back toward the aperture, to be radiated as an error lobe. If ψ was the inter-element phase required to scan the array to 55°, the angle of the error lobe will be $\theta_e = \sin^{-1}[(3\psi - 2\pi)/kd]$. At 8.25 GHz, the array is matched better at 55°, and the mismatch error lobe is indistinguishable from the remaining sidelobes. At 9.75 GHz, the lobe appears at 40°.

In the 8.25 and 9.75 GHz patterns, there are pairs of sidelobes at, respectively, -5° , -28° and $+3^{\circ}$, -18° . These are caused by the linelength phase shifts at the aperture. Those cables are trimmed modulo- 2π at 9 GHz. At all other frequencies, the inter-element phase shift will have periodic discontinuities, causing error sidelobes. This is a phenomenon associated with line-length phase shifters, rather than any peculiarity of the COSA architecture.

The most important feature of these patterns is that the main beam is at exactly 55° for all frequencies. The time delay steering has eliminated the squint that would have shifted the beam to 63.3° and 49.1° at 8.25

and 9.75 GHz, respectively. The same is true for the central null of the Δ patterns of Fig. 14.

4. SUMMARY

The important features of the completely overlapped subarray antenna design have been experimentally verified. Good pattern control is obtained over very wide bandwidths and wide scan angles. Low sidelobe sum and difference patterns are possible using only a single feed network, and amplitude weighting only at the subarray level. Time delay steering applied at the subarrays yields wide instantaneous bandwidth. Although substantial losses were accepted for expediency in this demonstration model, the design itself is quite efficient due to its space-feed structure.

ACKNOWLE DGEMENTS

The author credits Hugh L. Southall, now at AFSC/DL, with the initial design and fabrication of this antenna; and thanks him for sharing his knowledge and experience. Thanks also to the personnel of RADC's Ipswich site: Edward Martin, James Kenney and Calvin Perkins for measurement support; and Raymond Schofield for machinework.

REFERENCES

- 1. R. Tang, "Survey of Time-Delay Beam steering Techniques," Phased Array Antennas, Artech House, 1970. p. 254.
- 2. J. Frank, "Bandwidth Criteria for Phased Array Antennas," Phased Array Antennas, Artech House, 1970. p. 243.
- 3. R.L. Fante, "Systems Study of Overlapped Subarrayed Scanning Antennas," IEEE Trans. Antennas Propagat., AP-28, Sept. 1980, pp. 668-679.
- 4. H.L. Southall, "Completely-Overlapped-Subarray Fed Antenna for Broadband, Wide Scan Angle, Low Sidelobe Radar Applications," 1980 Antenna Applications Symposium, Monticello IL.
- G.V. Borgiotti, "An Antenna for Limited Scan in One Plane: Design Criteria and Numerical Simulation," <u>IEEE Trans. Antennas Propagat.</u>, AP-25, Mar. 1977, pp. 232-243.
- R.J. Mailloux, "Off-Axis Scanning of Cylindrical Lenses," <u>IEEE Trans.</u> <u>Antennas Propagat.</u>, AP-31, July 1983, pp. 597-602.
- 7. D.T. McGrath, "A High-Efficiency, Low Phase Error Waveguide Lens for a Transform Feed Antenna," 1984 Antenna Applications Symposium, Vol. I, ADA 153257.
- 8. W. Rotman and R.F. Turner, "Wide-Angle Microwave Lens for Line Source Applications," IEEE Trans. Antennas Propagat., AP-11, Nov. 1963, pp. 623-632.
- B. Tomasic and A. Hessel, "Linear Phased Array of Coaxially Fed Monopole Elements in a Parallel-Plate Guide, 1982 APS Symposium Digest, pp. 144-147.
- 10. S.A. Schelkunoff and H.T. Friis, Antennas: Theory and Practice, John Wiley and Sons, 1952, p. 527.

score is sociolos indescribant indicatant indicatant in

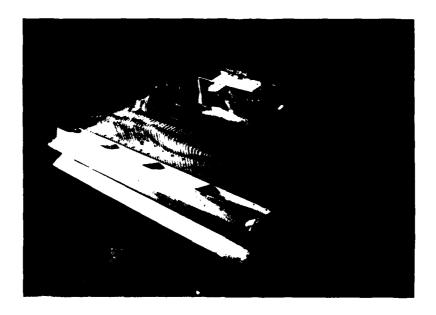


Figure 1. Completely Overlapped Subarray Antenna



Figure 2. Pedestal-Mounted Antenna

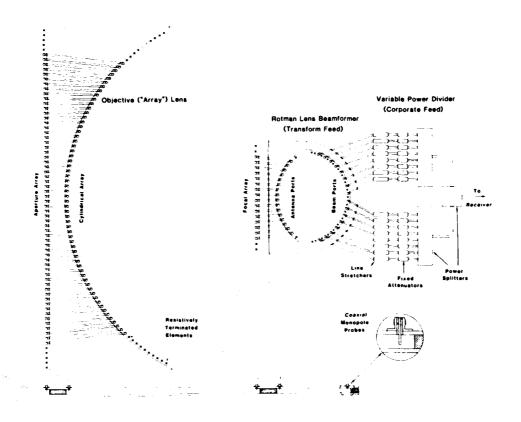


Figure 3. Hardware Outline Drawing

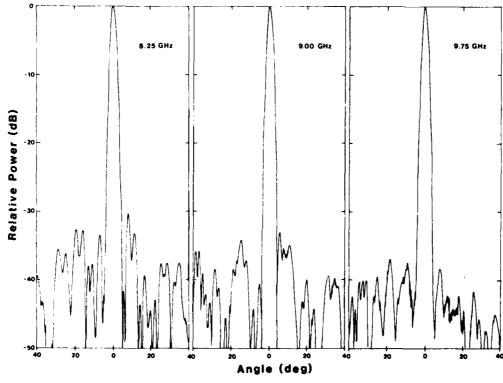


Figure 4. Measured Patterns of Objective Lens with 4-Way Power Divider Feed 370

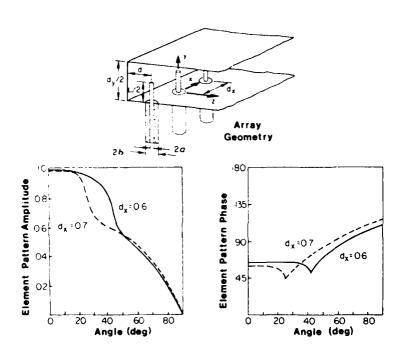


Figure 5. Array Geometry and Element Patterns (after Tomasic & Hessel)

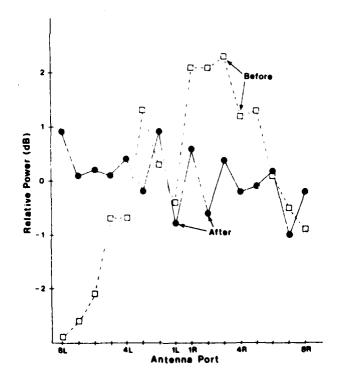


Figure 6. Measured Power at Rotman Lens Antenna Ports from Beam Port 1L, Before & After Addition of Dummy Beam Ports (9GHz)

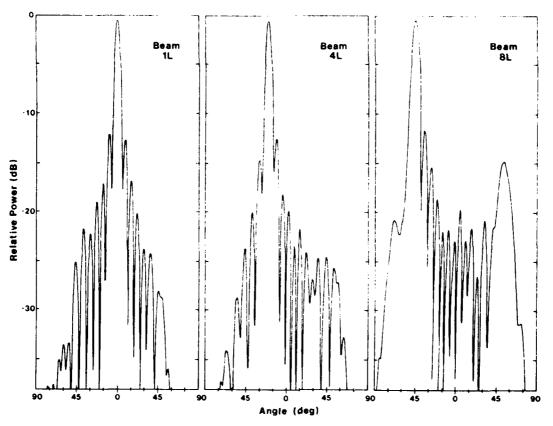


Figure 7. Measured Rotman Lens Beam Patterns (9GHz)

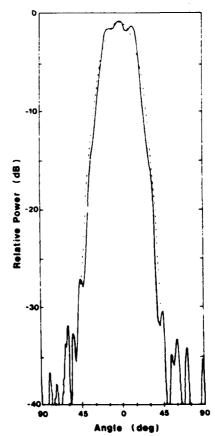


Figure 8. Rotman Lens Pattern with all 16 Beam Ports Driven by Corporate Feed. Dashed Line is Desired Pattern.

いる。最初というないは、自然のないのでは、

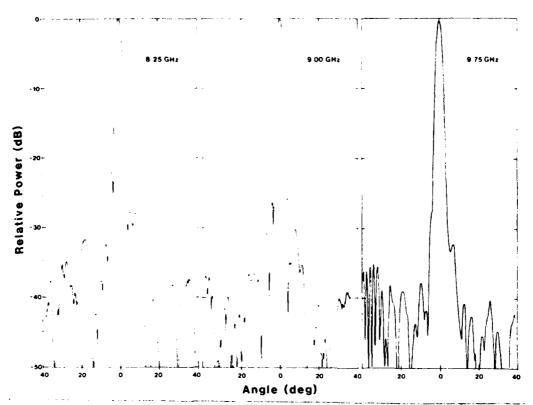


Figure 9. Measured Patterns of Complete Antenna, Broadside Scan

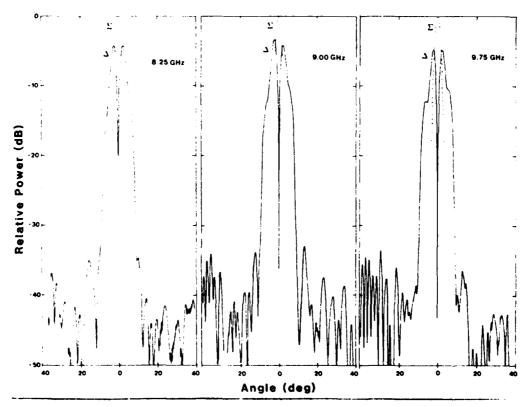
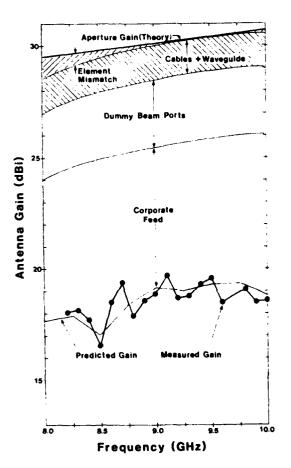


Figure 10. Measured Broadside Scan Difference Patterns



を見た。こうこと、Ample ススススススス

学科はいったいいでは関いられながながながら問わらっしからから問題で

Figure 11. Broadside Scan Gain Analysis

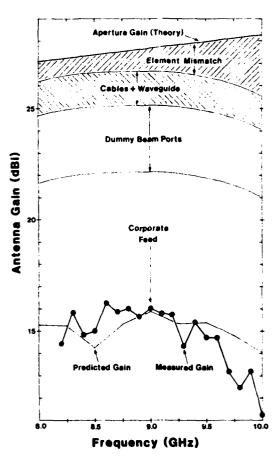


Figure 12. 55⁰ Scan Gain Analysis

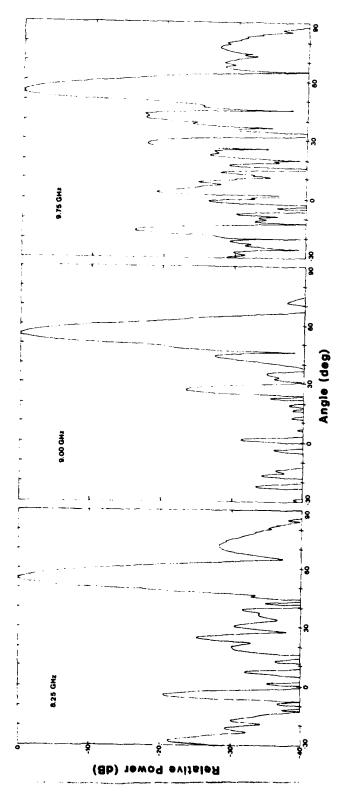
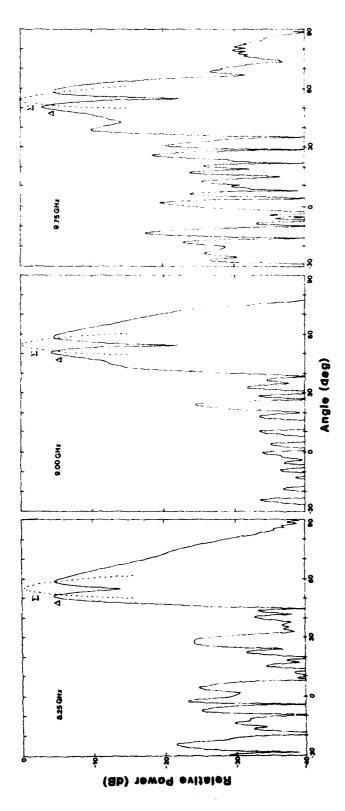


Figure 13. Measured Sum Patterns, 55º Scan



gure 14. Measured Difference Patterns, 55º Scan

HIGH EFFICIENCY MULTIBEAM ANTENNA DESIGN

P. INGERSON, C. A. CHEN

TRW Antenna Systems Laboratory

Redondo Beach, CA

I. INTRODUCTION

In many millimeter wavelength satellite communication systems, there is a need to provide multiple high gain independent beams covering an angular region of space. It is usually highly desirable to provide the multiple beams from a single aperture if possible to reduce size, weight and complexity of the antenna system. In addition to providing maximum gains, in many cases it is also required to have low sidelobe radiation patterns to minimize out of beam interference.

The desire to provide multiple high-gain beams from a single aperture (lens or reflector) usually leads to beam peak gains which are typically -3dB or more lower than one can achieve using a single optimum feed at the lens or reflector focus. As will be discussed, this is due to a fundamental limitation of conventional focusing lens or reflector type antennas. The problem is to provide the multiple beams from the antenna with gains comparable to the optimized single beam antenna.

The basic limitations of focusing antenna systems is that the secondary radiation pattern is directly related to the aperture size. In the present approach, this limitation is overcome by using non-focusing (diverging) reflector or lens antennas. These antennas can be designed to provide the required secondary beamwidth essentially independent from the aperture size.

Given a minimum required feed horn size or feed separation, a single non-focusing aperture can be designed using the method presented which will allow almost any beam to beam separation or cross-over level desired while providing beam gains which are essentially equal to the optimum single beam of a focused aperture.

The independence from feed to feed separations of this design technique is particularly useful in the cases where switches, receivers or amplifiers are to be placed as close to the feed elements as possible, since these components often determine the minimum allowable separations.

This paper describes the design of a 37 beam EHF (43.5 - 45.5 GHz) antenna providing high gain, contiguous beam coverage of the earth from a synchronous orbit satellite. The angular region of the earth from synchronous orbit is approximately \pm 8.68 degrees, requiring about a 2.9 degree beam separation and a 3.3 degree HPBW to provide contiguous coverage at the -3dB level or better as shown in Figure 1.

II. THEORY

II.a Conventional Reflector or Lens Design

A fundamental limitation arises when attempting to produce contiguous spot beams space approximately one half-power beamwidth apart from a single conventional reflector (or lens aperture). There is a fundamental disparity between the feed horn aperture size required to maximize the gain of the antenna and the horn size necessary to permit packing beams approximately one beamwidth apart. It can be shown that the feed horn diameter required to maximize gain is substantially larger then the horn diameter that will permit close (-3dB cross-over) beam packing in a single conventional focusing reflector or lens. Accordingly, horn aperture size that yield maximum gain lead to beam separations much

larger than one half-power beamwidth even though the feed horn apertures are contiguous. This fundamental limitation of a conventional reflector and lens is independent of the focal length to aperture diameter (F/D) ratio. This limitation is demonstrated in Figure 2 which shows the relative gain of a conventional reflector as a function of the reflector included angle (θ inc). Keeping the feed pattern constant, corresponding approximately to a 1 inch (\approx 4 wavelength (λ)) aperture feed horn, θ_{inc} was varied from the 'alue that yielded maximum gain for a 3.3 degree beam ($\theta_{\mbox{inc}} \simeq$ 32 degrees) to other values of $\theta_{\mbox{inc}}$ while maintaining the beamwidth constant at 3.3 degrees. Figure 2 shows that einc must decrease to approximately 15 degrees before -3dB beam cross-over is achieved. other words, if one uses 37 one inch diameter feed horns in a single conventional reflector to achieve earth coverage with 37 3.3 degree spot beams, the achievable aperture efficiency of each beam is approximately 3dB less than that obtainable from an optimized reflector design using a single 1.0 inch (4^{λ}) diameter feed horn.

II.b Alternative Reflector Design Techniques

There are three basic approaches that can be applied to the fundamental problem associated with close beam spacing (-3dB beam cross-over) to increase the minimum coverage gain, these are:

- o Increase the number of beams used to provide coverage
- O Use more than one reflector aperture to produce the collection of spot beams
- O Use non-focusing apertures which circumvent the fundamental limitation problem.

If we wish to fix the number of beams from system compelxity considerations, then only the last two approaches are applicable.

II.c Multiple_Reflector_Apertures

As pointed out, if the feed horn diemnsions are selected to maximize the reflector gain, the beams generated by two adjacent contiguous feeds will be spaced much further apart than one half-power beamwidth. One method of obtaining a pattern of contiguous spot beams crossing over at the -3dB level is to generate adjacent beams from separate reflectors. This technique is illustrated in Figure 3 which shows the feed horn sets assigned to three separate reflectors. Reflector No. 1 radiated 13 beams while reflectors No. 2 and No. 3 radiate 12 beams each. The beam positions produced by each feed set are also shown in the Figure. The closest spacing that occurs between beams produced by adjacent feed horns in the same set is about 1.73 x half-power beamwidth. This larger separation between beams produced by adjacent feeds allows the included angle of the reflector to be larger and much nearer to the optimum feed horn dimension.

The reflector diameter required for this three-reflector system is about 5 inches (20^{λ}) for each reflector. Because the feed horn dimension is now reasonably close to that of an optimum single feed producing a 3.3 degree beam, the gain loss from excessive illumination spillover is reduced to about 0.6dB as shown in Figure 2. The edge illumination is, however, still high and hence there is no means of controlling the sidelobe levels.

Sidelobe level control with high edge illumination is possible only using composite multiple feed clusters or using artificial edge tapering of the aperture using lossy material. The composite feed technique would require additional feed elements and a complex interconnecting feed network. The artificial edge tapering would substantially reduce the beam gain.

II.d Non-Focusing_Apertures

The fundamental limitation of focusing aperture can be circumvented by utilizing a non-focusing hyperbolic reflector (or diverging lens). differences between focusing and non-focusing apertures are depicted in Figure 4. The shaped reflector result can also be approximated quite closely by using a parabolic surface contour combined with a highly tapered aperture illumination and axial defocusing of the feed horn as shown in Figure 5. With axial defocusing the secondary beamwidth can be made essentially independent of the reflector diameter. With a hyperbolic reflector, any feed at the focus point located at the right side of reflector can be thought of as producing an image feed at its image focus point whose pattern HPBW is reduced by the reciprocal of the magnification factor M. The beamwidth of secondary pattern is then controlled by the magnification factor M and horn aperture and is essentially independent of the diameter of reflector unlike the parabolic reflector. The relationship between M, horn aperture and secondary HPBW is shown in Figure 6.

Therefore, by using the hyperbolic reflector, we can optimize the gain and/or sidelobe performance first and then adjust the diameter of the reflector to permit close (-3dB cross-over) beam packing. All 37 beams with -3dB cross-over, as shown in Figure 1 can be produced from a single 20.7 inch diameter reflector. The extremely low edge illumination (-30dB) utilized provides negligible feed illumination spillover, higher gain and beam efficiency, and very low sidelobes for the beam.

The advantages of the design technique are:

o Allows high-gain, high efficiency multiple beams from a single antenna aperture (lens or reflector)

- o Independent of feed size and feed to feed separation over a very wide range
- o Allows very wide range of beam to beam separations or cross-over levels
- o Allows efficient and simple sidelobe control by illumination taper

III. DETAIL ANTENNA DESIGN

The multi-beam antenna is shown in Figure 7 and the antenna system block diagram in Figure 8. The antenna system comprises a single reflector and 37 feed modules. The single reflector is an offset hyperboloid with 21.66 inch projected diameter, a 5.75 magnification and a 19.34 inch focal length. The feed modules are arranged in seven rows with trianglular planar grid patterns. As shown in Figure 9, this provides 37 independent beams of approximately 3.3 degrees HPBW covering a 10 degree elevation angle FOV on the earth. Each feed module comprises a feed horn, polarizer and, through RF switches, a downconverter/amplifier. The feed horn is a 1-inch square aperture multimode horn. In use, the IF outputs of the downconverters are connected to an IF switch which selects a number of possible beams for further signal processing.

To meet the reliability goals, the 37-horn feed system utilizes 44 downconverter amplifier modules. In the baseline redundancy scheme, there is one redundant downconverter for each row and a failure in any module in the row can be switched out as shown in Figure 10. With the redundancy switches, the probability of surviving over 10 years, with 3dB or less degradation for all 37 beams is estimated to be 98 percent. The baseline redundancy scheme requires 81 ferrite switches. The

downconverter/amplifier module is comprised of a fineline mixer, bandpass filter, and FET amplifiers.

The downconverter/amplifier module is 1.0 x 1.0 x 2.5 inches in size and as shown in Figure 11, with feed horn and switch included, weighs about 5 ounces. An IF frequency of 5.4 ± 1.0 GHz was selected so that the signal can be readily dehopped after the IF switch. Power from a local oscillator (LO) is distributed to the 44 modules by a waveguide power divider. Each module requires about 1.1 watts of dc power and 10 mW of LO power at 39.1 GHz. The LO drive source and IF switch are not considered part of the antenna study.

Key objectives of the antenna design are lightweight, minimum power consumption and high reliability. Consequently, the downconverter amplifier modules incorporate high efficiency diodes, require minimum LO drive, and are configured for a soft failure mode, using one redundant downconverter per row.

The breadboard unit of downconverter is shown in Figure 11. A performance summary is given in Table 1. For the performance estimates of the antenna, the measured pattern data of this breadboard feed was used as input to a computer program which is capable of calculating the secondary patterns of concaved hyperbolic surfaces with scanned feeds. The final calculated pattern coverage is shown in Figure 12. The performance estimates are given in Table 2. In the following section, the extremely close agreement between the measured and calculated results show that the computer generated designs are realizable.

IV. EXPERIMENTAL VERIFICATION OF BREADBOARD DESIGN

In order to verify the predicted performance characteristics of the antenna, a breadboard model was built. The breadboard model is comprised

of an offset hyperbolic reflector, and a subsection of the 37 element array of 12 feed horns and polarizers.

The experimental measurement of the breadboard model was divided into two parts. The first part was the RF far field measurement of the offset hyperbolic reflector with a single feed horn. This single feed horn was moved over the focal plane to find the best feed locations. Thirty-seven feed locations were then identified to obtain optimum coverage contour patterns. The measured coverage contour patterns were verified by the theoretical computer calculation inputting the measured 37 feed locations into computer software. It was understood that performance of the reflector with a single feed horn may be different from that with the horn within cluster due to mutual coupling within cluster. The blockage effects of the array were simulated by using a metal plate of the full array size about the feed horn.

The second part of the breadboard measurement was the RF far field measurement of the offset hyperbolic reflector with 12 feed horn cluster. In this measurement, the effects of mutual coupling within cluster were shown to be negligible.

IV.a RF_Measurement_of_Offset_Hyperbolic_Reflector_with_Single_Feed_Horn

The antenna configuration for these measurements is shown in Figure 13. The dimension of the offset hyperbolic reflector is 21.66 inches with a focal length of 19.34 inches. The feed horn was the 1-inch square aperture multi-mode horn which has excellent pattern characteristics over a wide beamwidth. The polarizer was a quarter wave plate vane made of Duriod. The axial ratio of this horn with polarizer over frequency band (43.5 to 45.5 GHz) was less than 0.3dB. The VSWR of the feed horn polarizer was less than 1.04 VSWR.

To demonstrate the coverage of the antenna, only 20 beams were needed due to symmetry in antenna configuration. In measuring these 20 beams, it was necessary to adjust the feed horn location to obtain the optimum coverage, up to 10 degrees elevation angle field of view on the earth. Figure 14 shows the typical measured contour patterns. The boresight beam, beam number one, is shown in Fgiure 14a. The sidelobe is well under 30dB with almost perfect circular contours. The beamwidth is 3.3 degrees. When the beam is scanned to position number 4, as shown in Figure 14b, it can see that beam contour shape is distorted slightly, although sidelobe is still well below -30dB. When the beams were scanned to the upper elevation direction (Figure 14c) and lower elevation direction (Figure 14d), the distortion of beam shape was different because the non-symmetrical offset hyperbolic reflector. The sidleobes were still well under -30dB. The mutual coupling within cluster in these measurements was not included beacuse of single feed horn measurement.

The 20 measured beam contours were then combined to show the contour coverage of the offset hyperbolic reflector. Figure 15a shows the composite contour coverage at 44.5 GHz. These figures show that the offset hyperbolic reflector can have the coverage up to 10 degrees elevation angle view.

The 20 experimental optimum feed locations found experimentally were then fed into a computer program to calculate the theoretical contour coverage. These theoretical contour coverages were then compared to the measured data as shown in Figure 15. This verified that the computer program developed for offset hyperbolic reflectors is very accurate.

IV.b RF_Measurement_of_Offset_Hyperbolic_Reflector_with_Feed_Cluster

The purpose of this measurement was to find both the effects of mutual coupling within the cluster and the blockage due to cluster.

A feed cluster with 12 feed horns as shown in Figure 16 was assembled. This feed cluster represents one-third of the 37 feed horns. 'From the measured patterns, it is shown that the effects of mutual coupling and blockage of cluster are negligible. The 24 measured contoursare combined as shown in Figure 17 to show the composite contour coverage of the offset hyperbolic reflector with the feed cluster. Figure 17b shows the theoretical calculated contour coverage. A comparison of Figures 17a and 17b again shows the contours are almost identical.

聞きていなからな金属をフランシンとの発育できたったからの金属なられるののでの時間なる

Table 1. Downconverter Performance Summary

RF FREQUENCY	43.5 - 45.5 GHz
IF FREQUENCY	6 - 8 GHz
LO FREQUENCY	39.1 GHz
LO POWER INPUT	10 dBm
DC BIAS	12V AT 92 mA
LO TO RP ISOLATION	> 25 dB
RF INPUT LEVEL AT 1 dB COMPRESSION	-7 dBm
CONVERSION GAIN	20 dG MIN
NOISE FIGURE	9.7 dB MAX
IF PORT VSWR	1.6:1 MAX
RF PORT VSWR	2:1 MAX
LO PORT VSWR	1.6:1 MAX
WEIGHT	3.1 OZ

Table 2. Performance Summary of High Gain Antenna

Frequency Band	43.5-45.5 GHz
Polarization	СР
Antenna Field-of-View	17.4 Degrees
Number of Beams	37
Peak of Beam Gains	≥ 34 dB
Minimum Coverage Gain	≥ 31 dB
Probability of All 37 Beams for 10 Years (3 dB or Less Degradation)	≥ 0.9

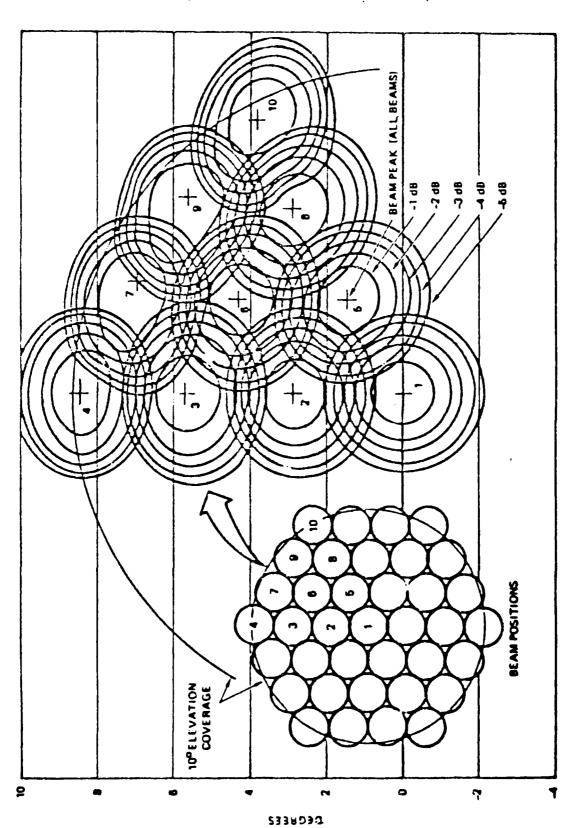


FIGURE 1. RELATIVE BEAM POSITIONS FOR CONTIGUOUS COVERAGE OF EARTH

FIGURE 2. REFLECTOR GAIN AS A FUNCTION OF REFLECTOR INCLUDED ANGLE (0_{INC}).

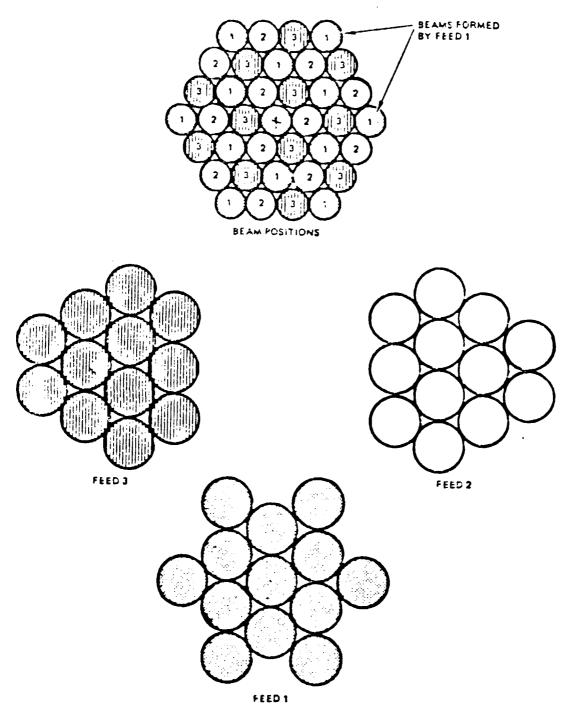
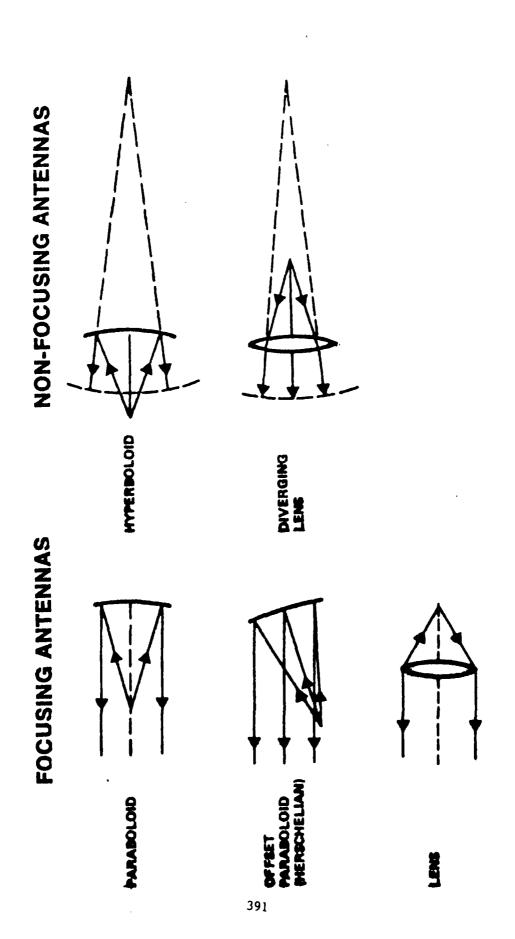


FIGURE 3. FEED HORN ARRANGEMENT FOR THREE REFLECTOR SYSTEM.



これもは、関ランないのでは、国際などないないは、国際の

FIGURE 4. EXAMPLES OF FOCUSING AND NON-FOCUSING ANTENNAS

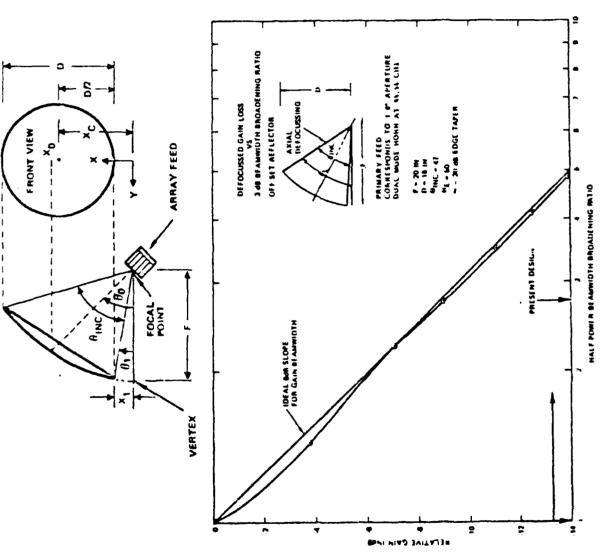
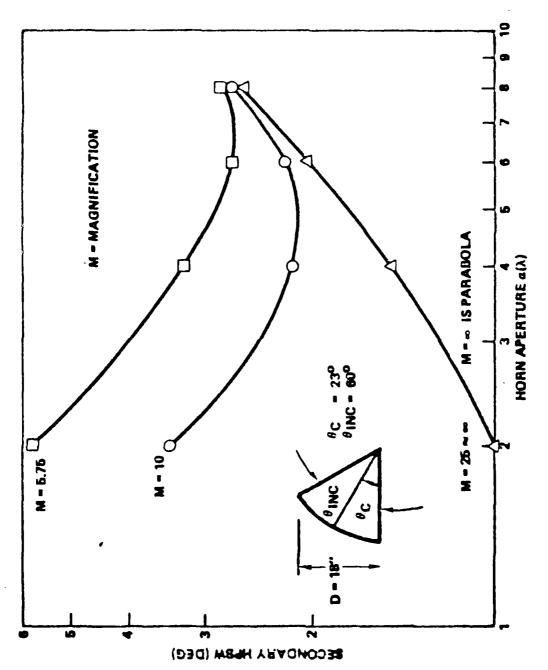
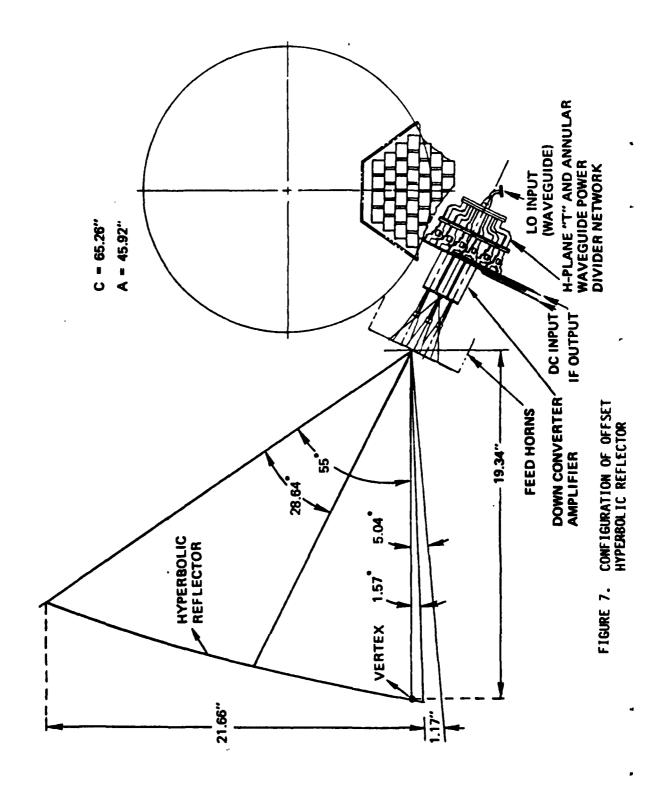


FIGURE 5. SECONDARY HALF-POWER BEAMWIDTH OF A DEFOCUSED PARABOLIC REFLECTOR WITH HIGH APERTURE ILLUMINATION TAPER.

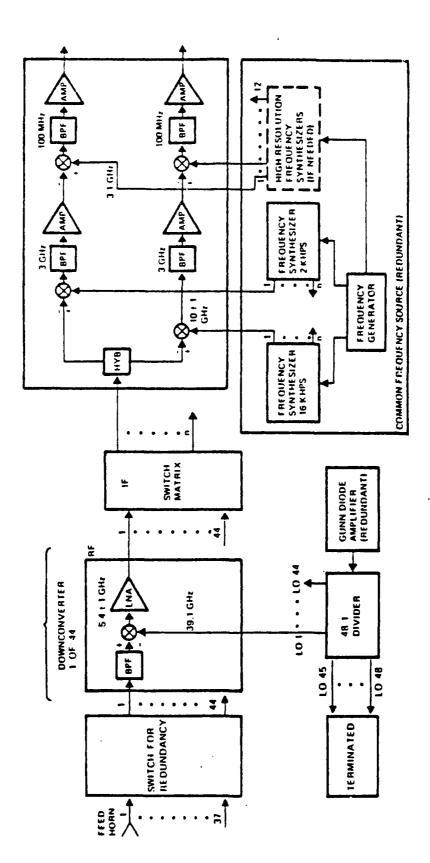


このなる 重しているのかに

FIGURE 6. SECONDARY HALF-POWER BEAMWIDTH OF A HYPERBOLA AS A FUNCTION OF HORN APERTURE AND MAGNIFICATION.

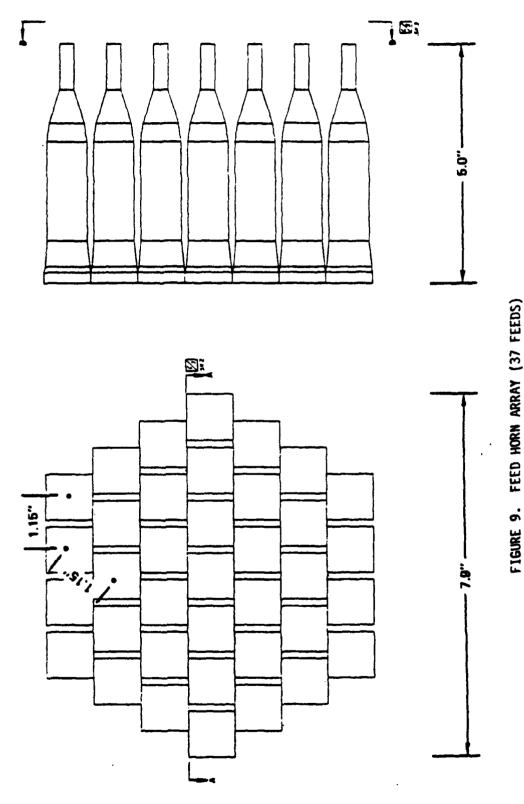


The state of the s



THE PROPERTY OF THE PROPERTY O

FIGURE 8. ANTENNA SYSTEM BLOCK DIAGRAM



396

TO SECURE OF THE PROPERTY OF T

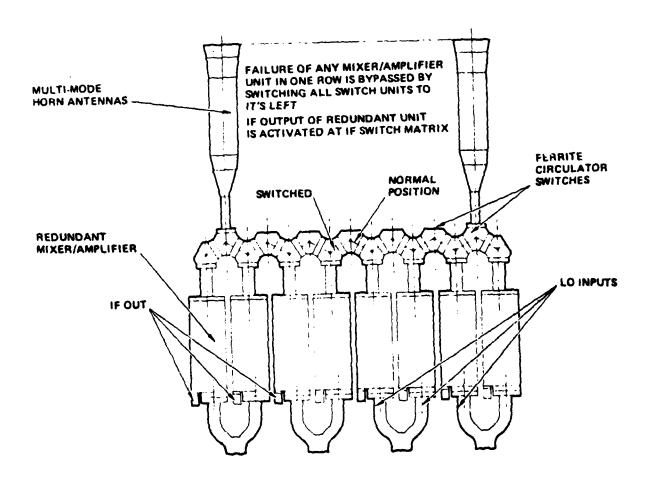
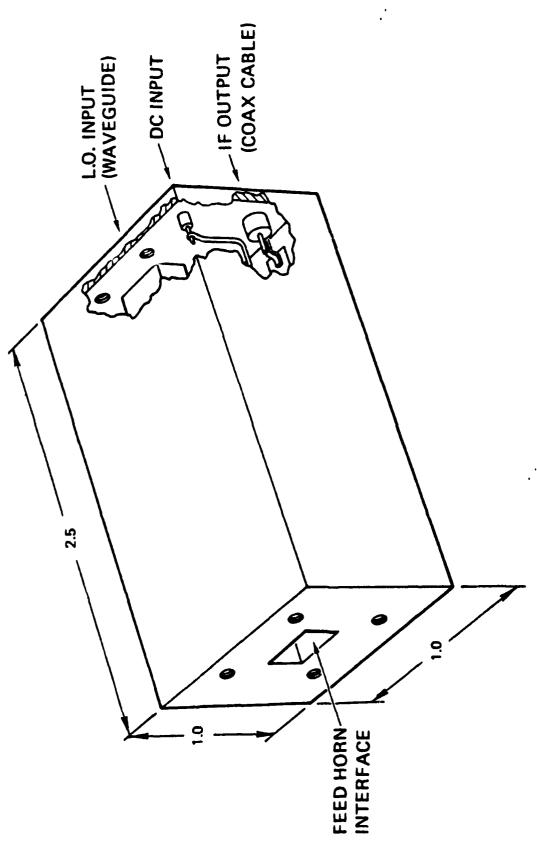


FIGURE 10. REDUNDANCY SCHEME USING FERRITE CIRCULATOR SWITCHES



CONTROL TO CONTROL DE CONTROL DE

FIGURE 11. DOWNCONVERTER CONFIGURATION

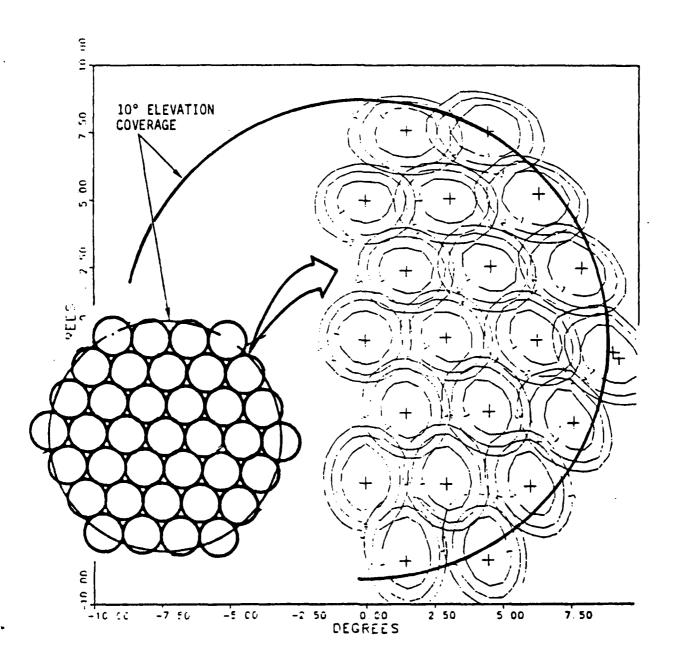


FIGURE 12. CALCULATED PATTERN COVERAGE

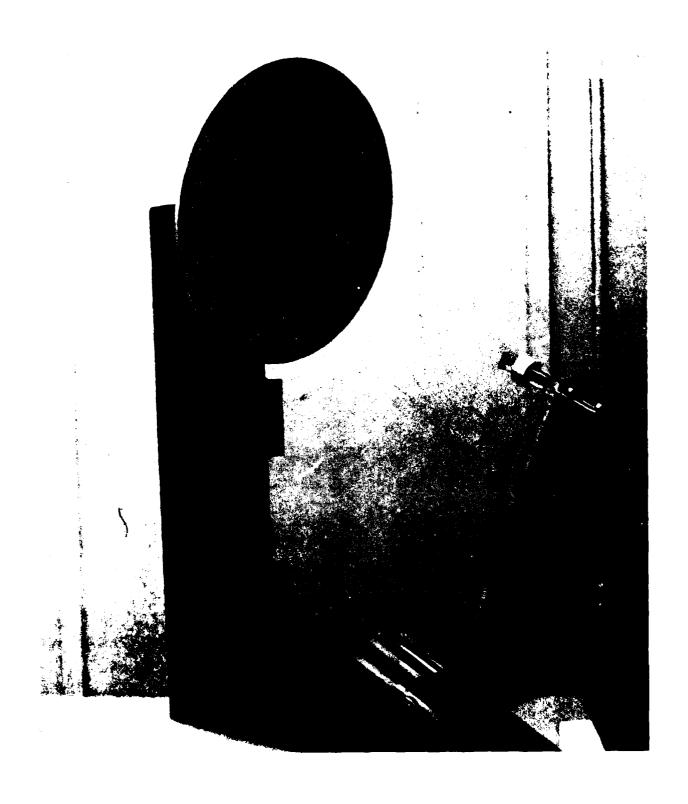
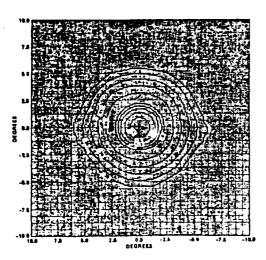
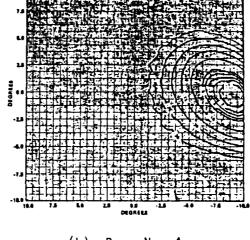


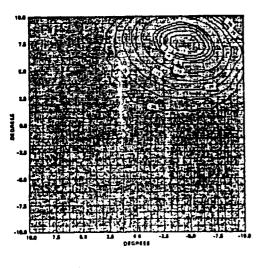
FIGURE 13. OFFSET HYPERBOLIC REFLECTOR



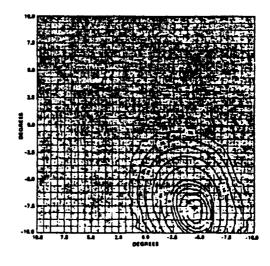
(a) Beam No. 1 Boresight Beam



(b) Beam No. 4



(c) Beam No. 12



(d) Beam No. 20

FIGURE 14. TYPICAL MEASURED CONTOUR PATTERN OF HYPERBOLIC REFLECTOR

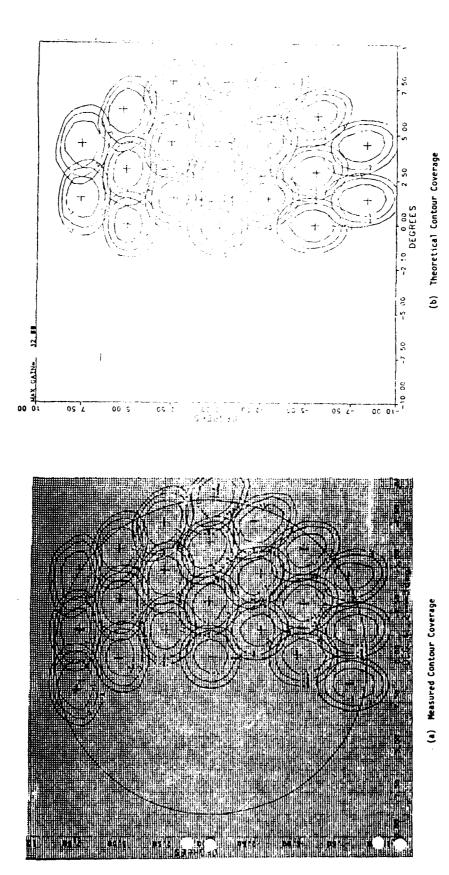


FIGURE 15. COMPARISON BETWEEN THEORETICAL AND MEASURED CONTOUR COVERAGE OF OFFSET HYPERBOLIC REFLECTOR

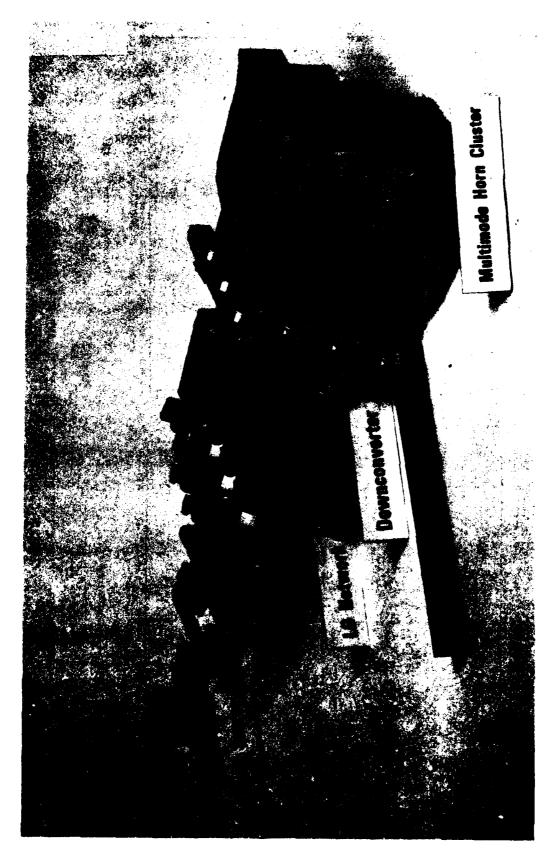


FIGURE 16. 12-ELEMENT CLUSTER

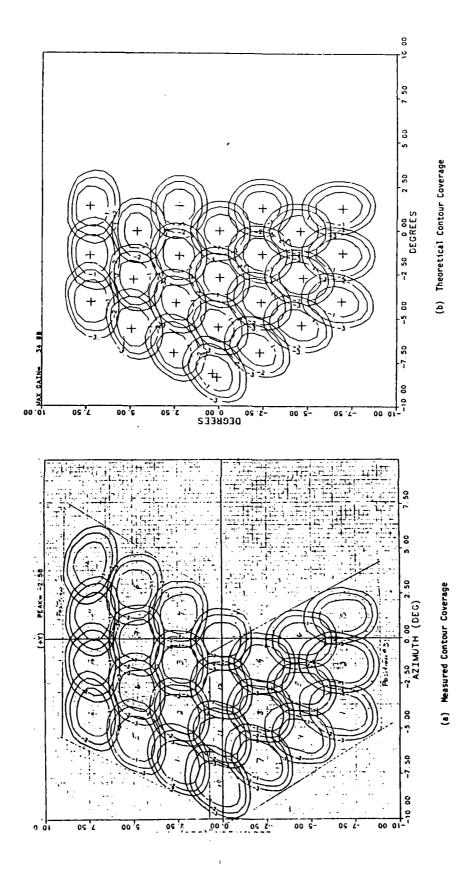


FIGURE 17. COMPARISON BETWEEN THEORETICAL AND MEASURED
CONTOUR COVERAGE OF OFFSET HYPERBOLIC REFLECTOR
WITH CLUSTER FEED

ではないなが、 なんのかない

ON THE USE OF THE NUMERICAL ELECTROMAGNETICS CODE (NEC) TO SOLVE FOR THE INPUT IMPEDANCE AND RADIATIVE EFFICIENCY OF LOADED, THIN-WIRE ANTENNAS

by

B. M. Halpern and R. Mittra

Electromagnetic Communication Laboratory
Department of Electrical & Computer Engineering
University of Illinois
Urbana, IL 61801

Presented at the 1985 Antenna Applications Symposium

Robert Allerton Park Monticello, IL September 18-20, 1985

1. INTRODUCTION

ANALYSIS CONSISSION OF THE PROPERTY OF THE PRO

In antenna engineering it is often necessary to compute certain parameters which are used to assess the input and radiative properties of antennas. Among these parameters are input impedance, directive gain, power gain, and efficiency, all of which are derived for a specified antenna geometry from a known feed network and the corresponding induced current over the antenna surface. The equations which govern the behavior of antennas are continuous mathematical operations which relate continuous currents on the antenna surface to a specified source field or feed. Since these equations cannot be solved analytically, they must either be discretized and solved numerically using a computer, or solved approximately using variational techniques. In either case, the solution obtained is an approximation to the original problem, and the figures of merit mentioned above will also deviate from their respective values. The purpose of this paper is to describe ways to minimize the difference between the computed and actual values of the aforementioned figures of merit for thin-wire antennas. It is shown herein that a code such as the Numerical Electromagnetics Code (NEC) of Lawrence Livermore National Laboratory [1] is a powerful tool in the analysis of thin-wire antennas provided that the model is accurate and the results are interpreted properly.

The directive and power gains are directly related to the radiated or far field of the antenna and thus exhibit little variation from their true values when small computational errors are superimposed on the current [2]. This is not always the case with the input impedance and radiative efficiency of antennas, as they depend highly on the terminal properties and near fields of the antenna as well. The subject of this paper is an assessment of the computational accuracy of the input impedance and radiative efficiency of thin-wire antennas using the Numerical Electromagnetics Code.

2. NUMERICAL SOLUTIONS OF THIN-WIRE ANTENNAS

When solving thin wire antenna problem, or a digital computer, a code such as NFC is used to solve a discretized form of the electric field integral equation which relates an applied, or incident. axially directed electric field to the axially directed induced, or scattered, electric field over the surface of the antenna. A problem of frequent interest is that of a vertical monopole or whip above a perfect ground as shown in Figure 1. The surface of the antenna is frequently modeled as a perfect electric conductor except at discrete points where lumped loads are to be placed. It is assumed that the antenna to be modeled is sufficiently thin so that the fields produced by all nonaxially directed currents are several orders of magnitude smaller than those produced by axially directed currents, and hence non-axial currents can be neglected. Further, it is assumed that the antenna is sufficiently thin that the induced current on the antenna can be modeled as a filamentary current along the axis of the antenna, even though the boundary condition that the tangential electric field must vanish is still enforced on the surface of the antenna. The latter is an application of the technique of extended boundary condition which is used to formulate scattering problems for closed surfaces [3]. When applied to thin wires, this technique, together with the foregoing assumption that the radial currents at wire ends can be neglected, is known as the thinwire approximation to scattering problems.

With no loss of generality, this discussion is confined to an antenna in which all currents flow in the z-direction. Similar expressions to those which follow could also be derived if the structure to be modeled is more complex and contains skew wires as well.

The thin-wire formulation for the whip antenna of Figure 1 yields the following integral equation:

$$E_{zz} = \frac{-1}{j\omega\epsilon_{o}} \left[\frac{d^{2}}{dz^{2}} + k^{2} \right] \int_{0}^{H} I(z')G(z,z') dz' + I(z)Z(z)$$
 (1)

where

I(z')= the unknown z-directed current along the axis of the antenna

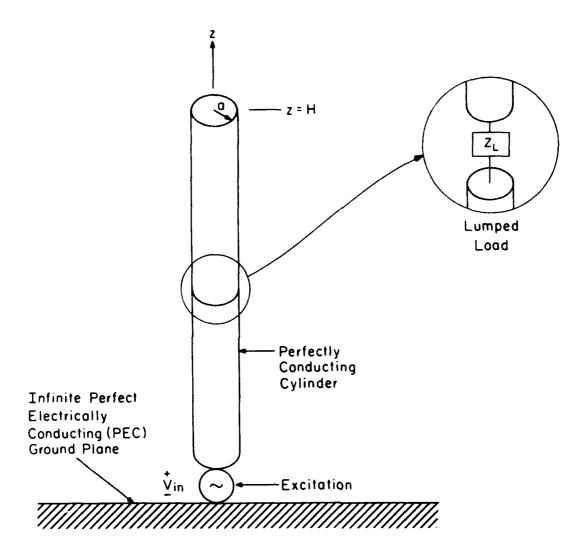


Figure 1. Vertical thin-wire monopole above infinite perfect ground plane.

$$G(z,z') = \frac{e^{-jk\sqrt{a^2 + (z-z')^2}}}{4\pi\sqrt{a^2 + (z-z')^2}}$$
 is the thin-wire approximation to the free-space

Green's function along the wire axis, often referred to as the "thin-wire kernel"

and Z(z) = the distribution of impedance loading along the antenna, which for lumped loads reduces to $Z(z) = \sum_{i=1}^{N} Z_i \, \delta(z-z_i)$

and
$$k = \frac{2\pi}{\lambda}$$
 = free space wave number.

The left-hand side of (1) is the source term which, for most thin-wire antennas, is modeled as a constant, highly localized, axially directed electric field incident on a small region of the surface and zero elsewhere. This is a field-theory model of a voltage source which is connected to the antenna across two closely spaced terminals. In NEC, two voltage source models are available. They are the "current-slope-discontinuity" (CSD) source and the "applied-electric-field" (AEF) source [1].

The CSD source model consists of a highly localized voltage source across a biconical junction of two wires as shown in Figure 2. The axial electric field generated by this model is approximated by that of a thin biconical transmission line with a point voltage source across the junction of the two cones [2]. This approximation also requires the charge, or "current-slope," to be discontinuous across the junction. The field produced by this model becomes more localized as the length-to-radius ratio (h/a) of the wires is increased and works best for wires with h/a > 1000. This is especially important in the computation of input impedance and is discussed in detail subsequently. Plots of the axial electric field and current over the feed region of the monopole of Figure 1 were generated using NFC and are shown for h/a = 100 and 1000 in Figure 3. The height of the antenna is one-tenth wavelength and the source is modeled using the CSD option.

The AEF source is simply a constant, sinusoidally varying electric field incident on a small, specified section of the antenna and zero elsewhere as shown in Figure 4. Physically, this source

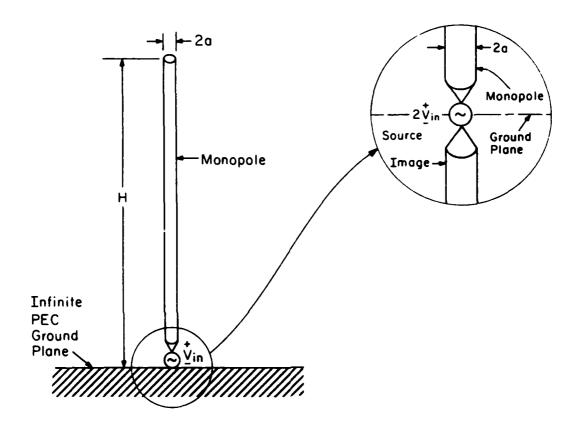


Figure 2. Vertical thin-wire monopole with Current-Slope-Discontinuity (CSD) source model.

represents a constant voltage across a wire gap at the antenna feed. This gap is usually electrically small; thus care must be taken to ensure that the section over which the AEF source is applied is very much less than a wavelength and significantly less than the length of the wire itself. This will result in a computed current which varies smoothly and is nearly constant over the feed region. This is shown to facilitate accurate computation of the input impedance, even for wires with h/a < 1000. Plots of the axial electric field and current in the vicinity of the AEF source for the vertical monopole described above are presented in Figure 5 for h/a = 100 and 1000. It is interesting to note that the axial field generated in response to the AEF source looks more like the desired pulse as h/a increases. The improvement in appearance of the axial near fields in response to both sources as h/a increases is a direct consequence of the increasing validity of the thin-wire approximation described previously as h/a becomes larger, thus making the wire appear thinner.

The right-hand side of (1) consists of two terms: the first of these represents the scattered field on the surface of the antenna due to the unknown induced current I(z), while the second represents the electric field across loads distributed along the axis of the antenna. At this point it should be emphasized that Equation 4 is only accurate for wires with radii that are several orders of magnitude less than the operating wavelength and for wire segments with length-to-radius ratios in excess of 8 when using the NEC code [1]. If the latter condition is not satisfied, a multi-term expansion for the free-space Green's function can be used to give more accurate results for short, thin wires. One such expansion, known as the "extended thin-wire kernel," is available in NEC and is discussed in detail in [1].

Equation 1 cannot be solved analytically, and thus it must be discretized and solved numerically with the aid of a digital computer. The most commonly used computational technique to discretize and numerically solve electromagnetic scattering problems is known as the method of moments. The moment method is used in NEC and is discussed briefly herein. For further information on the method of moments the reader is referred to [1] and [4].



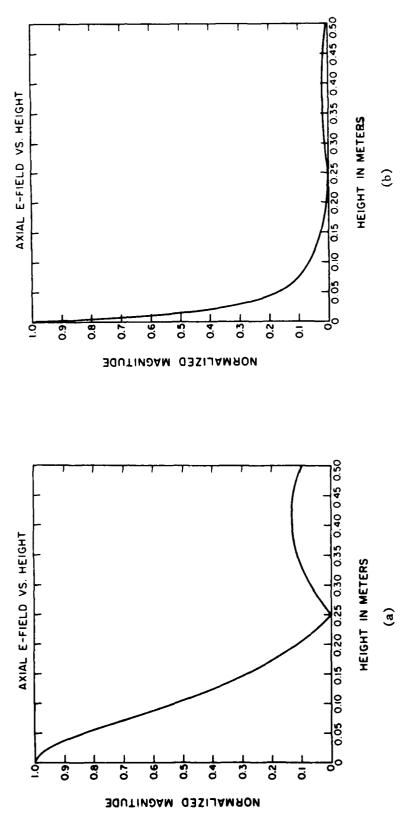


Figure 3. Scattered axial electric near-field over the source region for the monopole of Figure 2. H = 10 meters. H/ λ = 0.1. CSD source with V_{in} = 1.0 volt. Twenty uniform segments with thin-wire kernel.

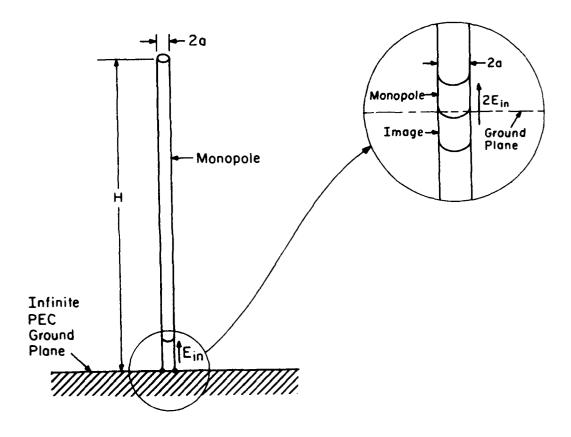
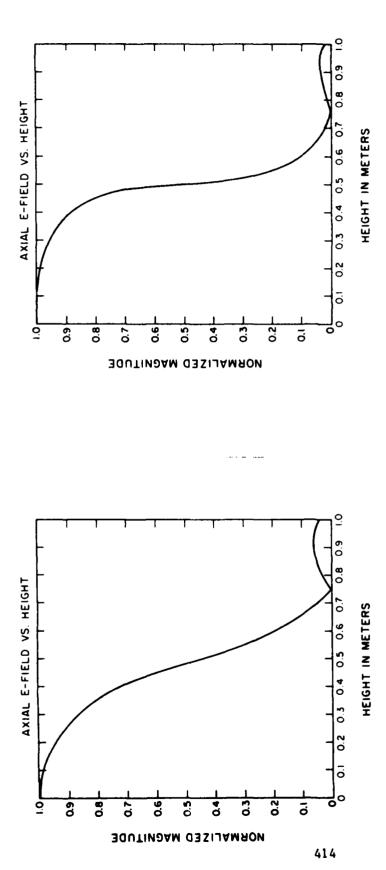


Figure 4. Vertical thin-wire monopole with Applied Electric Field (AEF) source model.



H = 10 meters, H/λ = 0.1, AEF source with \tilde{V}_m = 1.0 volt. Twenty uniform Figure 5. Scattered axial electric near-field over the source region for the monopole of Figure 4. segments with thin-wire kernel

(9)

(a)

Discretization of (1) begins by expanding the current I(z) in terms of a weighted set of basis functions. The bases are chosen to most accurately represent the current at all points along the wire. Within NEC the wire is divided into N segments, of length Δ_n . The current on each segment is represented by a weighted three-term basis function such as that given by Equation (6), for the n^{th} segment

$$I_n(z) = A_n + B_n \sin k (z - z_n) + C_n \cos k (z - z_n) \qquad /z - z_n / < \Delta n / 2$$
 (2)

where z_n is the center of the n^{th} segment and $k = 2\pi/\lambda_o$ is the free-space wave number. Each basis function contains three coefficients, two of which can be eliminated by enforcing continuity of the current (Kirchoff's Law) at wire junctions and a separate condition derived by Wu and King [5] which approximates the distribution of charge at wire junctions. For thin wires of constant radius, the charge is continuous across segment junctions. Since the axially directed current cannot change abruptly to zero at wire ends, a separate condition given by Equation (3) is enforced which relates the current to its derivative at free ends [1].

$$I_{N}(z_{N} + \Delta/2) = \frac{1}{k} \frac{J_{1}(ka)}{J_{0}(ka)} \frac{\partial I_{N}(z)}{\partial z} |_{z} = z_{N} + \Delta/2$$
 (3)

where J_n and J_1 are Bessel functions of order zero and one. Once the junction and end conditions have been applied, it remains to solve for the remaining N coefficients. This is done first computing the inner product of both sides of the integral equation for the expanded current with a set of N testing functions. In NEC the testing functions are impulses located at the center of each segment.

We now have a set of N equations for the N unknown coefficients used in the current expansion.

$$E_{z_{1}}(z_{m}) = \frac{1}{j \omega \epsilon_{n}} \left[\left[\frac{d^{2}}{dz^{2}} + k^{2} \right] \sum_{n=1}^{N} a_{n} \sum_{z_{n} - \Delta z_{n}/2}^{z_{n} + \Delta z_{n}/2} f_{n}(z') G(z, z') dz' \right]_{z=z_{m}}$$

$$- \sum_{n=1}^{N} a_{n} Z_{n}$$

$$m = 1 \dots N$$
(4)

where a_n are the unknown coefficients and f_n the unknown basis functions on each segment. For lumped loading, the impedances Z_n are the loading impedances which are assumed to be located at the center of each segment, and therefore contribute only to the self impedance or diagonal elements on the right-hand side of (4). The coefficients a_n are computed by inverting Equation (4) and using a procedure outlined in [1].

The use of impulses as testing functions is known as point matching. The advantage of using point matching in conjunction with a non-singular approximation to the free-space Green's function, such as the thin-wire kernel, is that the inner product can be performed simply and analytically, thus making for more efficient use of the computer. The disadvantage of using point matching is that the discretized operator equation (4) is only solved at the match points and for irregular distributions of current, significant sampling error can result. It is therefore highly recommended that as a check for accuracy, the axial near field be computed at all points on the antenna, from the computed current distribution, and analyzed to be certain that the boundary condition that the tangential electric field vanishes on the conductive surfaces away from the source and loads is satisfied. As a rule of thumb, a density of at least ten segments per wavelength will help ensure that sampling error because of point matching is not significant for most cases.

In many cases, the condition that the tangential electric field vanishes on the surface of perfectly conducting wires is not satisfied in the vicinity of free-wire ends, even when Equation 7 is applied. This is illustrated for a loaded antenna in Figure 6. The reasons for this are:

- 1) Fields due to currents on the wire ends were not taken into consideration.
- 2) Computational errors such as roundoff can also lead to inaccurate results.

In most cases, the latter is of little consequence, since word lengths in excess of 32 bits are commonplace on most modern computers. For thin wires, it should be noted that the axial current should be very small in the vicinity of free-wire ends; hence, the fact that the boundary condition on the tangential electric field is not exactly satisfied near the free end is usually of little or no consequence when computing either the input impedance or the radiation field. However, one

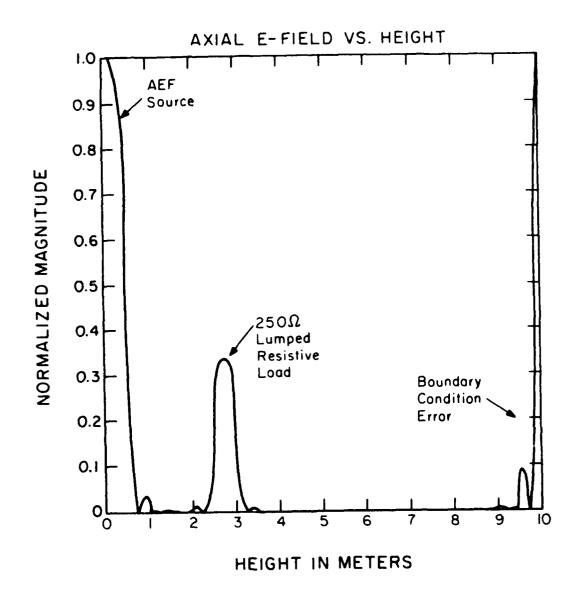


Figure 6. Scattered axial electric near-field over the entire axis for the antenna of Figure 4 with a 250Ω resistive point-load 2.5 meters above the base. H = 10 meters, $V_{in} = 1.0$ volt, $H/\lambda = .1$, and H/a = 100. Twenty uniform segments with thin-wire kernel.

should be very cautious about modeling a load near a free-wire end. In this case, there may be a significant current in the load which may lead to erroneous results in the presence of the non-zero tangential electric field near the end.

3. COMPUTATION OF SYSTEM PARAMETER OF WIRE ANTENNAS

By solving Equation (4) one obtains an approximation for the current along the axis of the antenna; however, knowledge of the current by itself is of little practical value to the antenna engineer. The parameters which are of interest are those which are used to evaluate the antenna in an operating environment, such as input impedance and radiative efficiency. All of these parameters are related to and computed from the current distribution; hence one must exercise caution to prevent errors in the computed current distribution from manifesting themselves in the aforementioned parameters. What follows is a brief discussion of some techniques that can be used to compute these parameters along with an assessment of their sensitivity to small variations or errors in the computed current. Once again, results obtained using NEC will serve as the basis for comparison.

3.1. COMPUTATION OF THE INPUT IMPEDANCE OF THE THIN WIRE ANTENNAS

One of the most widely sought parameters for antennas with a two-terminal feed is the input impedance looking into the feed port. This, after all, relates the antenna as a radiating element to the antenna as a circuit element. The input impedance, Z_m , to a two-terminal network as shown in Figure 7 is defined as the ratio of the input voltage, V_m , to the input current, I_m , in the limit as the spacing between the two terminals approaches zero [2]. Previously it was shown that for computational purposes, that the voltages across the input port must be modeled using a field-theory generator as an axial electric field incident over a very small portion of the structure. By invoking the principle of reciprocity [2], [6], one can show that the relation between the terminal voltage and current and the field-theory source is

PROCEEDINGS OF THE 1985 ANTENNA APPLICATIONS SYMPOSIUM VOLUME 2(U) ROME AIR DEVELOPMENT CENTER GRIFFISS AFB NY DEC 85 RADC-TR-85-242-VOL-2 MD-M165 535 2/4 F/G 9/5 UNCLASSIFIED NL 1



MICROCOPY RESOLUTION TEST CHART

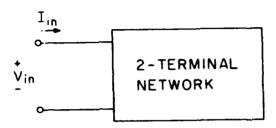


Figure 7. Two-terminal network used in defining input impedance.

$$V_m I_m = \int E_i(z) I(z) dz \tag{5}$$

where $E_r(z)$ is the axial electric field of the field-theory source in (1) and I(z) is the true current in the feed region. Integration is confined to the portion of the antenna over which $|E_{inc}| \neq 0$. By invoking reciprocity once more we obtain

$$\int E_{x}(z)I(z)\,dz = -\int E_{x}(z)I(z)\,dz + \int I^{2}(z)Z(z)\,dz \tag{6}$$

or
$$V_{in} I_{in} = -\int E_{s}(z) I(z) dz + \int I^{2}(z) Z(z) dz$$
 (7)

where E is the axial scattered field due to the computed current, I(z), and Z(z) represents any loading impedance on the antenna. Integration is over the portions of the antenna over which $|E| \neq 0$. The latter equation is of utmost importance since it represents the problem which was actually solved, whereas (5) represents the problem that would have been solved if (1) could have been solved exactly. From (7) one readily obtains

$$Z_{in} = \frac{V_{in}}{I_{co}} = \frac{-1}{I_{co}^2} \int \left[E_s(z) I(z) - I^2(z) I(z) \right] dz$$
 (8)

where Z_m is the input impedance looking into the antenna terminals and I_m is the current at the feed. Through the calculus of variations it can be shown that (8) is highly insensitive to small errors in the computed current and thus is an accurate representation of the input impedance. If the feed region is modeled as a perfect conductor and the computed scattered axial electric field is indeed highly localized to the immediate vicinity of the source, as is often the case with NEC. (8) reduces to the familiar form

$$Z_{rr} = \frac{-1}{I_{rr}^2} \int E_s(z) I(z) dz$$
 (9)

where integration is confined to the feed region over which $|E_s| \neq 0$. Due to the added complexity, one does not always wish to compute Z_m using (9) and approximations to this integral are frequently sought. One approximation that is frequently used is to take the ratio of the applied source voltage of the field-theory source to the computed current at the center of the feed region. This approximation is used in NEC and the conditions for its validity will be derived.

It was stated previously that $Z_m = \frac{V_m}{I_m}$, in the limit as the spacing between the input terminals of the antenna approaches zero. If such is the case, the input voltage is confined to an infinitesimally small region over which the current, I(z), is constant over the feed and equal to I_m . In the case of the applied field (AEF) source, the computed current, I(z), is nearly constant over the region that $|E_s| \neq 0$; hence, (9) can be approximated by

マンドラングの マンクマンマング にいいかから

$$Z_{re} = \frac{-1}{I_{re}^2} \cdot I_{re} \cdot \int E_{\epsilon}(z) dz. \tag{10}$$

The computed current and near field for the AEF source are shown in Figure 8 for vertical monopoles with H/a = 100 and 1000. The integral in (10) can also be interpreted as a voltage, V_s , where

$$V_{c} = \int E_{c}(z) dz. \tag{11}$$

If the numerical solution is a good approximation to (1) then $V_s = -V_m$, where V_m is the terminal voltage specified by the user in NEC, and (10) reduces to

$$Z_{in} = \frac{V_{in}}{I_{in}} \tag{12}$$

where I_{in} is specified in NEC as the current at the center of the segment over which the AEF source is applied. In Table 1, a comparison is made between Z_{in} computed using (12) and by numerically integrating (9) for unloaded and resistively loaded vertical monopoles of H/a = 1000, 100. The ground was modeled as a perfect, infinite ground plane. The results presented here indicate a very close agreement between the input impedance of thin-wire antennas computed using the stationary form of (9) and the NEC approximation (12). In each case, the current was nearly constant over the source region and the axial electric field integrated to -1.00 volts over this region. The assumed input voltage was 1.00 volts. The source region for this problem was taken as the lower most three segments, or 1.5 meters, of the antenna. Beyond this region, $E_s(z)$ has negligible magnitude as indicated by the plot in Figure 6.

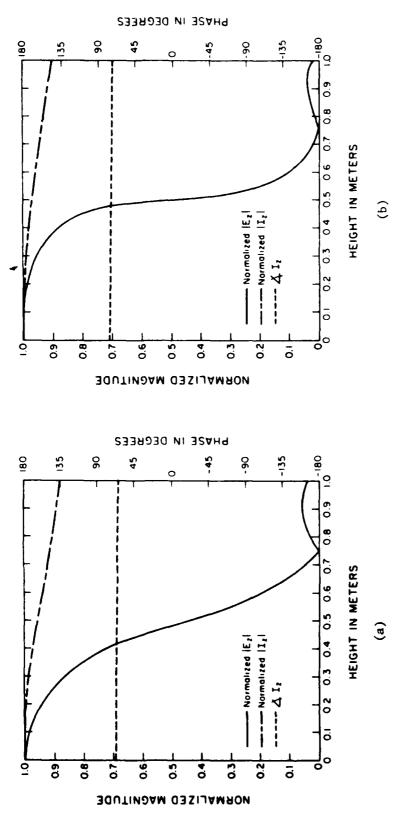


Figure 8. Computed axial current and scattered axial electric near-field for the monopole of Figure 4. H = 10 meters, H/ λ = 0.1, AFF source with V_m = 1.0 volt. Twenty uniform segments with thin-wire kernel

Unloaded,

#/1	Z _{in} from NEC output (A)	Z _{in} computed using stationary form
0.10	4,21 + 1295.9	2.3922 - 05.4
0. 33	149.4 + 1158.4	150.7 + 1158.4
0.50	579.5 - 5.98.4	8.795.1 - 1.252.8
0.67	41.1 - 168.8	40.7 - 168.6
1.00	223.4 - 3172.0	216.7 - 1173.6

Resistively loaded with point-load.

 $R = 250\Omega$, 2.75m above base.

H/ A	² In from NEC output (Q)	Z _{In} computed using stationary form (2)
0.10	130.3 - 1321.9	129.6 - 1321.2
0.33	237.9 - 1111.2	236.4 - 1112.4
0.50	140.6 - 1203.5	138.2 - 1202.5
0.67	33.7 - 176.1	33.4 - 175.8
1.00	115.8 - 133.7	115.0 - 134.7

Unloaded.

Н/ У	Zin from NEC output	Z in computed using stationary form (.)
d.10	4.30 - 149 6. 7	7.557 - 80.7
0.33	119.5 + 1244.3	120.3 + 1244.8
0.50	1,682 - 1,-60.	:005.5 - 2.607.7
0.67	91.8 - 1159.9	51.2 - 5159.0
1.00	886.2 - 5174.0	817.1 - 1207.3

Resistively loaded with point-load. R = 250Ω , 2.75m above base.

Н/ А	Z _{in} from NEC output	Z _{in} computed using stationary form
0.10	142.0 - 1510.9	141.3 - 5.09.7
0.33	369.0 + 135.9	369.2 + 133.8
0.50	478.7 - 1386.1	470.0 - j387.6
0.67	46.2 - 1159.7	45.7 - 5158.8
1.00	308.6 - 143.3	306.7 - 147.3

(b)

(a)

Z for antenna of Figure 4 computed using NEC approximation (12) and stationary form (9) with 1 as the current at the center in an integration over the first three segments (1.5 m). H = 10 m, H/ λ = 0.1, AEF source with V = 1.0 voit. Twenty uniform segments with thin-wire kernel. E and I sampled at 40 points per segment. Table 1.

A similar comparison is shown in Table 2 for the same antennas with the CSD feed. The axial near field and the corresponding current over the feed region are shown in Figure 9 for vertical monopoles with H/a = 100 and 1000, respectively. When H/a = 100, the current is not constant over the feed region and the scattered electric field exhibits irregular behavior there as well. The integrated voltage over the "main lobe" of the electric field is -1.10 volt. If we include the second and subsequent lobes in the feed region the integrated voltage is -0.80 volts. The input voltage is still assumed to be 1.00 volts. Due to the erratic behavior over the feed region, we do not expect good agreement between the input impedances computed using the NFC approximation and the stationary form. This is evidenced in Table 2. The erratic behavior over the source region for H/a = 100 can be explained in part by noting that the discontinuity in the charge due to the CSD source model is accurate only for filamentary wires with infinitesimally small feed regions [1] and [3]. For H/a = 1000, the feed region is much more confined and the current is nearly constant over this region as shown in Figure 9. Hence, as one would expect, agreement between the NEC approximation to Z_{in} (12) and the stationary form (9) is better for H/a = 1000.

3.2. COMPUTATION OF THE RADIATIVE EFFICIENCY OF THIN-WIRE ANTENNAS

The second parameter of concern in this paper is the radiative efficiency of wire antennas. The radiative efficiency, η , is defined as the ratio of the average radiated power to the average input power of the antenna.

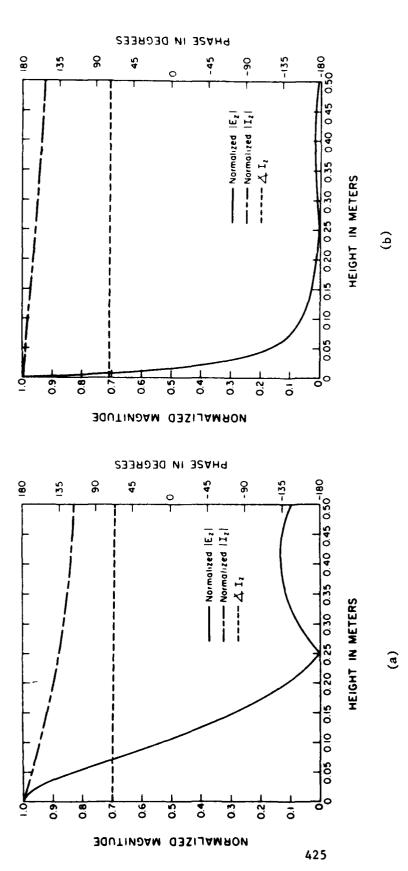
$$\eta = \frac{P_{rad}}{P_m} \tag{13}$$

In NEC the input power, P_m , is computed using the formula

$$P_{m} = \frac{1}{2} \operatorname{Re} \left[V_{m} I_{m} ^{*} \right]$$
 (14)

which assumes that the feed region is infinitesimally small. The radiated power is computed as

$$P_{rad} = P_{re} - P_{tox} \tag{15}$$



たらのな意見されたための意見はいってのなる意見がなるない。 できない 大人の 国际のない 大人の間間のない

Computed axial current and scattered axial electric near-field for the monopole of Figure 2. H = 10 meters, $II/\lambda = 0.1$, CSD source with $V_{in} = 1.0$ volt. Twenty uniform segments with thin-wire kernel. Figure 9.

Unloaded.	•		Un	Unloaded.	
7/2	Z _{in} from NEC output (Ω)	Z _{in} computed using stationary lum		H/ A	2 in from Ni
0.10	4.1 - 1725.6	3.35 - 1263.6		0.10	4.30 -
0.33	289.7 + 5173.5	228.6 + 3142.2	L	0.33	155.8 + j.
0.50	111.0 - 5264.3	93.7 - 1217.3		0.50	596.8 - J
0.67	34.6 - 173.7	28.5 - 160.0	,	0.67	45.8 - }
1.00	68.1 - 3157.7	58.4 - 1130.9		1.00	437.0 - j

Н/3	2 in from NEC output	7.10 computed using stationary form
0.10	4.30 - 1520.8	3,83 - ;465,4
0.33	155.8 + 1,286.0	140.4 + 1250.5
0.50	596.8 - 1753.9	521.9 - 3672.1
0.67	45.8 - 3158.4	40.7 - 1141.6
1.00	437.0 - j495.0	379.9 - 1442.6

Resistively loaded with point-load. $R = 250\Omega$, 2.75m above base.

Н/ У	2 in from NEC output	Zin computed using stationary form
	ì	· ·
0.10	123.9 - 1356.9	101.0 - 5288.8
0.33	200.2 - 1178.2	164.7 - 1143.2
0.50	79.6 - 1190.7	66.4 - 3156.0
0.67	27.5 - 178.5	0.55 - 164.0
1.00	90.1 - 374.1	75.0 - 160.0

Resistively loaded with point-load. $R = 250\Omega$, 2.75m above base.

Z _{in} computed using stationary form (3)	126.0 - 1479.9	366.0 - 312.5	310.3 - 5379.8	1.141.1	7,911 - 2,945
Z _{in} from NEC output (Ω)	141.2 - 3537.0	408.8 - 512.2	351.1 - j424.9	40.9 - 1157.9	279.9 - 1127.3
Н/ А	0.10	0.33	0.50	0.67	1.00

(e)

(a)

for antenna of figure 2 computed using NEC approximation (12) and stationary form (9) with 1 as the current at the base and numerical integration over the first three segments (1.5 m). H = 10 m, H/ λ = 0.1, CSD source with V = 1.0 voit. Twenty in uniform segments with thin-wire kernel. E and I sampled at 40 points per segment. Table 2.

Wa = 100; b) H/a = 1000 • where P_{loss} is the total power dissipated in the structure [1]. The power dissipated in the structure is computed directly as the sum of the average power dissipated in each of the M loads in the structure as stated by Equations (16) and (17).

$$P_{loss} = \sum_{n=1}^{M} P_{m} \tag{16}$$

where

$$P_m = \frac{1}{2} + I_m + {}^2R_m \tag{17}$$

and I_m is the current through, and R_m is the real part, or resistance of the m^{th} load. Equations (13)-(17) can be combined to yield

$$\eta = 1 - \frac{P_{loss}}{P_{in}}
= 1 - \frac{\sum_{m=1}^{M} |I_m|^2 R_m}{\text{Re}[V_m I_m^*]} .$$
(18)

Computations of the efficiency using (18) are inherently sensitive to errors in the assumed input voltage and current unless the current over the feed region is nearly constant and the integral of the scattered electric field over the feed region equals $-V_m$. Such is usually the case in NEC when the AEF source is used and when the CSD source is used for wire structures with $H/a \ge 1000$. Four alternate methods of computing the efficiency are presented below. All of these expressions involve integration of the current and thus are inherently less sensitive to small errors in computing the current.

A statement of conservation of energy is obtained by considering the real parts of the complex power of both sides of (1).

$$\frac{1}{2} \operatorname{Re} < E_{c}, I^{*} > = -\frac{1}{2} \operatorname{Re} < E_{c}, I^{*} > + \frac{1}{2} \operatorname{Re} < I, Z, I^{*} >$$
 (19)

Stated more simply, the input power equals the sum of the radiated power and the power dissipated in the structure. The input power is given by

$$P_{w} = \frac{1}{2} \operatorname{Re} \langle E_{i}, I^{*} \rangle$$

$$= \frac{1}{2} \operatorname{Re} \left[\int_{0}^{H} E_{i}(z) I^{*}(z) dz \right], \qquad (20)$$

the radiated power is given by

$$P_{r,ad} = -\frac{1}{2} \operatorname{Re} \langle E_s, I^* \rangle$$

$$= -\frac{1}{2} \operatorname{Re} \left| \int_0^H E_s(z) I^*(z) dz \right|. \tag{21}$$

and the power dissipated in the structure is given by

$$P_{loss} = \frac{1}{2} \operatorname{Re} < IZ , I^* >$$

$$= \frac{1}{2} \operatorname{Re} \left[\int_{0}^{H} I(z) I^*(z) Z(z) dz \right]$$
(22)

When point loads are used, (22) reduces to the discrete summation of (17). Since (1) could not be solved exactly, computation of the input power using (20) is ill-advised. As an alternative, the input power should be computed for the problem that was solved approximately by inverting (4). This is done in Equation (23)

$$\tilde{P}_{in} = -\frac{1}{2} \operatorname{Re} \left[\int_{0}^{H} \left[E_{s}(z) P^{*}(z) - I(z) P^{*}(z) Z(z) \right] dz \right]$$
(23)

where the tilde indicates that the input power is computed using the current obtained by solving the discretized Equation (4). If there are no loads over the source region and E_s is localized to the source region. (23) reduces to

$$\hat{P}_{ii.} = -\frac{1}{2} \operatorname{Re} \left[\int_{\text{source}} E_i(z) P(z) dz \right]$$
(24)

If the current is constant over the source region and the integral of the near electric field over this region equals $-V_{ij}$ then (24) reduces to (14), thereby validating the assumption of a point feed

when computing the radiative efficiency. The conditions for the validity of the assumption of a point feed are identical whether the input impedance or radiative efficiency is to be computed.

When (24) is substituted into (18) for P_m , an expression for the efficiency is obtained which assumes pointwise loading but makes no restrictions on the feed other than that it is localized to an unloaded portion of the antenna. Since the expression obtained using this procedure involves integration of the current, it is inherently less sensitive to small variations of the computed current about its true value.

The second method utilizes direct computation of the average radiated power using

$$P_{rad} = \frac{R^2}{2\eta_0} \int_0^{\pi} d\theta \int_0^{2\pi} d\phi \, (E_{rig})^2$$
 (25)

where $\eta_0 \approx 120\pi$ ohms is the intrinsic impedance of free space and

$$E_{for}(\theta,\phi) = \frac{jk \, \eta_0 \, e^{jE_F}}{4\pi R} \int_0^H I(z) \, e^{jkz \cos \theta} \, dz$$
 (26)

is the electric far field from a z-directed current at a distance R from the antenna [3]. Integration over θ in (25) is from 0 to $\pi/2$ if a ground plane is present as is the case for the vertical monopoles described herein. The efficiency could then be computed by substituting (25) and (17) into (15) and (13) to obtain

$$\eta = \frac{1}{1 + (P_{lost}/P_{tot})} \tag{27}$$

A third method of computing the efficiency which is also less sensitive to computational errors in the current involves computation of the input and radiated power directly using (24) and (25) and substituting these expressions directly into (13).

In the fourth method presented herein for computing the radiative efficiency, the radiated power is computed directly by computing the inner product of the scattered axial electric field and the conjugate of axial current over the entire structure as shown by Equation (21). The radiative efficiency is then computed by substituting (21) and (24) into (13) to yield

$$\eta = \frac{P_{vas}}{P_{vs}}$$

$$= \frac{\operatorname{Re}\left[\int\limits_{0}^{H} E_{s}(z) P(z) dz\right]}{\operatorname{Re}\left[\int\limits_{0}^{H} E_{s}(z) P(z) dz\right]}$$
(28)

This method yields an accurate computation of the radiative efficiency for the modeled antenna because neither point-sources nor point-loads are assumed as they were in the two methods stated previously by Equations (18) and (27). In addition, both the input and radiated powers are computed using integrals and thus are inherently less sensitive to small variations of the computed current about its true value. The only constraints are that the source region be localized and free of loads. If more than one source exists and the source regions are not free of loads, a more general expression for the efficiency is

$$\eta = \frac{\text{Re} \int_{0}^{H} E_{s}(z) I^{s}(z) dz}{\text{Re} \int_{0}^{H} \left[E_{s}(z) I^{s}(z) - I(z) I^{s}(z) Z(z) \right] dz}$$
(29)

A comparison is made in Table 3 of the efficiency of resistively loaded whip antennas of H/a = 100 and 1000 using Equation (28) and the efficiency computed using the NEC approximation (18) for both the AEF and CSD source models. These results show that the NEC approximation is valid when the AEF source is used. The NEC approximation is shown to yield marginal results for the CSD source when H/a = 1000 and even less acceptable results when H/a = 100.

IV. CONCLUSIONS

It is shown herein that when wire antennas are sufficiently thin, some simplifying assumptions can be used in conjunction with the method of moments to obtain a set of equations for the unknown structural current which can be solved with relative ease using a digital computer. When the input impedance and efficiency are computed using simple expressions that

$\overline{}$
8
-
11
'
Ŧ

H/A	Efficiency from NEC output (2)	Efficiency computed using Equation A8
0.10	1.4	3.1
0.33	25.2	25.7
0.50	2.64	+5.7
0.67	77.6	22.6
1.00	5.67	5'67

2
\subseteq
H
্য
\succeq

Н/ Л	Efficiency from NEC output (1)	Efficiency compured using Equation &8 (%)
0.10	7;	3,15
0.33	10.1	5.7
0.50	;· q.	C.C.
0.67	42.0	;;;e
1.00	38.5	

H/a = 1000

H/ Y	0.10	0.33	0.50	0.67	1.00
Efficiency from NEC output (1)	3.0	24.2	42.5	89.5	38.9
Efficiency computed using Equation 18 (I)	3.0	24.2	42.5	89.5	38.9

II/a = 1000

т/н	Efficiency from NEC output (1)	Efficiency computed using Equation 28 (I)
0.10	12.0	1.7
0.33	31.2	23.2
0.50	9.72	41.6
0.67	90.5	4.68
1.00	43.9	37.8

(P)

(a)

with the NEC approximation (18) and the less sensitive form (28). Numerical integration performed using Egand is sampled at 40 points per segment. 2500 point load located 2.75 meters above the base. Twenty uniform segments with thin-wire kernel. Radiative efficiency of 10-meter resistively-loaded vertical whip above perfect ground computed using AEF and CSD_sources Table 3.

a) AEF source; b) CSD source

assume a pointwise feed, as in NEC, these two parameters are very sensitive to errors in the computed current. Alternate formulas for both the input impedance and the efficiency that are less sensitive to small variations in the current about its true value are presented. It is shown that when the modeled feed region is small, the computed current is nearly constant over the feed region, and the integrated near-electric field over the feed region equals the negative of the input voltage, the alternate expressions reduce to the simple forms used in NEC. Comparisons between the input impedance and efficiency of thin-wire whip antennas computed using NEC alone and NEC in conjunction with the alternate forms are presented herein. For the simple geometry discussed herein, it is shown that NEC, alone, yields highly accurate results when the applied electric field (AEF) source is used in conjunction with wires with $H/a \ge 100$. The current-slope-discontinuity (CSD) source is shown to yield marginally acceptable results when used to model wire antennas with $H/a \le 1000$.

The agreement or disagreement between the data sets is shown to be directly related to how well the aforementioned criteria defining the validity of the simple expressions used to compute Z_m and η in NEC are met. It is highly recommended, therefore, that one should closely examine the computed current and near field over the surface of the modeled structure and then determine what simplifying forms, if any, are valid when computing the terminal properties of antennas.

REFERENCES

- [1] G. J. Burke and A. J. Poggio. Numerical Electromagnetic Code (NEC) Method of Moments. NOSC TD-116. Part 1. Program Description - Prepared for Naval Electronic Systems Command (Elex 3041). Original - July 18, 1977. Revised - January 1981.
- [2] E. C. Jordan and K. G. Balmain. Electromagnetic Waves and Radiating Systems, Englewood Cliffs, NJ: Prentice-Hall, 1968.
- [3] C. D. Taylor and Wilton, D. R., "The extended boundary condition solution of the dipole antenna of revolution." *IEEE Trans. Antennas and Propagat.*, vol. AP-20, no. 6, 1972.
- [4] R. F. Harrington, Field Computation by Moment Methods, Malabor, FL: R. E. Krieger Publishing
 Co., 1982...
- [5] T. T. Wu and R. W. P. King, "The tapered antenna and its application to the junction problem for thin-wires," *IEEE Trans. Antennas and Propagat.*, vol. AP-24, no. 1, 1976.
- [6] W. L. Stutzman and G. A. Thiele, Antenna Theory and Design, NY: J. Wiley and Sons, 1981.

ELECTROMAGNETIC ANALYSIS OF DIFLECTRIC HONFYCOMB SUPPORTS FOR FREQUENCY SELECTIVE SURFACES

Roy F. Jorgenson and Raj Mittra Electromagnetic Communication Laboratory Department of Electrical and Computer Engineering University of Illinois

H. Ohta, K.C. Lang and T.K. Wu Space and Communications Group Hughes Aircraft Company, El Segundo, CA

Abstract

This paper is concerned with the analysis of a plane wave incident upon a slab of lossy, dielectric honeycomb. Two methods are used in the analysis. The first replaces the structural medium with a simple dielectric using effective medium theories. The second is a full wave analysis that takes the structure into account. These methods are compared to each other and to experimental results.

1. Introduction

A frequency selective surface used in satellite applications is structurally supported by a dielectric slab, as shown in Figure 1, that must be light-weight yet strong. Structured dielectrics are the preferred support material since they have a higher strength to weight ratio than do simple dielectrics. One such structured dielectric slab is the dielectric honeycomb. As shown in Figure 2, the honeycomb backing affects the characteristics of the frequency selective surface by lowering the frequency of transparency by approximately 10%. It is therefore important to be able to characterize the behavior of an electromagnetic wave in the presence of a slab of honeycomb material.

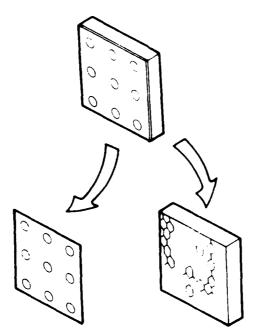


Figure 1. F.S.S. (left) supported by a dielectric honeycomb (right)

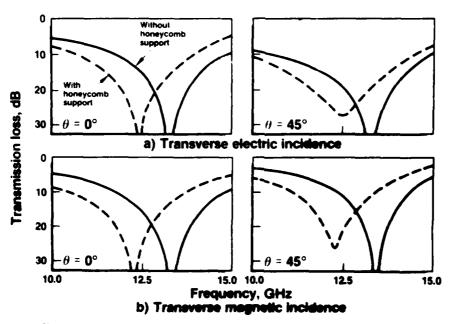


Figure 2. Measured transmission characteristics showing the effect of the dielectric honeycomb on the F.S.S.

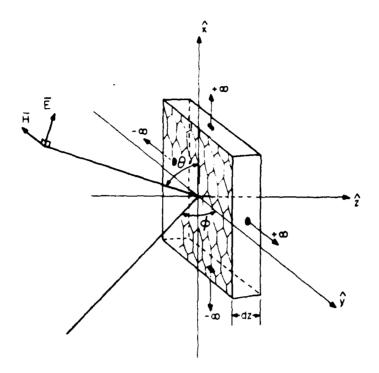


Figure 3. Problem geometry showing a plane wave incident upon an infinite honeycomb slab

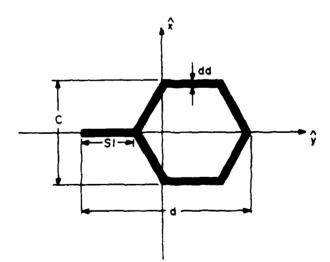


Figure 4. Unit cell of the honeycomb slab

In this paper, two methods are outlined to analyze an electromagnetic plane wave incident on a slab of lossy, dielectric honeycomb. The first method is very simple. It uses a quasi static model in order to remove the structure in the honeycomb and replace it with a homogeneous dielectric slab having an effective permittivity. This can be easily cascaded with the characteristics of the frequency selective surface. The second method is a full wave solution and is, therefore, more complex. It is based on an application of Floquet's theorem and the generalized scattering matrix. These two methods will be compared to each other and to experimental results.

2. Problem Geometry

The geometry of the problem under consideration is shown in Figure 3. A plane wave is incident on a slab of dielectric honeycomb which is infinite and periodic in both the x and the y directions but finite in the z direction. The axes of the honeycomb are aligned along the z axis. The unit cell, shown in Figure 4, is the structure that, when repeated in the x and y direction, gives the honeycomb its periodicity. The direction of propagation for the incident wave makes an angle θ with the positive x axis and ϕ with the positive y axis. Since an arbitrary field can be broken into a superposition of waves transverse electric (TI:) and transverse magnetic (TM) to a given direction, the scattered field response is calculated for an incident field TM to x and TF to x.

3. Effective Medium Approach

This method was used to gain an initial insight into how the honeycomb slab behaves. In past work with resistive strips, it has been established that at sufficiently low frequency, a structured medium, such as a honeycomb, exhibits characteristics similar to a simple dielectric with constitutive parameters equal to a weighted average of the parameters of the honeycomb walls and the parameters of the free space that fills the honeycomb. Further, we expect a slight amount of anisotropic behavior ($\epsilon > \epsilon_c = \epsilon_c$) since the walls of the honeycomb are parallel to z and the electric field in the z direction (\vec{E}) is more strongly influenced by the dielectric than \vec{E}_c or \vec{E}_c .

高層はは大名画がため、

A number of different ways of averaging the constitutive parameters have been proposed in literature for application to random inhomogeneous media such as smoke, hail and metallic powders. We propose to apply three of these effective medium theories (Maxwell-Garnet, Bruggeman, and Maxwell-Garnet for spheroids) to the honeycomb to obtain an effective permittivity. In practice, one often applies a number of these theories to the problem at hand and determines the validity of a particular theory by comparing the theoretical results to experimental measurements.

The honeycomb can be viewed as being composed of strips (labeled the inclusion) with a permittivity ϵ_{mc} embedded in a matrix of free space with a permittivity ϵ_{cat} as shown in Figure 5.

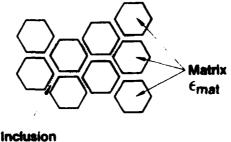


Figure 5. Definition of the inclusion and matrix

The volume fraction of the inclusions is known as the fill factor (f). An effective medium [1] is defined such that the unit cell of the original medium is invisible when embedded in it. This is equivalent to saying that the scattering amplitude in the forward direction is zero.

In all the following theories, the size of the inhomogeneities as well as the separation between inhomogeneities are assumed to be much less than a wavelength so that static field approximations can be made. The inhomogeneities must be large enough so that they can be described by macroscopic parameters. Finally, the fill factor must be small enough so that detailed geometrical configuration of interacting particles do not play a role. The procedure used in all the theories is to replace the unit cell by an object with a separable geometry such as a sphere or spheroid and then use the known static dipole moment of the sphere/spheroid to obtain the effective permittivity in terms of ϵ_{inc} and ϵ_{inc} .

3.1 Maxwell-Garnet for Spheres/Spheroids [2]

Originally proposed in 1904 by J.C.M. Garnet, the Maxwell-Garnet theory applies to the situation shown in Figure 6 where the inclusion particles are totally surrounded by the matrix. The inclusions were originally reduced to spheres but we will derive the relations for a spheroid inclusion with its major axis aligned along the honeycomb axes as shown in Figure 7. The sphere will be taken as a special case.

The average field at point (\vec{r}) is composed of contributions from fields in the matrix $<\vec{E}_{mit}>$ and from fields in the inclusion $<\vec{E}_{mi}>$

$$\langle \vec{E}_{ef}(\vec{r}) \rangle = (1-f_{e})\langle \vec{E}_{mat}(\vec{r}) \rangle + f_{e}\langle \vec{E}_{inc}(\vec{r}) \rangle$$
 (1)

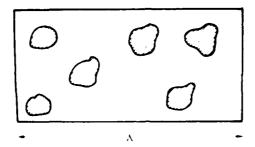


Figure 6. Isolated inclusions requiring the application of the Maxwell-Garnet theory

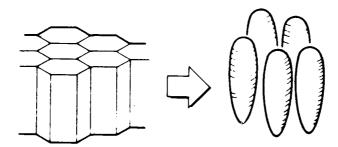


Figure 7. Reduction of cells in the honeycomb to equivalent spheroids

Similarly the average polarization is

$$\langle \vec{P}_{eff}(\vec{r}) \rangle = (1-f_{eff})\langle \vec{P}_{nor}(\vec{r}) \rangle + f_{eff}(\vec{r}) \rangle$$
 (2)

Assuming that the matrix and inclusions are both linear and isotropic, the average \vec{E} and average \vec{P} are related by

$$\langle \vec{P}_{mit} \rangle = \epsilon_m \chi_m \langle \vec{E}_{mat} \rangle$$
 (3)

$$\langle \vec{P}_{v+} \rangle = \epsilon_{ij} \chi_{v+} \langle \vec{E}_{mi} \rangle$$
 (4)

$$\langle \vec{P}_{eff} \rangle = \epsilon \langle \vec{\chi}_{eff} \rangle \langle \vec{E}_{eff} \rangle$$
 (5)

where $\nabla_{\mathcal{F}}$ is defined as the average susceptibility tensor. Combining equations (1) through (5) we obtain

 $(1-f_{-})(\xi_{|\vec{r}|} - \epsilon_{\text{max}}|\vec{1}) < \vec{E}_{\text{max}}(\vec{r}) > + f_{-}(\xi_{|\vec{r}|} - \epsilon_{\text{max}}|\vec{1}) < \vec{E}_{\text{max}}(\vec{r}) > = \vec{0}$ (6)

Because the overall medium is assumed to be statistically homogeneous, we must obtain a linear relationship between $\langle \vec{E}_{ma} \rangle$ and $\langle \vec{E}_{ma} \rangle$. If we look at an isolated spheroid in a uniform field $\langle \vec{E}_{max} \rangle$, we can get the relationship [3]

$$\langle \vec{E}_{xx} \rangle = \lambda / \langle \vec{E}_{xxx} \rangle$$
 (7)

where

では、Mなどとなったとは、自身でクランスとは、単立ので

$$\lambda_{j} = \frac{\epsilon_{mn}}{\epsilon_{mn} + L_{+}(\epsilon_{mn} - \epsilon_{mn})}$$
 (8)

and L_{\perp} are the depolarization factors [4]. Maxwell-Garnet for a spheroid becomes

$$(1-f_{-})(\xi_{eff_{-}} - \epsilon_{mat} \overline{1}) \overline{1} + f_{-}(\xi_{eff_{-}} - \epsilon_{ma} \overline{1}) \overline{\lambda} = \overline{0}$$

$$(9)$$

If the spheroid becomes a sphere then $L_j = 1/3$ and the above expression reduces to

$$\frac{\epsilon_{if} - \epsilon_{mii}}{\epsilon_{eff} + 2\epsilon_{mii}} = f - \frac{\epsilon_{mi} - \epsilon_{mii}}{\epsilon_{mi} + 2\epsilon_{mii}}$$
 (10)

which is the original Maxwell-Garnet expression for the effective permittivity in terms of the fill factor and the permittivity of the inclusion and the matrix.

3.2 Bruggeman Theory [5]

Bruggeman theory, developed in 1935, applies to the aggregate structure shown in Figure 8.

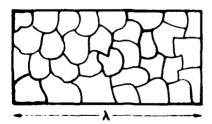


Figure 8. Aggregate structure requiring the application of Bruggeman theory

The inclusions and the matrix must be treated with structural equivalence so the unit cell is reduced to a sphere of radius a immersed in a dielectric with a permit tivity of $\epsilon_{i,k}$. The sphere has a probability of t (fill factor) that its permittivity is $\epsilon_{i,k}$ and 1 t that its permittivity is $\epsilon_{i,k}$. The dipole moment of each of these spheres is

$$\vec{p}_{in.} = 4\pi a^3 \epsilon_{i.ff.} \frac{\epsilon_{in.} - \epsilon_{i.f.}}{\epsilon_{in.} + 2\epsilon_{i.f.}} \vec{E}_{c.}$$
(11)

$$\vec{p}_{con} = 4\pi a^3 \epsilon_{cf} \frac{\epsilon_{con} - \epsilon_{cf}}{\epsilon_{con} + 2\epsilon_{cf}} \vec{E}_{co}$$
 (12)

Using the definition of an effective medium, the deviation produced by the polarization must vanish in the average.

$$f \vec{p}_n + (1 - f_n) \vec{p}_{n,n} = 0 {13}$$

or

$$f \frac{(\epsilon_{mi} - \epsilon_{eff})}{(\epsilon_{mi} + 2\epsilon_{eff})} + (1 - f) \frac{(\epsilon_{mii} - \epsilon_{eff})}{(\epsilon_{mii} + 2\epsilon_{eff})} = 0$$
 (14)

which is the Bruggeman expression for an effective permittivity.

3.3 Small Contrast Limit

If the contrast between the inclusion and the matrix becomes small i.e. $\Delta = \epsilon_{rrr} - \epsilon_{-rr} < 1 \text{ then all of the above theories reduce to the relationship}$

$$\epsilon_{cf} = / \epsilon_{co} + (1-f) \epsilon_{co}$$
 (15)

which is just the average of the two components.

3.4 Effective Medium Method: Conclusion

The advantage to this ar, reach is that it permits the use of relatively simple theoretical formulas as compared to those derived from a complex boundary value

problem. The second advantage is that the results yield a simple dielectric slab which is easy to cascade with frequency selective surfaces. The disadvantage is that this method does not show how the structure itself affects the waves, for example to what extent cross coupling exists between TL and TM incident waves. For this information we must turn to the more complex full wave analysis

4. Full Wave Analysis

In order to obtain a full wave solution for the honeycomb slab, an integral equation will be formulated where the unknown quantity is the total electric field across the unit cell shown in Figure 4. This equation will then be solved approximately by the method of moments.

4.1 Integral Equation Formulation

We know that in general

$$\vec{E}^{(r)}(\vec{r}) - \vec{E}^{(r)}(\vec{r}) = \vec{E}^{(r)}(\vec{r})$$
 (16)

Where \vec{E}_{-} is the unknown total field, $\vec{E}_{-}^{(n)}$ is the unknown field scattered by the dielectric and $\vec{E}_{-}^{(n)}$ is the known plane wave incident upon the honeycomb. We must now find a relationship between $\vec{E}_{-}^{(n)}$ and $\vec{E}_{-}^{(n)}$. First the dielectric in the problem is replaced by an equivalent polarization current, $\vec{J}(x,y,z)$, radiating in free space. $\vec{E}_{-}^{(n)}(\vec{r}_{-})$ may then be found by convolving $\vec{J}(x,y,z)$ over the unit cell with the periodic Green's function $\vec{G}(x,y,z)(x',y',z')$ which is defined as the electric field produced by an infinite array of periodic point sources radiating in the x-y plane [6].

$$\vec{E}^{soft}(x,y,z) = \vec{G}(x,y,z)(x',y',z') * \vec{J}(x',y',z')$$
 (17)

To derive the periodic Green's function we note that the geometry is periodic in x and y (period of c and d respectively) and that the incident field is a plane wave with propagation constants of k, k, k. Floquet's theorem states that the fields in the x-y plane are periodic in x and y except for the phase shift introduced by k, and k, of the incident wave. We can, therefore, define a Fourier series for the function f(x,y) by

$$f(x,y) = \sum_{n=1}^{\infty} \sum_{n=1}^{\infty} F_{n} \cdot e^{\gamma(\alpha_{n} + \beta_{n} \cdot y)}$$
(18)

where

$$|F_{mn}| = \frac{1}{cd} \int_{-\infty}^{\infty} \int_{2\sqrt{d}/2}^{2\sqrt{d}/2} f(x,y) e^{-x_{n} + \alpha_{n} + x_{n} + \beta_{n} + y} dx dy$$
 (19)

and

$$\alpha_{m} = k_{n} + \frac{2\pi m}{c} \qquad m = -\infty, \dots, -1, 0.1, \dots, \infty$$
 (20)

$$\beta_n = k_y + \frac{2\pi n}{d} \qquad n = -\infty, \dots, -1, 0, 1, \dots, \infty$$
 (21)

The array of point sources located at x',y' in each unit cell and represented by

$$\vec{J}_{py}(x,y,z) = \begin{pmatrix} \hat{x} \\ \hat{y} \\ \hat{z} \end{pmatrix}_{py=-\infty}^{\infty} \sum_{y=-\infty}^{\infty} \delta(x-x'-mc')\delta(y-y'-nd')\delta(z-z')$$
 (22)

can be equivalently represented as an infinite set of current sheets

$$\vec{J}_{j}(x,y,z) = \frac{1}{cd} \begin{bmatrix} \hat{x} \\ \hat{y} \\ \hat{z} \end{bmatrix} \sum_{n=1}^{\infty} \sum_{n=1}^{\infty} e^{z(\alpha_{j_0}(x,x,x) + \beta_{j_0}(y-y,x))} \delta(z-z')$$
 (23)

through the use of the Fourier series

The electric field response at z due to the single current sheet

$$\vec{J}_{cs}(x,y,z) = \begin{vmatrix} \hat{x} \\ \hat{y} \\ \hat{z} \end{vmatrix} e^{-i\alpha_{m}x + \beta_{m}y}$$
(24)

is

$$\vec{E}_{cs}(x,y,z) = -\frac{1}{2\gamma_{mn}\omega\epsilon_0} \begin{bmatrix} k_0^2 - \alpha_{cn}^2 & -\alpha_{cn}\beta_{c} & \pm\alpha_{cn}\gamma_{mn} \\ -\alpha_{cn}\beta_{c} & k_0^2 - \beta_n^2 & \pm\beta_{c}\gamma_{mn} \\ \pm\alpha_{cn}\gamma_{mn} & \pm\beta_{c}\gamma_{mn} & \alpha_n^2 + \beta_n^2 \end{bmatrix} \begin{vmatrix} \hat{x} \\ \hat{y} \\ \hat{z} \end{vmatrix} \times$$
(25)

$$e^{j(\alpha_m x + \beta_n y)}e^{-j\gamma_{n,n}(z+z')}$$
 for $z \geq z'$

where

$$\gamma_{mn} = \begin{cases} + \sqrt{k_0^2 - \alpha_m^2 - \beta_n^2} & \text{if } k_n^2 > (\alpha_m^2 + \beta_n^2) \\ -j \sqrt{(\alpha_m^2 + \beta_n^2) - k_n^2} & \text{if } k_n^2 < (\alpha_m^2 + \beta_n^2) \end{cases}$$
 (26)

 k_{ij} is the free space propagation constant. Rewriting the above equation in shorter form we obtain

$$\vec{E}_{c}(x,y,z) = \tilde{\vec{G}}(\alpha_m,\beta_c) \begin{vmatrix} \hat{x} \\ \hat{y} \\ \hat{z} \end{vmatrix} e^{j(\alpha_m x + \beta_n + e^{-j(\gamma_{min} + e^{-y})})}$$
(27)

The response due to the array of point sources (the periodic Green's function) is a sum of the responses to the current sheets according to equation (27)

$$\vec{G}(x,y,z||x|',y',z') = \frac{1}{cd} \sum_{m=-\infty}^{\infty} \sum_{n=-\infty}^{\infty} \tilde{\vec{G}}(\alpha_m,\beta_m) e^{j(\alpha_m+y-y')+\beta_m(y-y-y)} e^{-j(y_{m,n}+y-y')}$$
(28)

The double summation can be viewed as the inverse Fourier transform to return to the space domain.

Substituting the periodic Green's function shown above into equation (17) and performing the convolution we obtain

$$\vec{E}^{(\gamma)}((x,y,z)) = \int \int_{-\infty/2-d}^{\infty/2} \int_{d}^{d/2} \frac{1}{cd} \sum_{m=-\infty}^{\infty} \sum_{n=-\infty}^{\infty} \tilde{\vec{G}}(\alpha_{m},\beta_{n}) e^{j(n-(\gamma-\gamma))+j\beta_{m}(y-\gamma)} \times$$
 (29)

$$e^{-i\sum_{n}(\hat{A}_{n})}$$

$$=\sum_{m=-\infty}^{\infty}\sum_{n=-\infty}^{\infty}\tilde{G}(\alpha_{m}.\beta_{n})e^{j(\alpha_{m}.z+\beta_{n}.z)}\int_{z}\tilde{J}(\alpha_{m}.\beta_{n}.z^{*})e^{-j\gamma_{mn}(z-z^{*})}dz^{*}$$
(30)

where $\tilde{J}(\alpha - \beta, z')$ is the Lourier transform of the current in the x y direction. We use the boundary condition [7]

$$\vec{J}(x,y,z) = j\omega\epsilon_0(\epsilon_r(x,y,z) - 1)\vec{E}^{tot}(x,y,z)$$
(31)

or

$$\widetilde{J}(\alpha_{n},\beta_{n},z) = j\omega\epsilon_{0}F.T.\left[(\epsilon,(x,y,z)-1)\overrightarrow{E}^{tot}(x,y,z)\right]$$
(32)

to obtain the needed relation between \vec{J} and \vec{E}^{tot} . F.T. is the two-dimensional Fast Fourier transform with respect to α_m and β_n . Also note that from 0 to Δz , ϵ , is invariant in z.

Substituting equation (32) into (30) and this into the original equation (16) we obtain the desired integral equation.

$$\vec{E}^{tot}(x,y,z) = j\omega\epsilon_{0}\sum_{m=-\infty}^{\infty}\sum_{n=-\infty}^{\infty}\left[\tilde{\vec{G}}(\alpha_{m},\beta_{n})\int_{z^{2}}F.T.\left[\left(\epsilon_{r}(x',y')-1\right)\vec{E}^{tot}(x',y',z')\right]\times\right]$$

$$e^{-z/2\epsilon_{m}+1}e^{-z/2}dz'e^{-z(\alpha_{m},x'+\beta_{m},y')} = \vec{E}^{tot}(x,y,z')$$

4.2 Solution by Method of Moments [8]

We will expand the total \vec{E} field across the cell as a sum of k1 basis functions.

$$\vec{E}^{tot}(x,y,z) = \sum_{k=1}^{k-1} a_k \vec{B}_k$$
 (34)

Equation (33) becomes

$$\sum_{k=1}^{k-1} a_k \left| \vec{B}_k - j \, \omega \epsilon_0 \sum_{m=-\infty}^{\infty} \sum_{n=-\infty}^{\infty} \vec{G} \left(\alpha_{m}, \beta_{k} \right) \int_{\mathbb{R}} F T_n \left| \left(\epsilon_n \left(x, y \right) - 1 \right) \vec{B}_k \right| \times \right|$$
(35)

$$\left|e^{-\gamma (\mathbf{y}_{mn}+\cdots+\beta_{n})}\right| dz \left|e^{\gamma (\mathbf{u}_{mn}+\boldsymbol{\beta}_{n}\boldsymbol{x})}\right| = \vec{E}^{mn}\left(x,y,z\right)$$

Next we form a matrix equation

$$\vec{Z}\vec{a} = \vec{b} \tag{36}$$

by performing an inner product on both sides of equation (35) with k1 different testing functions $\vec{T}_l(x,y,z)$. \vec{a} is the column vector of unknown coefficients

$$\vec{a} = [a_1 \cdots a_{k-1}]^T , \qquad (37)$$

 $ec{b}$ is a column vector representing the forcing function

$$b_i = \langle \vec{T}_l(x, y, z) | \vec{E}^{inc}(x, y, z) \rangle$$
 $l = 1 \cdots k 1$ (38)

and \vec{Z} is the impedance matrix where

$$Z_{lk} = \langle \vec{T}_l(x,y,z), \vec{b}_k(x,y,z) \rangle - j \omega \epsilon_0 \langle \vec{T}_l(x,y,z), \sum_{m=-\infty}^{\infty} \sum_{k=-\infty}^{\infty} \tilde{\vec{G}}(\alpha_m,be) \times$$
 (39)

$$\int FT \left[\left(\boldsymbol{\epsilon}_{i} \left(\boldsymbol{x}_{i} \cdot \boldsymbol{y}_{i} \right) - 1 \right) \vec{B}_{k} \left(\boldsymbol{x}_{i} \cdot \boldsymbol{y}_{i} \cdot \boldsymbol{z}_{i}^{T} \right) \right] e^{-j \left[\sum_{m,i} \mathbf{1}_{i} - z_{i}^{T} \right]} dz \left[e^{-j \left[\sum_{m,i} \mathbf{1}_{i} - z_{i}^{T} \right]} dz \left[e^{-j \left[\sum_{m,i} \mathbf{1}_{i} - z_{i}^{T} \right]} \right] \right]$$

$$= \int_{0}^{\Delta_{i}} \int_{0}^{2\pi} \int_{0}^{2\pi} \int_{0}^{2\pi} \vec{T}_{i} \left(\boldsymbol{x}_{i} \cdot \boldsymbol{y}_{i} \cdot \boldsymbol{z}_{i} \right) \cdot \vec{B}_{k} \left(\boldsymbol{x}_{i} \cdot \boldsymbol{y}_{i} \cdot \boldsymbol{z}_{i} \right) dv - j \omega \boldsymbol{\epsilon}_{0} c d \int_{0}^{\Delta_{i}} \sum_{m=1}^{2\pi} \sum_{m=1}^{2\pi} \tilde{G} \left(\boldsymbol{\alpha}_{m} \cdot \boldsymbol{\beta}_{n} \right) \times$$

$$(40)$$

$$\int_{0}^{\infty} F.T. \left[(\epsilon_{i}(x,y)-1)\vec{B}_{k}(x,y,z') \right] \tilde{T} \left[(\alpha_{m},\beta_{n},z) dz' dz \right]$$

and where $\tilde{T}'(\alpha_m, \beta_n, z)$ in the second term is the conjugate of the two-dimensional Fourier transform of the testing function. The double summation can now be viewed as a discrete inner product of two discrete functions.

We will now choose our basis function to be a Floquet harmonic in x and y and a pulse in z of length Δz .

$$\vec{B}_{t}(x,y,z) = \vec{B}_{t,1,t,2}e^{j(\alpha_{t,1}x + \beta_{t,2}y)}P(\Delta z)$$
(41)

 $\vec{B}_{i,1|i,2}$ contains information about the components of the \vec{E} field normalized to unity for the particular Floquet harmonic chosen. These components depend on whether the harmonic is TE to x or TM to x. Both types must be included in the basis functions. The testing function is chosen identically to the basis function except that it exists only in the dielectric. This truncation serves to spread out \hat{T} over all values of α_m and β_n .

$$\vec{T}_{\varepsilon}(x,y,z) = \vec{T}_{I1/2}(\epsilon_{\varepsilon}(x,y)-1)e^{-\frac{1}{\varepsilon}\alpha_{I1}x+\beta_{I2}z}P(\Delta z)$$
(42)

where

$$\epsilon_{(x,y)} = \begin{cases} 2.0 & \text{if } x, y \text{ is located in the dielectric} \\ 1.0 & \text{if } x, y \text{ is not located in the dielectric} \end{cases}$$
 (43)

With the above choice of basis and testing function, term 1 in the impedance matrix expression (equation 40) becomes

Term $1 = cd\vec{B}_{k,1,k,2}^{\top} \cdot \vec{T}_{k,1,k,2}^{\top} \cdot F.T. \left[(\epsilon_{k}(x,y)-1)e^{-j(\alpha_{i1}x+\beta_{i2}y)} \right]_{\otimes k,1,k,2} \Delta z$ (44) where F.T. is the Fast Fourier transform of the testing function (11,12) evaluated at the mode numbers of the basis function (k1,k2). Term 2 is evaluated by performing the integrations in z analytically. Care must be exercised to use the proper $\tilde{G}(\alpha_{ij},\beta_n)$ depending on the position of the observation point (z) with respect to the source point (z'). Let $\tilde{G}=\tilde{G}_{kl}$ for z>z' and $\tilde{G}=\tilde{G}_{Ll}$ for z<z'. Then Term 2 becomes

$$Term 2 = j \omega \epsilon_0 cd \sum_{m=-\infty}^{\infty} \sum_{k=-\infty}^{\infty} \vec{B}_{k+k,2} \vec{T}_{k+k,2} FT \cdot \left[(\epsilon_r(x,y) - 1)e^{j(\alpha_{k+1}x + \beta_{k,2}y)} \right] \times$$

$$\left[\tilde{G}_{L/} + \tilde{G}_{I/} \right] \left[\frac{\Delta z}{j\gamma} - \frac{e^{-\gamma j\Delta} - 1}{\gamma^2} \right] FT \cdot \left[(\epsilon_r(x,y) - 1)e^{j(\alpha_{l+1}x + \beta_{l+2}y)} \right]$$

$$(45)$$

The right hand side of the expression (36) becomes

$$b_t = \vec{T}_t \cdot \vec{E}^{n_x} F T \left[(\epsilon_x(x,y) - 1) e^{-\frac{1}{2} (\epsilon_x(x,y) - 1)} \right]_{\epsilon_x = 0}^{\epsilon_x = \epsilon_x + \epsilon_x + \epsilon_y + \epsilon_y} e^{-\frac{1}{2} \gamma_{\text{tot}} \frac{\Delta}{2}} \sin(\frac{\gamma_{\text{tot}} \Delta z}{2})$$
(46)

where F.T. is the Fast Fourier transform of the testing function evaluated at the 0,0 mode number.

4.3 Generalized Scattering Matrix [9]

Upon solution of the matrix equation (36) for the coefficients \vec{a} , we have an approximate expression for the total field across the unit cell. Since we approximated the field in the z direction by a single pulse, this solution is only valid for thin slabs. In order to find the characteristics of a thicker slab, we must cascade a series of these identical thin slabs using the generalized scattering matrix.

The first step in calculating the scattering matrix is to determine the scattered fields on either side of the slab (at 0 and at Δz) by substituting $\vec{E}^{ra}(x,y,z)$ into the expression for the scattered field and find the scattered fields for each of the k1 Floquet harmonics specified as basis functions.

$$\vec{E}_{n,n}^{(co)}(x,y,z) = j \omega \epsilon_0 \int_{\Delta_z} \tilde{G}(\alpha_n,\beta_n) e^{-j \sum_{n,n} 1/z + z^{-1}}$$

$$F.T. \left[(\epsilon,(x,y) - 1) \vec{E}^{tot}(x,y,z) \right] dz' e^{j (\alpha_n - 4\beta_n)/z}$$

$$(47)$$

where m,n are the mode numbers of the k1 basis functions. The scattered fields on the left side of the slab are the reflected fields which lead to the S_{11} submatrix. The scattered fields on the right side are added to the incident field to give the transmitted field which lead to the S_{21} submatrix. These fields are then broken up into waves TE to x and TM to x for each mode.

We now define the generalized scattering matrix as

$$\vec{S} = \begin{bmatrix} S_{11} & S_{12} \\ S_{21} & S_{22} \end{bmatrix} \tag{48}$$

Where S_{11} is the power reflected in the z direction at z=0 normalized by the incident power in the z direction at z=0. S_{21} is the transmitted power in the z direction at $z=\Delta z$ normalized to the incident power in the z direction at z=0. Because the geometry of the slab is symmetrical with respect to z, $S_{12}=S_{21}$ and $S_{22}=S_{11}$. Fach of the elements in the above matrix is itself a sub-matrix. For example

$$S_{11=} = \begin{bmatrix} S_{11|II|III} & S_{11|IM|IIE} \\ S_{11|II|IIM} & S_{11|IM|IIM} \end{bmatrix}$$
 (49)

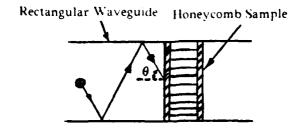
where TF/TM represents the TF response given a TM incident wave. Each element in the sub-matrix is a $K.1\times K.1$ sub-sub-matrix where K1 is the number of modes taken as basis functions. The N_1,N_2 element of this sub-sub-matrix is given by

$$\frac{a_{m,1,n,1} \int_{-\pi/2-d/2}^{\pi/2} \int_{\mathbb{R}^2} \left| \vec{E}_{m,1,n,1}^{(r)} \times \vec{H}_{m,1,n,1} \right| t|_{x} \right| \cdot \hat{z} ds}{\int_{-\pi/2-d/2}^{\pi/2} \int_{\mathbb{R}^2} \left| \vec{E}_{m,2,n,2}^{inc} \times \vec{H}_{m,2,n,2} \right| inc \right| \cdot \hat{z} ds}$$
(50)

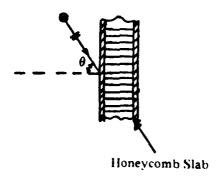
where t represents the transmitted wave used for S_{21} calculations and r the reflected wave for the S_{11} calculations. The numerator is the square root of the scattered power passing through the unit cell in the z direction for the $N_1 = m$ 1+n 1 mode. $a_{m,1,n,1}$ contains the phase information for the scattered field. The denominator is the square root of the incident power passing through the unit cell in the z direction for the $N_2 = m$ 2+n 2 mode.

5. Experimental Methods [10]

A waveguide technique was used to obtain the permittivity of a honeycomb slab. As shown in Figure 9, the honeycomb sample in a waveguide is equivalent to a honeycomb panel illuminated by a plane wave with an incident angle of



(a) Honeycomb sample in waveguide



(b) Equivalent honeycomb slab illuminated by a plane wave at incident angle $\theta = \sin^{-1}(\lambda/\lambda_c)$

Figure 9. Waveguide measurement technique

$$\theta = \sin^{-1} \frac{\lambda}{\lambda_{c}} \tag{51}$$

where λ is the wavelength of the incident wave and λ_c is the cutoff wavelength of the waveguide. Therefore, by measuring the insertion phase delay and the insertion loss of the honeycomb sample in the waveguide, we can determine the effective permittivity of the corresponding honeycomb panels.

The measurement technique is as follows: A WR175 waveguide without the honeycomb sample is connected to a network analyzer (HP8409) and the system is calibrated over the frequency band from 10 to 15 GHz. The honeycomb is inserted into the waveguide and the amplitude and phase of the S_{12} parameter is measured. From this measurement, an equivalent simple dielectric is calculated which exhibits the same insertion loss and phase delay (S_{12}) for the given frequencies and incident angles. Results of these measurements will be given in the results section (Table 3).

6. Results

We will examine the S parameters for the case of normal incidence on two different structured slabs using the methods developed above. Case one is meant to demonstrate the additional information provided by the full wave analysis over the effective medium theories (in this case the small contrast theory). Case two is meant to compare the two analytic methods with experimental results for an actual honeycomb. The slabs in both cases are 0.001m thick and the frequency is 10 GHz. The unit cell for slab one is a square dielectric filling one-quarter of a square cell. The cell side is 0.00693m long. The matrix is free space and the inclusion is a loss-less dielectric with $\epsilon_r = 2.0$. The unit cell slab for two is the honeycomb shown in Figure 4 with S1=0.00367m and dd = 1.62×10^{-4} m. The matrix is free space, but

the inclusion is slightly lossy (ϵ , = 3.29 - j.0757) being a composite reinforced with Kevlar 49 and bonded with Fpon 828 epoxy.

For the effective medium approach, the fill factor is 0.25 for slab one and 0.0255 for slab two. The spheroid is defined by taking the length of the major axis to be equal to the length of the unit cell (0.001m). The area of the inclusion in the x-y plane is collapsed into a circle, and the diameter of this circle is taken to be the length of the minor axis of the spheroid. Once the effective epsilon is calculated, the scattering parameters are calculated for the simple dielectric slab 0.001m thick.

In the full wave approach, we must decide how many points should be taken in the two-dimensional F.F.T. to describe the unit cell's structure, and how thick the slab can be so that a single pulse describes the field in the z direction. Both of these questions are answered numerically. The number of points are determined by deciding on how accurate the scattered fields should be and then increasing the number of sampling points until this accuracy is achieved. Since the approximate scattered fields will oscillate about the true scattered fields with increasing numbers of sampling points, we must increase the number of points beyond where the accuracy criterion first appears to be satisfied in order to insure true accuracy. In unit cell one. 25×25 points were taken leading to an accuracy of 10⁻³ while in unit cell two, 45 points were taken in the \hat{x} direction and 77 in the \hat{y} direction to achieve 10⁻² accuracy (thinner structure). The slab thickness (0.001m) was arrived at by comparing the program solution of a simple dielectric slab to the analytical solution in order to understand the relation of slab thickness and relative dielectric constant to accuracy. The thickness that gave 10^{-3} accuracy for a slab composed entirely of inclusion was used as a worst case estimate for the honeycomb slab. The results are

Scat/Inc	Scat mode #	S11		
		Full Wave	Small Con	
TE/TE	-1,-1	(194E-02,+.252E-02)	(+.000E+00,+.000E+00)	
	-1,+0	(294E-02,+.382E-02)	(+.000E+00,+.000E+00)	
	-1.+1	(194E-02,+.252E-02)	(+.000E+00,+.000E+00)	
	+0,-1	(171E-01,131E-01)	(+.000E+00,+.000E+00)	
	+0,+0	(566E-02,237E-01)	(607E-02252E-01)	
	+0.+1	(171E-01,131E-01)	(+.000E+00,+.000E+00)	
	+1,-1	(194E-02,+.252E-02)	(+.000E+00,+.000E+00)	
	+1,+0	(294E-02,+.382E-02)	(+.000E+00,+.000E+00)	
	+1,+1	(194E-02,+.252E-02)	(+.000E+00,+.000E+00)	
TM/TE	-1,-1	(+.585E-02,759E-02)	(+.000E+00,+.000E+00)	
	-1,+0	(117E-12,118E-12)	(+.000E+00,+.000E+00)	
	-1,+1	(585E-02,+.759E-02)	(+.000E+00,+.000E+00)	
	+01	(896E-13,692E-13)	(+.000E+00,+.000E+00)	
	+0,+0	(170E-17,144E-16)	(+.000E+00,+.000E+00)	
	+0,+1	(+.896E-13,+.692E-13)	(+.000E+00,+.000E+00)	
	+11	(+.108E-01,+.223E-02)	(+.000E+00,+.000E+00)	
	+1.+0	(+.117E-12,+.119E-12)	(+.000E+00,+.000E+00)	
	+1.+1	(+.585E-02,759E-02)	(+.000E+00,+.000E+00	

Table 1. S_{11} parameter calculated by the full wave analysis compared to the small contrast theory for a square block of dielectric filling 1/4 of a square unit cell. The side of the unit cell is 0.00693 m. $\epsilon_r = 2.0$. Only TE/TE and TM/TE results are shown since TE/TM and TM/TM are similar.

スタンの 自己 ファイン をおして こうきかな 国内 カラマンダ 大幅 同

Scat/Inc	Scat #	S21		
	mode #	Full Wave	Small Con	
TE/TE	-1,-1	(183E-02.+.237E-02)	(+.000F+00,+.000E+00)	
	-1,+0	(294E-02,+.382E-02)	(+.000E+00,+.000E+00)	
	-1.+1	(183E-02.+.237E-02)	(+.000E+00,+.000E+00)	
	+0,-1	(158E-01,122E-01)	(+.000E+00,+.000E+00)	
	+0,+0	(+.973E+00,232E+00)	(+.972E+00,233E+00)	
	+0,+1	(158E-01,122E-01)	(+.000E+00,+.000E+00)	
	+1,-1	(183E-02,+.237E-02)	(00 + <u>3</u> 000.+,00+ <u>3</u> C·00.+)	
	+1.+0	(294E-02.+.382E-02)	(+.000E+00,+.000E+00)	
	+1.+1	(183E-02.+.237E-02)	(+.000E+00,+.000E+00)	
TM/TE	-1,-1	(516E-02.+.670E-02)	(+.000E+00,+.000E+00)	
	-1.+0	(126E-12,538E-13)	(+.000E+00,+.000E+00)	
	-1.+1	(+.516E-02,670E-02)	(00+3000.+,000E+00)	
	+0,-1	(+.835E-13,+.645E-13)	(+.000E+00,+.000E+00)	
	+0,+0	(+.169E-17,+.144E-16)	(+.000E+00,+.000E+00)	
	+0,+1	(835E-13,646F-13)	(+.000E+00+.000E+00)	
	+1,-1	(+.516E-02,670E-02)	(+.000E+00,+.000E+00)	
	+1,+0	(+.125E-12,+.543E-13)	(+.000E+00,+.000E+00)	
	+1,+1	(516E-02,+.670E-02)	(+.000E+00,+.000E+00)	

Table 2. S_{21} parameter calculated by the full wave analysis compared to the small contrast theory for a square block of dielectric filling 1/4 of a square unit cell. The side of the unit cell is 0.00693 m, ϵ , = 2.0 Only TE/TE and TM/TE results are shown since TE/TM and TM/TM are similar.

Solution Method	S11	\$21
Small Contrast	(148E-02,585E-02)	(+.977E+00,214E+00)
Maxwell-Garnet	(787E-03334E-02)	(+.977E+00,211E+00)
Bruggeman	(809E-03,344E-02)	(+.977E+00,212E+00)
M-G Spheroid	(660E-03,283E-02)	(+.977E+00,211E+00)
Full Wave	(329E-02,125E-01)	(+.975E+00,221E+00)
Experimental	(258E-02,687E-02)	(+.976E+00,215E+00)

Table 3. S_{11} and S_{21} calculated by all the effective medium theories and the full wave analysis using only the 0.0 mode. These are compared to measured experimental results for a honeycomb unit cell. S1=0.00367 m. $dd = 1.62 \times 10^{-4} m$, and $\epsilon_r = 3.29 - j$ 0.0757.

shown in Table 1 through 3

7. Conclusion

We have seen that of the effective medium theories, the small contrast approximation provides the best agreement to both experiment and to the 0.0 Floquet harmonic of the full wave solution. Further, these results are obtained several orders of magnitude quicker than a full wave solution and are easily cascaded with the F.S.S. parameters. The full wave solution, on the other hand, provides information on how higher order modes behave and how the structure changes the polarization of the incoming wave. We found that some of the higher order modes are as large as the 0.0 mode implying that structure does play an important role. Also note that in Table 1, the scattered fields are showing two-fold symmetry around the 0.0 mode due to the two-fold symmetry of the unit cell.

One of the major problems with the full wave analysis is the need to take so many sampling points to describe the thin-shell structure, although we do not need to zero pad as we do with non-periodic structures. Future work will concentrate on increasing the efficiency of the full wave analysis, possibly through the use of acceleration techniques for the slowly convergent series.

8. References

- [1] Niklasson, G.A.; Gravenqvist, C.G. and Hunderi, O. (1981) Effective medium models for the optical properties of inhomogeneous materials, *Applied Optics* 20 (No. 1):26-30.
- [2] Bohren, C.F. and Battan, L.J. (1982) Radar backscattering of microwaves by spongy ice spheres. *Journal of the Atmospheric Sciences* 39:2623-2628

- [3] Stratton, J.A. (1941) Electromagnetic Theory, McGraw-Hill, New York, pp.205-215.
- [4] Osborn, J.G. (1945) Demagnetizing factors of the general ellipsoid. *Physical Review* 67 (No. 11,12):351-357.
- [5] Bohren, C.F. and Battan, L.J. (1980) Radar backscattering by inhomogeneous precipitation particles, *Journal of the Atmospheric Sciences* 37:1821-1826.
- [6] Wright, S.M. (1984) Efficient analysis of infinite microstrip arrays on electrically thick substrates. Ph.D. thesis. University of Illinois at Urbana-Champaign.
- [7] Harrington, R.F. (1961) Time-Harmonic Electromagnetic Fields, McGraw-Hill, New York, pp. 27,186.
- [8] Harrington, R.F. (1968) Field Computation by Moment Methods. Krieger, Malabar, FL.
- [9] Mittra, R. and Lee, S.W. (1971) Analytical Techniques in the Theory of Guided

 Waves, MacMillan Company, New York, pp.207-217.
- [10] Wu. T.K., Private communication

APPLICATION OF PLANAR NEAR FIELD MEASUREMENT TECHNIQUES FOR SPACE ANTENNAS

R.D. WARD AND M.A. SCHULZ HUGHES AIRCRAFT COMPANY SPACE AND COMMUNICATIONS GROUP EL SEGUNDO, CALIFORNIA

ABSTRACT

Space antenna designs have progressed significantly during the past decade. Recent designs combine requirements for high spatial (sidelobe) isolation and high polarization isolation for dual polarized use.

Conventional far field ranges offer various disadvantages. Ground reflections may contaminate low sidelobe antenna measurements. Cross polarization measurements reuqire a source correction when the cross polarization level of the source antenna is comparable to or worse than that of the antenna under test. Intermediate ranges (less than $2D^2/\lambda$) may require correction for near field effects. Furthermore, the high price of land and the considerable expense of maintaining equipment out-of-doors make the construction and operaton of such ranges a very ambitious endeavor.

In addition to offering an attractive solution to these problems, near field antenna measurement offers other advantages. Since a near field facility can be indoors, all-weather, RF shielded operation is possible. The facility's considerable automation capability allows unattended operation. Also, the antenna under test at a planar near field range need not move during the measurement.

This paper reviews development by the Hughes Aircraft Company's Space and Communications Group (SCG) of a planar near field range for testing satellite antennas at SCG's El Segundo, California, facility. Features of the range are discussed, and certain problems encountered in its operation are described.

INTRODUCTION

In early 1982 the Hughes Aircraft Company Space and Communications Group (SCG) was awarded a contract for the Intelsat VI communications satellite. Several problems were identified with using the existing far field range facility for systems testing on the Instelsat VI antennas (Figure 1). The most significant problems were: 1) range reflections, 2) near field effects due to short range length, 3) inadequacy for

making cross polarization measurements, 4) RF interference, and 5) mechanical support of the antenna to simulate a zero gravity environment. These problems and the high estimate of cost of developing an adequate far field range at the SCG El Segundo, California site led to the decision to construct a planar near field range for satellite antenna measurements.

FACILITY

The near field test facility adjoins the satellite integration (high bay) area; large double doors between the two areas facilitate movement. The facility is large enough (50 feet long by 40 feet wide with a 40 foot ceiling height) to allow testing of the Intelsat VI satellite with all antennas deployed.

Although the facility was not designed as an RFI free enclosure, its walls are double lined with metal sheets, and the inside is covered with RF absorbant material. Problems previously encountered with the outdoor range concerned externally generated signals detected in the passband of the satellites being tested. Tests show that this facility provides an effective isolation of approximately 60 dB in the frequency bands of interest.

MECHANICAL DESIGN

As mentioned previously, the facility is designed for planar near field scanning. Figure 2 shows the scanner structure in the assembled state. The scanner can measure an area 21 feet on a side, (horizontally and vertically). Horizontal scanning is provided by moving the large truss structure (carriage) on two cylindrical rails located at the top and bottom of the scanner. Vertical scanning is accomplished by moving the probe platform (to which the near field probe antenna is attached) along two smaller rails mounted to the carriage. Both sets of rails have supports that are adjustable in three dimensions for precise alignment. Two dc servo motors serve as drives. One motor moves the carriage horizontally; the other moves the probe platform vertically. For movement along each axis, motive force is translated from each motor by a gear reducer and a chain drive; a controller for each motor ensures uniform motion and precise positioning; and a laser interferometer system for each axis provides precise position information (Figure 3).

MEASUREMENT SYSTEM

Theory requires that the near field amplitude and phase of the antenna under test be measured over a planar surface. The system is designed to time multiplex measurements while switching frequency, polarization, and antenna beam. Up to six beams may be sampled in any sequence. Many of the satellite antennas built by Hughes

SCG feature multiple beam designs. One of these, the Intelsat VI, hemi/zone antenna, achieves sixfold frequency reuse through a combination of spatial and polarization isolation. Figure 4 is a block diagram of the measurement system. The amplitude and phase measurements are made by a network analyzer, and the analog outputs are digitized for computer processing.

The transform used requires that the near field measurement points be evenly spaced in two dimensions. Also, for efficiency, near field measurements are made while the measuring probe is in motion. To satisfy these requirements, the position of the probe is constantly monitored by the computer. The outputs of the two interferometers are read, and analog-to-digital conversion of the network analyzer output is initiated, at the appropriate time. The system is monitored for late measurements to allow for optimum adjustment of the scan rate.

Many of the antennas that must be measured have requirements for low side-lobes and high polarization purity. Therefore, the measurement system is required to have a large dynamic range (>50 dB). To achieve this, low noise amplifiers are placed as close to the output of the antenna under test as is practical.

It is important for the signal level to remain above the system threshold. Figure 5 shows the effect of measuring with a signal level that drops below the threshold during the scan. In this case, the phase output of the network analyzer becomes nearly constant at the low levels, resulting in distortion at boresight when the Fourier transform is applied. To eliminate the distortion, the scan area was reduced to exclude the low levels. Figure 6 shows the resulting pattern.

Another problem resulting from the large dynamic range is RF leakage that bypasses the near field probe and (or) the antenna under test. Because of this problem, care must be taken with those shielding points at which radiation may occur (for example, at coax or waveguide interfaces).

NEAR FIELD PROBES

A key element in planar near field antenna measurements is the near field probe. This antenna, which is usually designed for low or medium gain, is scanned over the measurement plane to characterize the antenna under test. The algorithm used requires measurements of two orthogonal polarizations. Figure 7 shows dual polarized probes for performing near field measurements. With this probe, the two orthogonal measurements are made simultaneously, and a second measurement scan is not required.

To correct the patterns of the antenna under test for the probe pattern, the probe must be accurately calibrated. Figure 8 shows the results of correction for the probe pattern. Clearly, the effect of correction on the cross polarized pattern of the antenna under test is significant. In this case, it results from the cross polarization ratio of the probe being of the same order as that of the antenna under test. Near field cross

polarization measurements in many cases are likely to give more accurate results than far field results because they include source (probe) correction, which typically is not done on a far field range.

TEST CONTROL AND ANALYSIS

An HP 1000 minicomputer is used for automated test control and test data analysis. Test data is collected on the system disk and is processed at the conculsion of the measurement.

The devices that are interfaced to the computer for automated measurement and test control include:

- a two-axis motor controller
- a two-axis laser interferometer
- a frequency synthesizer
- analog-to-digital converters
- RF switches
- programmable attenuators
- power meters
- a time code generator

The pattern measurement software is designed to run unattended, and test progress can be monitored remotely via modem. Automatic test restart of the measurement is initiated in the event of a laser fault.

Data analysis consists of the fast Fourier transform (FFT), inverse FFT, the probe correction, and the antenna pattern graphics.

Near field to far field data transformation requires several steps. Before transformation, the near field data is zero padded (that is, the near field amplitude is set to zero) to the required array size. The FFT is applied, and the data is transformed into far field vector (K) space. The transformed data is windowed, and an inverse FFT is applied. The data is again zero padded to the original array size, and the FFT is applied a second time. This technique results in higher resolution in the region around which the data is windowed without additional sampling in the near field. Figure 9 shows a transform pair (near field pattern versus far field pattern).

Application of the FFT to the near field data results in a far field pattern as it would appear (theoretically) at an infinite range length. This transformation offers some advantages over far field measurements which often occur in practice. For high gain antennas (such as the Intelsat VI hemi/zone antenna), testing at a range length less than $2D^2/\lambda$, can result in noticable pattern distortion due to phase error. Also, boresight errors can occur when parallax is improperly accounted for on ranges of a finite length. Parallax correction becomes particularly complicated when several antennas are mounted on the same structure.

In addition to antenna patterns, the near field system developed has the capability to derive satellite system parameters, such as for EIRP and flux density. The techniques for these measurements use the near field scan data, the transformed data, and the probe input (flux density) or output (EIRP) power. These techniques are very useful because they do not require moving the satellite to a far field antenna range to derive the desired parameters.

TEST RESULTS

Several satellite antennas have been measured with the near field test facility. Figure 10 shows the Morelos T-1 satellite during near field tests. This satellite, which is designed to provide domestic communications to Mexico, features two reflector antennas for 4 GHz, 6 GHz, and 12 GHz beam coverage and a planar array antenna for 14 GHz coverage. Note that, although minimal mechanical support is required for near field testing, the requirements for far field testing can be significant. (See Figure 1.) This is because the antenna under test remains stationary during the measurement. Figure 11 compares near field pattern measurements with far field measurements for a typical Hughes satellite antenna.

CONCLUSION

Applying the concept of planar near field techniques and subsequently developing this facility for testing satellite antennas provides the Hughes Space and Communications Group with an effective alternative to developing a larger far field range. Several difficult problems associated with testing state of the art satellite antennas have been eliminated. The facility already is highly automated and offers further growth potential to satisfy future requirements.

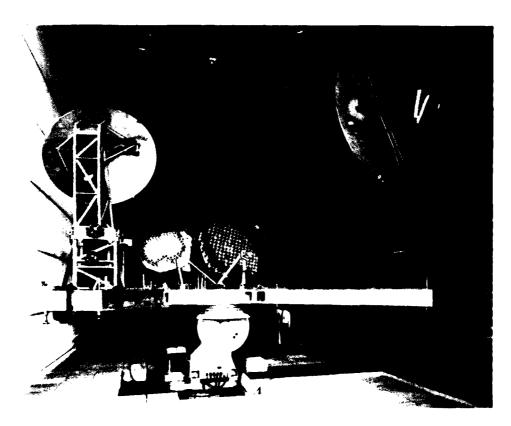


FIGURE 1. INTELSAT VI HEMI/ZONE ANTENNAS



FIGURE 2. NEAR FIELD SCANNER ASSEMBLY

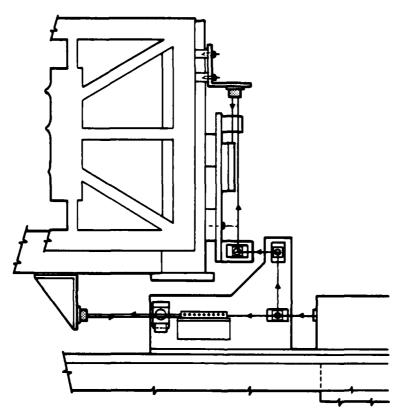


FIGURE 3. NEAR FIELD LASER CONFIGURATION

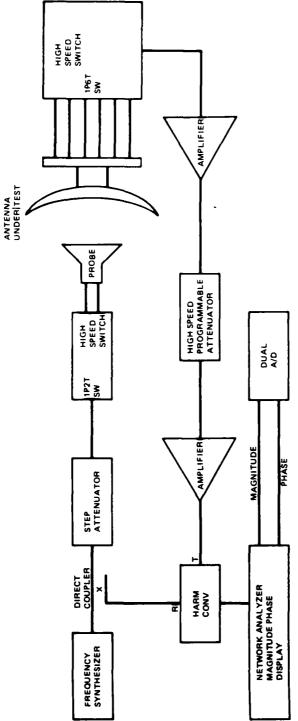


FIGURE 4. NEAR FIELD MEASUREMENT SYSTEM BLOCK

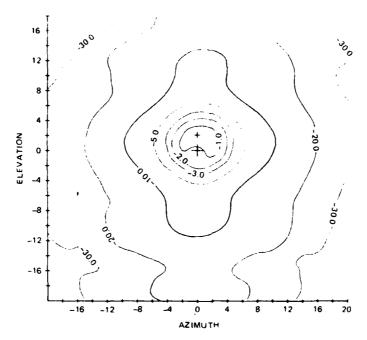
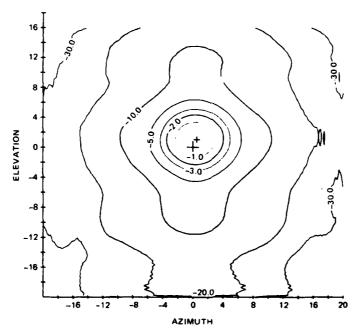


FIGURE 5. MEASUREMENT WITHOUT SCAN AREA REDUCTION



では、100mmので

FIGURE 6. MEASUREMENT WITH SCAN AREA REDUCED TO EXCLUDE LOW LEVELS

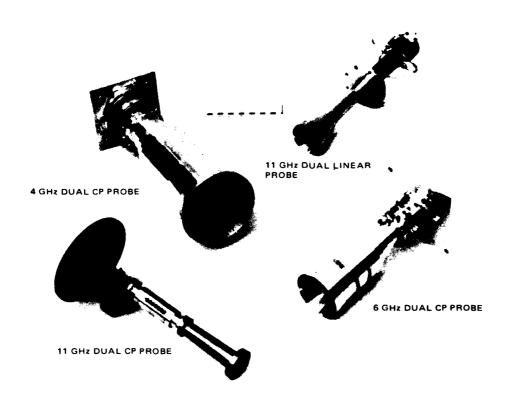
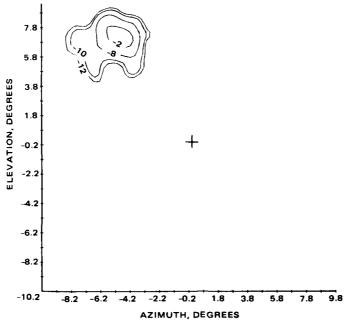


FIGURE 7. DUAL POLARIZED PROBES





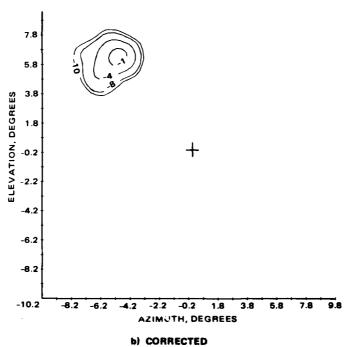


FIGURE 8. EFFECTS OF PROBE PATTERN CORRECTION

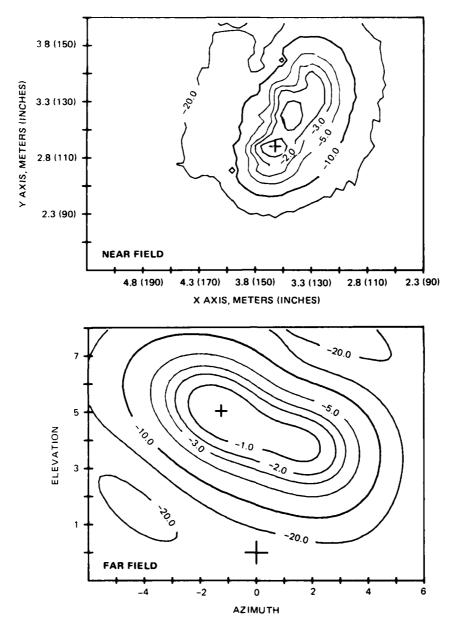


FIGURE 9. NEAR FIELD/FAR FIELD TRANSFORM PAIR

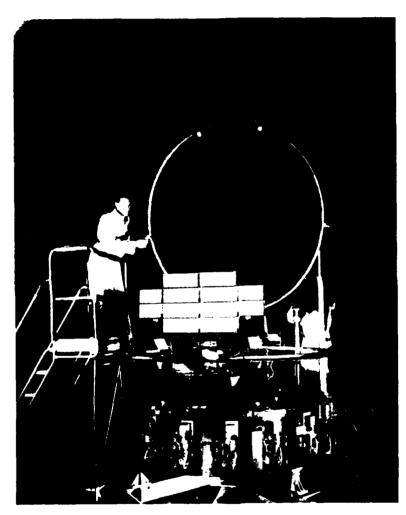


FIGURE 10. MORELOS T-1 NEAR FIELD TEST

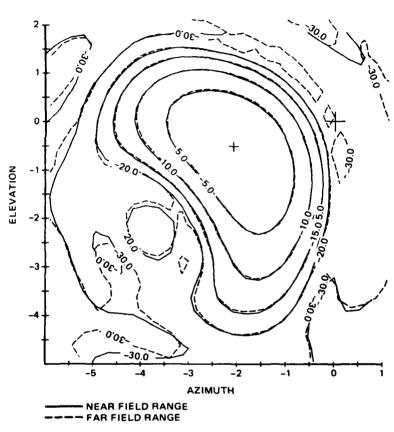


FIGURE 11. NEAR FIELD/FAR FIELD TEST COMPARISON

EVALUATION OF A VHF SATELLITE ANTENNA SYSTEM

CONNIE W. THOUSAND
Member of Technical Staff
Antenna Technology
Rockwell International Corporation
Strategic Defense and Electro-Optical
Systems Division
Defense Electronics Operations
Anaheim, CA 92803

1. ABSTRACT

A highly specialized VHF pattern measurement range has been constructed for the measurement of two circularly polarized antennas. Unusual measurement problems were created by the satellite size and the low VHF frequencies of the antenna system. The two antenna systems operate over bandwidths of nearly fifty percent and are capable of receiving both right and left hand circular polarization. Due to the long wavelengths involved, surface currents on the satellite and its solar panels are a significant factor in the net antenna performance.

The maximum dimensions of the satellite are nearly equal to the twenty foot wavelength of the lowest frequency to be tested; therefore, although the antenna directivity is low, the aperture to be tested may be as large as one square wavelength.

Even though the range shown in Figure 1 appears to be a conventional horizontal configuration, there are two specialized

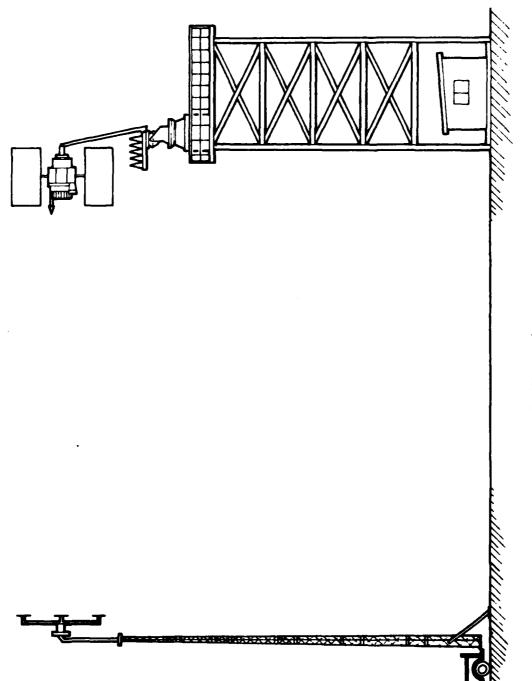


Figure 1. Range Configuration

features that have significantly reduced measurement errors due to ground reflections and multiple scattering between the two closely spaced towers.

2. RANGE CONFIGURATION

Since a remote controlled battery powered source transmitter is used inside the satellite to eliminate the possible effects of a detector cable on pattern results, that which is normally considered the source antenna is referred to as the receiving array in this configuration.

The horizontal range distance was set at 102 feet, which is $2D^2/\lambda$ at the highest test frequency for the maximum aperture presented by the satellite. It was desirable to use an array to place a pattern null in the specular reflection zone of the range as shown in Figure 2.

This array was initially a four (4) element array consisting of four (4) crossed dipole elements fed in quadrature and backed by a reflector with parasitic elements between the dipoles and the reflector for increased bandwidth (designed by Howard King and Dr. Jimmy Wong of Aerospace Corp.). The dimensions of this array are shown in Figure 3.

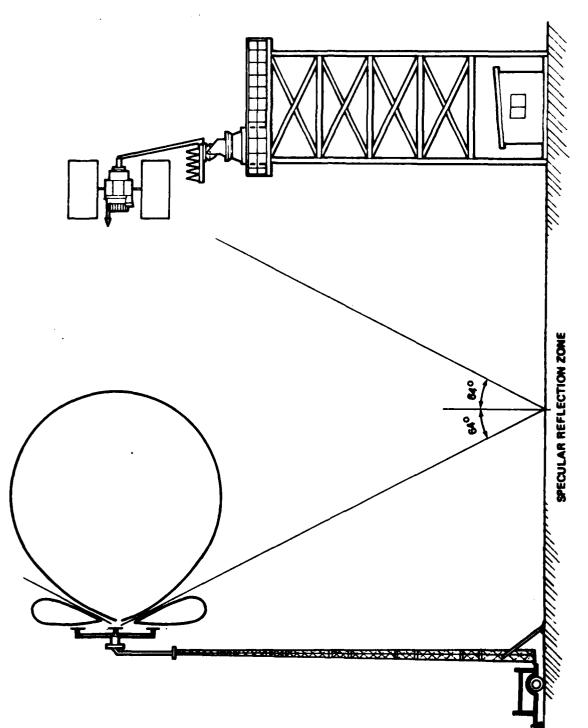


Figure 2. Theoretical pattern of receiving array on test range

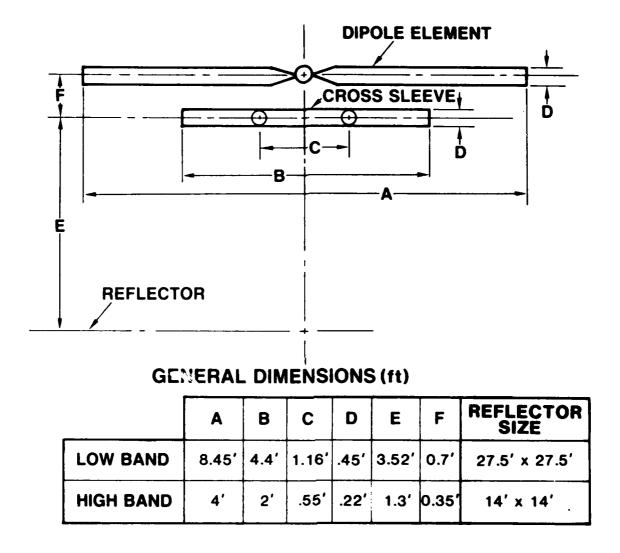
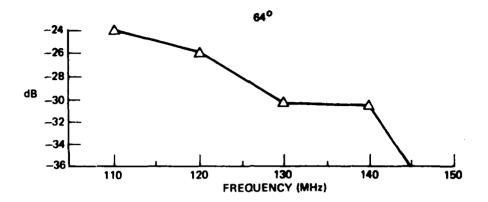


Figure 3. Dimensions of King/Wong, 4 element receiving array

The array spacing was set to a dimension that maintained the energy in this zone at least 25 dB below the pattern maximum throughout the 50 percent band to be tested. This array was tested and as portrayed in Figure 4, performed as expected.

From an analysis by Dr. C. J. Chen, of Rockwell International, multiple scattering (depicted in Figure 5) between this receiving array and the satellite can introduce significant measurement errors. The worst case, for example, is when the satellite solar panels are at 0 degrees, which presents the largest plane reflecting surface area normal to the range boresight axis.

The multiple scattering is then magnified if the receiving array antenna is backed by a reflecting screen. Possible interference to signal ratios for such conditions are shown in Figure 6. Since the measurement of axial ratio is the most sensitive to error caused by reflections, it is desirable to significantly reduce the multiple scattering cross section of the receiving array. Figure 7 shows the desired interference to signal ratio to achieve from 0.5 dB to 1.5 dB measurement accuracy. To reduce the receiving array scattering aperture enough to achieve these levels requires both eliminating the reflector screen and the use of non-resonant array elements, approximately 0.2 λ long. Figure 8 shows the scattering aperture



dB = LEVEL BELOW PATTERN MAXIMUM AT SPECULAR REFLECTION ZONE

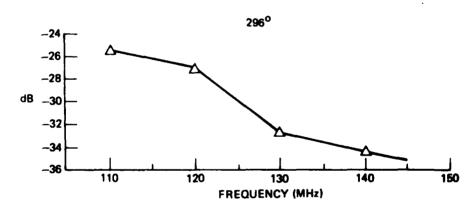


Figure 4. Energy in specular reflection zone for King/Wong, 4 element array

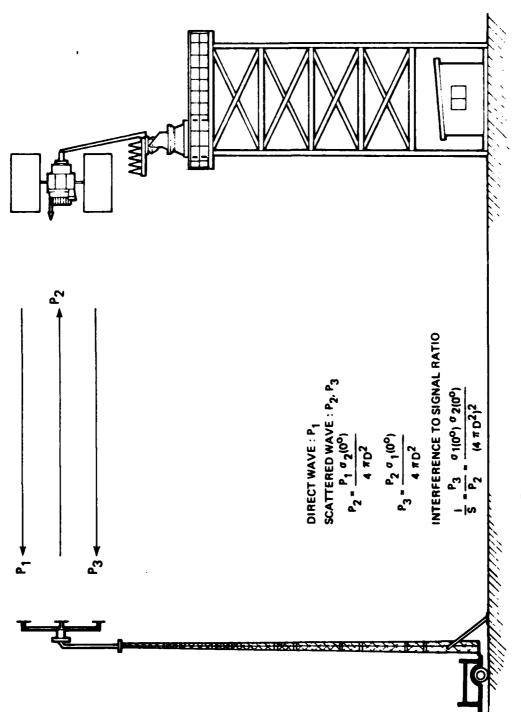


Figure 5. Multiple scattering

GPS: MODELED AS A RECTANGULAR PLATE OF EFFECTIVE SIZE 5.08 X 7.43 M

$$\sigma = \frac{4 \pi A^2}{\lambda^2}$$
 FOR BROADSIDE INCIDENCE

f	50 MHz	100 MHz	150 MHz	
λ	6M	ЗМ	2M	
σ	σ 497		4475	
10 LOG ø	26.9	32.9	36.5	

$$\frac{1}{S} = \frac{{}^{\sigma}GPS {}^{\sigma}DIPOLE}{(4 \pi D^2)^2}$$

D = 27.43 M (=90')

10 LOG $(4 \pi D^2)^2 = 79.5 dB$

f	50 MHz	100 MHz	150 MHz
<u> </u>	-26.8 dB	-26.8 dB	-26.8 dB

Figure 6c. Interference to signal ratio for multiple scattering between satellite and resonant dipoles

IF DIPOLES ARE BACKED BY A GROUND PLANE 27.5' X 27.5'

f	50 MHz	75 MHz	100 MHz	150 MHz
σ3	16.7	3638	6468	14553
10 LOG 0 3	32.1	35.6	38,1	41.6
1 (dB)	-20.4	-16.9	-14,4	-10.9

$\sigma = 1.2 \lambda^2$ FOR RESONANT DIPOLES

f	50 MHz	100 MHz	150 MHz	
λ	6M	3M	2M	
σ	43.2	10.8	4.8	
10 LOG 0	25.8	19.8	16.4	

Figure 6b. Scattering cross-section vs. frequency for resonant dipoles

IF DIPOLES ARE BACKED BY A GROUND PLANE 14' X 14'

f	100 MHz	150 MHz	
<i>o</i> 3	434	977	
10 LOG (σ ₃)	26.4	29.9	
1 (dB)	26.2	-22.6	

Figure 6d. Interference to signal ratio for multiple scattering between satellite and reflectors (ground planes)

Figure 6. Interference to signal ratios

Axial ratio without interference = A dB Allowable range of axial ratio with interference = A dB \pm bdb Interference to Signal Ratio I/S

b	1/\$	PERCENT ERROR IN E FIELD	
.5 dB	-30.8 dB	6 percent	
1.0 dB	-25 dB	12 percent	į
1.5 dB	-21.3 dB	18 percent	

Figure 7. Axial Ratio vs. Interference to Signal Ratio.

for elements from 0.1 to 0.5 λ . As shown, if normalized to 0.5 λ resonant element, the scattering aperture of a 0.2 λ element is 24.1 dB lower.

Using non-resonant elements does lower the array efficiency due to VSWR mismatch, but transmitter power levels from +20 dBm to +30 dBm proved to be adequate for the 102' range spacing.

From this analysis, and the weight limitation of the mobile tower, a non-backplaned array with non-resonant elements was built, tested and utilized. This array is also made of four (4) crossed elements fed in quadrature, through a remote controlled transfer switch, to permit changing polarization sense during testing as shown in Figure 9. One spacing of this array was chosen to provide the lowest energy possible in the specular reflection region over the entire band. Representative patterns of this array are shown in Figures 10, 11 and 12, and the energy in the specular reflection zone is graphed in Figure 13.

3. SATELLITE TESTS

Two methods are used to derive axial ratio. The test equipment set-up is shown in Figure 14. In the first method, the satellite is spun on axis, against a fixed linear receiving antenna. This is equivalent to the standard spinning linear method

For $R_L = 0$, $X_T = 0$, $R_T = 50$, $a/\lambda = .0035$

L/x	R_{R}	XA	As	10 LOG (As/Ao)	Ae	10 LOG (Ae/A ₁)
.5	73	25	.109 ² (=Ao)	O dB	.074 ² (=A ₁)	0 dB
.4	40	-50	.56 ²	-2.9 dB	.070 ²	-0.2 dB
.3	22	-105	$.011\lambda^2$	-10.0 dB	.025 ²	-4.7 dB
.2	4	-180	.00042 ²	-24.1 dB	.0052 ²	-11.5 dB
.1	2	-240	.000031 ²	-35.4 dB	.00077 ₂ 2	-19.8 dB

Figure 8. Examples of Element Length vs. Scattering Aperture.

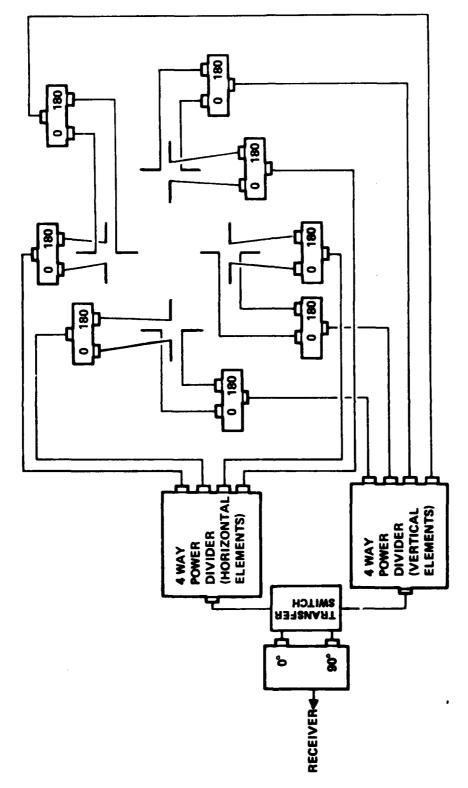


Figure 9. Receiving array feed system

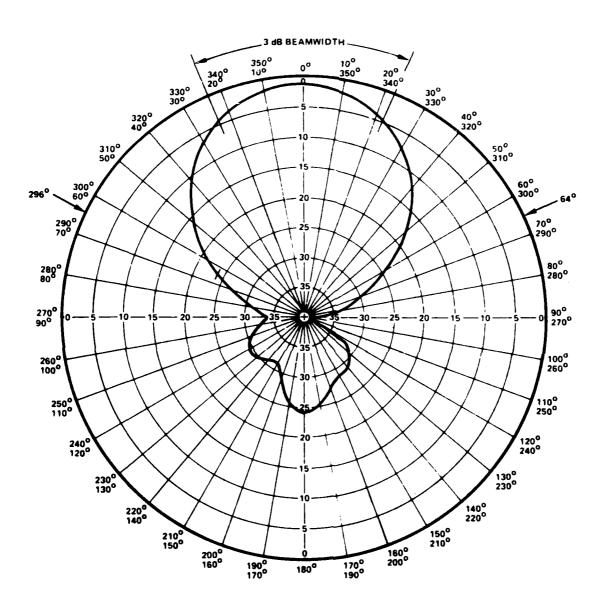


Figure 10. Radiation pattern for non-backplaned, shortened element array for 110 MHz

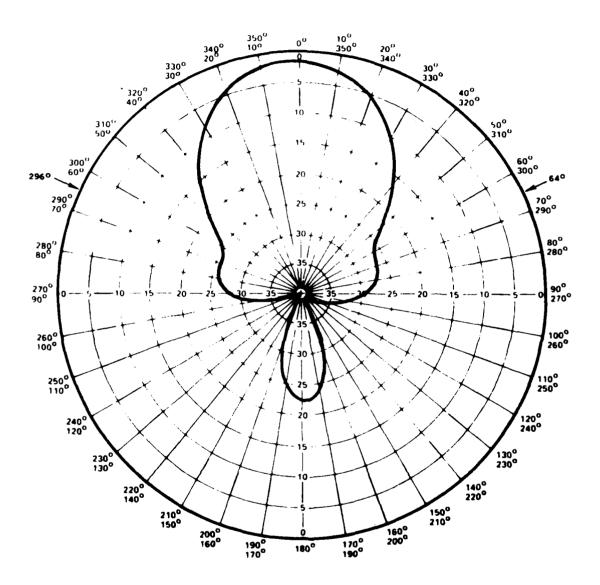


Figure 11. Radiation pattern for non-backplaned, shortened element array for 130 MHz

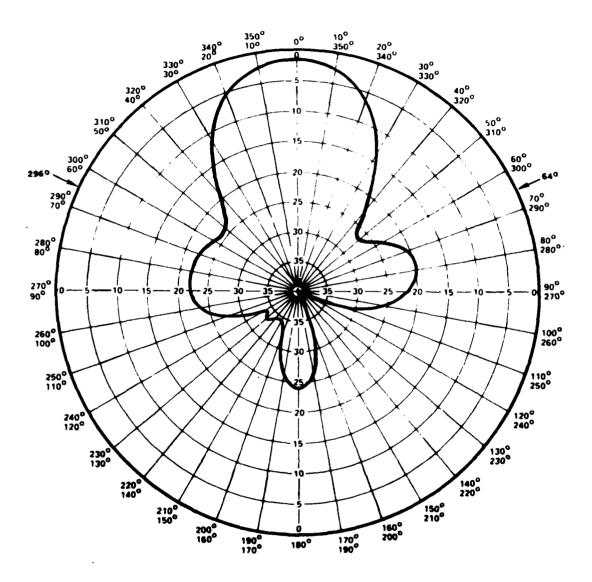
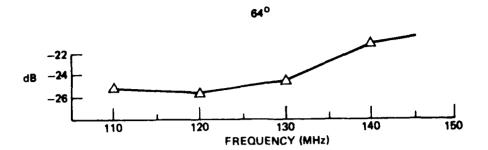


Figure 12. Radiation pattern for non-backplaned, shortened element array for 146 MHz



dB = LEVEL BELOW PATTERN MAXIMUM AT SPECULAR REFLECTION ZONE

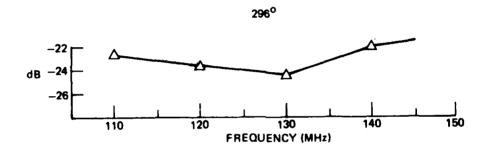
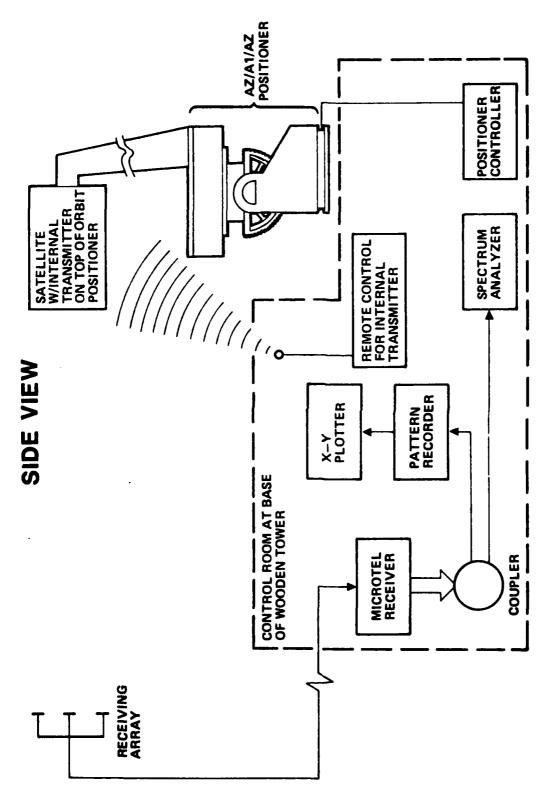


Figure 13. Energy in specular reflection zone for non-backplaned, shortened element array



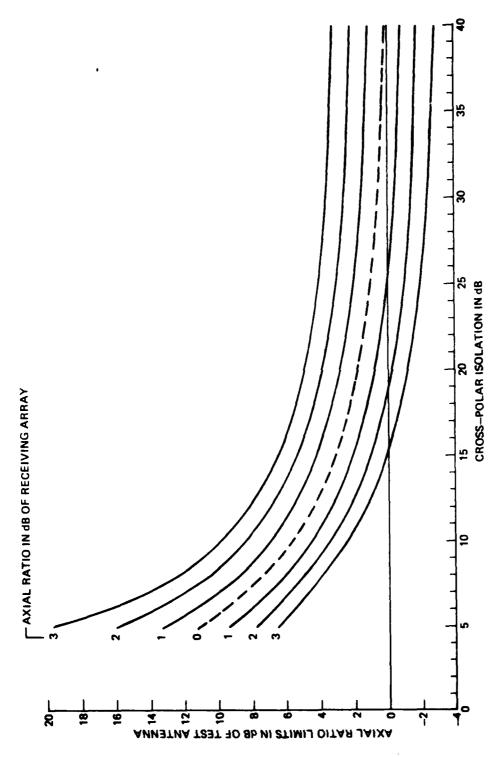
CONTROL OF THE CONTRO

Figure 14. Range set-up for axial ratio tests

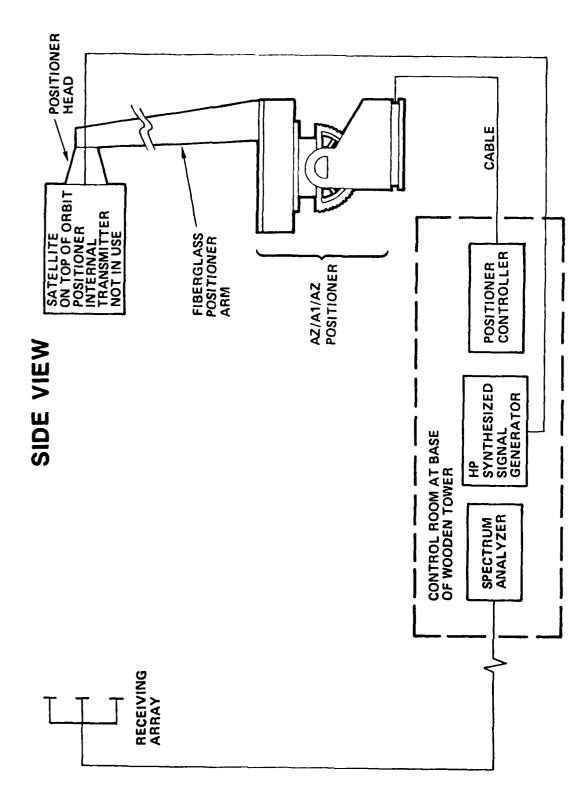
of determining axial ratio. This method is only valid when the satellite is oriented normal to the range boresight axis where the resulting pattern is the equivalent of a polarization pattern. These patterns are taken with the receiving array phased for horizontal linear, and then again for vertical linear. The axial ratio is determined by averaging the value of these two patterns.

Off axis, however, pattern amplitude variations are superimposed on the polarization ellipse. Therefore, in the second method, the axial ratios for the off axis angles are computed from the isolation levels between the right and left hand polarization senses. Since the receiving array does not exhibit perfect circular polarization, axial ratio cannot be directly computed from the isolation data; therefore, the analysis by Dr. Allen Love of Rockwell International (depicted in Figure 15), is used to bracket the actual value of axial ratio.

The set-up for measuring gain is shown in Figure 16. For gain testing, the array is re-configured to provide either horizontal or vertical linear response to eliminate some problems in accurately correcting for polarization loss between two (2) elliptically polarized antennas. Gain is measured for both horizontal and vertical linear states of the receiving array to arrive at an averaged level. Two element Yagi antennas were calibrated for use as a standard gain reference.



Axial Ratio limits of test antenna vs. cross-polar isolation with receiving array Axial Ratio as parameter Figure 15.



STATE OF THE PROPERTY OF THE P

「おいている」では、これでは、100mmでは、100m

Figure 16. Range set-up for gain testing

AUTOMATED THREE-ANTENNA POLARIZATION MEASUREMENTS USING DIGITAL SIGNAL PROCESSING

John R. Jones and Doren W. Hess Scientific-Atlanta, Inc.

Abstract

In this paper we present a three-antenna measurement procedure which yields the polarization of an unknown antenna to an accuracy comparable to that of the improved method of Newell. The complete method is based on step-scan motion of the two polarization axes on which the antenna pairs are mounted. As a special case this step-scan procedure includes the usual single axis polarization pattern method of polarization measurement.

This three-antenna polarization measurement method can be readily automated and is carried out straightforwardly with the assistance of a minicomputer for data acquisition and data reduction. The data reduction method is based on conventional digital Fourier transform techniques and has the advantage of inherent noise rejection. It utilizes a large number of sample points which greatly overdetermine the parameters to be measured.

The method has been verified experimentally with measurements made on multiple overlapping sets of three antennas, as is conventional for this kind of procedure. The data are presented for broad-beam antennas of the type used as near field probe horns.

I. Introduction

The purpose of a polarization measurement is to determine the tilt angle, axial ratio and sense of the electric field polarization ellipse by means of a procedure carried out on an antenna measurement range. In general, these parameters are functions of direction, and therefore in general a polarization measurement of the field of an antenna must be made at each pattern direction of interest. Such solid angle measurements of polarization require knowledge

of the polarization of the range antenna with which the measurement is made.

When the range antenna itself has unknown polarization characteristics, a three-antenna polarization measurement is performed to determine the polarization characteristics of the range antenna. Because of the complexity of the data reduction associated with a three-antenna polarization measurement procedure, such a procedure is usually limited to determining the polarization of an antenna in only one direction of the radiation pattern. By performing polarization pattern measurements on each of the three possible pairs of antennas in a three antenna set one is able to ascertain the axial ratio, tilt angle, and sense of the polarization ellipse for each of the three antennas. Usually, the polarization for the direction of the peak of the beam for each of the three antennas is measured. The only a-priori knowledge required is the approximate tilt angle (within 45°) of one of the antennas in the three antenna set and the fact that one of the antennas is reciprocal.

A number of different procedures have been devised in the past for performing three-antenna measurements of the complex polarization ratios of antennas. Newell and Kerns^[1] and Joy and Paris^[2] independently developed three-antenna phase/amplitude polarization measurement methods in the early 1970's. Newell, Baird, and Wacker^[3] described the NBS extrapolation technique for the measurement of polarization and gain in 1973 and gave some experimental results obtained using the method. All polarization measurement methods up to this time had a requirement for accurate measurement of phase. In fact, in certain unusual measurement situations, all the polarization information derives from the phase measurement.

In 1975^[4] Newell recognized that a three-antenna polarization measurement method could be devised such that almost all of the information from the measurement derives from the amplitude measurement. Newell's method, as it has come to be called, requires only that the sense (either positive or negative) of the 180° phase change associated with the null in the polarization pattern be known. This insensitivity to the measurement of phase is the primary advantage of Newell's method, and is responsible for the improved accuracy of the method compared to those described in references 1-3. The method of polarization measurement described in this paper, like

Newell's method, depends on the fact that the form of the functional dependence of the measured quantities on the desired unknown polarization parameters is known. Instead of assuming phase information, as is done with Newell's method, this new method uses the measured phase information but selectively removes measurement errors by digital signal processing, thereby improving the accuracy of the measurement.

The selective removal of errors is accomplished by a one- or two-dimensional discrete Fourier transform (DFT) which filters the measured data as a function of angle in the spatial frequency domain and leaves only the spatial frequency components that vary with angle as polarization patterns ideally should. A method of polarization measurement using a one-dimensional discrete Fourier transform was implemented in 1981 by workers at the Technical University of Denmark^[5], but the method described herein based on a two-dimensional discrete Fourier transform has not been described before in the literature. The mathematical foundation for the method is described briefly in the next section.

II. Mathematical Basis

The three antenna method is carried out by measurement of the polarization patterns between successive pairs of antennas. The measurement configuration has one antenna transmitting an illuminating wavefront that is received by the second antenna. For a given pair the relative received phasor or normalized voltage response is given by the matrix product

$$\hat{\mathbf{v}} = (\mathbf{w}_r \ \mathbf{w}_r) = \mathbf{w}_r^{\dagger} \ \mathbf{w}_r \tag{1}$$

where the superscript † denotes the complex conjugate of the transpose of a matrix and where the W $_{\rm T}$ and W $_{\rm t}$ are the column matrices

$$W_{t} = \begin{bmatrix} \cos \gamma_{t} \\ \\ \\ \sin \gamma_{t} \end{bmatrix} \qquad W_{r} = \begin{bmatrix} \cos \gamma_{r} \\ \\ \\ \\ \sin \gamma_{r} \end{bmatrix} \qquad (2)$$

 W_t is the polarization column vector of the transmitting antenna--i.e. W_t is the polarization column vector of the wave which is incident on the receiver. W_r is the polarization column vector of the receiving antenna--i.e. W_r is the polarization column vector of the wave to which the receiving antenna is perfectly polarization-matched.

The polarization matrices are related mathematically to the angles which specify the polarization of a wave by the location of its corresponding point on the Poincaré sphere $^{[6]}$. See Figure 1 for an illustration of the Poincaré sphere showing the polar angle 2γ and the longitude δ_c . Each point of the Poincaré sphere is associated with a particular polarization state of a wave. There is a one-to-one mapping between points on the sphere and possible polarization states of the wave. The polar angle 2γ and the longitude δ_c are shown designating the polarization of the wave, with the poles of the sphere designating left-hand and right-hand circular polarization states.

If the antennas are physically rotated about the range axis, which is the line-of-sight joining them, the polarization matrices take on the following parametric dependence on the rotation angles ϕ and χ :

$$W_{t}(\phi) = \begin{bmatrix} \cos \gamma_{t} e^{+j\phi} \\ \\ +j\delta_{ct} -j\phi \\ \\ \sin \gamma_{t} e \end{bmatrix}$$
(3)

and

$$W_{\mathbf{r}}(\chi) = \begin{bmatrix} \cos \gamma_{\mathbf{r}} e^{-j\chi} \\ \\ \\ \sin \gamma_{\mathbf{r}} e \end{bmatrix}$$
(4)

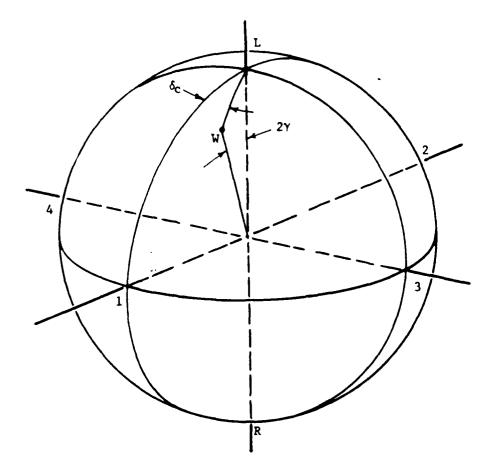


Figure 1. Poincare sphere with polar angle 2γ and longitude δ shown. Each point on the sphere is associated with a particular polarization state of a wave.

Then

$$\hat{V} (\phi, \chi) = \cos \gamma_t \cos \gamma_r e^{j(\phi + \chi)} +$$

$$\sin \gamma_t \sin \gamma_r e^{-j(\phi + \chi + \delta_{cr} - \delta_{ct})}$$
(5)

where the time dependence $e^{+j\omega t}$ has been assumed. The angles ϕ and χ are the angles through which the transmitting antenna and receiving antenna respectively are rotated in the clockwise direction as each is viewed from the other. Figure 2 illustrates the coordinate systems for the polarization measurements and defines the rotation angles.

Equation (5) will be recognized as a simple two-dimensional Fourier series in the angles ϕ and χ . Only two spatial frequency components in each variable are present—the positive and negative single cycle per cycle harmonics.

The coefficients of the Fourier series can be computed from the known parametric dependence of \hat{V} on ϕ and χ by inversion:

$$\cos \gamma_{t} \cos \gamma_{r} = \left(\frac{1}{2\pi}\right)^{2} \int_{0}^{2\pi} \int_{0}^{2\pi} \hat{V}(\phi,\chi) e^{-j(\phi + \chi)} d\phi d\chi \qquad (6)$$

and

$$\sin \gamma_{t} \sin \gamma_{r} e = \left(\frac{1}{2\pi}\right)^{2} \int_{0}^{2\pi} \int_{0}^{2\pi} \hat{v}(\phi, \chi) e^{+j(\phi + \chi)} d\phi d\chi$$

$$(7)$$

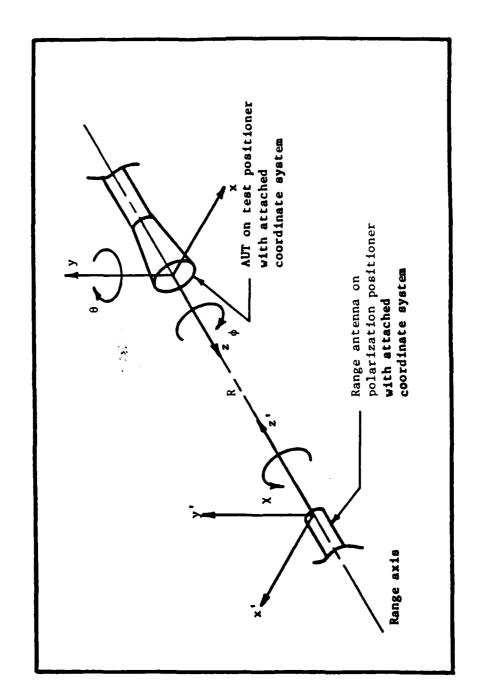


Figure 2. Coordinate system for polarization measurement

Taking the ratio of these two quantities we get that

$$M = \left(\frac{\sin \gamma_{t}}{\cos \gamma_{t}}\right) \left(\frac{\sin \gamma_{r}}{\cos \gamma_{r}}\right) = \tan \gamma_{t} e^{+j\delta_{ct}} \tan \gamma_{r} e^{-j\delta_{cr}}$$

$$= \hat{\rho}_{ct} \hat{\rho}_{cr}$$
(8)

where $\hat{\rho}_{ct}$ is the circular polarization ratio for the transmitting antenna and $\hat{\rho}_{cr}$ is the receiving circular polarization ratio for the receiving antenna.

Using the relation for a reciprocal antenna between the receiving circular polarization ratio and the transmitting circular polarization ratio that

$$\hat{\rho}_{cr} = \hat{\rho}_{ct} \tag{9}$$

we see that this result (8) becomes simply

$$\hat{\rho}_{c} \hat{\rho}_{c}^{\dagger} = M \tag{10}$$

where $\hat{\rho}_{ct}$ is written $\hat{\rho}_{c}$ and $\hat{\rho}_{c}$ has replaced $\hat{\rho}_{cr}$. Now, both circular polarization ratios for the two antennas refer to transmission and the prime differentiates the two antennas.

Once we have the products of the complex circular polarization ratios for each of the three antenna pairs determined from successive polarization measurements, we can compute each of the circular polarization ratios from three equations in three complex unknowns derived as follows. For simplicity of notation we define the products of the complex circular polarization ratios as

$$\hat{\rho}_{CA} \hat{\rho}_{CB} = M_{AB}$$

$$\hat{\rho}_{CA} \hat{\rho}_{CC} = M_{AC}$$

$$\hat{\rho}_{CB} \hat{\rho}_{CC} = M_{BC}$$
(11)

where the quantities \mathbf{M}_{AB} , \mathbf{M}_{AC} , and \mathbf{M}_{BC} are complex numbers derived from the data reduction.

The solutions for the circular polarization ratios are given by

$$\hat{\rho}_{CA} = \sqrt{\frac{M_{AB} M_{AC}}{M_{BC}}} \qquad \hat{\rho}_{CB} = \sqrt{\frac{M_{AB} M_{BC}}{M_{AC}}} \qquad \hat{\rho}_{CC} = \sqrt{\frac{M_{AC} M_{BC}}{M_{AB}}}$$
(12)

Resolution of the sign ambiguity inherent in taking the square root follows from an <u>a-priori</u> knowledge of the approximate tilt angle of one of the three antennas.

Once the complex circular polarization ratio for an antenna is known, the axial ratio, tilt angle, and sense of polarization may be computed from it. The details of this computation are given in Hollis, Lyon, and Clayton. [6]

III. Experimental Procedure

The experimental procedure for any three-antenna polarization measurement method is to measure the relative received phasor voltage for the three antennas taken pairwise. The voltage as a function of rotation about the line of sight is recorded. This rotation is described by the angles ϕ and χ as shown in Figure 2. The measured data is reduced using expressions for the

polarization parameters in terms of the relative received phasor voltage such as those given in Section II.

Initial alignment of the antenna coordinate system is important with any three-antenna polarization measurement method because of the need to maintain a constant orientation reference for measurement of the tilt angle. The coordinate systems of the antennas in the measurement must be defined by mechanical reference devices such as bubble levels mounted on the antennas. The measurement procedure described herein is used to measure directly the polarization of antennas in the coordinate systems so defined. No coordinate system redefinition is required. In practice, this means that the antennas are mounted with their mechanical reference devices in their reference orientation (e.g. with their bubble levels level). The angular offsets in φ and χ corresponding to this condition are noted and these offsets used to define the zero rotation angles for the coordinate systems.

The three-antenna polarization measurement method described herein is based on step-scan motion of the two polarization axes on which the antenna pairs are mounted. The complex voltage (phase and amplitude) at the port of a receiving antenna is measured by a phase/amplitude receiver and digitally recorded as one of the antennas is scanned. This scanning consists of rotating the source antenna through an angle ϕ = 360° or the receiving antenna through an angle χ = 360°.

For single scan polarization measurements, which are reduced to polarization parameters by means of a one-dimensional DFT, this is the only measurement that is required for each antenna pair. The sample increment has only a secondary influence on the accuracy of the measurement. Our experimental results indicate that no further improvements in measurement accuracy result from use of sample increments less than 1°.

For multiple scan polarization measurements, the axes are rotated in a step-scan fashion. Following acquisition of single scan data as described above, the polarization axis which was not used for the scan (logically, this axis may be referred to as the step axis) is rotated through a discrete angular increment and the scan is repeated. The phase and amplitude data are

recorded as functions of both the step and scan axis angles (ϕ and χ) and a two-dimensional DFT is used for reduction of the measured coupling data to polarization parameters. As in the single scan measurements neither the step nor the scan angle increment has a profound influence on the accuracy of the measurement. Our experimental results indicate that no further improvements in measurement accuracy result from use of step angle increments less than 15°.

ではないという。

IV. Experimental Results

A set of three single-ported antennas and one dual-ported, dual-polarized antenna was used to verify the measurement method. All possible combinations of the five antennas (the dual-ported antenna is considered to be two antennas and its two ports are referred to in the tables as antennas number 4 and number 5) were measured, with the results shown in Tables I and II.

For the single scan measurements shown in Table I the total variation in the measured axial ratio appears to be very large. However, because the axial ratio approaches infinity for nearly linear antennas, total variation in the axial ratio is a deceptive measure of accuracy. Note that the total variation in polar angle 2 γ for all the antennas is 0.29° - 0.44°. This is a true indication of the size of the locus of uncertainty on the Poincaré sphere, while axial ratio variation is not. Note in particular that for antenna #2, with an axial ratio of 28.44 dB, a 0.78 dB total variation corresponds to a larger locus of uncertainty on the Poincaré sphere than does the 5.67 dB variation for antenna number 3 with an axial ratio of 49.31 dB, the 9.44 dB variation for antenna number 4 with an axial ratio of 57.50 dB or the 2.74 dB variation for antenna number 5, with an axial ratio of 38.92 dB.

The single scan measurements shown in Table I indicate the degree of accuracy achievable using a one-dimensional discrete Fourier transform for reduction of the polarization pattern data. Such a DFT tends to reject random phase and amplitude errors in the measurement such as stray reflections in the test volume. However, periodic errors, such as rotary joint phase and VSWR wow, are not rejected by the one-dimensional DFT since they have the same

TABLE I
RESULTS OF THREE-ANTENNA SINGLE SCAN
POLARIZATION MEASUREMENTS

1									Anten	Legend for table: Antenna set number	Antenna numbera
Trible-Autron STT 1										~ ~ ~ ~ ~ ~ ~ ~ ~ ~ ~ ~ ~ ~ ~ ~ ~ ~	2, 2, 2, 2, 2, 2, 2, 2, 2, 2, 2, 2, 2, 2
Paristration Pari						THREE-ANTEN	NA SET			• ^	2,4,5
Interactio (48) 44,30 47,42 47,14 (5,59.45) 56.59 - - Interactio (48) 184.59 48.94 48.94 48.94 48.94 48.95 56.50 - - - Share maje (48) 177.91 177.87 177.87 177.87 177.87 177.87 - <t< th=""><th>Antenna Number</th><th>Polarization Parameter</th><th>-</th><th>~</th><th>3</th><th>•</th><th>~</th><th>٠</th><th>7</th><th>Nominel Velue</th><th>Total Variation</th></t<>	Antenna Number	Polarization Parameter	-	~	3	•	~	٠	7	Nominel Velue	Total Variation
Tilt couple (deg) 68.55 58.54 59.07 59.01 59.01 59.01 50.00		Aziel ratio (43)	46.30	47.82	47.14	\$8.65	56.58	1	,	53.40	13.55
Principal Prin		Tilt ougle (deg)	86.95	88.94	88.94	89.07	10.68	ı	1	88.98	0.13
Noter angle 37 (deg) 90.56 90.47 90.50 90.17 1 Lattinde 6_c (deg) 177.91 177.89 177.87 178.14 178.02 28.08 26.73 Natal ratio (88) 28.28 28.10 28.17 28.08 26.73 Natal ratio (88) 28.28 28.10 28.17 90.53 90.51 Lattinde 6_c (deg) 90.44 90.45 90.46 90.53 90.51 Lattinde 6_c (deg) 175.31 175.10 175.08 178.94 178.99 178.94 Lattinde 6_c (deg) 175.32 175.13 175.34 178.94 178.99 178.94 Lattinde 6_c (deg) 0.84 178.34 178.94 178.94 Lattinde 6_c (deg) 0.84 90.54 90.54 Lattinde 6_c (deg) 65.12 90.54 Lattinde 6_c (deg) 90.54 Natal ratio (deg) 90	7	200	ij	3	1	THE	3	ı	ı	RAK	1
Amini ratio (48) 17.91 17.89 17.89 17.81 17.81 17.89 17.81 17.81 17.89 17.81 18.02 -		Polar angle 2y (deg)	90.56	90.47	90.50	90.12	90.17	1	ı	90.36	0.44
Mariel ratio (48) 24.29 24.10 24.17 28.69 23.73 90.51 Enemos		Latitude 6 _C (deg)	177.91	177.89	177.87	178.14	178.02	,	,	177.97	0.27
Tite angle (deg) 90.44 90.45 90.46 -		Axial racto (4B)	20.20	28.10	28.17	;	I	28.68	28.73	28.44	8 2.0
Polar angle 2γ (δοg) 94.42 94.51 94.47		Tilt sagie (deg)	90.44	90.45	90.46	,	ı	90.53	90.51	90.46	6,0
Polar angle 27 (deg) 94.42 94.51 94.47 -	7	=======================================	X	X		•	1	ă	¥92		,
Latitude \$_c\$ (deg) -179.13 -179.10 -179.08 - -178.94 -178.96 - Amial ratio (deg) 45.51 - - 50.24 - 51.18 - Somes Latitude \$_c\$ (deg) -0.84 - 179.54 - 179.48 - Polar angle \$_f\$ (deg) -0.84 - - 179.54 - 199.68 - Intitude \$_c\$ (deg) -0.84 - - 99.65 - - 199.68 - Intitude \$_c\$ (deg) - 62.12 - - - 99.56 - - - 199.68 -		Polar angle 2y (deg)	94.42	94.51	44.47	ı		94.12	94.19	94.34	0.39
Marial ractio (48)		Latitude & (deg)	-179.13	-179.10	-179.08	•	ı	-178.94	-178.98	-179.05	0.19
Tilt eagla (deg) 179.56 179.54 - 179.46 180 - 180 - 180 180 - 180 180 - 180		Anial rotio (43)	45.51	ı	ı	50.24	•	51.18	,	16.34	2.63
Some LMR -		Mit segis (deg)	179.56	1	•	179.54	•	179.48	•	179.53	0,10
Poler angle 2y (deg) 89.39 -	9	2000	•	ı	1		1	3	1	5	,
Latitude 6_c (deg)		Poler angle 2y (deg)	89.39	ŀ	1	89.65	,	89.68	1	89.57	0.29
Marial ratio (db) - 62.12 54.69 - 52.68 Tilt augle (dg) - 15.63 69.56 Shows Polar angle 2 (deg) - 15.6 90.21 - 90.27 Latitude 6 (deg) - 179.26 177.08 Tilt augle (deg) - 91.40 Shows Polar angle 27 (deg) - 91.40 Tilt augle (deg) - 91.40 Shows Polar angle 27 (deg) - 91.50 Tilt augle (deg) - 91.33 Tilt augle (deg) 177.08 Tilt augle (deg) 177.08 Tilt angle 27 (deg) 177.23 Tilt 277.23		Latitude 6 _c (deg)	-0.84	•		-0.91	١.	-1.04	1	-0.93	0.20
Tilt angle (deg) - 89.63 89.56 Shows Poler angle 2 (deg) - 100 - 100 - 177.23 Initiative 6 (deg) - 177.26 177.23 Tilt angle (deg) - 91.43 91.39 91.32 Folar angle 2 (deg) - 177.26 Initiative 6 (deg) - 177.23 91.39 91.32		Azial ratio (48)	•	62.12	ı	,	3	1	47 65	3	
Polar angle 2, (deg)		Tilt angle (deg)	1	19.63	•	•	89.50	ı	89.56	89.59	0.0
Poler angle 2 (deg)	4		ı		ı	•	3	1		Ħ	,
Auticlede d _c (deg) - 179.26 - 179.11 - 179.11 Auticl ratio (db) - 40.80 38.06 38.39 38.29 38.75 Tilt augle (deg) - 91.46 91.33 91.39 91.41 Sense		Poler angle 2 (deg)	•	16.69	1	,	90.21	1	90.27	90.13	0.36
Amini ratio (45) 40.40 34.06 34.05 34.39 34.75 This angle (46g) 91.46 91.33 91.39 91.41 Seece RES		Latitude & (deg)		179.26	•	•	179.15	1	179.11	179.17	61.0
This sage (deg) 91.46 91.33 91.39 91.39 91.41 Soone BEE REG REG REG REG REG REG REG REG REG R		Azial ratio (48)	1	ı	40.80	36.0	36.39	36.29	34.75	36.92	2.74
Seese DEE REE		Tile angle (deg)	1	•	91.46	91.33	91.39	91.39	91.41	91.40	
mg) 91.05 91.43 91.38 91.40 91.32	'n		•	1	1	ij	ij	1	3		
172.08 -177.35 -177.23 -177.22		Polar angle 2y (deg)	1	,	91.05	61.19	91.38	91.40	91.32	91.32	0,38
K1-2/1- 77-1/1- C3-1/1- C3-1/1- C3-1/1-		Latitude & (deg)	•	1	-177.08	-177.35	-177.23	-177.22	-177.19	-177.21	0.27

TABLE II
RESULTS OF THREE-ANTENNA MULTIPLE SCAN
POLARIZATION MEASUREMENTS

とうののは、ことととなるとと、こののののののので

Control Branch Control Branch

								Legend	Legend for table: Antenna set number	Antenna numbers
									-264	L.2.1 1.2.4 1.2.5 5.5.1
									~ ~	2,3,5
					THREE-ANTENNA SET	A SET			,	2,4,5
Antenna Number	Polarization Parameter	-	~	ſ	4	~	٠	^	Nominal	Total Verietion
	Azial ratio (48)	52.05	53.22	52.96	54.91	52.81	ı	ı	53.38	2.10
	Tilt sagle (deg)	10.01	86.98	88.97	89.04	89.00	ı	ı	89.00	0.0
-	Passe .	Ħ	•	1	RAR	1	ı	ı	#	ı
-	Polar angle 2y (deg)	90.26	90.25	90.26	90.21	90.26	1	•	90.25	0.05
	Longitude 6 (deg)	178.02	177.96	177.94	178.08	178.01	ı	,	178.00	91.0
	Azial ratio (4B)	28.67	28.66	28.80	ı	ı	28.91	28.78	28.76	0.25
	Tilt omele (deg)	90.43	90.47	90.49	1	•	90.51	90.52	90.48	0.09
2	Seee	#	=	7	1	,	5	XIII Z	=	ı
ı	Polar angle 2y (deg)	94.22	94.22	94.16	ı	ı	94.11	94.17	94.18	0.11
	Longitude & (deg)	-179.14	-179.06	-179.02		1	-178.98	-178.96	-179.03	0.18
	Agial ratio (48)	49.69	•	1	50.73	•	52.90	1	51.21	3.21
	Tilt angle (dag)	179.57	ı	•	179.57	ı	179.50	1	179.55	0.07
	3	•	1	1	•	•	3	1	1	•
)	Polar angle 2y (deg)	89.62	ı	ı	89.67	1	8.74	ı	89.68	0.12
	Longitude 6 (deg)	-0.86	•	ı	-0.86	ı	-1.00	1	-0.91	41.0
	Aziel rocie (4B)	•	55.05	ı	•	55.70		52.69	54.57	3.01
	Tilt angle (dag)	1	89.62	1	1	89.59	ı	19.56	89.59	90.0
4	***	•	3		ı	1	1			1
	Polar angle 2y (deg)	•	90.20	t	ı	90.19	ı	90.27	90.22	0.08
	Longitude & (deg)	1	179.24	•	1	179.18	1	179.12	179.18	0.12
	Antel rects (48)	1	•	39.37	36.53	38.90	39.01	39.44	39.06	0.91
	Mit ongle (dog)	ı	1	91.43	91.34	91.38	91.42	91.40	91.39	0.09
~	; ;	ı	ı	ij	1	1	ij	9		1
•	Polar angle 2y (deg)	•	ı	91.23	91.36	91.30	91.28	91.22	91.28	0.14
	Longitude & (deg)	1	•	-177.13	-177.32	-177.24	-177.17	-177.19	177.21	0.15

period as the polarization pattern (2π) . But these periodic errors (in particular, rotary joint errors) are dependent only on the rotation angle of one polarization positioner (the one in which they are mounted), while the polarization pattern is dependent on the rotation angle of both polarization positioners. Therefore, the periodic errors in the measurement do not vary in the same way as the polarization pattern does as a function of both measurement angles, ϕ and χ , and they will tend to be rejected by the two-dimensional DFT in ϕ and χ which is used to reduce multiple scan polarization measurements.

Table II shows the results of multiple scan measurements on the same antennas. For multiple scan measurements, periodic as well as random errors tend to be filtered out, resulting in a 2 or 3 to 1 improvement in measurement accuracy over single scan measurements. Work on computer-simulated data indicates that multiple-scan data reduction (a two-dimensional instead of a one-dimensional DFT) reduces periodic errors by about 20 dB.

V. Conclusions

We have demonstrated an automated, highly accurate method of polarization measurement. The method is restricted to use under far-field conditions. The method is implemented as part of the spherical near-field subsystem of the Scientific-Atlanta 2022B antenna analyzer option 08A. The measurements required are simply phase/amplitude polarization patterns for multiple source orientations. No redefinition of coordinate systems (as in Newell's method) is required, and polarization parameters are computed automatically and displayed in the format shown in Figure 3. The automation makes this method easier to use than manual methods. This method has the further advantage that no longitudinal translation is needed to average out stray signals. Stray signals are rejected by the step-scan rotation.

POLARIZATION PARAMETERS FROM FILE DF1MS3

	FREQUENCY (MHz) 13888.8	AXIAL RATI (dB) 53.22	0		LT ANGLE DEGREES) 88.98
	ALT	ERNATIVE POLAR	RIZATION	REPRESENTATIONS	
BASIS	COMPLEX AMPLI		RATIOS HASE Grees)	POINCARE SPHE POLAR ANGLE (DEGREES)	RE COORDINATES LONGITUDE (DEGREES)
CIRCULAR	1.8	744 17	7.958 #	90.25	177.96
LINEAR	55.69	969 -	6.9888	177.94	-6.99
DIAGONAL	. 90	65 <i>0</i> -	2584	87.96	25

Figure 3. Sample polarization parameters output list.

VI. References

- 1. Newell, A. C., and Kerns, D. M., "Determination of both polarisation and power gain of antennas by a generalised 3-antenna measurement method", Electronics Letters, Vol. 7, No. 3, pp.68-70, February 11, 1971.
- 2. Joy, E. B., and Paris, D. T., "A practical method for measuring the complex polarization ratio of arbitrary antennas", <u>IEEE Transactions on Antennas and Propagation</u>, Vol. AP-21, No. 4, pp. 432-435, July, 1973.
- 3. Newell, A. C., Baird, R. C. and Wacker, P. F., "Accurate measurement of antenna gain and polarization at reduced distances by an extrapolation technique", <u>IEEE Transactions on Antennas and Propagation</u>, Vol. AP-21, No. 4, pp. 418-431, July, 1973.
- 4. Newell, A. C., "Improved polarization measurements using a modified three antenna technique", Proceedings of the IEEE International Antennas and Propagation Symposium, Session 15, pp. 337-340, Urbana-Champaign, IL, June 2-4, 1975.
- 5. Christensen, E. L., et. al., Experimental spherical near-field antenna test facility, phase 2: Final Report, ESA Contract No. 3916/79/NL/DG, Vol.1, Facility description and measurement results, Technical University of Denmark, December, 1981.
- 6. Hollis, J. S., Lyon, T. J. and Clayton, L., eds., Microwave Antenna Measurements, Scientific-Atlanta, Inc., Atlanta, GA, 1970.

SIMPLE EXPRESSIONS FOR THE PHASE CENTERS OF SMALL HORN ANTENNAS

Peter R. Franchi

Electromagnetic Sciences Division Rome Air Development Center Hanscom AF Base, MA

ABSTRACT

Simple analytic expressions that locate the phase centers of small ${\rm TE}_{10}$ mode rectangular and conical horns are presented. These expressions relate the phase center displacement (from the horn aperture center) to the E plane and H-plane horn dimensions and to the horn flare lengths. The equations compare well both with more elaborate derivations and also to measurements made on several different sized horns. Because these expressions are quite accurate and not mathematically cumbersome, they are useable in many practical situations, replacing commonly used measurement techniques.

Introduction

Expressions for location of phase centers of small horn antennas should be in simple form to be useful to antenna designers. The most commonly used way for determining the phase center location is by measurement. Determining the phase center location by analysis is usually very complex and time consuming. (1,2,3,4) In this paper, the location of the phase center in the E and H planes is obtained in a simple fairly accurate form by a series of approximations.

The approach described here relates the aperture phase variation of the horn to a spherical wave front radiated from the actual phase center. More accurately stated, the phase center is determined by matching the far field main beam phase variation, in a best fit match, to a spherical wave front. The center of that spherical wave is the phase center.

Rather than comparing the entire phase variation over the main beam, only the phase at the angles where the power is down by 3-dB together with the phase at boresight are used. This is a three point approximation to the spherical wavefront. The 3-dB angles are chosen both for simplicity and because they probably match the angles most experimentalists would choose. Other reasonable angles should also give accurate results.

Phase Center Derivation

Assume that the field pattern phase at the 3-dB angles is ϕ_1 . This phase minus the boresight phase, ϕ_0 , gives the horn phase

deviation with respect to the horn aperture center. It can be expressed as a physical length, ϵ ,

$$\phi_1 - \phi_0 = \frac{2\pi\varepsilon}{\lambda} \tag{1}$$

Figure 1 shows the geometry of the problem,

with R_0 the distance from the horn aperture to an arbitrary point in the far field; ΔL the displacement of the phase center from the horn aperture; a, the radius of a spherical wavefront passing through the arbitrary point and R the distance from the horn aperture center to the spherical wavefront at an angle θ from the boresight direction. Let θ_3 refer to the 3 dB angle (203 is the horn beamwidth.)

$$a^2 = (\Delta L)^2 + R^2 - 2R\Delta L \cos (180 - \theta_3).$$
 (2)

also

$$a = R_0 + \Delta L \tag{3}$$

and

$$\varepsilon \cong R-R_0.$$
 (4)

If $R_0 > \epsilon$, then

then

$$\varepsilon \cong \Delta L (1-\cos\theta_3)$$
 (5)

and
$$\varepsilon \simeq \Delta L \frac{\theta_3^2}{2}$$
, for $\theta_3 < 1$. (6)

2

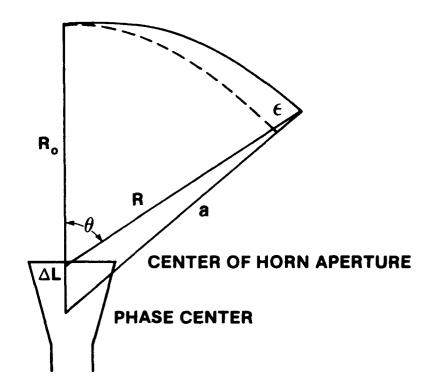


Figure 1

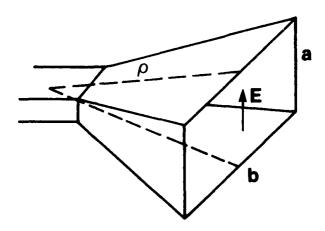


Figure 2

(The condition $\theta_3 < 1$ is almost met by any horn aperture larger than a waveguide opening). The phases of the horn at boresight, ϕ_0 , and at θ_3 , ϕ_1 , are easily derived.

In Figure 2, p is the E-plane flare length. The two flare lengths (Eplane and H plane) will be slightly different in general, unless the waveguide height and width are proportional to a and b.

Assume that the far field pattern can be expressed independently in the E and H planes. Thus $g_E(\mu)$, the far field pattern for the E plane, assuming a quadratic phase error across the aperture, represented by $^{(6)}$

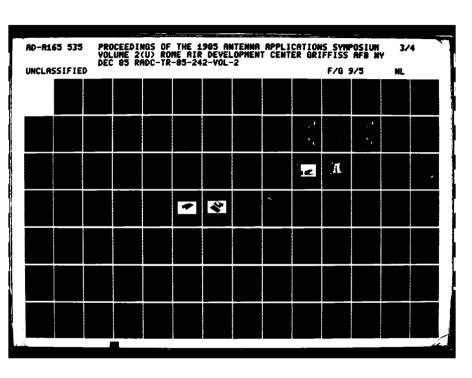
$$g_{E}(\mu) \approx a/2[g_{E0}(\mu) + j\beta g_{E0}(\mu)]$$
 (7)

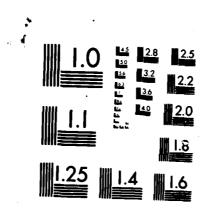
where β is the phase error at the edge of the horn aperture and g_{E0} is the unerrored pattern of a uniform aperture of width a and μ is is $\pi a\lambda \sin \theta$. From equation (7) the phase of $g_E(\mu)$ at $\mu = 0$ (boresight) is:

$$\phi_0 = \tan^{-1} \left(\frac{\beta g_{E0}^{(0)}}{g_{E0}^{(0)}} \right).$$
 (8)

The phase at the 3 dB point is:

4





MICROCOPY RESOLUTION TEST CHART

$$\phi_1 = \tan^{-1} \left(\frac{\beta g''g_0(\mu_3)}{g_{E0}(\mu_3)} \right) . \tag{9}$$

The E-field across the horn is assumed uniform so that

$$g_{EO}(\mu) = \frac{\sin \mu}{\mu} \tag{10}$$

and

$$g_{E0}^{"}(\mu) = -\frac{\sin\mu}{\mu} - \frac{2\cos\mu}{\mu^2} + \frac{2\sin\mu}{\mu^3}$$
 (11)

Then

$$g_{E0}^{(0)} = 1.00$$
 , $g_{E0}^{"}(0) = 1/3$,

$$g_{EO}(\mu_3) = -\frac{1}{\sqrt{2}}$$
 and $g_0(\mu_3) = .16092$,

and

$$\phi_0 - \phi_1 = \tan^{-1} - \left(\frac{\beta}{\gamma}\right) \tan^{-1}(\beta.2275).$$
 (12)

For β < 2,

$$\phi_0 - \phi_1 \approx .1058 \,\beta$$
 . (13)

Combining equations 1, 6 and 13 gives

$$\frac{\Delta L}{\lambda} = \frac{.1058 \text{ B}}{\pi \theta_3^2} \qquad . \tag{14}$$

For uniform illumination, θ_3 = .443 λ/a and

$$\frac{\Delta L}{\lambda} \simeq .1716 \beta \frac{a^2}{\lambda^2} \qquad . \tag{15}$$

Since β is the phase difference at the edge of the horn relative to the center,

$$\beta \simeq \frac{2\pi}{\lambda_g} (\ell_e - \ell_c), \qquad (16)$$

where $\ell_{\rm C}$ = is the physical length from the flare center to the aperture center, $\ell_{\rm e}$ is the length from the flare center to the horn edge in the E-plane and $\lambda_{\rm g}$ is the guide wavelength at the horn aperture. Thus,

$$\ell_{c} - \ell_{c} = \sqrt{\rho^{2} + (a/2)^{2}} - \rho \tag{17}$$

$$\stackrel{\mathbf{a}^2}{=} \frac{\mathbf{a}^2}{8\rho} \tag{18}$$

Assuming that the horn phase velocity is proportional to the arc length b +' in the H plane at the aperture,

$$\lambda_{g} = \frac{\lambda}{\left[1 - (\lambda_{g}/2b^{\dagger})\right]^{1/2}}$$
 (19)

where

$$b = b' \frac{2 \sin \psi/2}{\psi} \tag{20}$$

and ψ is the total horn flare angle. Thus

$$b = b^{-} \left[1 - \frac{\psi^{2}}{24} + \dots \right] = b^{-} \left[1 - \frac{\psi^{2}}{24} \right].$$
 (21)

Expanding the expression for λ_g ,

$$\lambda_g = \lambda \frac{\lambda^2}{8B^2} - \frac{\psi^2}{12} + \frac{3}{128} + \frac{\lambda^4}{b^2} \dots$$
 (22)

$$\lambda_g \cong \lambda \left[1 + \frac{\lambda^2}{8b^2} + \frac{3}{128} \frac{\lambda^2}{b^2} \left[\frac{\lambda^2}{b^2} - \frac{4\psi^2}{9} \right] + \dots \right]$$
 (23)

if
$$\psi \approx 3/2 \lambda/b$$
. (24)

Since b should range between 1λ to 6λ for small horns and ψ between 20^{0} and 80^{0}

$$\lambda_g \cong \lambda \left[1 + \frac{\lambda^2}{8b^2}\right]$$

For very small flare angles ($\psi \approx 0$), a better approximation is

$$\lambda_{g} = \frac{\lambda_{o}}{\sqrt{1 - (\lambda_{2}b)^{2}}} , \qquad (25)$$

so that

$$\frac{\Delta L}{\lambda} = \frac{.135(a/\lambda)^4}{(\rho/\lambda)(1+1/8(\lambda/b)^2}$$
 (26)

For very small flare angles and b \approx 1, a better approximation for $\lambda g/2$ gives

$$\frac{\Delta L}{\lambda} = \frac{.135(a/\lambda)^4 \frac{2}{1-2b}}{\rho/\lambda} . \tag{27}$$

In the H-plane, the same approach is used only the basic horn illumination is now a cosine taper. This gives the errorless pattern

$$g_{H}(M) = \frac{\cos \mu}{\frac{4\mu^{2}}{1 - \frac{\pi^{2}}{2}}}.$$
 (28)

The phase at boresight is given by (6) with $g_E(0)$ replaced by $g_H(0)$,

$$g_{Ho}^{(0)} = 1.0$$
 and $g_{Ho}^{(0)} = -.1874$

so
$$\phi_0 = \tan^{-1}(\beta.1894) \approx \beta.1894$$
.

At the 3 dB angles, $\mu_3 = .5945\pi$ and

$$\phi_1 = \tan^{-1} \frac{\beta g_{HO}(M_3)}{g_{HO}(\mu_3)}$$
, where (29)

$$g_H(\mu_3)$$
 = .707 and $g_H^{11}(\mu_3)$ = -.07234 ϕ_1 = $\tan^{-1}(\beta.1023) \approx \beta.1023$ and $\Delta \phi \cong .0871\beta$.

As before,

$$\frac{\Delta L}{\lambda} = \frac{\phi_0 - \phi_1}{\pi \theta_3^2} \tag{30}$$

$$\theta_3 = .5945 \frac{\lambda}{b}$$
 and $\phi_0 \sim \phi_1 = .0871\beta$

$$\frac{\Delta L}{\lambda} = \beta \frac{b^2}{\lambda^2}$$

where

$$\beta \simeq \frac{2\pi}{\lambda} \frac{b^2}{8\rho} \frac{1}{(1 + .125(\lambda/b)^2)}$$
 (31)

Thus

$$\frac{\Delta L}{\lambda} = .0616 \frac{(b/\lambda)^4}{\rho/\lambda(1 + 1/8 (\lambda/b)^2)}$$
(32)

noting again that ρ for the H plane phase center will in general be

slightly different than the ρ for the E-plane, and for small flare angle horns with small be dimension, the factor $1+\frac{\lambda^2}{8b}$ should be replaced by $1+\frac{\lambda^2}{2b}$.

The phase centers for conical horns in both planes can also be found in the same manner. In this case the E-field, $g_{E0}^{\;(\mu)}$, is given by: (7)

$$G_{EO}(\mu) \propto \frac{J_1(\mu)}{\mu}.$$
 (33)

The three dB angle is

$$\theta_3 = .521 \lambda/d \tag{34}$$

where d is the conical horn diameter. These give

$$\frac{\Delta L}{\lambda} \equiv \frac{.0934(d/\lambda)^4}{\rho/\lambda}$$
 (35)

where the factor $1 + \frac{1}{2} (\lambda/b)^2$ has been ignored. It could be replaced by $1 + (\lambda/b)^2(.29)$. For the H plane, $g_{HO}(\mu)$ is given by (8)

$$g_{HO}$$
 $\alpha \frac{J_1'(\mu)}{\rho^2 - \mu^2}$ (36)

where p is the first root of $J_{1}^{\ \prime}(\mu).$ For this pattern, the three dB angle

9

$$\theta_3 = .653 \frac{\lambda}{d}. \tag{37}$$

This expression again assumes $\lambda/g \approx \lambda$.

With equations (26) and (32), the E and H-plane phase centers of a pyramidal horn, and with equations (35) and (38), the E and H plane phase centers of a conical horn are described.

Comparisons and Experimental Results

Equations 26 and 32 are used in Figure 4 to compare these results with square horn theoretical results of Mueldorf(4). The results of $\mathrm{H}_{\mathrm{u}}^{(1)}$ for sectoral horns are plotted in Figure 5 with the phase centers determined from equations 27 and 32. These figures show quite good agreement between our approximate results and a more rigorous derivation.

Table 1 gives the comparison of the experimental measurements of the two phase centers of five pyramidal and Table 2 a conical horn with the phase centers derived from the appropriate equation.

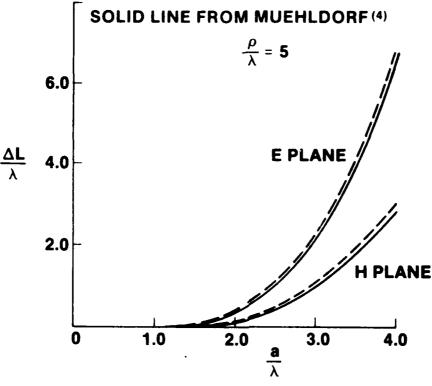


Figure 3. Square Horns

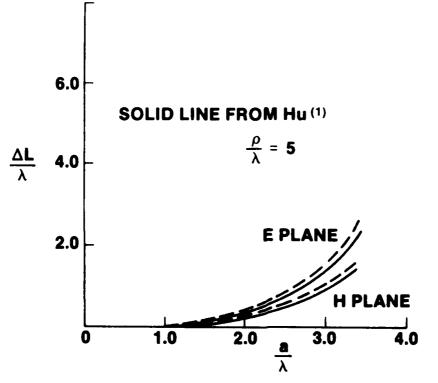


Figure 4. Sectoral Horns

TABLE I: Experimental Results

Pyramidal Horns

a	b	PΕ	ΔL _E meas	ΔLE	ΔL _H meas	ΔL _H
1.84	3.47	4.84	+.12 .13	.15	.88 ± .12	.78
4.68	5.97	7.56	3.88	3.93	4.13	4.37
3.25	8.38	18.84	.50	.37	8.44	8.11
2.13	2.88	5.39	.31	.23	.19	.30
2.00	3.44	10.17	.25	.10	.50	.36

TABLE: Experimental Results

Conical Horns

d	ρ	Δ L _E measured	Δ L _E	Δ L _H measured	ΔLH
8.00	12.40	14.81	14.85	7.13	7.47*
4.00	8.72	1.88	1.76	.75	•65

^{*}Corrected for inadequate field distance

In general the measured results compare quite well.

Conclusions

Four simple but reasonably accurate expressions have been derived for the phase centers of pyramidal and conical horns. Centrol of

こうしょう とうこうしゅう アイカー のない ないない

antenna astigmatism in reflectors that use horns as a primary feed is now simple. For example, any rectangular horn with the H field dimension, b, set equal to 1.22 times the E field dimension, a, will give coincident phase centers. As a second example, a limit of $\lambda/16$ separation between phase centers and an equal illumination of 10 dB in both planes, (this sets b \cong 1.38a) give an expression for the smallest horn length, ρ , $(\rho/\lambda) = .7(a/\lambda)^4$ with the dimension "a" set by the f/D ratio.

All the equations have been derived for the observation point at infinity, the use of a horn with a reflector or lens that is at a finite and possibly close distance might change the effective phase center. The factor to account for this effect is easily derived. The effective phase is

$$\frac{\Delta L_{\text{eff}}}{\lambda} = \frac{\Delta L}{\lambda} + \frac{\rho \lambda_g}{R \lambda}$$
 (38)

where R is the distance from the horn to the reflector or lens.

からなる。他は、からからは、これになっている。これになっているのでは、これになっている。

References

- 1. Y.Y. Hu, "A Method of Determining Phase Centers and Its Applications to Electromagnetic Horns," Journal of the Franklin Institute, vol. 271, pp. 31-39, Jan. 1961.
- 2. E.R. Nagelberg, "Fresnel Region Phase Centers of Circular Aperture Antennas," IEEE Trans. Antennas Propag., vol. AP-13, No. 3, pp. 479-480, May 1965.
- 3. I. Ohtera and H. Ujiie, "Nomographs for Phase Centers of Conical Corrugated and TE_{11} , Mode Horns," IEEE Trans. Antennas Propag., vol. AP-23, No. 6, pp. 858-859, Nov. 1975.
- 4. E.I. Mueldorf, "The Phase Center of Horn Antennas," IEEE Trans. Antennas Propag., vol. AP-18, pp. 753-760, Nov. 1970.
- 5. W.L. Bowen, L.J. Chu, "The Theory of the Electromagnetic Horn," Proc. IRE, vol. 27, pp. 51-64, Jan. 1939.
- 6. S. Silver, Microwave Antenna Theory and Design, Lexington, MA, Boston Technical Publishers, 1964.
- L.J. Chu, "Galculation of the Radiation Properties of Hollow Pipes and Horns," J. Appl. Phys., vol. 11, pp. 603-610, Sept. 1940.
- 8. C.W. Horton, "On the Theory of the Radiation Patterns of Electromagnetic Horns of Moderate Flare Angles," Proc. IRE, vol. 37, pp. 744-749, July, 1949.

SHAPED-BEAM EARTH COVERAGE HORN ANTENNAS* †

bу

Joseph C. Lee, Walter Rotman

Massachusetts Institute of Technology, Lincoln Laboratory Lexington, Massachusetts

Abstract

The second of th

Earth coverage antennas are used on communication satellites to cover the whole visible portion of the earth. Due to the earth curvature and satellite orbit geometry, there are path-length differences within the covered area. To compensate for this path length and any atmospheric attenuation differences, more radiated power should be directed toward the edge, than toward the center, of the covered area. Conventional pencil-beam antennas with unshaped radiation patterns are inefficient for this application in the sense that more power is radiated toward the nadir where the path length is least and that less power (typically 4 dB down from peak) is radiated toward the edge of coverage where the path length is longest. To overcome this difficulty, antenna beam-shaping techniques are needed. This paper will present two practical shaped-beam earth-coverage horn antennas for a synchronous orbit satellite. One is a double-flare

^{*}This work has been sponsored by the Department of the Air Force.

t"The views expressed are those of the authors and do not reflect the official policy or position of the U.S. Government."

smooth horn utilizing dual modes for beam symmetry and aperture phase differences for beam shaping. The other is an angle-limited corrugated horn with a beam-shaping zoned lens. Preliminary data of Q-band breadboard models for both types of antennas showed improvements of at least 1.0 dB in minimum edge-of-earth gain, compared to an optimized single mode corrugated horn. Design considerations with measured patterns and gains for the two antennas are included.

I. INTRODUCTION

Earth coverage antennas are used on communication satellites to cover the whole visible portion of the earth. The portion of the earth visible to a satellite is a function of the satellite altitude. It covers less area at low than at high altitude. At geosynchronous orbit (Fig. 1) of 22,300 miles, the visible area of the earth surface covers up to 81.44° in latitude for the north and south hemispheres, an area very close to the limit of a whole hemisphere. When the antenna is boresighted at nadir on the earth equator, the cone angle at the edge of the earth is 8.6° from the axis. To provide some margin for satellite pointing uncertainty, 9° will be used as the cone half angle for earth coverage antenna evaluation. Due to the earth curvature and satellite orbit geometry, there are path length differences within the covered area. To compensate for this path length and any atmospheric attenuation differences, more radiated power should be

directed toward the edge than toward the center of the covered area.

An ideal earth coverage antenna at synchronous orbit should have: 1) circular symmetric patterns, 2) zero spillover beyond $\theta = 9^{\circ}$, and 3) an appropriate inverse taper between the central axis and edge of the covered earth disc to compensate for the path length and atmospheric attenuation differences. The path length attenuation difference between the nadir and the edge of the earth is 1.32 dB and the atmospheric loss difference is about 1.4 dB in Q-band (\approx 40 GHz).

With a finite-size antenna, it is impossible to attain this ideal beamshape. But it can be approached with increasing aperture size.

II. ANALYSIS

Conventional pencil-beam antennas with unshaped radiation pattern are inefficient for earth coverage application in the sense that more power is radiated toward the nadir where the path length is least and that less power (typically 4 dB down from peak) is radiated toward the edge of coverage where the path-length is longest. To overcome this difficulty, antenna beam-shaping techniques are needed.

Several synthesis techniques for generating the desired far-field patterns with various amplitude and/or phase distributions over a finite aperture have been theoretically

evaluated in a recent paper 1. Here we will first start with some basic analyses and then go directly to present two practical shaped beam earth-coverage horn antenna designs.

The gain of a uniformly illuminated sector beam radiation pattern within a semi-flare cone angle $\theta_{\rm e}$ and with no side lobes is given by:

$$G = 10 \log \left(\frac{2}{1 - \cos \theta} \right).$$

For θ_e = 9°, G = 22.11 dBi. This value can be used as an upper bound design goal for geosynchronous earth coverage antennas.

A single corrugated horn hybrid-mode horn antenna optimized for earth coverage built in Lincoln Laboratory² has a minimum edge gain ($\theta = 9^{\circ}$) of 17.8 dBi. This horn had an almost ideal Gaussian-shaped beam, and represents nearly an optimum design for a conventional beam shape. We will use this value of 17.8 dBi as our reference for measuring any improvement in antenna performance achieved in going to the shaped-beam approach.

III. DOUBLE FLARE HORN ANTENNA

Concave antenna beam patterns can be obtained by conical horns loaded with dielectric sheets³ or dual-mode corrugated horns⁴. Here we will discuss the double-flare horn. Timofeyeva⁵ first introduced this type of horn and presented its near field patterns for Cassegrain feed applications. The shadow region formed due to the flare-angle change provides the aperture

amplitude taper and the phase difference across the aperture indents the peak of the radiation pattern which otherwise would be a pencil beam. The horn characteristics can be analyzed from a dual-mode point of view 6 . The $TM_{11}^{\circ}/TE_{11}^{\circ}$ phase conversion factor is given by $Tomiyasu^7$. The differential phase relation between the two modes is found in Potter's original work on dual-mode horns 8 . This mode conversion by changes in the flare angle allows one to use a much shorter differential phase correction section (90° versus 300° or 660° for the improved and the original Potter horn, respectively). Therefore, the bandwidth is broadened to well over 10%.

A 0-band double-flare horn was designed and built. Figure 2 gives the pertinent dimensions. Radiation patterns and gains were measured from 42 to 47 GHz in 0.5 GHz steps. In this frequency range, all measured radiation patterns have a 1 to 2 dB dip in the boresight direction of the horn. The E- and H-plane cuts follow each other fairly close to within 1 dB. Figure 3 is a typical measured pattern at the frequency of 44.5 GHz. Preliminary measured gain on the boresight axis and the E- and H-plane average gain at a 9° angle from axis are given in Table I.

TABLE I. Double-Flare Horn Measured Gains

Frequency GHz	On-axis Gain dBi	9° Off-axis Gain dBi
43.5	18.52	19.20
44	18.64	19.14
44.5	18.97	18.90
45	19.10	19.10
45.5	18.85	19.20

The measured E- and H- plane differences in gain at 9° off axis over the frequency range of 43.5 to 45.5 GHz are less than 0.5 dB. The average gain is thus a good approximation to the actual gain. Compared to the 9° off-axis gain of the single-mode optimized corrugated horn of 17.8 dBi, a minimum improvement of 1.1 dB has been achieved with the double-flare horn. Some studies of the effects of parameter changes on the electrical characteristics of the horn are being continued.

IV. HORN LENS ANTENNA

Another shaped beam earth-coverage antenna is an angle-limited corrugated horn with a beam-shaping zoned lens 9 . A $J_1(x)/x$ aperture distribution with 3 phase reversal zones is used in the design (where $x = \beta_m r$, m = 3, $\beta_m = 10.17$, r = normalized aperture radius). Geometric optics and ray tracing techniques are used in accordance with scalar fields from the feed. Figure 4 is a scaled drawing of the horn-lens. The radiation patterns of this antenna have been measured from 39 to

46 GHz. At the high frequency end, the radiation pattern turned out to be too narrow. The best frequency range over a 2 GHz bandwidth was found to be from 39.5 to 41.5 GHz. Figure 5 shows the measured E- and H- plane patterns at 40.5 GHz. At this freuency, the lens diameter to wavelength ratio is 15.3. The measured on-axis and the E- and H- plane average gains at a 9° angle from boresight axis are given in Table II.

TABLE II. Measured Gain of Horn-lens Antenna at 9°

Frequency GHz	On-axis Gain dBi	9° Off-axis Gain dBi
39.5	21.15	19.65
40.0	21.00	19.60
40.5	21.10	19.60
41.0	20.90	20.1
41.5	21.75	20.25

Compared to the 9° off-axis gain of the single-mode optimized corrugated horn of 17.8 dBi, a minimum improvement of 1.8 dB has been achieved with the horn-lens antenna.

V. CONCLUSIONS

Two practical broadband earth-coverage horn antennas were designed, built and tested. Definite improvements of 1.1 and 1.8 dB over the performance of the optimized simple-mode horn are

achieved. The double-flare horn antenna has a very simple geometry which can be useful at submillimeter wavelengths. The horn-lens antenna has very good pattern symmetry and broad bandwidth characteristics. Its dielectric weight and loss can be reduced by special zoning techniques, which would however reduce the bandwidth.

Acknowledgments

The authors are grateful to Dr. A. J. Simmons and Mr. W. C. Cummings for their support of the study program, to Ms. A. Leifer for programming the horn-lens design equations and to Messrs.

R. Piccola, J. McCrillis, and T. Borge for their assistance in the antenna measurements.

REFERENCES

- 1. Walter Rotman and Shih-Ming Shih, "A Comparison of Synthesis Techniques for EHF Earth Coverage Lens Antennas," in IEEE AP-S International Symposium, Vancouver, Canada, (June 1985), p.485.
- 2. D. C. Weikle, "Earth Coverage Corrugated Horns (44.5 GHZ and 26.7 GHz)", Technical Report 656, Lincoln Laboratory, M.I.T. (July 1983), (Presented at USAF symposium Allerton Park 1984). AD-A133241.
- 3. Toshio Satoh, "Dielectric-loaded Horn Antenna", IEEE Trans. on AP (Mar. 1972), p. 199.
- 4. A. W. Love, "Two-Hybrid-Mode, Earth Coverage Horn for GPS", in IEEE AP-S International Symposium, Vancouver, Canada, (June 1985), p. 575.
- 5. A. A. Timofeyeva, "A Wide-Band Horn Radiator with Axisymmetric Polar Diagram", Telecomm and Radio Eng., Vol. 27/28, Sept 1973, p. 121.
- 6. S. B. Cohn "Flare-angle Changes in a Horn as a Means of Pattern Control", Microwave Journal, Vol. 13, Oct. 1978, p. 41.
- 7. K. Tomiyasu, "Conversion of ${\rm TE}_{11}$ " mode by a large Diameter Conical Junction", IEEE Trans. on MTT, (May 1969), p. 277.
- 8. P. D. Potter, "A New Horn Antenna with Suppressed Side-lobes and Equal Beamwidths", Microwave Journal, Vol. $\underline{6}$, June 1963, p. 71.
- 9. Per-Simon Kildal and K. R. Jakobsen, "Scalar Horn with Shaped Lens Improves Cassegrain Efficiency", IEEE Trans. on AP, (Oct. 1984), p. 1094.

SATELLITE EARTH COVERAGE CONFIGURATION

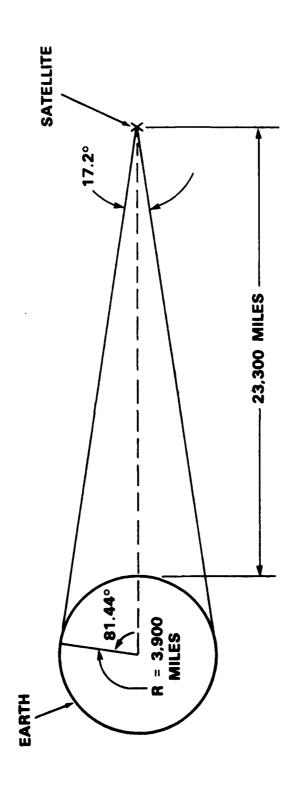


Figure 1.





DOUBLE-FLARED EARTH COVERAGE HORN Q-BAND

こうことのない。

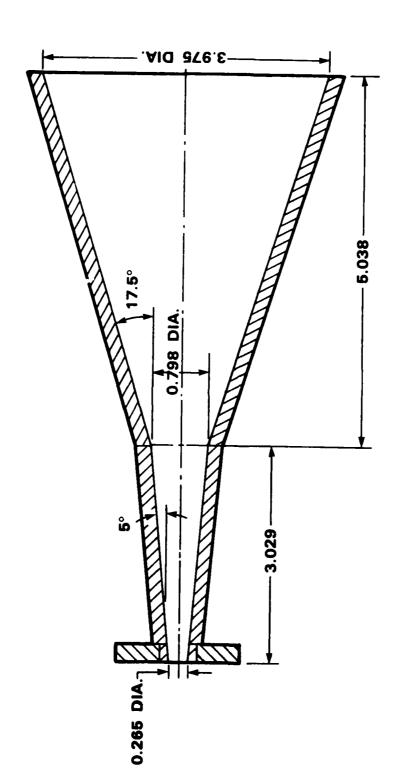
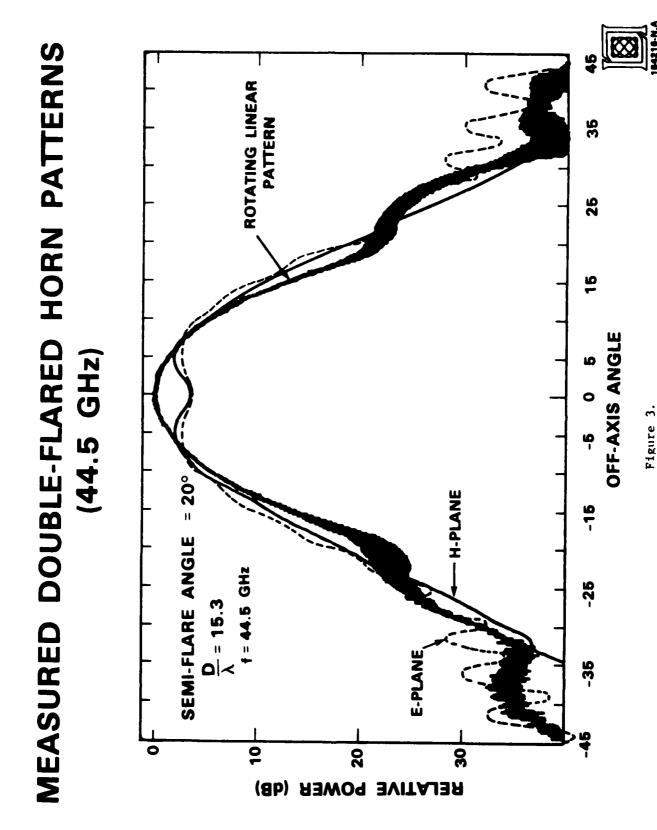
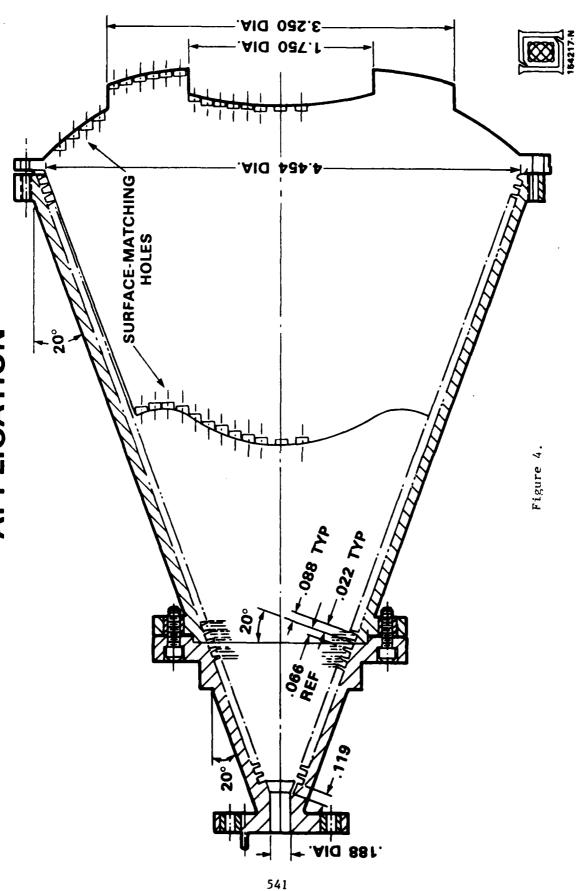
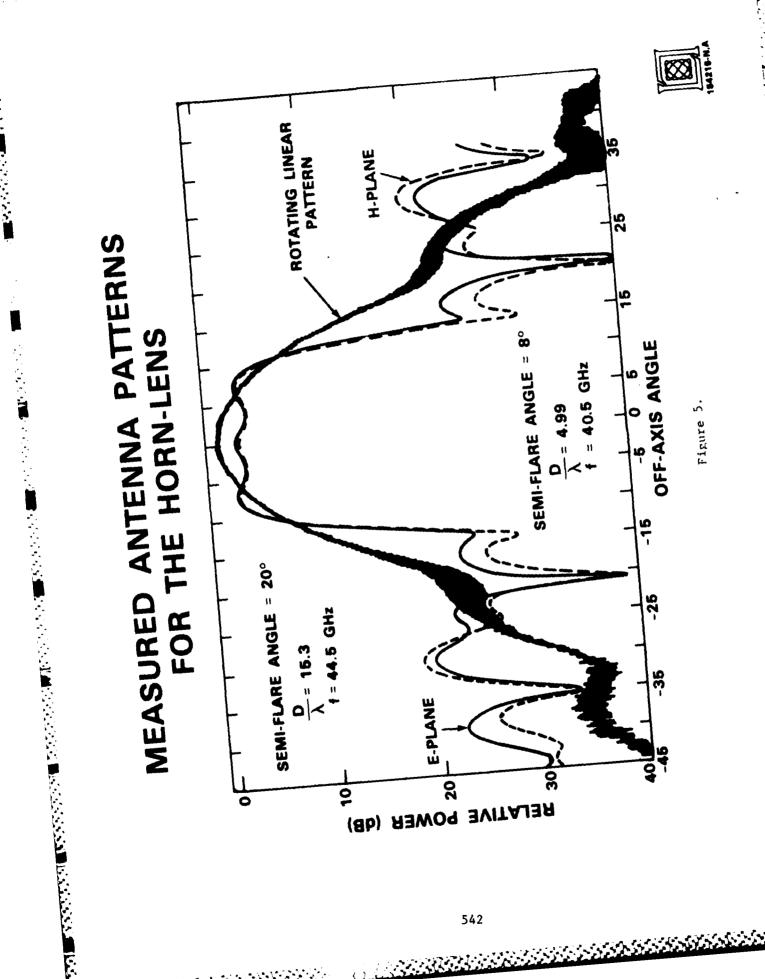


Figure 2.



ZONED DIELECTRIC LENS FOR EARTH-COVERAGE APPLICATION





CONTRACTOR OF THE PROPERTY OF

CIRCULAR ARRAY OF COAXIALLY-FED MONOPOLE ELEMENTS IN A PARALLEL PLATE WAVEGUIDE - EXPERIMENT

Boris Tomasic

Rome Air Development Center Electromagnetic Sciences Division Hanscom AFB, MA 01731

ABSTRACT

Circular ring arrays of coaxially-fed monopole elements between two circular parallel plates with E-plane (radial) flare are appealing for applications requiring scanning of a uniform beam 360 degrees in azimuth.

The performance of a circular array of coaxially-fed monopole elements radiating into an infinite parallel plate region has been analyzed in [1] and [2].

This paper describes the experimental effort and presents measured data for active impedance, coupling coefficients and element patterns. A 64-element circular ring array of coaxially-fed monopoles in a parallel plate waveguide was constructed. The measured values show excellent agreement with theoretical results. This agreement strongly suports the validity of the analysis, and furnishes a firm basis for a systematic and accurate array design.

This work was supported by the Rome Air Development Center under project No. 2305J303.

1. INTRODUCTION

Circular ring arrays of coaxially-fed monopole elements between two circular parallel plates with E-plane (radial) flare are of interest for various antenna aplications. In particular they are very attractive for radar and communication applications because of their uniform circumferential radiation characteristic and 360 degree azimuth coverage capabilities. In view of its simplicity, low cost, polarization purity, reasonably wide bandwidth and power handling capability, the coaxially-fed linear monopole is an attractive choice for an array element in a parallel plate waveguide.

Performance of a coaxially-fed monopole element in a circular ring array radiating into an infinite parallel plate region has been analyzed in [1,2].

To validate the theory, a 64-element circular ring array of coaxially -fed monopoles in a parallel plate waveguide, and a one and two-half element waveguide simulator were constructed. The array and element construction is described. An illustrative method of selection of optimal geometry for element match in an array environment, as well as the dependence of important design parameters on the array and element geometry, is discussed. The measured data is presented for active impedance, coupling coefficients, and element patterns. The measurements show an excellent agreement with theoretically predicted results.

These results strongly support the validity of the previously reported analysis, and furnish a firm basis for accurate design of a circular ring array radiating into a parallel plate waveguide region.

2. ARRAY DESCRIPTION

The experimental array is shown in Figs. 1 and 2. The array contains 64 elements between two circular parallel plates with an E-plane (radial) flare as schematically shown in Fig. 3. The flare is to simulate an infinite parallel plate region. In Fig. 3 the top plate is partially removed to display the section of the array. Fig. 4 shows schematically the top and side view of the array with relevant dimensions.

The circular ring array of coaxially-fed monopoles of length ℓ in a parallel plate waveguide of height h (only the TEM mode propagates since h $< \lambda/2$). The ring, of radius B, contains N equispaced identical monopoles, each located coaxially a distance s above a perfectly conducting circular cylindrical surface of radius A. The probe radius is a $<< \lambda$ while the inner and outer radii of the coaxial lines are a and b, respectively. The coaxial feed-lines are filled with teflon ($\epsilon_{\rm r}=2$) and have characteristic impedance $Z_{\rm c}=50$ ohms.

The array element spacing is chosen to be d=0.4 $\lambda_{\rm C}$ (0.945") and the parallel plate separation h=0.369 $\lambda_{\rm C}$ (0.872") (which corresponds to the height of the standard C-band rectangular waveguide) at a center frequency f_C=5.0 GHz. The probe length and probe to cylindrical ground distance were selected so that the equivalent infinite linear array (also called the reference array) shown in Fig. 5 would be matched at broadside scan i.e.: ℓ =0.233 $\lambda_{\rm C}$ (0.550"), s = 0.163 $\lambda_{\rm C}$ (0.385"). The array elements shown in Fig. 6 were Omni Spectra's Flange Mount Jack Receptacles with a = 0.01 $\lambda_{\rm C}$ (0.025") and b = 0.034 $\lambda_{\rm C}$ (0.081").

To observe the creeping wave grating lobe ripple effect in the element pattern, an inter-element spacing d = 0.6 $\lambda_{\rm C}$ (0.945") was also chosen. This was achieved simply by increasing center the frequency from f_c=5.0 GHz to f_c=7.5 GHz, while retaining the same top and bottom parallel plates with radial flare. Probes and the cylindrical ground (parallel plate spacer) however, were replaced in order to match the corresponding reference array at broadside scan. The new dimensions were: ℓ =0.25 $\lambda_{\rm C}$ (0.393"), h = 0.369 $\lambda_{\rm C}$ (0.580").

In summary, coupling coefficients and element patterns of a 64-element circular ring array of coaxial monopole elements radiating into a parallel plate region were measured for two array element spacings (a) d = 0.4 $\lambda_{\rm C}$ and (b) d = 0.6 $\lambda_{\rm C}$. In both cases, equivalent infinite linear arrays were matched at broadside scan. The respective array element dimensions are:

(a)
$$f_c = 5.0 \text{ GHz}$$
 ($\lambda_c = 2.360^\circ$) (b) $f_c = 7.5 \text{ GHz}$ ($\lambda_c = 1.574^\circ$)

 $d = 0.4 \lambda_c$ (0.945°) $d = 0.6 \lambda_c$ (0.945°)

 $N = 64 \text{ (kB} = 25.6)$ $N = 64 \text{ (kB} = 38.4)$
 $A = 3.915 \lambda_c$ (9.240°) $A = 5.870 \lambda_c$ (9.240°)

 $A = 5.870 \lambda_c$ (9.625°) $A = 6.115 \lambda_c$ (9.625°)

 $A = 0.369 \lambda_c$ (0.872°) $A = 0.369 \lambda_c$ (0.580°)

 $A = 0.233 \lambda_c$ (0.550°) $A = 0.250 \lambda_c$ (0.393°)

 $A = 0.163 \lambda_c$ (0.385°) $A = 0.016 \lambda_c$ (0.385°)

 $A = 0.010 \lambda_c$ (0.025°) $A = 0.016 \lambda_c$ (0.025°)

 $A = 0.034 \lambda_c$ (0.081°) $A = 0.051 \lambda_c$ (0.081°)

 $A = 0.051 \lambda_c$ (0.081°)

 $A = 0.051 \lambda_c$ (0.081°)

 $A = 0.051 \lambda_c$ (0.081°)

 $A = 0.051 \lambda_c$ (0.081°)

 $A = 0.051 \lambda_c$ (0.081°)

MONOPOLE ELEMENT DESIGN

The array elements shown in Fig. 6 were Omni Spectra's Flange Mount Jack Receptacles (model No. 204 CC, part No. 2052-1201-00) with a = 0.025" and b = 0.081". The element dimensions (ℓ and s) were determined by the requirement that an equivalent infinite linear array would be matched at broadside scan (ϕ_0 =0°) and center frequency f_c . For this purpose, Figs. 7 and 8 display a contour plot of the magnitude of the active reflection coefficient vs. probe length (ℓ / λ) and vs. probe to ground distance s/ λ , for both element spacings (a) d/ λ_c = 0.4, and (b) d/ λ_c = 0.6, respectively. It is seen that in case (a) for ℓ / λ = 0.233, s/ λ = 0.163, and in case (b) for ℓ / λ = 0.250, s/ λ =0.245, the active reflection coefficient $\Gamma_a(\phi_0$ =0°) = 0.

Figs. 9 and 10 compare active impedance dependence on scan angles ϕ_0 at f_C of a circular array with those of an equivalent linear array. In the circular array case, discrete values of ϕ_0 are given by $\sin \phi_0 = \upsilon/kB$, where $\upsilon = 1, 2, \ldots, N-1$. The Smith chart normalization is 50 ohms. A region of overlap may be noticed $(0^\circ < \phi_0 < 30^\circ)$ which justifies the above element matching scheme. For $\phi_0 > 30^\circ$, curves gradually depart from linear ones, due to the curvature effect.

For the above geometry, Fig. 11 shows the active impedance of the reference linear array at broadside scan vs. frequency. It is seen that the frequency bandwidth corresponding to a VSWR of 2:1 is approximately 40%.

4. WAVEGUIDE SIMULATOR

To validate the numerical results for active admittance a one and two-half element waveguide simulator was constructed [3,4,5]. The single mode simulator for array (a) is shown in Figs. 12 and 13. The simulator waveguide dimensions as shown in Fig. 14 are 2d x h, i.e., approximately 1.872" x 0.872" which corresponds to standard C-band rectangular waveguide. The waveguide was terminated in a matched load with a VSWR < 1.02 over the frequency band 4 to 6 GHz. In view of Fig. 15 and the relation

$$\sin \phi_0 = \frac{\pi}{2kd}, \qquad (1)$$

it is seen that the device simulates scan conditions from 52° off-broadside at 4.0 GHz through 40° off-broadside at $f_c = 5.0$ GHz to 32° off-broadside at 6.0 GHz.

The active reflection coefficient measurement was performed with an HP-8410 Network Analyzer. The measurement test setup is shown in Fig. 16.

Fig. 17 shows the theoretical and the measured active impedance vs. frequency. The Smith chart normalization is 50 ohms. Excellent agreement between theoretical and measured results may be observed across the operating band. The two results for the active reflection coefficient differ less than 1% in magnitude and less than 3 degrees in phase.

5. COUPLING COEFFICIENTS

Coupling coefficients for the circular array (b) and its infinite linear reference array are presented in Fig. 18. As expected the linear array, coupling coefficients decay monotonically with element number p. Also, as will be seen in the next figure, for elements distant from the excited monopole (p=0) the coupling is primarily due to the parallel plate guide TEM mode, the amplitude of which decays as $1/\sqrt{r}$. As expected in the circular array, the coupling coefficients initially follow that of the linear array. For elements far from the excited one (p=0), the coupling coefficients decrease exponentially, which indicates that the main contribution is primarily due to a single creeping wave.

Fig. 19 exhibits the phase of the coupling coefficients for the array geometry of Fig. 18. For convenience we define coupling coefficients SP as

$$SP = |SP| e$$
 (2a)

where

$$\phi_p = k dp + \Delta \phi_p$$
, $k = \frac{2\pi}{\lambda}$. (2b)

The second term in (2b) is plotted in Fig. 19 while the first term represents the phase delay (for linear array) from the reference element (p=0) to element p of the TEM mode in the parallel plate waveguide. Thus, for elements close to the excited one the coupling is due to the TEM mode, plus contributions of higher non-propagating

parallel plate waveguide modes. For elements further removed, the coupling is primarily due to the TEM mode.

Coupling coefficients were measured down to -55 dB in amplitude which corresponds approximately to the seventh element from the excited reference element (p=0). Beyond this low amplitude level, reflection from the aperture of the E-plane flare influenced the measured results.

Figs. 20 and 21 present a comparison between the measured (open circles) and theoretical (solid circles) coupling coefficient values in amplitude and phase, respectively. The difference between the two results is less than 1.0 dB in amplitude and less than 5 degrees in phase.

6. ELEMENT AMPLITUDE PATTERN

Fig. 22 shows the amplitude of element (field) pattern of circular array (b) and its equivalent infinite linear array. It is observed that both patterns exhibit a substantial drop-off near

$$\phi_{\text{EGL}} = \arcsin\left(\frac{\lambda}{d} - 1\right). \tag{3}$$

In the linear array case this drop-off is caused by an end-fire grating lobe condition and in the cylindrical array by its quasi-linear counterpart as discussed in [6] for a cylindrical array of axial strip-dipoles. The curves of Fig. 22 also exhibit a ripple in the broadside region, whose amplitude diminishes with closer element element spacings and becomes negligible for $d/\lambda = 0.5$. The ripple is due to the interference of the direct single element radiation

(with linear array element pattern) with grating lobes of corresponding quasi-linear subarrays excited by the guided creeping wave as illustrated in Fig. 23.

The element pattern was measured on the far-field range. The axis of rotation was at the location of the receiving (reference) element which was connected to a 20/20 Scientific Atlanta Antenna Analyzer while other elements were terminated in 50 ohm coaxial loads.

Figs 24 and 25 show a comparison between measured (solid curve) and the calculated (dashed curve) element pattern amplitude for both, (a) and (b) arrays, respectively. From these figures it is seen that in the shadow region the patterns fall off exponentially which indicates that it is primarily due to a single creeping wave with an angular attenuation constant proportional to $(kA)^{1/3}$.

In the theoretical result the ripple in the $\phi=180^{\circ}$ region, similarly to that found on a conducting cylinder, is a result of the interference of two creeping waves traveling in opposite directions around the cylinder. Unfortunally it could not be observed experimentally because of reflections from the aperture of the E-plane flare that limited reflection-free amplitude pattern measurements to -30 dB level.

For better exposition of creeping wave grating lobe ripples in the broadside region of the element pattern in Fig. 25, Fig. 26 shows the same curves on a linear scale. Excellent agreement between measured and theoretical results may be observed.

7. ELEMENT PHASE PATTERN

Design of a cylindrical array requires knowledge of the element phase center location. It was found that the flattest element pattern phase in the broadside region is obtained for the phase reference location near the monopole.

Fig. 27 exhibits the calculated element pattern phase for the geometry of Fig. 22. One observes that for both the circular and its equivalent linear array, the phase varies only by a few degrees up to the EGL drop-off. Thus the EGL position essentially determines the limit of usefulness of the element, both in amplitude and phase.

Figs. 28 and 29 show a comparison between measured (solid curve) and the calculated (dashed curve) element pattern phase of (a) and (b) circular arrays, respectively. Excellent agreement between measured and the theoretical results may be observed.

8. CONCLUSIONS

The close agreement of the experimental and the theoretical results for active impedance, coupling coefficients, and element patterns strongly supports the validity of the analysis previously reported, and furnishes a firm basis for the matched element design method that was developed.

The knowledge of the element patterns in the array environment and of the phase center location which has been experimentally verified to be near the element serves to improve the design accuracy of conformal arrays.

ACKNOWLEDGEMENTS

The author thanks Mr. James P. Kenney and Mr. Jeffrey S. Herd for performing the experimental work, and Dr. Hans Steyskal for the use of his cylindrical array antenna for experimental purposes.

REFERENCES

- Tomasic, B. (1985) Circular array of coaxially-fed monopole elements in a parallel plate waveguide - Theory. Paper presented at the ISAP meeting, Kyoto, Japan.
- 2. Tomasic, B. (1985) Circular array of coaxially-fed monopole elements in a parallel plate waveguide - Theory. Paper presented at the ISAE meeting, Beijing, Peoples Republic of China.
- 3. Tomasic, B. and Hessel, A. (1985) Linear phased array of coaxially-fed monopole elements in a parallel plate waveguide. RADC report to be published.
- 4. Tomasic, B. and Hessel, A. (1982) Linear phased array of coaxially-fed monopole elements in a parallel plate guide.

 Paper presented at the IEEE/AP-S meeting, Albuquerque, NM.
- 5. Tomasic, B. and Hessel, A. (1985) Linear phased array of coaxially-fed monopole elements in a parallel plate waveguide - Experiment. Paper presented at the IEEE/AP-S meeting, Vancouver, Canada.
- Herper, J.C., Hessel, A. and Tomasic, B. (1985) Element pattern of an axial dipole in a cylindrical phased array
 Part I, IEEE Trans. on Ant. and Prop., p.259, Vol. AP-33.



Fig. 1 A 64-element circular array antenna

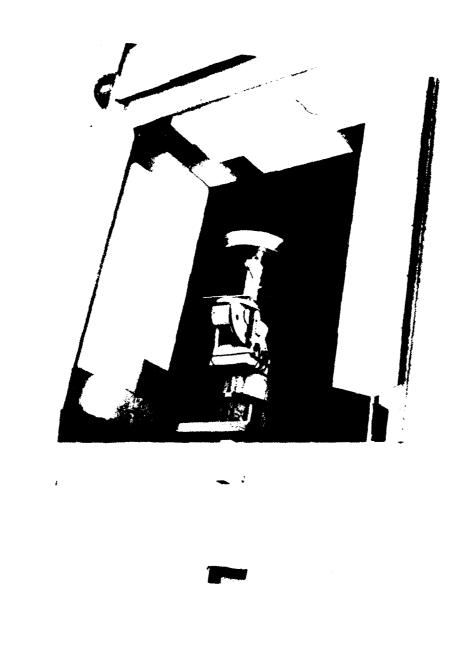


Fig. 2 A 64-element circular array antenna in a far-field anechoic chamber

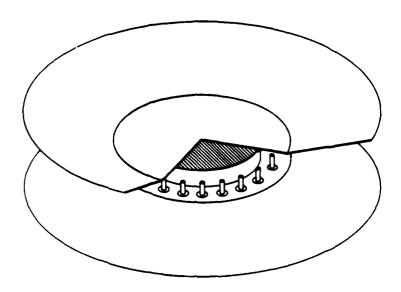


Fig. 3 Circular array of coaxial monopoles in a parallel plate waveguide

スカスを通用のネタスタタを置っていいいなり **自**

ジント **職職の かりつか 投資** こうたい から音 阿の こいから 配置 なってもの 全面 あんらい オタ 全層 あんり

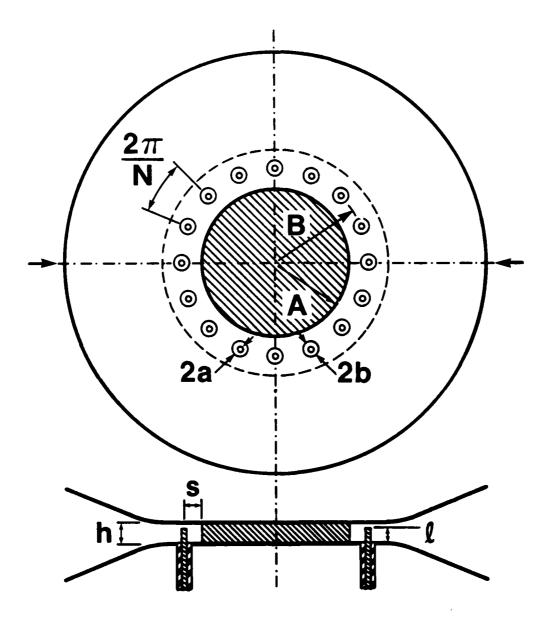


Fig. 4 Top and side view of circular array

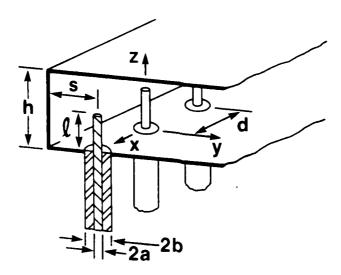


Fig. 5 Linear array of coaxial monopole elements in a semi-infinite parallel plate waveguide

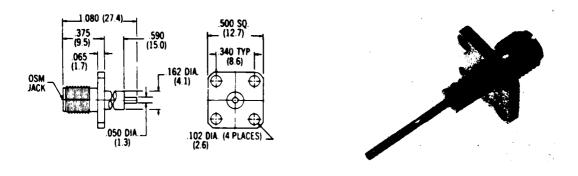


Fig. 6 Coaxial monopole element

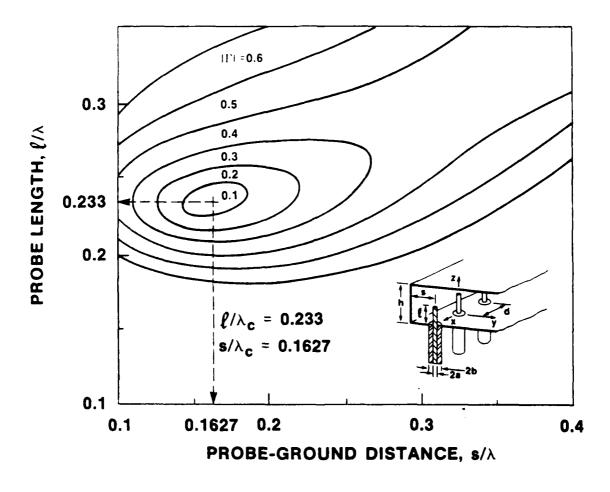


Fig. 7 Linear reference array (a) active reflection coefficient -amplitude vs. probe to ground distance and vs. probe length (d/ λ_c = 0.4, ϕ_o = 0°)

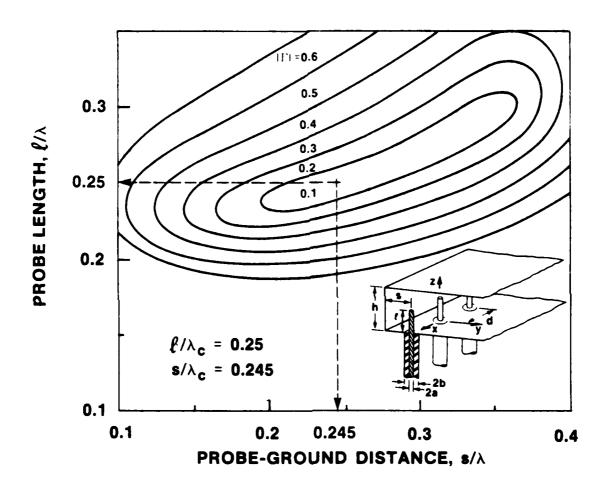


Fig. 8 Linear reference array (b) active reflection coefficient - amplitude vs. probe to ground distance and vs. probe length $(d/\lambda_c = 0.6, \phi_o = 0^0)$

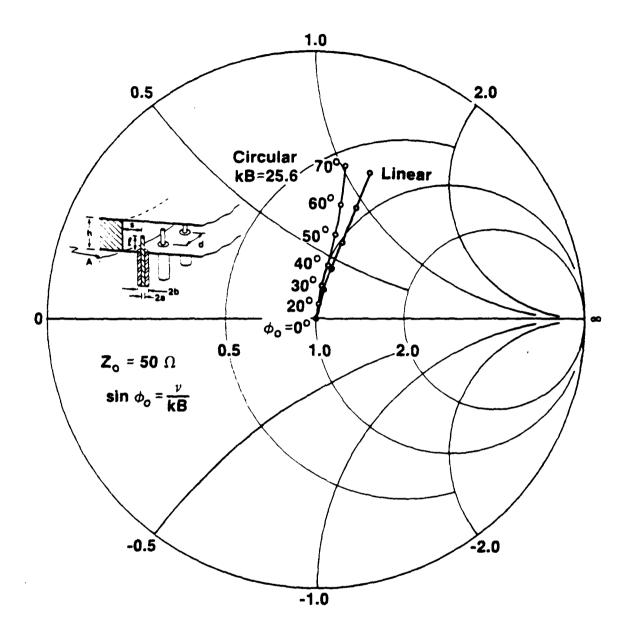


Fig. 9 Active impedance of circular array (a) and its equivalent linear array vs. scan

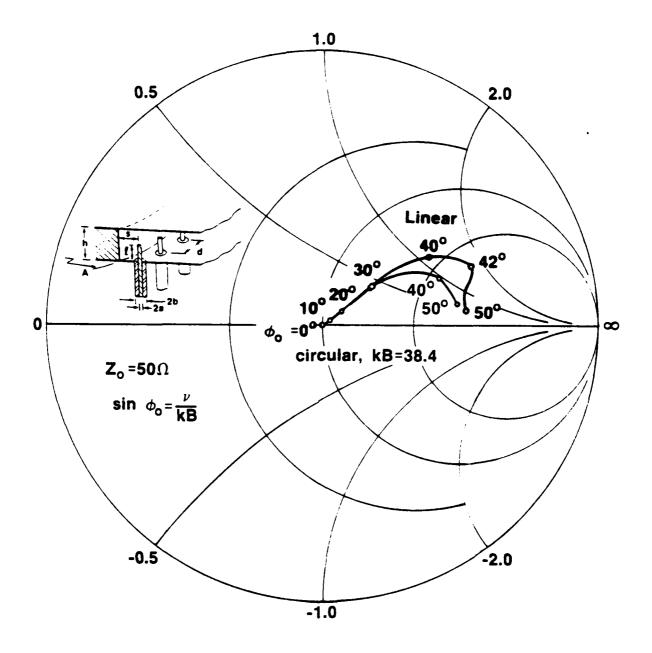


Fig. 10 Active impedance of circular array (b) and its equivalent linear array vs. scan

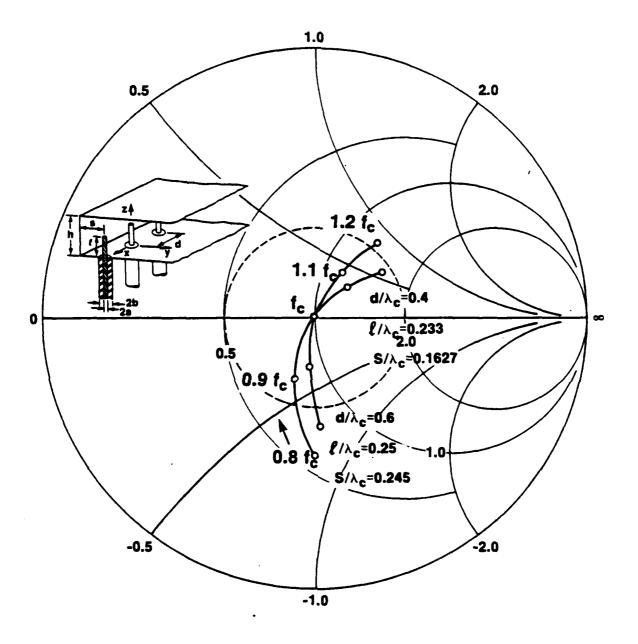


Fig. 11 Active impedance of (a) and (b) linear reference arrays vs. frequency

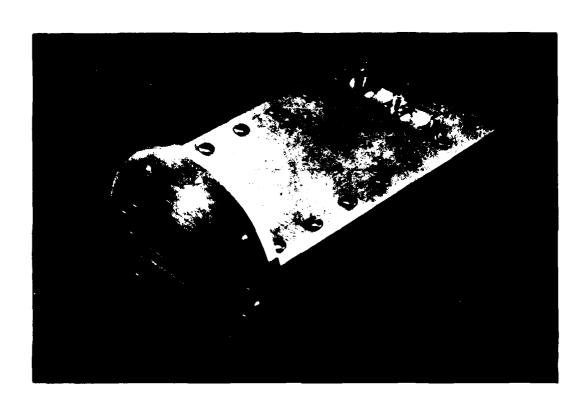


Fig. 12 A one and two-half element waveguide simulator

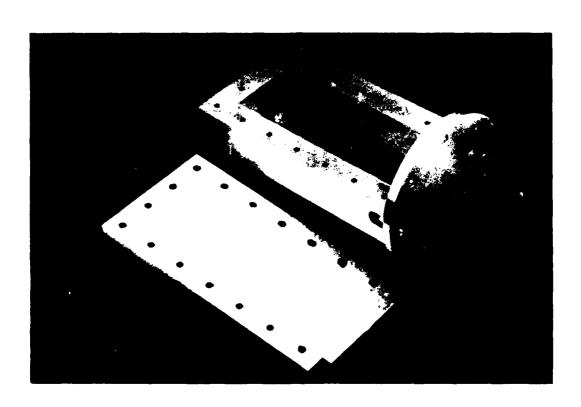


Fig. 13 A one and two-half element waveguide simulator

(top side removed to display the monopole elements)

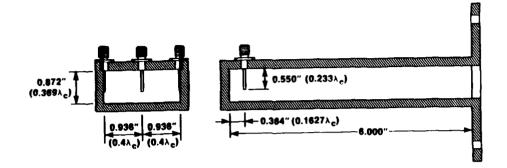


Fig. 14 A one and two-half element waveguide simulator dimensions

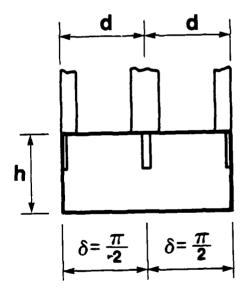


Fig. 15 Crossection of waveguide simulator pertaining to relation between frequency and scan angle

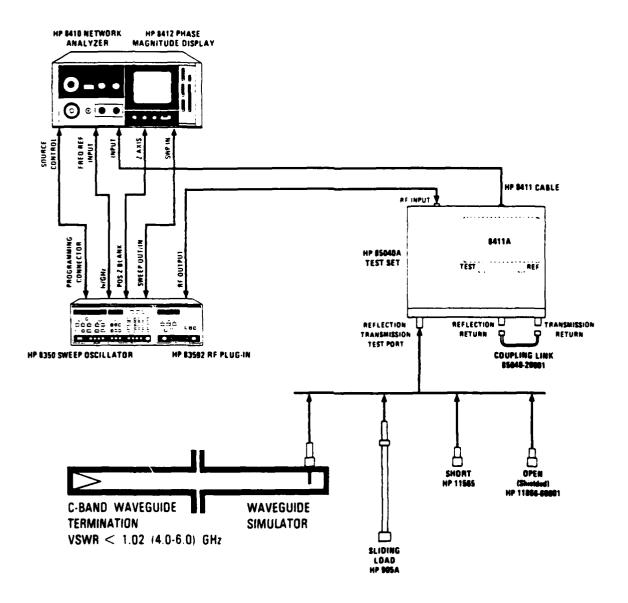


Fig. 16 Active reflection coefficient mesurements test setup

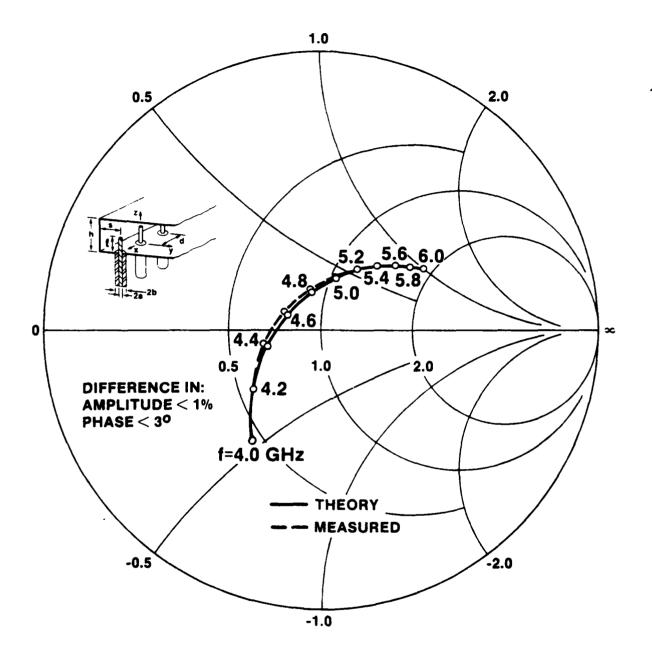


Fig. 17 Active impedance vs. frequency - theory and simulator measurements

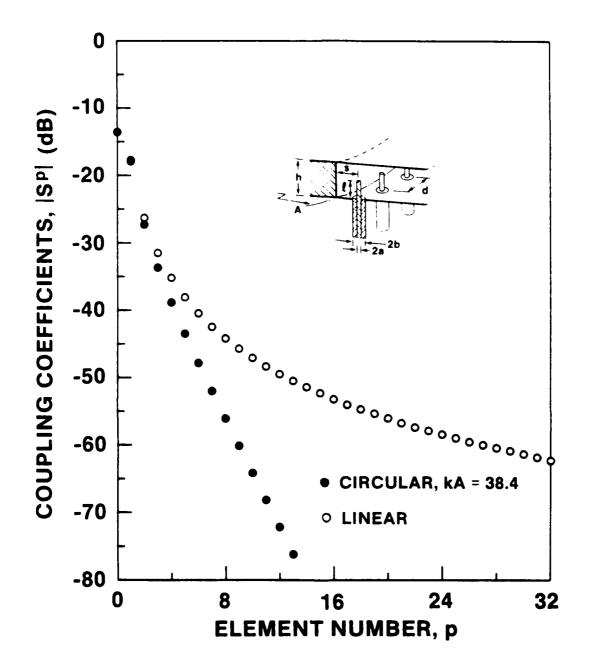


Fig. 18 Coupling coefficients amplitude for circular array (b) and the reference linear array

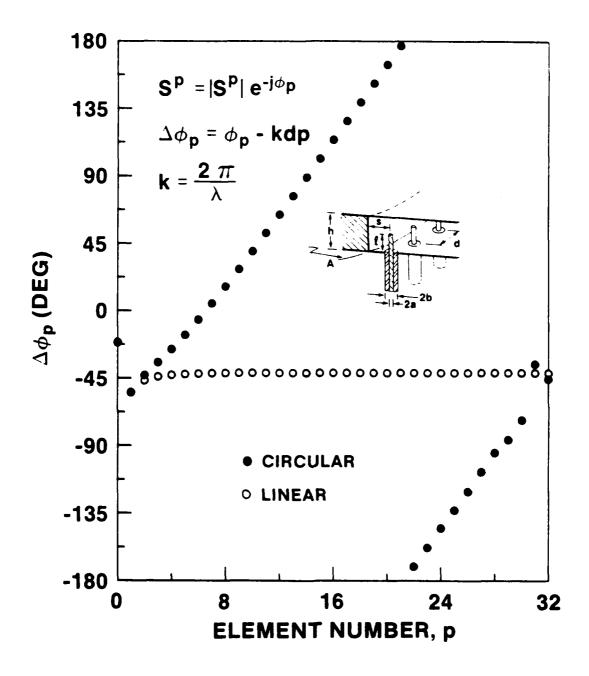


Fig. 19 Coupling coefficients phase for circular array (b) and the reference linear array

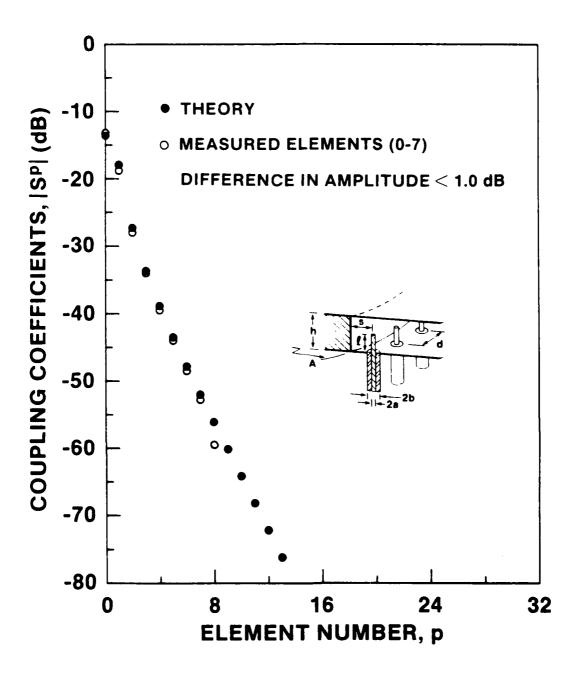


Fig. 20 Theoretical and experimental amplitude of coupling coefficients for circular array (b)

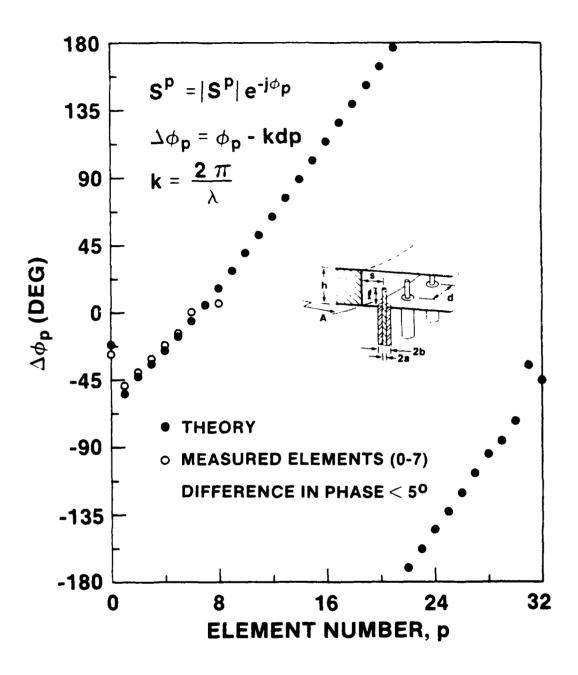


Fig. 21 Theoretical and experimental phase of coupling coefficients for circular array (b)

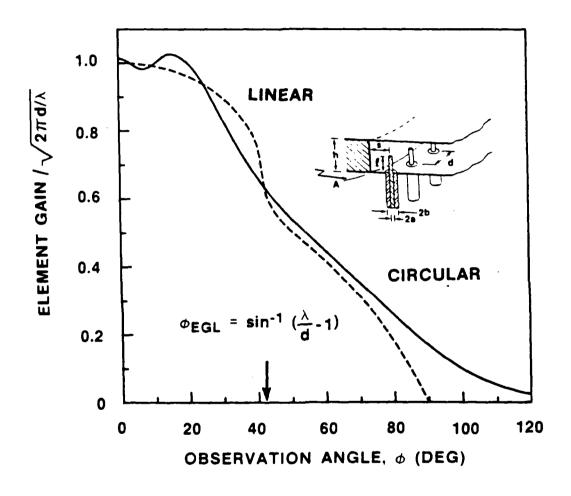


Fig. 22 Amplitude of element pattern of circular array (b) and its equivalent infinite linear array

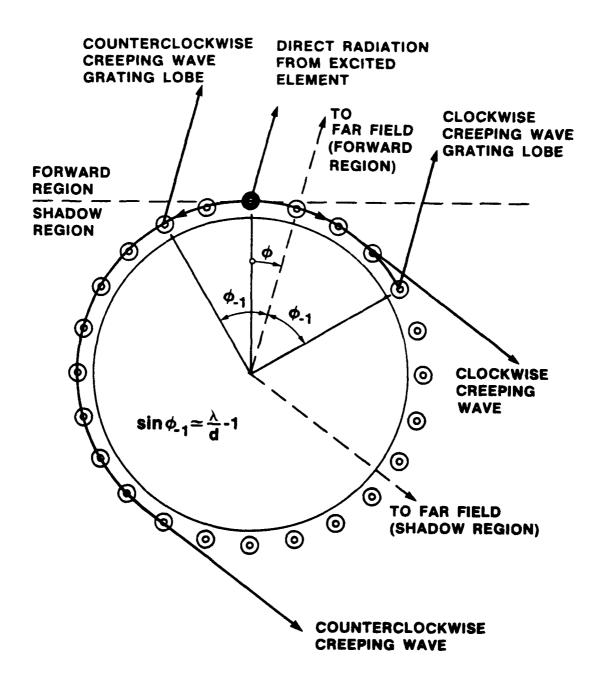


Fig. 23 Wave contributions to element pattern

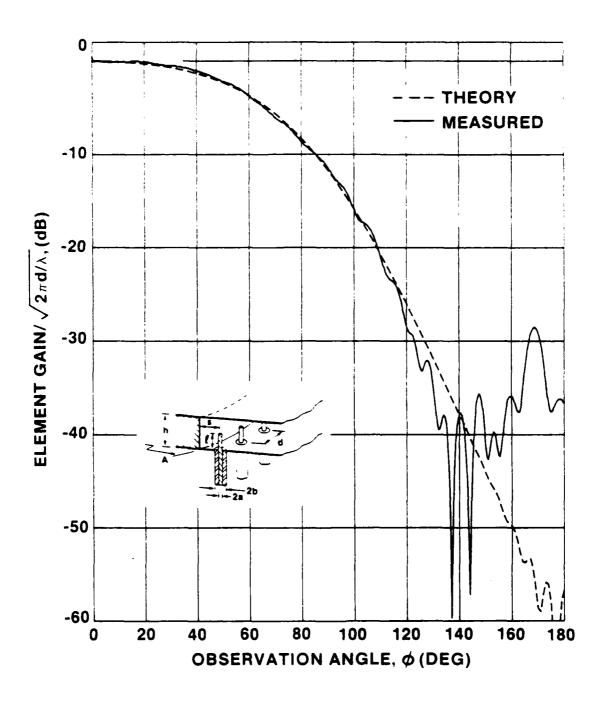


Fig. 24 Theoretical and experimental element pattern amplitude for circular array (a) (log scale)

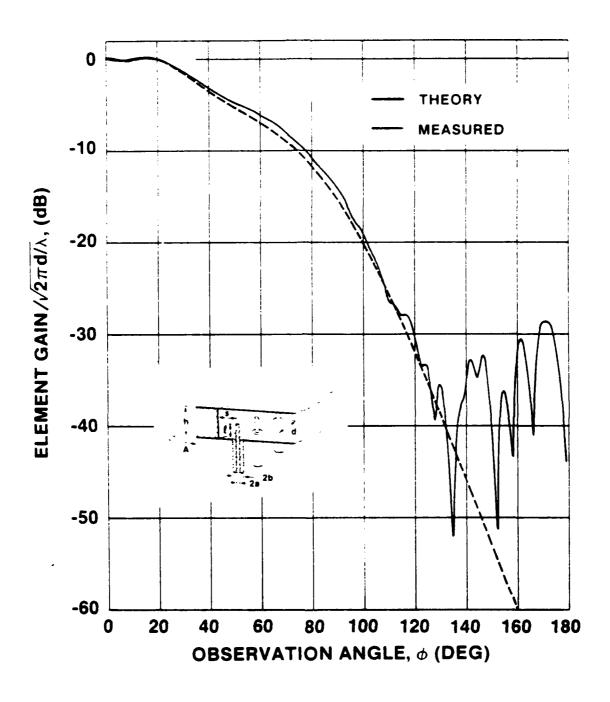


Fig. 25 Theoretical and experimental element pattern amplitude for circular array (b) (log scale)

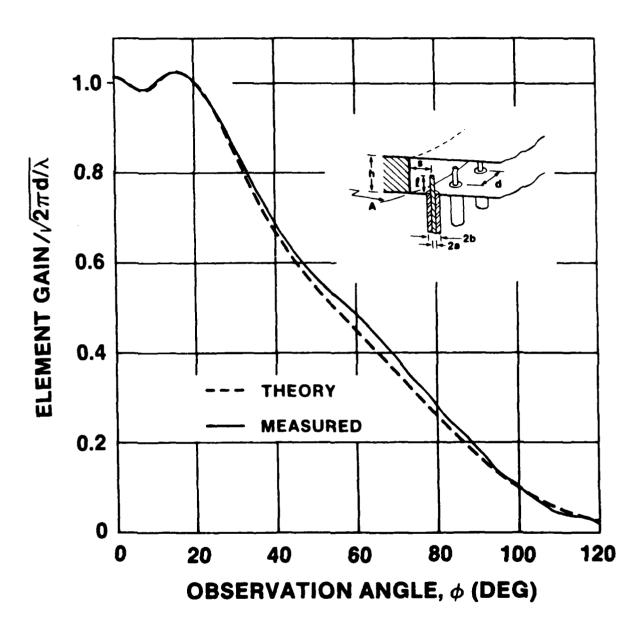


Fig. 26 Theoretical and experimental element pattern amplitude for circular array (b) (linear scale)

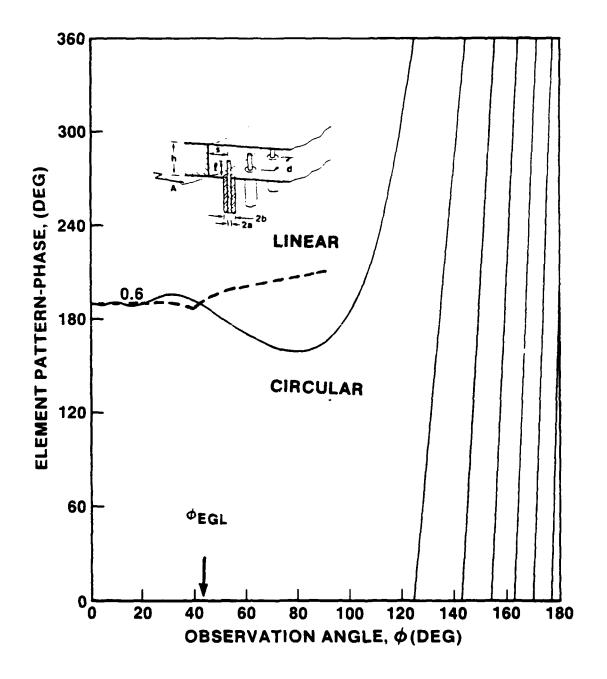


Fig. 27 Phase of element pattern of circular array (b) and its equivalen linear array

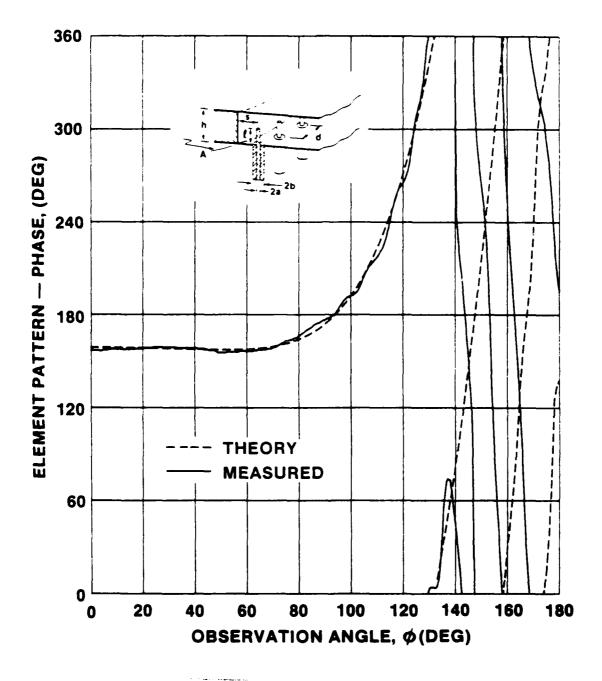


Fig. 28 Theoretical and experimental element pattern phase for circular array (a) $(d/\lambda_c = 0.4)$

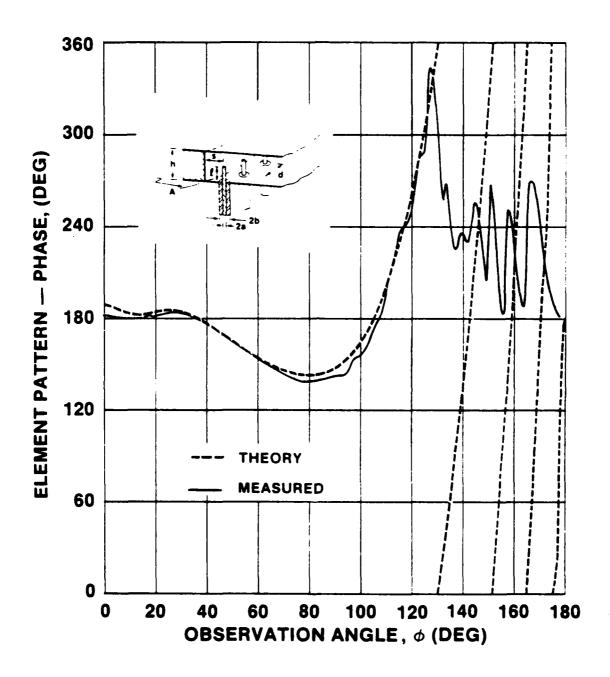


Fig. 29 Theoretical and experimental elemnt pattern phase for circular array (b) $(d/\lambda_c = 0.6)$

VHF SATELLITE ANTENNA SYSTEM

Michael R. Matthew
Member of Technical Staff
Antenna Technology MC:DD18
Strategic Defense and Electro-Optical Systems Division
Defense Electronics Operations
Rockwell International Corporation
Anaheim, California 92803

ABSTRACT

The VHF antenna system described here will be on the Global Positioning Satellite System. The antennas are designed to receive circularly polarized signals with a design goal of a 6 dB axial ratio. Due to limited space on the satellite, they are electrically small in size. The low-band antenna (43 percent bandwidth at VHF) is a set of four meandering monopoles (designed by Dr. Alan W. Love, based on the meandering monopole patent by Mr. Howard E. King and Dr. Jimmy L. Wong) fed by a quadripole network. They are arranged on the rear bulkhead of the satellite to provide for best circular polarization. The high-band antenna has a bandwidth of 32 percent at VHF and is positioned on the forward bulkhead on an extended ground plane. antenna is a crossed-dipole turnstile antenna (designed by Dr. Alan W. Love) fed by a quadrature hybrid. Both antennas, using directional couplers, have self-test verification provisions. An interesting feature is that due to the electrically small size of the low band antennas, the antennas act as probes which sample

currents on the satellite surface and solar panels. The antenna system receives well from directions toward and away from the earth. The YSWR, polarization, gain, and reception patterns must be measured with the antennas mounted on a full scale mockup of the satellite. The antennas are developed to have a large bandwidth, good axial ratio, and an acceptable gain and VSWR.

2. HIGH BAND VHF ANTENNA SYSTEM

インスのの 自動を入るののの 自動物

このでは最かないないない。自身であることでは、世界がないないのは、

こうことは意見のことのなる意見のななられる。

2.1 Description of Antenna and VSWR Performance

The high-band antenna has an operating bandwidth from 109-151 MHz. It is a crossed-dipole turnstile antenna which is fed by a quadrature hybrid as in the circuit schematic Figure 1. It is situated on the forward bulkhead of the satellite with an extended ground plane as may be seen in Figure 2. The antenna dipole element is 44" in length which is (.40) wavelengths at 109 MHz. The parasitic element which is provided for greater bandwidth is 40" in length which is .37 wavelengths at 109 MHz . It is seen that this is electrically short; however, this is necessary to prevent interference with the solar panels. The high-band antenna is depicted to Figure 3. The Voltage Standing Wave Ratio was within the specification of 6:1. This was accomplished by using an adjustable balun. The fully extended position was chosen for best performance as shown in Figure 4. The VSWR of the high-band antenna for both ports is within the specification

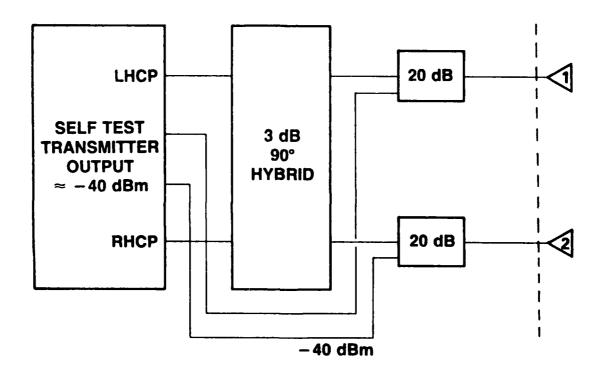


Figure 1. High-Band Antenna Circuit Diagram

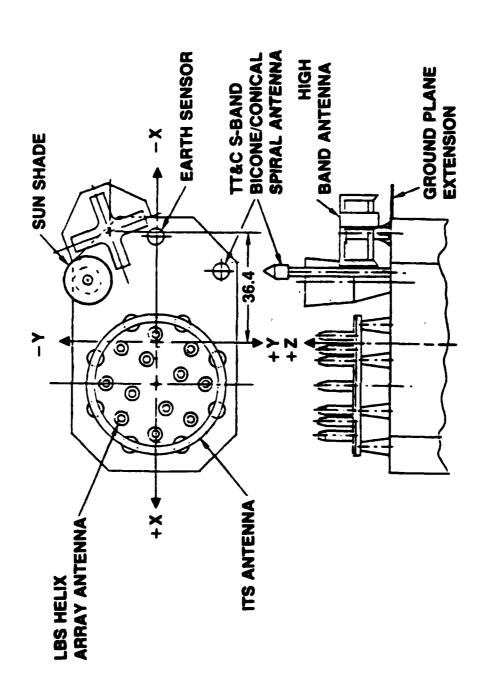


Figure 2. High Band Antenna GPS Location

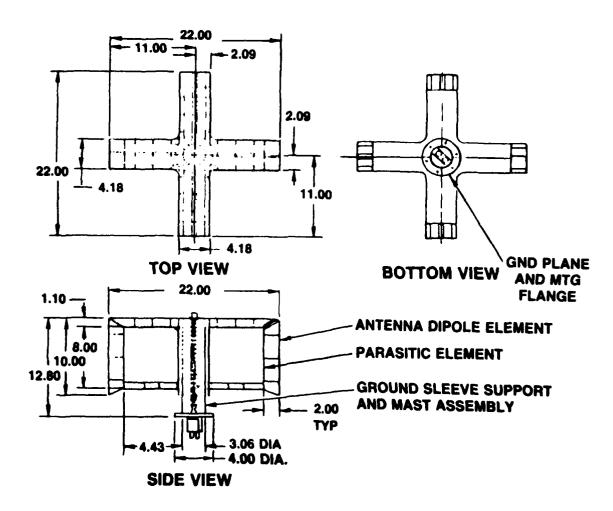


Figure 3. High Band Antenna

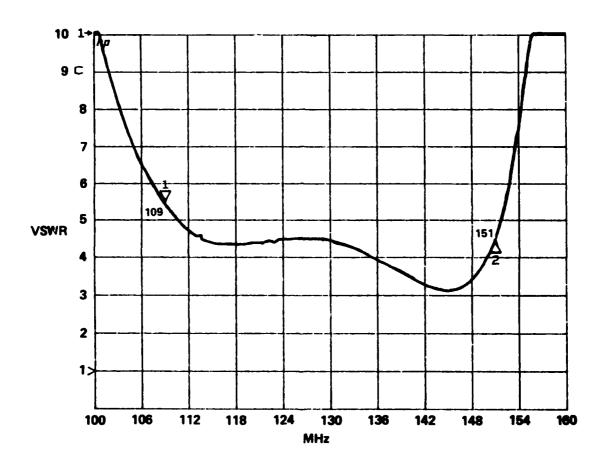


Figure 4. High-Band Antenna VSWR (Port 2)

across the band, and as expected has two nulls at approximately 115 MHz and 145 MHz, due to the antenna dipole element and the parasitic dipole element as in Figure 5.

2.2 Self Test Verification for High Band Antenna

The self test verification for the high band antenna using the reversed directional coupler scheme did not perform exactly as intended. To provide for a null in the power measurement a 180° difference in each antenna with identical impedance must exist. Due to the quadrature hybrid this was not possible, and it was not feasible to add a 90° line over the bandwidth for self test purposes. However, failure cases had power losses which had enough significant difference from operating conditions to provide a viable self test network.

2.3 High Band Antenna Axial Ratio

The crossed-dipole turnstile was utilized to provide for reception of circularly polarized signals with a design goal of 6 dB axial ratio. Data for the axial ratio on axis is provided in Figure 6. Worst case axial ratio is approximately 5.5 dB at 100 MHz for right hand circular polarization at solar panel angle 0°. Generally, the axial ratio for most cases is 4 dB or less, with the higher axial ratios appearing at the lower part of the

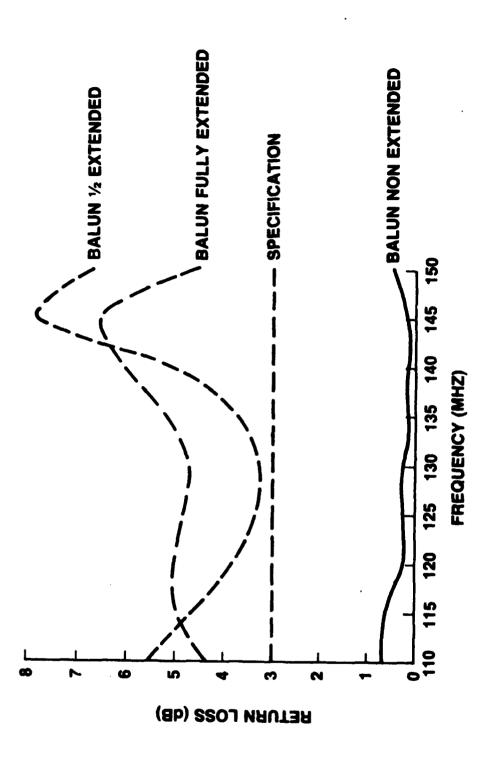
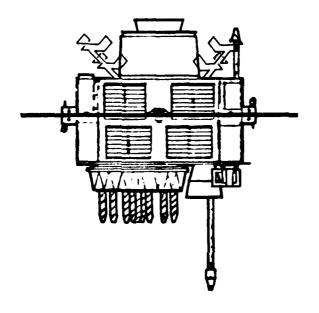
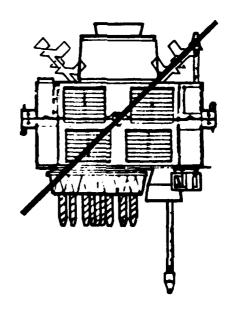


Figure 5. Determination of Balun Position on High-Band Antenna (Mock up, Port 1)

SOLAR PANEL POSITION

FREQ (MHz)	00		45°		90°		135°	
	RHCP	LHCP	RHCP	LHCP	RHCP	LHCP	RHCP	LHCP
109	4.88	4.2	2.0	3.3	2.9	3.2	4.0	3.3
120	2.5	1.1	1.4	1.2	3.1	.3	3.7	1.7
130	2.9	1.0	2.5	.8	2.9	1.0	2.8	1.0
140	.8	1.0	2.1	1.7	2.0	.6	2.2	1.1
151	1.0	.8	2.3	2.0	1.5	.4	2.2	.7





0º POSITION

45° POSITION

Figure 6. High-Band Axial Ratio (dB)

frequency band. Solar panel position did not appear to have much effect on the axial ratio. The axial ratios for the $\theta=7^{\circ}$, and $\theta=14^{\circ}$ were also satisfactory due to wide beamwidth and are not discussed in this paper.

2.4 High Band Antenna Gain

The gain measurements are also within the specification of $-6~\mathrm{dB_{ic}}$. The gain tends to be highest at around 130 MHz and tends to tail off as the outer limits of the frequency band are reached as shown in Figure 7.

2.5 High Band Antenna Summary

The high-band crossed dipole turnstile antenna on the extended ground plane was basically a well behaved antenna system. The parasitic element helped create a larger bandwidth, along with the "tuning" of the movable balun. The solar panels for the high band antenna did not appear to have any major effect.

3. LOW BAND ANTENNA VHF ANTENNA SYSTEM

3.1 Description of Low Band Antenna

The low band antenna has an operating bandwidth from 48-54 MHz and 73-75 megahertz. The low-band antenna is a set of four meandering monopoles fed by a quadripole network with directional

SP ∢ 0°		SP ∢ 45 0		SP ≪ 90°		SP ∢ 135°	
RHCP	LHCP	RHCP	LHCP	RHCP	LHCP	RHCP	LHCP
1.17	2.43	2.77	3.32	2.36	3.35	2.84	3.20
2.14	2.67	1.96	2.44	1.88	3.04	1.86	2.05
5.00	4.97	4.38	5.05	4.19	4.93	4.04	5.44
3.94	3.02	3.87	3.09	3.72	3.42	2.98	3.48
1.17	- 0 .14	0.52	0.25	1.46	0.89	0.60	1.14
	1.17 2.14 5.00 3.94	RHCP LHCP 1.17 2.43 2.14 2.67 5.00 4.97 3.94 3.02	RHCP LHCP RHCP 1.17 2.43 2.77 2.14 2.67 1.96 5.00 4.97 4.38 3.94 3.02 3.87	RHCP LHCP RHCP LHCP 1.17 2.43 2.77 3.32 2.14 2.67 1.96 2.44 5.00 4.97 4.38 5.05 3.94 3.02 3.87 3.09	RHCP LHCP RHCP LHCP RHCP 1.17 2.43 2.77 3.32 2.36 2.14 2.67 1.96 2.44 1.88 5.00 4.97 4.38 5.05 4.19 3.94 3.02 3.87 3.09 3.72	RHCP LHCP RHCP LHCP RHCP LHCP 1.17 2.43 2.77 3.32 2.36 3.35 2.14 2.67 1.96 2.44 1.88 3.04 5.00 4.97 4.38 5.05 4.19 4.93 3.94 3.02 3.87 3.09 3.72 3.42	RHCP LHCP RHCP LHCP RHCP LHCP RHCP RHCP <th< td=""></th<>

Figure 7. High-Band Antenna Gain (dBic)

couplers to provide self test capability. The circuit schematic is shown in Figure 8. The antennas are configured on the rear bulkhead of the spacecraft to provide for good axial ratio. However, the antennas are set apart by 104° and 76° to eliminate interference with solar panels. The position of the antennas may be noted in Figure 9. The meandering monopole is utilized to create a "longer" electrical length (see Figure 10) for the antenna without increasing the length of the antenna. The actual length of the vertical elements of the antenna is approximately 24° (.1 λ) at 48 MHz. The total length of the meandering monopole is about 110". The extra length increases the efficiency of this extremely short antenna.

3.2 Low Band Antenna as Current Probe on Satellite

The meandering monopole must be physically small to prevent interference from the solar panels. The concept is to use the monopole as a current probe exciting surface currents on the satellite and solar panels. This method is effective because the circumference of the satellite and solar panels are on the order of a wavelength which may lead to resonance. The position of the solar panels is also extremely critical to the axial ratio and gain measurements.

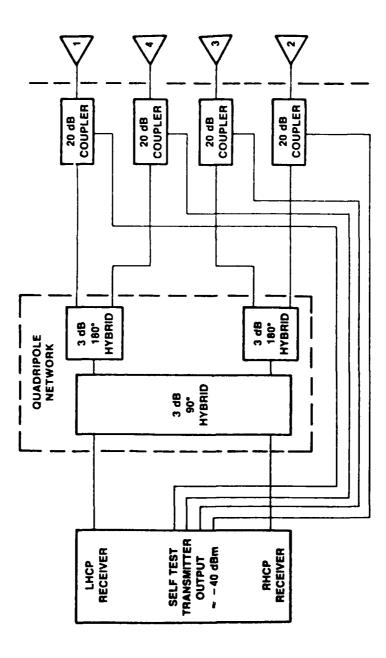


Figure 8. Low Band Antenna Circuit Diagram

STATES AND STATES OF THE STATE

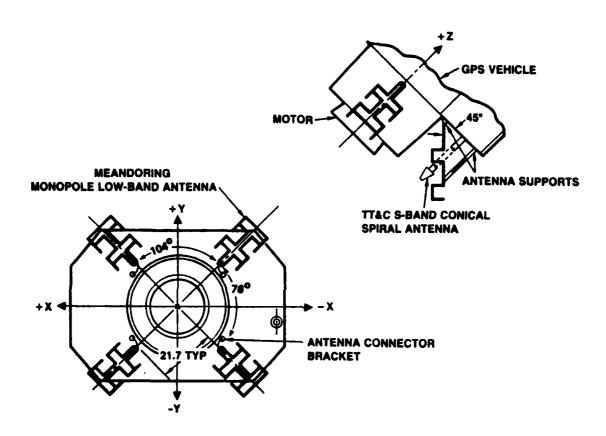


Figure 9. Low-Band Antenna Location

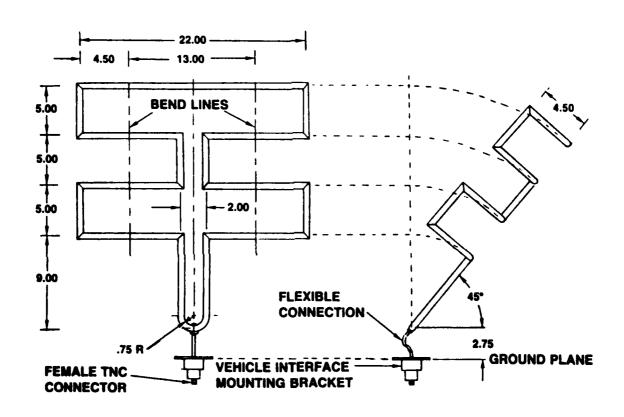


Figure 10. Meandering Monopole Configuration

3.3 Low Band Antenna VSWR

The voltage standing wave ratio was expected to be 6:1. However, the antenna was changed from its original position to allow for clearance of the solar panels. The height of the antenna over the satellite was changed from five inches to 2-3/4". The antennas were also shifted from a separation of ninety degrees apart to that of a 104° and 76° apart, and the monopole was shifted in over the interconnect assembly instead of being two inches away. These conditions resulted in a voltage standing wave ratio which did not meet expectations. At 48 MHz, the VSWR was 12:1 and from 73-75 MHz the VSWR was usually 8:1. The VSWR on the satellite mockup is provided in Figure 11.

3.4 Low Band Antenna Axial Ratio

The meandering monopoles were positioned on the satellite to provide for reception of circular polarized signals with a design goal of 6 dB axial ratio. As seen in Figure 12, the axial ratio was measured at the various solar panel positions and at the on-axis position. Axial ratio was also measured at e = 7° and e = 14° and was slightly degraded. However, they are not discussed in this paper. The low-band antennas act as current probes exciting the satellite and solar panels. With right hand circular polarization, the worst case solar panel positions appears to be when the solar panels are perpendicular and parallel to the

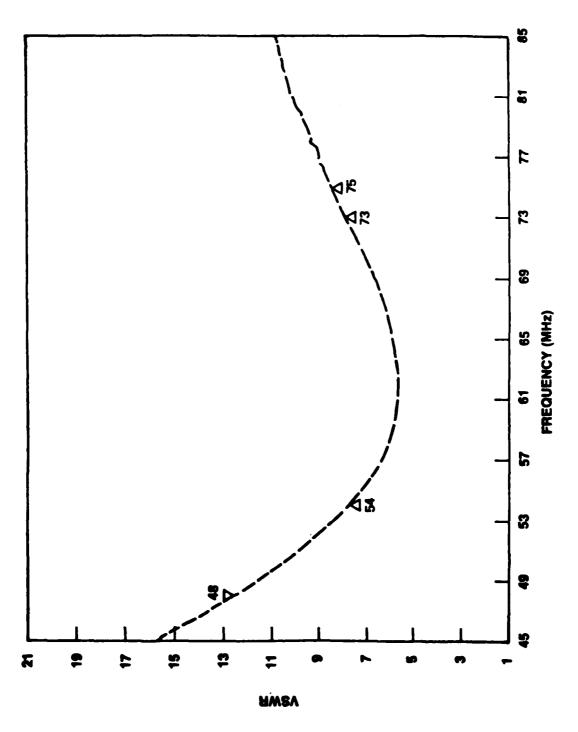


Figure 11. VSWR of Low-Band antenna

FREQ (MHz)	00		45°		90°		135°	
	RHCP	LHCP	RHCP	LHCP	RHCP	LHCP	RHCP	LHCP
48	5.9	3.1	1.35	1.2	6.5	8.55	3.8	5.73
50	4.75	6.4	3.13	1.6	7.8	4.55	2.37	5.7
52	3.65	6.7	3.32	2.4	7.75	4.6	2.35	1.82
54	5.2	7.55	3.9	3.65	7.8	5.8	3.1	3.6
73	7.8	22.1	5.4	7.85	8.25	10.9	4.37	9.7
75	7.6	23.85	4.65	8.25	8.4	10.5	3.92	9.3

Figure 12. Low Band Axial Ratio (dB) at $\theta = 0$

satellite. Best case conditions appear to be with solar panel angles at 45° and 135°. Perhaps this could be due to interaction of the fields at the positions and some of the vectors cancelling out. Left hand circular polarization seemed to follow the general trend as established by RHCP, however, the axial ratios are slighter higher. Also for 73-75 MHz, the axial ratio for solar panel position at 0° is almost linear.

3.5 Low Band Antenna Gain

The gain is shown in Figure 13. For most cases, the gain is within the specification of -6 dBic. 48 MHz has lower gain due to its high VSWR and 73-75 MHz due to the high axial ratio. Solar panel angle seems to have only a slight effect on the gain.

3.6 Low Band Antenna Self Test Verification

The self test verification used the directional couplers in reversed position. The result should be as indicated in Figure 14 for one antenna with varying VSWR versus three identical impedance antennas. With all antennas matched, the self test verification will result in a transmission loss of approximately -55 dB (see Figure 15). With one antenna open, the transmission loss is -35 dB (see Figure 16). Thus a failure of one antenna may be detected. However, if two antennas (or all four antennas) feeding into the same quadrature hybrid(s) fail and have the same

FREQ (MHz)	SP < 0°		SP < 45°		SP ∢ 90°		SP ∢ 135°	
	RHCP	LHCP	RHCP	LHCP	RHCP	LHCP	RHCP	LHCP
48	- 4.40	- 2.26	- 1.97	- 2.09	- 3.48	- 3.47	- 4.06	- 5.34
50	- 0.80	- 1.30	- 1.02	- 0.44	- 2.41	- 1.56	- 2.61	- 2.75
52	- 0.20	- 1.21	- 1.20	- 0.87	1.79	- 1.33	- 2.33	- 3.28
54	- 0.56	- 1.47	– 1.27	- 1.08	- 2.03	- 1.80	- 2.00	- 3.32
<i>7</i> 3	- 3.19	- 4.96	- 2.97	- 3.79	- 2.19	- 2.32	- 5.16	- 4.83
75	- 4.12	- 6.08	- 4.00	- 5.05	- 3.46	- 3.14	- 6.54	- 6.49

Figure 13. Low-Band Antenna Gain (dB_{ic)}

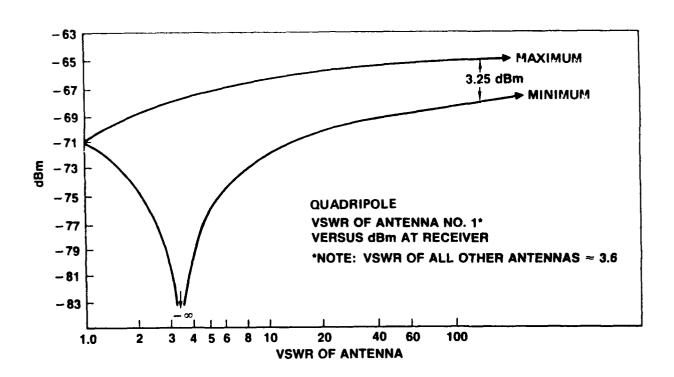


Figure 14. Low-Band Antenna Self-Test Concept for Quadripole Network

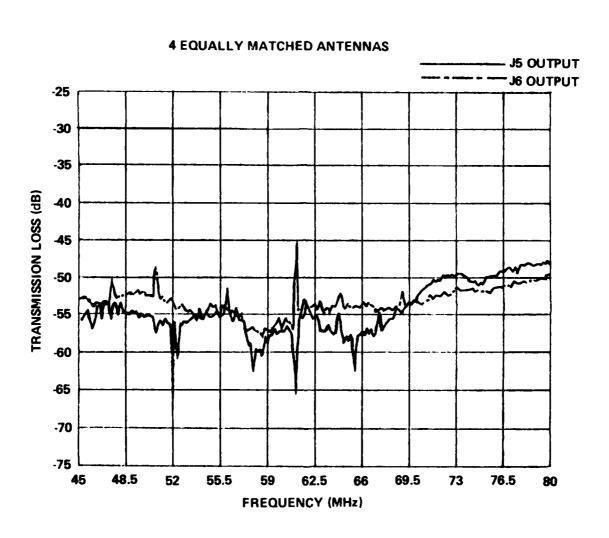


Figure 15. Low-Band Self Test (4 Equally Matched Antennas)

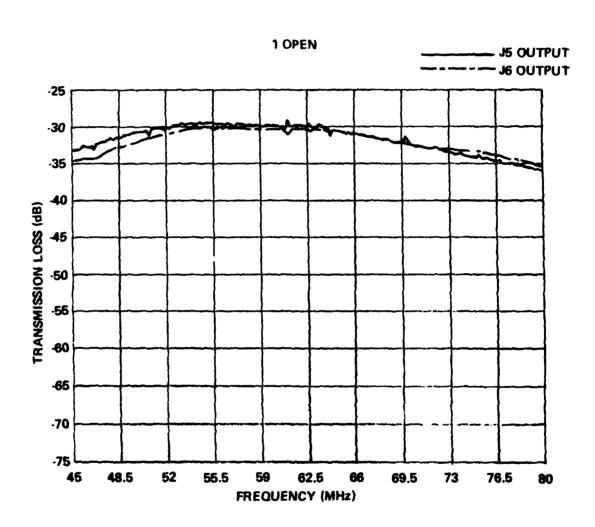


Figure 16. Low-Band Self-Test (1 Open)

resulting impedance, a null condition will also result. The self test verification will verify if any antennas fail in operation with the exception mentioned above.

3.7 Summary of VHF Satellite Antenna System

The high-band and low-band antennas perform well as antenna systems on the satellite. The low-band antenna does not meet the VSWR specification due to its shift in position in order to provide clearance for the solar panels. However, the high and low-band antennas for most cases do meet the system requirements. Several design considerations for large bandwidth antennas at VHF are the shape of the satellite, the position of the solar panels, to provide for clearance, and the position of the antenna above the satellite bulkhead.

ACKNOWLEDGEMENTS

- Design for High Band and Low Band Antenna, by Dr. Alan
 W. Love, Mr. Howard E. King, and Dr. Jimmy L. Wong
- Axial Ratio and Gain Data, and Analysis of Low Band Self Test, provided by Connie W. Thousand.
- 3) Transmission Loss Data for Self Test and VSWR Data, provided by David A. Katko.

A SIMPLE TECHNIQUE TO CORRECT FOR CURVATURE EFFECTS ON CONFORMAL PHASED ARRAYS

John Antonucci
Peter Franchi
Electromagnetic Sciences Division
Rome Air Development Center
Hanscom AFB, MA 01731

ABSTRACT

The curvature of conformal phased array antennas distorts the radiation pattern when the beam is scanned. The distortion occurs because the amplitude taper appears skewed when the beam is scanned. If an antisymmetric taper is added in the proper proportion to a symmetric taper, the symmetry of the original taper can be largely recovered. Typically, the sum and difference aperture illuminations of an antenna can provide the needed symmetric and anti-symmetric functions. A relatively simple and practical technique of using the sum and difference networks in combination to correct for curvature effects is demonstrated. This technique uses a variable power divider to distribute the power in a prescribed proportion at an arbitrary scan angle to the sum and difference channels. The re-distributed power at the elements restores to a large degree the original aperture illumination for the scanned direction. The optimum amount of signal to be distributed to achieve the maximum restoration is found as a function of scan angle and curvature. The technique can be used to improve any sum and difference illuminations. In this paper cosine and sine illumination functions respectively, are used for the sum and difference illuminations to demonstrate the technique.

1. INTRODUCTION

The development of phased array antennas has, for the most part, been for antennas on planar surfaces. The large phased array antennas, for example, Pave Paws, Aegis, Cobra Dane, and Cobra Judy, are planar arrays. Interest has developed in phased arrays on curved surfaces because of the anticipated need for antennas conformal to aircraft. When scanning, curvature has a detrimental effect on the antenna's radiation pattern; the pattern becomes distorted and the sidelobes are increased. The effect is influenced by factors such as the element pattern, the extent of curvature, and the antenna size, and becomes especially pronounced as the scan angle increases. 1,2,3

The purpose of this paper is to demonstrate a relatively simple and practical technique to correct for curvature effects. A straightforward approach to correct the antenna pattern would be to adjust the amplitude and phase of each individual radiating element. This procedure would be unwieldy and highly impractical. Introducing either attenuators or power dividers into the system in order to control the amplitude of each element would greatly increase both rf network and controlling network complexity In addition, cost, errors, failure rate, weight, and space limitation problems would considerably increase. Attenuators would also introduce power loss.

The concept described in this paper is to restore, as much as possible, the original aperture taper by adding, as a function of scan angle, some of the energy in the difference network to the energy in the sum

network. Consideration of the aperture taper in the projected aperture plane gives insight into the cause of the pattern distortion. At scan angles other than zero degrees, the projected aperture taper appears skewed; the greater the scan angle, the greater the skewness. By adding in the proper proportion an anti-symmetric taper to the symmetric taper, the symmetry of the original broadside taper can be largely restored. This correction can be easily implemented with the sum and difference networks of the conformal phased array antenna and a simple variable power divider.

2. EXAMINATION OF FIRST ORDER CURVATURE EFFECTS

2.

The approach in this study is to investigate the effect of curvature on an antenna radiation pattern based on geometrical considerations only. Phenomena, such as creeping waves and mutual coupling will be neglected. The physical model is an array of a fixed number of elements (65 in this case) and a fixed element spacing $(\lambda/2)$. The projection of the curved array on to a straight line perpendicular to the beam direction would result in a projected array which is shorter than the original planar array. The radiating elements on the curved surface are positioned differently in three dimensional space compared to the elements on the planar surface; this difference distorts the wavefront from the equivalent plane surface thereby distorting also the radiation pattern. Primarily, this first order effect on the close-in sidelobes will be addressed in this paper. Grating lobe effects will not be examined.

Of the different types of aperture illuminations, only one will be considered in order to demonstrate the effect of curvature and the

correction technique. The aperture will have a cosine illumination with each element having a cos^{1.5} (Y) pattern, where Y is a general angular variable. This element pattern approximates measured array element patterns and is accurate for patch radiators, narrow slots, or dipoles on a cylinder in which the E-field is along the cylindrical axis. Blockage effects are included. The element radiates only up to the line drawn from it through the next succeeding element (very nearly the tangent line). Although a section of a ring array is being investigated, the results apply to the principle plane cut of a section of a cylindrical array formed by the three dimensional extension of the ring array. There are no cross polarization considerations in this model.

Figure 1 demonstrates a cosine aperture illumination (showing nine elements) which changes at a scan angle, θ_0 . In the broadside direction, the taper is a slightly distorted, but symmetrical projection of a cos (π n/K) aperture amplitude distribution for the sum pattern, where n is the element number in which the center element is zero, and K is the total number of element spacings. At the scan angle, θ_0 , the figure shows how the taper becomes skewed due to the displaced positions of the elements along the line of projection. For example, the center element's position is no longer at the center of the projection line. The center element retains the peak amplitude value of the cosine taper, and therefore, the maximum amplitude is shifted off center. The other elements follow accordingly. In this manner the original taper becomes skewed. Figure 2 depicts the same phenomenon taking place for a $\sin(2\pi$ n/K) amplitude

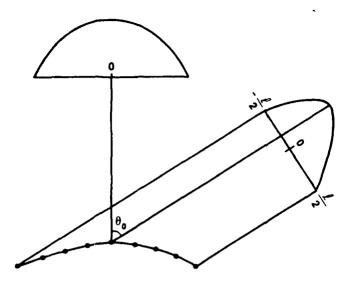


Figure 1. Cosine aperture illumination on a conformal phased array antenna. At the scan angle, θ_0 , the illumination becomes skewed.

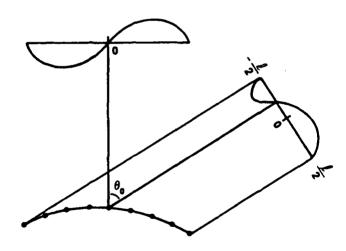


Figure 2. Sine aperture illumination on a conformal phased array antenna. At the scan angle, θ_0 , the illumination becomes skewed.

distribution for the difference pattern. As the scan angle increases, or as S/R, S being the surface length, and R being the radius of curvature, increases, the center element is shifted further off center and the asymmetry increases. This distance off center serves as an indicator of distortion. The above discussion dealt with the dependence of the field at the aperture due only to excitation coefficients of the elements and not to their individual patterns. The element pattern must, however, also be included in order to obtain the total field. Therefore, the general discussion of the field at the aperture would include a multiplying factor, Ae, which is the amplitude of the element pattern and is a function of scan angle.

Figure 3 shows, for an arbitrary scan angle, the position of the elements on the projection plane and the distortion of the amplitude taper as compared to a cosine illumination function in that plane. The center element is at the origin of the x, y coordinate system, and the other elements are numbered accordingly. The cosine value of the nth element is $\cos(\pi \ n/K)$ where, for convenience, the total number of elements, K+1, is chosen to be odd. The distance of the nth element along the x axis is found to be given by the following equation:

$$X_n = 2R \sin(ns/2R) \sin(\pi/2 - \theta + ns/2R)$$
 (1)

where R is the radius of curvature, θ is the scan angle, and s is the surface length between two consecutive elements. A plot of X_n versus the $\cos(\pi n/K)$ illumination (the peak amplitude being normalized to one)

reveals the kind of distortion which is depicted in Figure 3. The same type of distortion argument holds for the difference function, which is given by $\sin(2\pi n/K)$. This is shown in Figure 4. The cosine curve in the projection plane is shown in the X', Y' coordinate system. The cosine curve here is given by:

$$Y' = \cos(\pi X'/2) \tag{2}$$

$$Y' = \cos[\pi(X_n - h)/\ell]$$
 (3)

where

$$h = R[1 - \cos(Ks/2R)] \sin \theta \tag{4}$$

$$\ell = 2R \sin(Ks/2R) \cos \theta \tag{5}$$

h being the distance the center element shifts off of the geometrical center, & being the length of the array in the projection plane.

There is one more contributor to the distortion of the radiation pattern. It is the change of the density of the elements in the projection plane. This causes a change in the field density. Increasing the element density is equivalent to increasing the field that would otherwise be present if the elements were uniformly spaced. Consider the field of the nth element to be E(n), and the effective field E'(n). F(n) will be referred to as the density function and is given by E'(n)/E(n) or:

$$F(n) = 2\ell/K(X_{n+1} - X_{n-1})$$
 (6)

with X_{n+1} and X_{n-1} defined by equation 1.

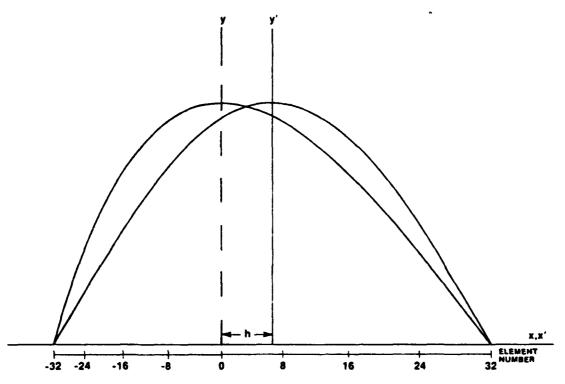


Figure 3. Distortion in the projection plane of cosine amplitude taper on curved surface.

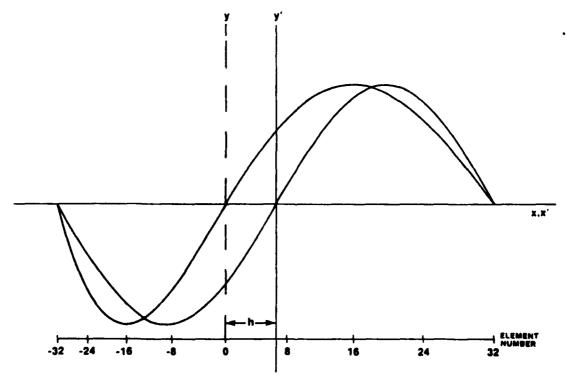
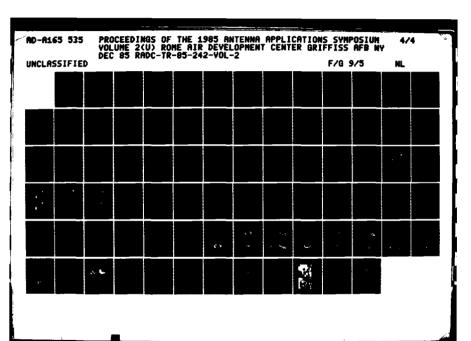


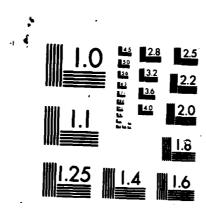
Figure 4. Distortion in the projection plane of sin 27 amplitude taper on curved surface.

The effective amplitude taper in the projection plane is $F(n) \ A_e \ cos(\pi n/K)$

RESTORATION OF THE BROADSIDE APERTURE TAPER

The cos (γ) curve and the sin (2γ) curve are both distorted in the projection plane. By adding these two functions, the original cosine taper can be approximated in the projected plane. This addition is accomplished by using the sum port and difference port simultaneously. The power is distributed, without loss, by a variable power divider. 4 The idea behind a variable power divider is to split the signal entering in one arm and then, by phase adjustments, control the amount of power going into its two output ports. Each port is part of a network which generates across the array, a $\cos (\gamma)$ and a $\sin (2\gamma)$ distribution respectively. Figure 5 shows the variable power divider in the antenna system. The signal from the sum port, Σ , is distributed between the sum and difference ports, Σ' , and Δ' , respectively. A portion of the signal in the difference network is added, at the elements, to the signal from the sum network. For the receive mode, the principle of reciprocity applies. The optimum fraction of power to be distributed to each port can be found that achieves a best fit to the cos (Y) taper in the projection plane at a particular scan angle. Generally, if A and B are designated the amplitude of the energies in the sum and difference ports respectively, then A and B will be chosen such that A cos (γ) + B sin (2γ) approximates cos (Y'), where Y' is the variable in the projection plane. The best





MICROCOPY RESOLUTION TEST CHART
**ATIONAL RUPEBLE OF STANDARDS-1963-A

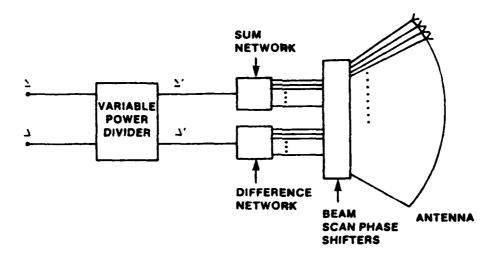


Figure 5. Variable power divider incorporated into the antenna system.

fit would be to obtain the minimum error between the shape of the corrected curve and the undistorted cosine curve. Since we are matching curve
shapes, the curves are to be normalized; the corrected curve is to be
normalized to one. The difference between the two curves at the nth
point is expressed by:

$$\delta_{\rm n} = G(B)F(n)A_{\rm e}[A\cos(\pi n/K) + B\sin(2\pi n/K)] - \cos(\pi X^{\rm t}/t)$$
 (7)

G(B) is the normalizing factor, and varies with B.

$$G(B) = [1/[F(n)A_e(A cos(\pi n/K) + B sin(2\pi n/K))]]_{max}$$
 (8)

The constraint in the addition of the two networks is that the total power remains constant. If the input power is normalized to one, then

$$A^2 + B^2 = 1 (9)$$

9.

Ultimately, the equation used to match the distorted curve to a cosine curve with uniformly spaced elements is the following:

$$\delta_{n} = G(B)F(n)A_{e}[\sqrt{1-B^{2}}\cos(\pi n/K) + B\sin(2\pi n/K)] - \cos[\pi(X_{n}-h)/\ell]$$
 (10)

The total deviation between the two curves is the sum of the δ_n 's over all n. Since the absolute value of δ_n is of interest, it is mathematically convenient to use δ_n^2 instead of δ_n . The value to be calculated is the sum of the squares of the deviations, ϵ , which is defined as:

$$\varepsilon = \sum_{n=-K/2}^{K/2} \delta_n^2 \tag{11}$$

Taking $\delta \varepsilon / \delta B = 0$ yields B_0 , the value of B for which ε is a minimum. The values of B_0 as a function of scan angle, θ , with S/R as a parameter, and for A_e equal to $\cos^{*75}\theta$ (a cosine to the 1.5 power radiation pattern) are shown in Table 1. There were no values chosen in which element blockage was present. Blockage occurs according to the following formula:

$$\theta_{\rm B} > \pi/2 - S/2R + s/2R \tag{12}$$

Since, when S/R = 2, $(S = 32\lambda, R = 16\lambda, s = \lambda/2)$ blockage occurs at 33.6° , the case of S/R = 2 and $\theta = 40^{\circ}$ was not used. Figure 6 shows how the error, ε , varies with scan angle for particular values of S/R. The graph demonstrates the extent of which the error is reduced by introducing

10.

0 °	B _o		
	S = 1.07	S/R = 1.6	S/R = 2
20 °	.105	.169	.227
.30°	.165	.264	.351
40°	.238	.376	

Table 1. Correction factor, B, as a function of scan angle, θ_0 and the curvature factor, S/R, for the cosine to the 1.5 power element radiation pattern case.

the correction. When there is no correction, or B_0 equals zero, it is observed that the curve of ε versus θ follows approximately a $\tan^2\theta$ curve. This dependency is to a large degree verified by the graph in Figure 6. The equation is approximate, but reasonably accurate. It shows the variation of pattern distortion as the scan angle is changed. The solid curve shows the extent of the uncorrected amplitude taper error, which, in turn indicates the degree of distortion of the radiation pattern. The dashed curve is the residual error after correction. Both the uncorrected and the corrected error at broadside are finite because the broadside curvature effects were not readjusted initially.

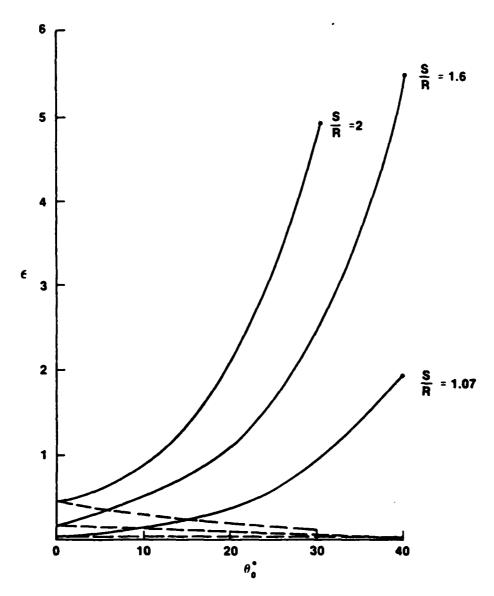


Figure 6. Error, ε , versus scan angle, θ .

4. CURVATURE EFFECTS ON RADIATION PATTERN

The power radiated at an arbitrary scan angle, θ_0 , can be obtained by considering the scan angle direction of each element, and taking into account the path length difference of each element. The E-field in the scan angle direction, θ_0 , is:

$$E(\theta) = \sum_{n=-K/2}^{K/2} A_e(\theta_o) A_n e^{j\phi_n} e^{-jkz_n(\theta_o)}$$
(13)

where $A_e(\theta_0)$ is the nth element's amplitude due to the element radiation pattern in the direction of $\theta_0 \bullet$

$$A_{e}(\theta_{o}) = \cos^{p}(\theta_{o} - ns/R)$$
 (14)

p being a constant defining the element pattern. A_n and ϕ_n are the magnitude and phase respectively of the nth element's excitation coefficient. A beam is steered to the θ_0 direction by having ϕ_n equal to $kZ_n(\theta_0)$. The value of $Z_n(\theta_0)$ is:

$$Z_{n}(\theta_{0}) = 2R \sin(ns/2R) \cos(\pi/2 - \theta_{0} + ns/2R)$$
 (15)

The E-field in the θ direction, relative to a θ_0 scan angle direction is:

$$E(\theta) = \sum_{n=-K/2}^{K/2} A_e(\theta) A_n e^{jkz} n^{(\theta_0)} e^{-jkz} n^{(\theta)}$$
(16)

The value of the power, P, is obtained by using equation (16) in the following equation:

The effect of curvature on the radiation pattern is predominantly a function of θ_0 , ns/R, and consequently, Ks/R, or S/R, the array's subtended angle. To demonstrate the effect of curvature, the radiation pattern, P, is obtained as a function of S/R (with θ_0 constant) and as a function of θ_0 (with S/R constant). Both the number of elements, K + 1, and the element spacing, s, are held constant.

A reasonable choice for the element pattern is p=1.5 since a patch radiator, a slot, or a dipole in an array exhibits very nearly this dependency. Figures 7a, 7b, and 7c show the radiation plots using a $\cos^{1.5}(\gamma)$ element pattern and cosine aperture taper for various values of scan angle, θ_0 , and subtended angle, S/R. The number of elements used is 65, the element spacing is $\lambda/2$, and λ is .1 meters. The correction is most pronounced as the scan angle is increased and/or the subtended angle is increased. The figures show the increase of the near-in sidelobe levels as a function of scan angle, and subtended angle; the uncorrected and corrected patterns are shown. The improvement of the distorted pattern is substantial, showing the correction works well. The pattern is very much restored in the near in sidelobes. Moreover, there is no detriment in the corrected pattern in the rest of the 360° coverage. There is a greater improvement in the larger scan angles, as was predicted from the discussion on errors.

The difference pattern was not discussed earlier because it is not a primary concern. However, the application of the correction for the

optimum sum pattern results in an improvement of the difference pattern.

The crucial criterion of a difference pattern is the mainbeam null depth;

the deeper the mainbeam null, the better the pattern. One example of the

improvement of the difference pattern is shown in Figure 8.

Table (2) depicts the improvement of the mainbeam null depth which can be seen to be significant. The improvement decreases slowly as the curvature increases. There is not a significant variation with a change of the scan angle. A better difference pattern can be obtained by sacrificing some of the correction of the sum pattern.

o°	S R	MAINBEAM NULL (-dB)		IMPROVEMENT
		UNCORRECTED PATTERN	CORRECTED PATTERN	IN dB
20°	1.07	23.20	30.66	7.46
	1.6	19.70	25.72	6.02
	2	17.78	22.50	4.72
30°	1.07	19.71	27.35	7.64
	1.6	16.20	22.40	6.20
	2	14.24	19.27	5.03
40°	1.07	17.24	24.92	7.68
	1.06	13.68	20.06	6.38

Table 2. Values of mainbeam null of uncorrected and corrected difference patterns as a function of scan angle, and subtended angle. A cosine to the 1.5 power element pattern was used.

こうですっている。最初ななのもなる。最初ではいいというと

5. CONCLUSION

The results demonstrate the value of the correction technique. It is a simple, practical technique expending no additional power and yet offers quite a high level of improvement. It is worthwhile to compare an amplitude correction curve with a result obtained by Ludwig. 3 Ludwig used an iterative algorithm in which the complex weights of each element was adjusted in order to synthesize an ideal pattern. Although he used a Taylor aperture illumination, the two results are still, to some extent, comparable. For his case, using a 40° scan angle and S/R = 0.8, the peak of the corrected amplitude taper shifts, in terms of his array, by about three and one half elements. Using our technique, for $\theta_0 = 40^{\circ}$ and S/R = 1.07, there is approximately the same shift. The realization of the iterative algorithm in an actual system is highly improbable, but our corrector can be easily implemented. We demonstrated our technique using a cosine aperture taper. If a Taylor illumination was employed, we would use a Taylor, Bayliss addition. Generally, any symmetric and antisymmetric functions are to be combined. Another study may be to use the technique in order to increase the power in the mainbeam for large scan angles. In that way, the extent of large angle scanning can be augmented and made possible by the existence of curvature.

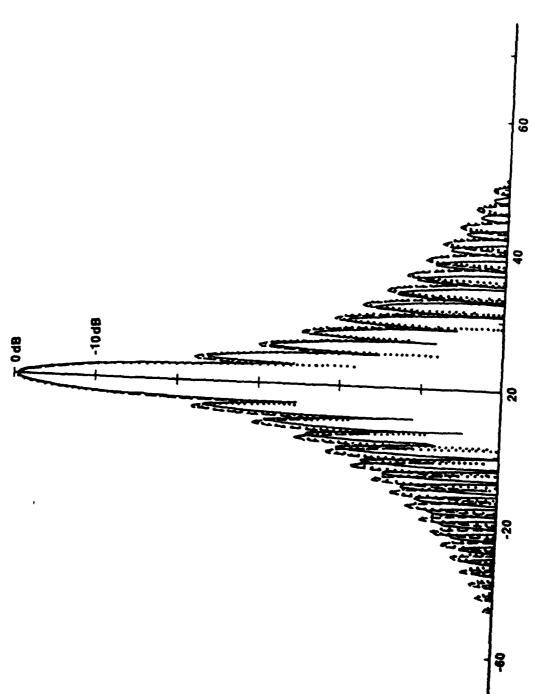
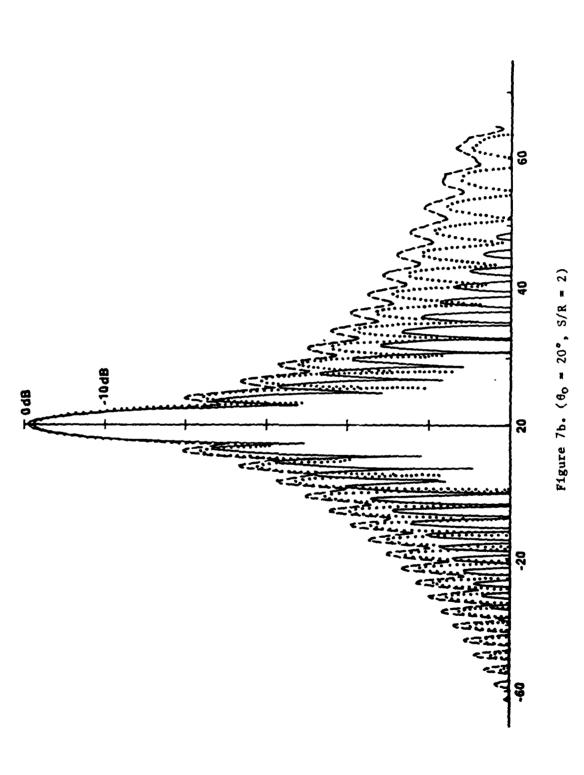
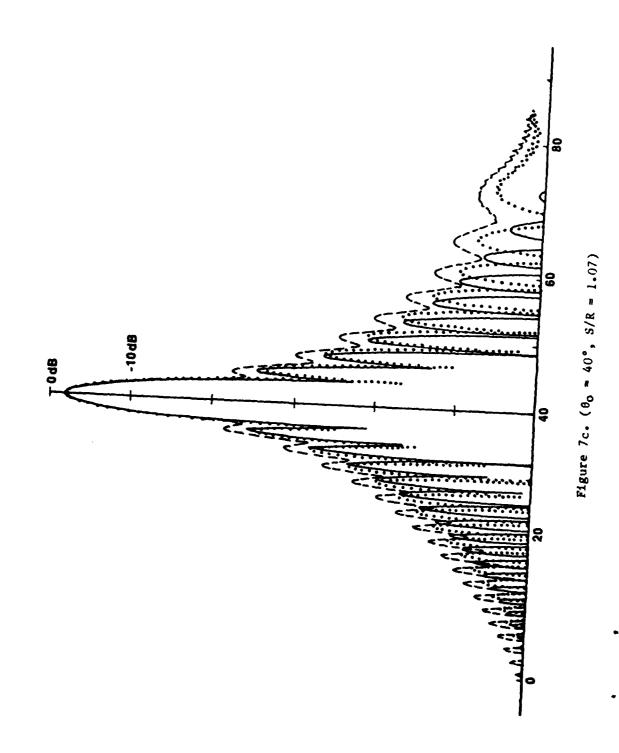
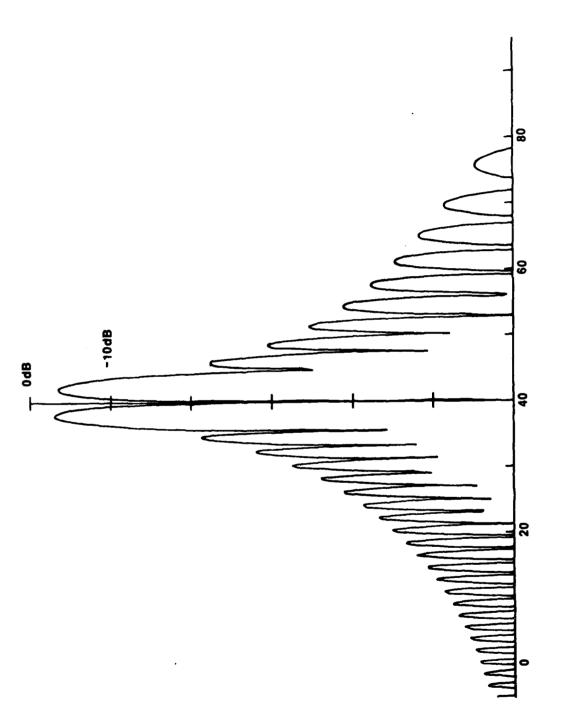


Figure 7a. (0 = 20°, S/R = 1.07)







Pigure 8a. ($\theta_0 = 40^{\circ}$. The planar array)

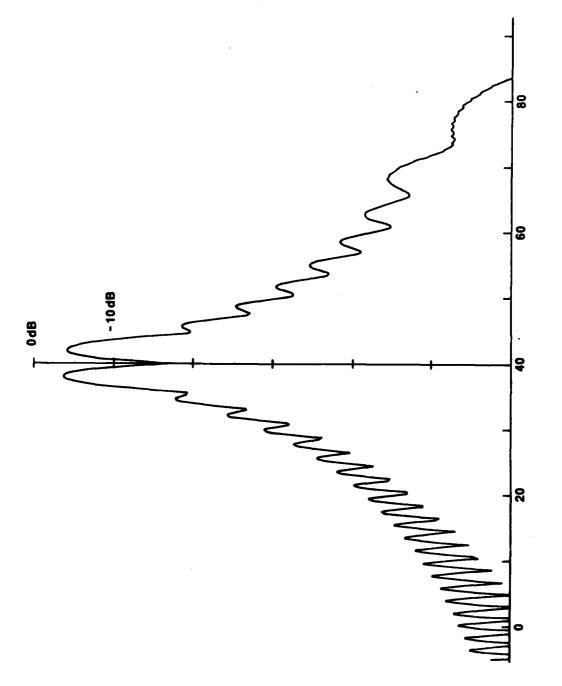


Figure 8b. (0, = 40°, S/R = 1.0

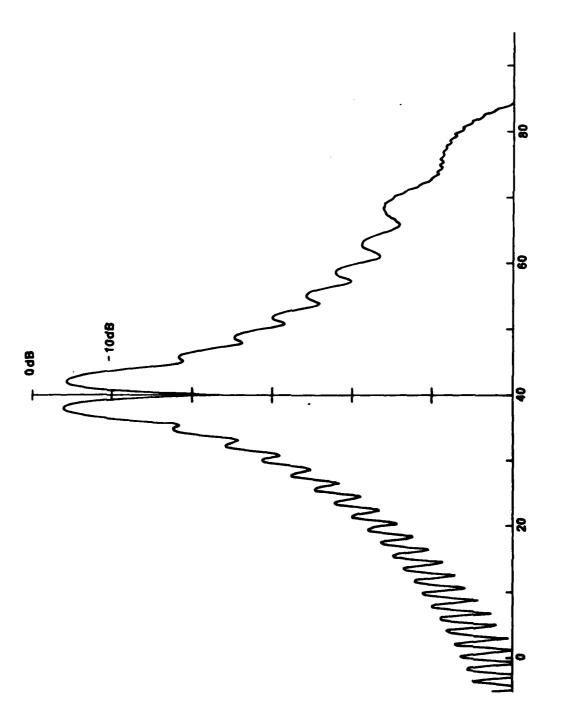


Figure 8c. ($\theta_0 = 40^{\circ}$, S/R = 1.07. The corrected pattern.)

References

- 1. Wojtowicz, J., Ramsey, K.G., and Fontana, T. (1963) Conformal Array Analysis, Proceedings of the 1983 Antenna Applications Symposium, RADC-TR-84-52, Vol. 2.
- 2. Herper, J.C., Hessel, A., and Tomasic, B. Element Pattern of an Axial Dipole in a Cylindrical Phased Array, Part 1: Theory, IEEE Trans., AP-33, No. 3, March 1985.
- 3. Ludwig, A.C. (1985) Antenna Curvature Analysis, RADC-TR-85-131.
- 4. Rudge, A.W., Milne, K., Oliver, A.D., and Knight, P. (1982) The

 Handbook of Antenna Design, Vol. 1, p. 490, Peter Peregrinus Ltd.

 London, U.K.

OPTIMIZATION FOR ANTENNA ARRAYS IN AN ARBITRARY INTERFERENCE ENVIRONMENT

Andrew Y. Piatnicia† and Yuen T. Lo University of Illinois at Urbana-Champaign Electromagnetics Laboratory

ABSTRACT

A method for maximizing the signal-to-interference ratio of an antenna array while maximizing the directivity has been developed in this paper. This method is formulated for an arbitrary array in an arbitrary interference environment. The objective is achieved by defining a null space of a matrix A associated with the interference power. Numerical examples for planar arrays of short monopoles subjected to point and distributed interference sources illustrate the method.

1. INTRODUCTION

An antenna system when used for receiving a desired signal is facing in reality a hostile environment, which is usually contaminated with noises, interferences, and even deliberately made jamming signals. In a communication center, such as a shipboard system in particular, many antennas, supporting structures, and other obstacles are jampacked in a small space. All of them can cause a serious deterioration of the intended signal quality. In fact, the signal wave reflected from the turbulent

Now at Westinghouse Electric Corporation, Baltimore, Maryland

water or moving objects can reach the antenna and have an undesirable fading effect on the incoming signal directly from the transmitter. Even for transmitting, it may also be desirable to reduce the antenna radiation below a very low level in some directions. Following the work by Lo, Lee, and Lee on the maximization of the signal-to-noise ratio (SNR), this paper considers the optimization problem for an arbitrary array in an aribtrary interference environment, such that the signal-to-interference ratio (SIR) is maximized.

The interference source can be distributed over a finite angular sector, such as the reflected signal from the water or a large obstacle, or concentrated in a single direction as if it were a point source. The latter is a special case of the former, when the sector is vanishingly small, and the Dirac delta-function can be used to describe its distribution. But this difference can result in a significant difference in the property of a matrix (A) associated with the received interference power. A can be positive definite or positive semidefinite. In reality, there is no true point source in the mathematical sense, and, therefore, the division of these two types of interferences is somewhat artificial and not sharply defined. Numerical results for these interferences can be meaningfully interpreted, only if the computer accuracy and system noise are known beforehand. This problem is addressed here.

For point interference sources, it is well known that the array should be designed to have nulls in all the interference directions. In a linear array with equally spaced elements, this is easily accomplished by imposing certain zeros of the polynomial which represents the array pattern function. This approach is used by Drane and McIlvenna², who, in addition, maximized the directivity (D) with the remaining degrees of freedom of the problem. However, for a more general case, such as a two- or three-dimensional array with nonuniform spacings and with the interferences of both types simultaneously distributed in space, this problem becomes much more complicated. The objective of this paper is to provide solutions to these problems with a few typical numerical examples.

2. FORMULATION

The problem discussed here is that of finding the excitations (J>) for an antenna array, such that the signal to interference power ratio (SIR) is optimum. The equivalent problem of finding the optimum signal-to-noise power ratio has already been formulated by Lo et al. Their formulation will be followed here. In addition, there are cases in which the interference can be reduced to zero (or SIR = ∞), and then it is obviously desirable to find the J>, for which the directivity (D) is maximum, with the condition that SIR = ∞ . (It will be seen later that, in practice, SIR = ∞ may mean that it is numerically

several orders of magnitude larger than all other quantities under consideration.) All the derivations will be made for an arbitrary array and for any arbitrarily distributed interference, which can be coherent, incoherent, or a combination thereof.

Following Lo et al., let $\{J = (J_1, \ldots, J_n), \text{ where } J_i \text{ is} \}$ the excitation, excluding a cophase factor, of the ith antenna element located at (x_i, y_i, z_i) . The array factor,

$$P(\theta,\phi) = \sum_{i=1}^{n} J_{i} \exp j(\psi_{i} - \psi_{i}^{0})$$
 (1)

where

 $\psi_i = x \cos \phi \sin \theta + y \sin \phi \sin \theta + z \cos \theta$ and the ith element cophasal factor

$$\psi_{\mathbf{i}}^{o} = x_{\mathbf{i}} \cos \phi_{\mathbf{o}} \sin \theta_{\mathbf{o}} + y_{\mathbf{i}} \sin \phi_{\mathbf{o}} \sin \theta_{\mathbf{o}} + z_{\mathbf{i}} \cos \theta_{\mathbf{o}}$$

The signal direction is specified by the angles θ_0 and ϕ_0 .

Thus, the signal power is proportional to $\langle JCJ^*\rangle$, where the product $V_1^{><}V_1^{-}$ defines the matrix C with $\langle V_1^{-} = (1, \ldots, 1)$.

* indicates the complex conjugate.

$$SIR = \langle JCJ^* \rangle / \langle JAJ^* \rangle$$

where the denominator is proportional t_0 the interference power. For incoherent interference,

$$\langle JAJ^{*}\rangle = \frac{1}{4\pi} \int_{A\pi} |P(\theta,\phi)|^{2} |g(\theta,\phi)|^{2} I(\theta,\phi) d\Omega \qquad (2)$$

where $I(\theta,\phi)$ is the magnitude of the interference power density. In this case,

$$A = \frac{1}{4\pi} \int_{4\pi} V^{*} > \langle VI(\theta, \phi) | g(\theta, \phi) |^{2} d\Omega$$
 (3)

where $\langle V = (\exp j(\psi_1^o - \psi_1), ..., \exp j(\psi_n^o - \psi_n)).$

The formulation for coherent interference is similar. The major difference between coherent and incoherent interferences is that the integration is performed before or after forming the product $V^*>< V$. In the case in which the interference consists of both types or several coherent regions but incoherent among the regions, incorporating them all into A is a straightforward matter. The directivity can be found from SIR by setting $I(\theta,\phi)=1$ for all θ and ϕ . For this case, A is denoted by B. From the definition, C, A, and B are hermitian. In fact, C is positive semidefinite and B is positive definite. A can be positive definite or positive semidefinite, depending on the interference distribution. This is explained in the next chapter.

3. SOLUTION

In general, the incoherent interference distributions, which will be considered numerically in Chapter 4, can be classified into the following four different types:

1 -- Interference over a non-vanishingly small solid angle region;

- 2 -- sliced interference source from ϕ_1 to ϕ_2 with a fixed θ_1 or from θ_1 to θ_2 for a fixed ϕ_1 ;
- 3 -- point interference source; and
- 4 -- any combination of 1, 2, and 3.

Interferences 2 and 3 are really special cases of 1, as the distribution in one of the angular regions becomes a delta function. For example, interference 2 is simply type 1 with a delta function distribution, $\delta(\theta-\theta_{\rm fixed})$ or $\delta(\phi-\phi_{\rm fixed})$. Similarly, interference 3 is type 1 with delta functions $\delta(\theta-\theta_{\rm fixed})$ $\delta(\phi-\phi_{\rm fixed})$.

Since the pattern function can have nulls, for interferences of type 2 or 3, it is possible to design an array with nulls in the directions of those interferences. As a result, for these cases SIR can, theoretically speaking, be infinity. But, in practice, this implies only a very large number. Therefore, an optimum design for those cases should be one with directivity in the signal direction maximized, while the nulls in the prescribed interference directions are maintained. The number and the directions of nulls an array can have depend on the number of elements as well as on the array geometry. These ideas will be set forth next in the following three cases:

<u>Case 1.</u> When A is positive definite, then the solution of the problem of optimizing SIR is equivalent to that of optimizing the signal-to-noise ratio. This problem has already been solved

のののでのMMMできないという。 新聞のできるとのでは、「これのできるのでは、MMMMM になるのでは、MMMMM です。

by Lo et al., and the solution will be used here. J > for optimum D (DO) is

$$J > = B^{*-1} V_1 > \tag{3}$$

and J> for optimum SIR (SIRO) is

$$J > = A^{*-1} V_1 > \tag{4}$$

Case 2. A is positive definite, but some eigenvalues (λ) of A are so small, as compared with other eigenvalues, that one can treat A as if it were positive semidefinite within the working precision. In doing so, the method developed below for case 3 can be applied.

Case 3. When interference type 2 and/or 3 is present, then A can be positive semidefinite and the interference could be nulled out. As stated above, for practical purposes, this case and case 2 may be found equivalent numerically. This is discussed next.

3.1 Matrix A Positive Semidefinite

Let A be positive semidefinite. This implies that $\langle JAJ^*\rangle$ or equivalently $\langle J^*A^*J\rangle$ can equal zero for some nontrivial $J\rangle$. This means that there exists a subspace of excitation vectors for which SIR = ∞ . It will now be shown that the eigenvectors of A^* which correspond to the zero eigenvalue comprise the basis vectors of the homogeneous solution space of $\langle J^*A^*J\rangle = 0$.

Since A^* is hermitian and positive semidefinite, it has real non-negative eigenvalues, λ_1 , ..., $\lambda_n \geq 0$. Thus, $\langle J_1^*A^*J_1^* \rangle = \langle J_1^*\lambda_1 J_1^* \rangle = \lambda_1 \langle J_1^*J_1^* \rangle$, where $J_1^* \rangle$ is the eigenvector corresponding to λ_1 . For a nontrivial $J_1^* \rangle$, $\lambda_1 \langle J_1^*J_1^* \rangle = 0$, if and only if $\lambda_1^* = 0$. The dimension of the null space of $\langle J_1^*A^*J_1^* \rangle$ equals the multiplicity of the zero eigenvalue λ_1^* . (In practice, one has to decide on an upper bound below which the eigenvalues could be treated as zero. This upper bound could be 10^{-q} , with q set according to the system noise.) But all the eigenvectors are independent. Consequently, the eigenvectors with corresponding eigenvalues of value zero form a basis of the null space. Let the columns of the matrix P be these eigenvectors. Now, any linear combination of these vectors is also a solution to $\langle J_1^*A^*J_2 \rangle = 0$ or $\langle J_1^*A^*J_2 \rangle = 0$. Thus, one can let

$$J\rangle = Py\rangle \tag{5}$$

where y_i , the ith element of y>, is a complex constant by which the eigenvector in the ith column of P is multiplied. Thus, it is meaningful to define the optimum J> to be that which maximizes D under the constraint of SIR = ∞ , i.e., for J> in the subspace spanned by P. In other words, the objective is to determine y> which maximizes

$$D = \frac{\langle yGy^*\rangle}{\langle yKy^*\rangle} \tag{6}$$

where

いたのとの「これのことのなる」というというと言うというとなる。

$$G = P^{t}CP^{*} \tag{7}$$

$$K = P^{t}BP^{*}$$
 (8)

Both matrices K and G are hermitian, and K is positive definite.

The details of obtaining the solution are identical to those already worked out by Lo et al., for the similar problem of optimizing D without constraints. The results are

optimum
$$J > = PK^{*-1}p^{*t}v_{i} >$$
 (9)

and

$$D = \langle v_1 P^* K^{-1} P^t v_1 \rangle$$
 (10)

where $\langle V_1 = (1, ..., 1)$.

4. DISCUSSION OF RESULTS

In the following discussion, A with at least one eigenvalue of the order of magnitude of the rounding unit (for example, 10^{-14} , for the Cyber), will be called positive semidefinite. Otherwise, A will be called positive definite. The computed and graphed absolute values of the array pattens for various interferences along with the computed values of the SIRs and Ds illustrate the capabilities and limitations of the theory discussed in Chapter 3. The arrays considered are in the xy-plane. The array elements are short monopoles (sinθ pattern) over a perfect ground plane and parallel to the z-axis. In addition, they are spaced uniformly with spacings X along the x-axis and Y along the y-axis, all measured in the wavelength λ. The spacings between elements have been kept larger than 0.5λ to avoid the

problems of supergain. The closed-form solution for the elements in B has already been obtained by Lo et al.

$$b_{nm} = b_{mn}^{*} = \frac{1}{2} \exp j(-\psi_{nm}^{o}) \left[\frac{\sin 2\pi \rho_{nm}}{2\pi \rho_{nm}} + \frac{\cos 2\pi \rho_{nm}}{(2\pi \rho_{nm})^{2}} - \frac{\sin 2\pi \rho_{nm}}{(2\pi \rho_{nm})^{3}} \right]$$
for $n < m$ (11)

$$b_{nn} = \frac{1}{3}$$
 (12)

where

$$\psi_{nm}^{O} = 2\pi\rho_{nm} \sin \theta \cos(\phi - \alpha_{nm})$$
 (13)

$$\psi_{nm}^{0} = 2\pi\rho_{nm} \sin \theta_{0} \cos(\phi_{0} - \alpha_{nm})$$

$$\rho_{nm} = \left[(x_{n} - x_{m})^{2} + (y_{n} - y_{m})^{2} \right]^{1/2}$$
(13)

$$\alpha_{nm} = \tan^{-1} \left[(y_n - y_m) / (x_n - x_m) \right], \ 0 \le \alpha_{nm} \le \pi$$
 (15)

The subscripts n and m are referring to the nth and mth antenna elements, respectively. The elements of A are found by numerical integration. Two types of patterns were plotted for each array. The first type represents patterns for an array excited to give the optimum SIR (SIRO) (Equation (4), for A being positive definite), or the optimum D (DO) (Equation (5), for A being positive semidefinite) with the constraint that the received interference power is at a numerically very small value. The second type represents patterns of the same array but excited for maximum D only (Equation (3)). Although, some arrays are subjected to different combinations of interference distributions, only one pattern for the unconstrained DO needs to be plotted. To prevent confusion, these plots do not have interfrence distributions drawn on them. Unless otherwise noted, the plotted patterns are all in the xy-plane, i.e., $\theta=90$ and all angles are in degrees. To show the "nulls" in detail, the central portion is expanded in all plots and the expansion factor can be seen from the scales in the plots. The signal (S) direction has always been set along the positive x-axis, i.e., $\theta_0=90$ and $\phi_0=0$. The signal power has been assumed to equal unity, always. For comparison, SIR and D for uniform excitation (U) have also been calculated for each array.

The information for all the examples considered is summarized in Figures 1 - 3. (All figures have been placed after Chapter 5.) When following the discussion for Figures 4 - 15 to be given later, the use of these figures is recommended. In these figures, sketches of patterns for SIRO or for DO with constraint (depending on which is applicable) are included. All the data under the heading I describe the type of interference the particular array has been subjected to. For example, in Figure 1, in the first column under I, (2-1): 2 and (2-2): 1 stand for type 2 distributions of intensities 2 and 1, respectively, (i.e., they are 2 and 1 times stronger than the signal). The numbers 1 and 2 after the dash are used to denote the regions of interference which are specified by the angles following each intensity value. There are M rows of array

elements with N elements each parallel to the y-axis. The rest of the notations used in Figures 1-3 will become clear in the discussion below.

4.1 Matrix A Positive Definite

Therefore andresses properties between the

In order to demonstrate the versatility of the theory, a 2×10 array subjected to all three types of interference distributions (1,2,3) is considered. The distributions with the results are summarized in Figure l(a). It turns out that SIRO is very good, but D for SIRO is two orders of magnitude smaller than DO. This situation is changed drastically if a type 2 interference of small intensity and wide distribution is added in (Figure l(b)). Now D for SIRO is 80.4 and SIRO = 945.5, which is still much higher than the SIR of 49.1 when D is maximized.

4.2 Matrix A Positive Semidefinite

As discussed before, for some interference distributions, A can have zero as an eigenvalue. Since all computers have a finite accuracy, numerically, how small a quantity can be regarded as zero is a very relevant question. To this end, one needs to decide upon the upper bound (10^{-q}) below which the eigenvalues of A will be treated as zero. At the same time, one must consider that generally the larger the null space of A, the larger the corresponding DO with constraint, as derived from Equation (6). The choices of q = 7, 8, 10 have provided good

results for type 2 (or 3) interferences as discussed below. Clearly, the SIR so obtained depends on q, but for sufficiently large q the dependence can become insignificant. Numerically, the resulting solution can thus be considered as optimum in the sense that the signal is maximum under the constraint that SIR is kept sufficiently large. As before, DO without constraint will be referred to simply as DO.

Figure 7 depicts the pattern for DO with constraint for a 2×10 array subjected to two type 3 interferences. On the one hand, SIRO $\stackrel{?}{=} 10^{15}$, which is much higher than SIR = 53.7 for DO and than SIR = 66.3 for U as shown in Figure 2(a). On the other hand, DO with constraint = 102.3 compares favorably with DO = 138.3, and D = 112.3 for U. For this computation, q = 13 resulted in 18 columns for P in Equation (5). In spite of the fact that DO with constraint is optimum, the asymmetry of the interference distributions was apparently sufficient to shift the main beam a little off the direction of the signal.

In the following example, the element spacing of a 3 \times 20 array is assumed to be 0.6 λ . A type 2 interference of intensity 1000 is distributed from ϕ = 175 to 185 (centered on the negative x-axis) in the θ = 90 plane as shown in Figures 2(b) and 8. Thus, the signal and the type 2 distribution are in the same plane. Because of the symmetry in this example, the pattern is

symmetric as seen in Figure 8. The inference is virtually nulled out completely (SIR $\stackrel{*}{=} 10^{12}$). A clearer view of this is shown in the magnified center portion of the pattern in Figure 8. D with constraint is 214.6, a value that approaches DO = 222.1 (Figure 2(b)), leaving D = 144.6 for U far behind. Again, the SIRs for DO and U (8.3 and 0.6) are miniscule by comparison with SIRO of 10^{12} . For this example, q = 10 with a resulting 51 columns for P.

One may be inclined to think that the high SIRO in the previous example was only possible because the type 2 interference was highly confined. This is not the case. Figure 10 shows the pattern for DO with constraint for a 3 \times 22 array that is subjected to a type 2 interference distributed over the entire second and third quadrants in the θ = 90 plane as indicated in Figure 3(a). It turns out that SIRO is more than ten million times larger than the SIRs for DO and U, while the Ds for all three excitations are on the same order of magnitude (Figure 3(a)). For this case, q = 8, resulting in 19 columns for P.

As a final example, we consider, for academic interest, a 3×22 array in an environment with type 2 interference of an intensity 10^3 times stronger than that of the signal, and distributed in the region θ = -5 to +5 at θ = 80. Recall that the signal is always assumed to be in the ϕ = 0 and θ = 90 direction

which is close to the interference. The results for optimum SIR as well as those for optimum D are summarized in Figure 3(b) with detailed patterns shown in Figures 12 and 13. As it should be. SIRO = 10 is ten orders larger than the SIR of 0.26 for the DO case and 0.25 for the U case. However, the D associated with SIRO is only 2.9, substantially smaller than DO = 481.6 and D =346.5 for the uniform excitation. It is of particular interest to examine the patterns in the $\theta = 90$ plane for two cases: SIRO and DO as shown in Figures 12 and 13. For the former, a large lobe (actually the main beam) is directed in the interferencefree region in the left half space, and in contrast a much smaller lobe is in the signal direction. This paradoxical result can be explained by the fact that the integrals in SIR, being weighted by the zero interference intensity in the left half space, can still result in a very large value of SIR. For Figure 13 where D is optimum, the main beam is pointed to the signal and also to the nearby interference, thus resulting in, not surprisingly, a high value of D but a very small value of SIR. This is more clearly seen in Figures 14 and 15 which are the patterns in the conical cut with $\theta = 80$. The main beam is practically lying completely in the interference region. One should not be surprised by these results since optimizing SIR is a problem totally different from that for optimizing D, and one does not necessarily imply the other, particularly when the

signal and interference are close to each other. However, to differentiate them more effectively, a larger array should be used. On the other hand, to avoid a large back lobe shown in Figure 12, a background interference (or noise) in the left half space should be assumed.

In the above study, q was chosen to be 7 which results in 57 columns for P. One may wonder what would happen to the results if q is decreased. It turns out that a choice of q = 2 increases the number of columns in P to 60. This increase produces a marginal change in DO with constraint, from 2.9 to 2.95, but reduces SIRO dramatically from 10 to 3277. Thus, for a good approximate solution to SIRO, as stated earlier, a sufficiently large q should be used in order to obtain a better "null" space so that the interference contribution can be kept small.

One may also wonder, whether or not it is feasible to compute accurately the eigenvectors that comprise the columns of P. It may not be, considering that the corresponding eigenvalues are very small. Fortunately, one can compute accurately the eigenvectors associated with large eigenvalues, say larger than 10^{-q} . Then the null space can be accurately determined from the vectors orthogonal to these eigenvectors.

4.3 Sensitivity Test for Optimum Excitations

The sensitivity of the optimum excitation (J_0) giving SIRO was tested for the three examples shown in Figures 2(a), 2(b), and 3(a) by injecting a random error uniformly distributed between -3% to +3% into each component of J_0 >, real and imaginary parts, independently. The perturbed SIRO is referred to as PSIRO. For completeness, J> for DO was perturbed similarly, resulting in a perturbed DO (PDO). The results are shown in Table 1. Clearly, the PSIROs are very much smaller than the SIROs, indicating that the astronomically large value of SIRO in all the examples should not be taken seriously. However, the PSIROs are still much larger than the SIRs for PDO or DO. Thus, the ideal values of SIRO may be unobtainable in reality, but the optimum excitation J_0 can still give a much superior SIR as compared with other excitations. As expected, the random errors do not affect other quantities significantly because of the large element spacings used.

5. CONCLUSION

An optimization technique for arbitrary arrays in arbitrary interference environments has been developed.

The interference environments can be generally separated into two kinds: those consisting of interference distributions that cannot be nulled out completely, and those that can. For

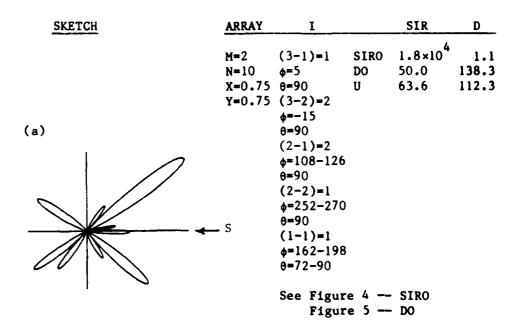
TABLE 1. Results of Perturbing the Real and Imaginary Components of J> for SIRO and DO by a Uniformly Distributed Error of a Maximum of ± 3%.

	SIR (Figure 2(a))	D
SIRO PSIRO PDO	$ \begin{array}{c} 10^{15} \\ 1.7 \times 10^{5} \\ 3.2 \times 10^{5} \\ 15.1 \times 10^{5} \\ 53.6 \\ 54.1 \\ 54.0 \end{array} $	102.3 101.9 102.6 102.1 138.2 138.2
	SIR (Figure 2(b))	D
SIRO PSIRO PDO	10 ¹² 7930.0 2510.0 4540.0 7.8 8.3 8.5	214.6 214.3 214.5 214.5 221.9 221.9 222.0
	SIR (Figure 3(a))	D
SIRO PSIRO	10 ⁹ 3399.0 5607.0 3848.0	364.4 363.6 364.4 364.3
PDO	35.1 34.6 35.6	482.8 482.9 482.9

the first kind, the optimum excitation for maximum signal-tointerference ratio (SIR) can be determined from the conjugate
inverse of a positive definite matrix A associated with the
interference distribution. For the second kind, since the
interference can be nulled out, the optimum excitation is
defined to be one which maximizes D (i.e., the desired signal)
under the constraint that the interference remains nulled out.

The method used consists of first finding the null space eigenvectors of a positive semidefinite matrix A, and then determining the excitation vector in this space which maximizes D. In practice, the type of interference that can be "nulled out" (i.e., brought below a prescribed insignificantly low level) need not be limited to point sources, but can be distributed over a sufficiently small solid angle. Thus, at the heart of the method described here lies a decision about which eigenvalue of A can be treated as if it were zero. This decision should be made based on the overall system noise. Examples for interference distributions of various types have been examined numerically. The sensitivity of SIR due to random errors in the excitations has been tested, as well. The results show clearly that the optimization of SIR and the optimization of D are in general incompatible. In fact, the maximized SIR can be many orders of magnitude larger than the SIR obtained if only D is maximized. Therefore, the criterion for designing a receiving array is different from that for designing a transmitting array.

ことのは、これでは、これのでは、これのでは、これがないのでは、これがないのでは、これのないのでは、これのないのでは、これのないのでは、これのないのでは、これのないのでは、これのないのでは、これのないのでは、



	ARRAY	I	· • · • · •	SIR	D
	**	(3-1)="	SIRO	945.5	80.4
		(3-2)="	DO	49.1	138.3
		(2-1)="	U	61.8	112.3
		(2-2)="			
		(2-3)=.2			
		♦= 5−108			
(b)		0=9 0			
		(2-4)=.2			
4		φ=126-162			
- *	- 5	0=9 0			
		(2-5)=.2			
		4=198-252			

See Figure 6 -- SIRO

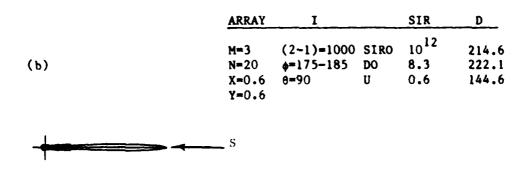
Figure 1 (a), (b). Summary sheet pertaining to radiation pattern plots. The quotation marks, ", imply the same as that in the figure above.

| 10日のこのイインと関われているののでは関われているのでは関節になるなどの関節であれる。|

θ=90 (2-6)=.2 φ=270-355 θ=90 (1-1)="

SKETCH	ARRAY	I		SIR	D
(a)	M=2 N=10 X=0.75 Y=0.75	(3-1)=1 φ=5 θ=90 (3-2)=1 φ=-15 θ=90	SIRO DO U	10 ¹⁵ 53.7 66.3	102.3 138.3 112.3
	S				

See Figure 7 - SIRO



See Figure 8 -- SIRO Figure 9 -- DO

Figure 2 (a), (b). Summary sheet pertaining to radiation pattern plots.

<u>s</u>	KETCH	ARRAY	I		SIR	D
(a)		M=3 N=22 X=0.75 Y=0.75	T	SIRO DO U	10 ⁹ 35.9 15.4	364.4 483.7 307.2
+	-	_ s				

See Figure 10 — SIRO Figure 11 — DO

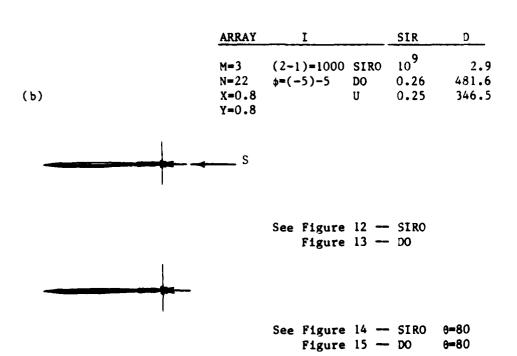


Figure 3 (a), (b). Summary sheet pertaining to radiation pattern plots.

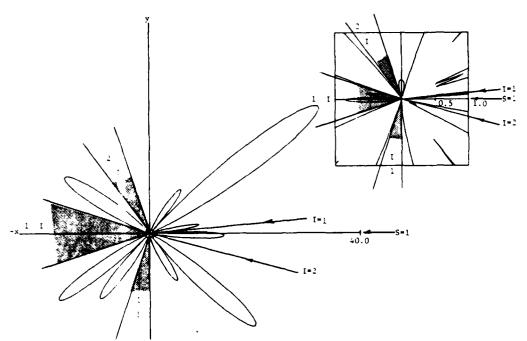


Figure -. Radiation pattern of a 2 × 10 array excited for optimum SIR.

For details of the interference distribution, I, refer to Figure 1(a).

The center portion is expanded at the upper right.

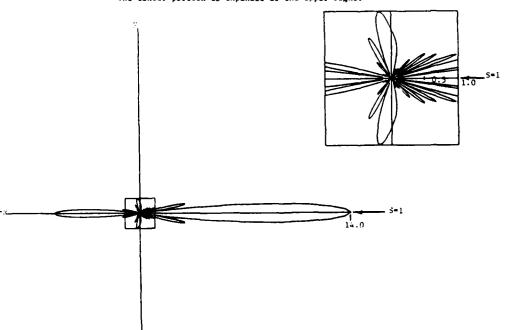


Figure $\frac{1}{2}$ Radiation pattern of a 2 × 10 array excited for optimum D. The center portion is expanded at the upper right.

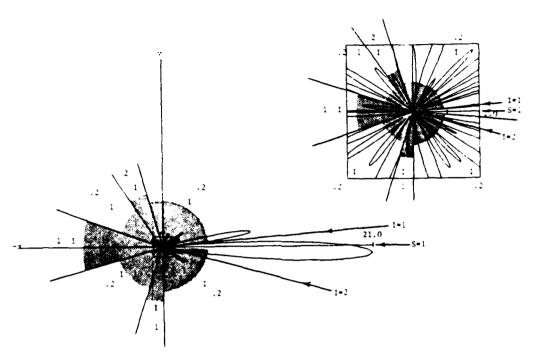


Figure 5. Radiation pattern of a 2 \times 10 array excited for optimum SIR. For details of the interference distribution, I, refer to Figure 1(b). The center portion is expanded at the upper right.

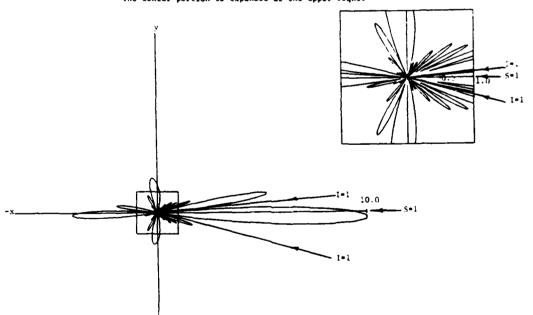


Figure 7. Radiation pattern of a 2 × 10 array excited for optimum D with constraint. For details of the interference distribution, I, refer to Figure 2(a). The center portion is expanded at the upper right.

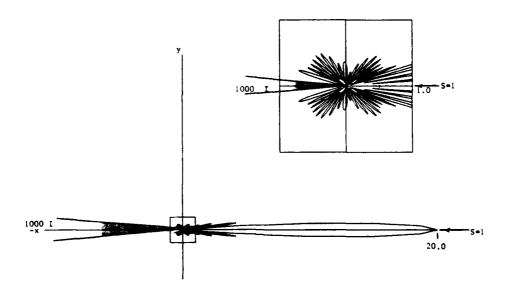


Figure 3. Radiation pattern of a 3 \times 20 array excited for optimum D with constraint. For the interference distribution, $T_{\rm c}$ refer to Figure 2(b). The center portion is expanded at the upper right.

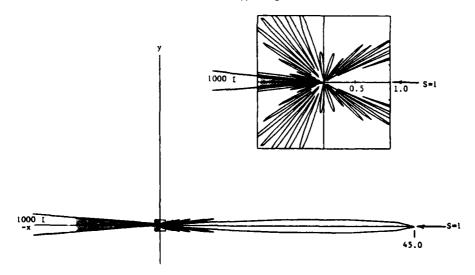


Figure 9. Radiation pattern of a 3 \times 20 array excited for optimum 0. For the interference distribution, I, refer to Figure 2(b). The center portion is expanded at the upper right.

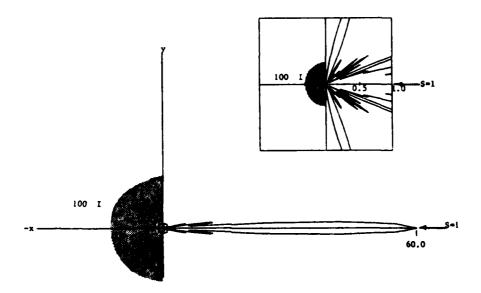


Figure 10. Radiation pattern of a 3 \times 22 (spacings: x = y = 0.75) array excited for optimum D with constraint. For the interference distribution, I, refer to Figure 3(a). The center portion is expanded at the upper right.

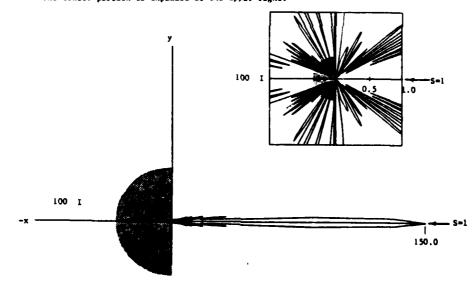
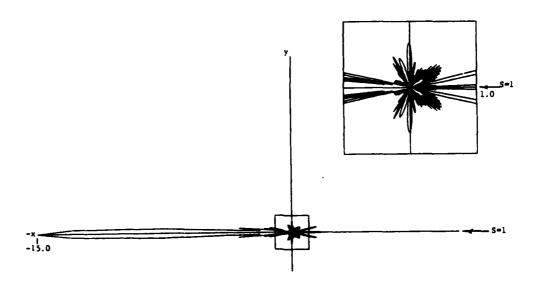


Figure 11. Radiation pattern of a 3 \times 22 (spacings: x = y = 0.75) array excited for optimum D. For the interference distribution, I, refer to Figure 3(a). The center portion is expanded at the upper right.



PARTICIONAL PROPERTY PROPERTY INC.

Figure 12. Radiation pattern of a 3 \times 22 (spacings: x = y = 0.8) array excited for optimum D with constraint. For the interference distribution, I, refer to Figure 3(b). The center portion is expanded at the upper right.

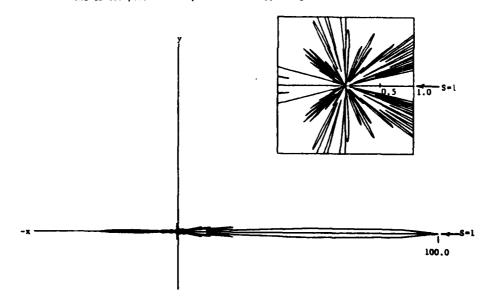


Figure 13. Radiation pattern of a 3 \times 22 (spacings: x = y = 0.8) array excited for optimum D. For the interference distribution, I, refer to Figure 3(b). The center portion is expanded at the upper right.

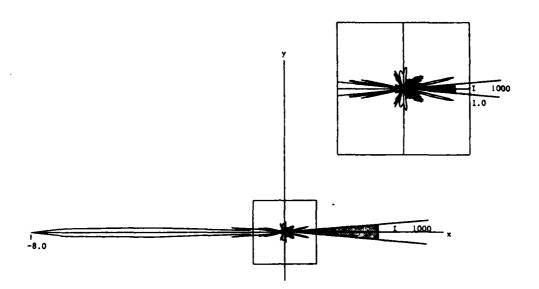


Figure 14. Radiation pattern in the cone with semiconical angle $\theta=80^\circ$ of the array in Figure 12.

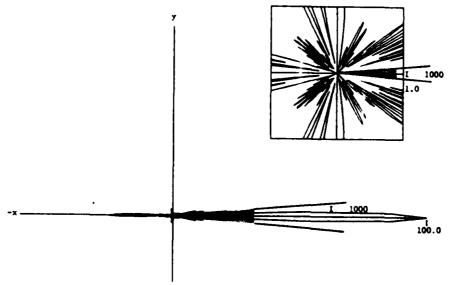


Figure 15. Radiation pattern in the cone with semiconical angle $\theta=80^{\circ}$ of the array in Figure 13.

Acknowledgement

The presentation of this paper is supported by Westinghouse Electric Corporation, Baltimore, MD.

LIST OF REFERENCES

- 1. Y. T. Lo, S. W. Lee, and Q. H. Lee, "Optimization of directivity and signal-to-noise ratio of an arbitrary antenna array," Proceedings of the IEEE, vol. 54, no. 8, pp. 1033-1045, August, 1966.
- C. Drane, Jr., and J. McIlvenna, "Gain maximization and controlled null placement simultaneously achieved in aerial array patterns," <u>Radio and Electronic Engineer</u>, vol. 39, no. 1, pp. 49-57, January 1970.
- 3. Andrew Y. Piatnicia, "Optimization for antenna arrays in an arbitrary interference environment," M.S. Thesis, University of Illinois at Urbana-Champaign, August 1985.

WIDEBAND MONOPULSE ANTENNA DESIGN

Konsell Brandsky. Robbooks Landskyld Landskyld. Activities.

THE THEORY OF THE PROPERTY INCOME.

David L. Thomas Watkins-Johnson Company 2525 North First Street San Jose, California 95131-1097

Abstract

Antennas to provide monopulse direction-of-arrival in a dense multi-polarized signal environment, over a wide instantaneous RF bandwidth, are a challenge to the designer. Solutions to some of the associated problems are presented, along with a description and performance data for a wideband monopulse antenna system.

CONTRACTOR CONTRACTOR SOURCE STATES OF THE PARTY OF THE P

CONTROL CONTROLS IN THE CONTROL BUSINESS INCOMESTS

The monopulse reflector antenna described uses a unique array feed configuration to reduce the apparent phase center separation, thereby increasing bandwidth, along with absorber techniques to control the illumination function and elevation beamwidth. Primary and secondary patterns of the DF antenna, along with sidelobe blanking antenna data, are presented for an operational system. Photographs and diagrams of the antennas are included. This antenna configuration is currently deployed as part of an ESM feasibility demonstration system.

1.0 INTRODUCTION.

Techniques for monopulse direction finding (DF) have been used for many years in radar systems. Monopulse allows almost instantaneous determination of direction of arrival based on a single pulse rather than a train of pulses. A narrow RF bandwidth of the antenna is adequate for most radar applications because only a narrow frequency range is needed for tracking. Electronic surveillance, on the other hand, requires antennas that will "listen" over a wide RF bandwidth. Wideband monopulse direction finding antennas for surveillance applications present some challenging problems for the antenna designer. These problems and some solutions are presented here.

2.0 <u>DESIRABLE FEATURES OF A WIDEBAND MONOPULSE</u> <u>SYSTEM.</u>

Desirable features of a wideband monopulse surveillance antenna system are as follows. The antenna beamwidth must be large enough to cover an adequate instantaneous field of view (FOV), while the gain must be high enough to provide sufficient system sensitivity. High DF accuracy, usually the most important characteristic of a monopulse system, is achieved through careful selection of pattern shapes and processing techniques. Since the incoming signal polarization is usually unknown, circular polarization with a low axial ratio is normally required so that the DF accuracy is not a function of the incoming

signal polarization. Also, ambiguities due to reception of unknown signals through the sidelobes must be eliminated, usually through the use of auxiliary sidelobe blanking antennas. All of these features should ideally be obtained over a sufficiently wide RF bandwidth to meet the surveillance requirements.

3.0 MONOPULSE FEEDS EXCITATION TECHNIQUES.

THE PROPERTY OF THE PROPERTY O

Often a reflector antenna is required to provide high gain for system sensitivity and a limited field of view for spatial filtering in a dense signal environment, rather than a "wide open" DF antenna with a wide beamwidth and low gain. Assuming a parabolic reflector properly sized for the desired beamwidth, the critical items become types of feeds and methods of excitation for efficient reflector illumination and optimum DF accuracy.

Figure 1 shows two schemes for determining direction of arrival (DOA) in one plane by two-channel comparison. For left-right beams, the amplitude ratio of the two beam outputs is a function of the coordinate angle, and the change in the amplitude ratio versus angle is relatively constant across the FOV. For sum-difference beams, the amplitude ratio of the two outputs is a function of the coordinate angle, and their phase difference indicates left or right of the boresight null. Because of the steep difference null, however, the change in the amplitude ratio versus coordinate angle increases sharply

near boresight, thus providing higher DF accuracy than the left-right scheme.

Since the feeds are used individually rather than in an array in the left-right scheme, use of frequency independent feeds can provide frequency independent reflector illumination. In the sum-difference array, however, the sum pattern illumination is narrower than the difference pattern, and the array factor further narrows the illumination patterns as the frequency is increased. Thus, although the sum-difference scheme provides higher DF accuracy near boresight, which is advantageous for tracking applications, achieving efficient reflector illumination over a broad frequency range is more difficult than with the left-right scheme.

4.0 FEED TYPES.

Assuming that sum-difference monopulse is desired because of its higher DF accuracy near boresight, two types of broadband, circularly polarized feed elements are considered. Figure 2 compares arrays of both conical and flat cavity backed spirals in sum-difference configurations. Flat spirals have the limitation that, while phase center separation in wavelengths is small at the lowest operating frequency with spirals touching, the separation in wavelengths increases with increasing frequency until the reflector becomes underilluminated at higher frequencies. Alternatively, conical spirals with a 15 to 20 degree cone

angle can be placed such that the base separation in wavelengths at the lowest operating frequency is the same as the tip separation in wavelengths at the highest operating frequency, thus providing constant reflector illumination over the entire spiral frequency range. However, since the phase center of the array moves along the length of the conical spiral as frequency changes, axial defocusing of the reflector results, causing a loss of efficiency. The major drawback with the conical spiral approach is the interaction or coupling of the spirals when placed close together, which results in deterioration of the array pattern at various frequencies across the band. Coupling between adjacent flat spirals is much less and has no significant effect.

Thus, while conical spirals appear to be well suited for a broadband monopulse feed array, considerable experimentation is required to solve the coupling problem, if it can be solved! On the other hand, a technique that makes the phase centers "appear" closer together could cause a flat spiral array, or an array of horns or some other elements, to be useful as a feed over a reasonably broad frequency band. Such a technique is presented in paragraph 6.0.

5.0 TWO-ELEMENT FEED ARRAY.

これのないのは、これのこのでは、これのことのできないようなない。

A simple two-element feed array, as shown in Figure 3, has limited use as a broadband feed as explained in paragraph 4.0. As shown in Figures 4 through 6, the sum pattern narrows rapidly as frequency

increases. The secondary, or reflector, patterns in Figures 7 and 8 show a flattening and then a dip in the sum pattern caused by the first nulls and first sidelobes of the feed pattern moving onto the reflector. Measured data indicates that a pair of contiguous flat spiral or circular horn feeds in the sum-difference mode will illuminate a reflector over a useful bandwidth ratio of about 1.6:1.

6.0 THREE-ELEMENT FEED ARRAY.

A technique that extends the bandwidth of a reflector with sum-difference feeds of fixed spacing is shown in Figure 9. The purpose of the third element is to cause the element spacing S to appear smaller for the sum mode, thus broadening the sum illumination pattern, while leaving the spacing unchanged for the difference mode, which is already sufficiently broad.

The network in Figure 9 is easiest to analyze in the transmit mode, and since the circuit elements and antennas are reciprocal, the analysis applies also to the receive mode. A signal injected into the sum port is split equally between the two circuit halves. In the left half, it is split again with half going to antenna B and half going to the hybrid that feeds antenna A. The signal in the right half is similarly split between antenna C and the hybrid that feeds A. Since the signals into the hybrid that feeds A are of equal amplitude and phase, all of the energy appears in antenna A (neglecting hybrid losses) and no

energy appears in the difference port load. Thus for the sum mode, the circuit elements A, B, and C are in phase and have a 1:2:1 power ratio, respectively.

ので 風味 そうていかい 国際になったののでき 間景なる

いったから言葉がたいから、自動などのなどは難なめなりです。他のなったのは難にのなるななないは難なななないない。

A signal injected into the difference port is divided in exactly the same way, except that all of the energy into the hybrid feeding A appears in the difference port load with no energy going into antenna A, due to the inputs to that hybrid being of equal amplitudes and opposite phase. Thus the difference mode excites elements B and C only with equal amplitudes and 180 degrees phase difference.

Referring to the triangular array in Figure 9, note that for the sum mode, the energy in B combines with half the energy in A resulting in a center of phase half way between elements B and A. Likewise, the energy in C combines with the other half of the energy in A resulting in a center of phase half way between elements C and A. These two subarrays, with phase centers spaced S/2 apart, are now arrayed to produce a sum mode pattern equivalent to that of a two-element array of spacing S/2. The difference mode pattern is that of a two element array of spacing S, since the power in element A is zero for difference mode excitation.

Patterns of an array of three flat cavity-backed spirals fed as in Figure 9 are shown in Figures 10 through 12. Note that the sum and difference patterns have approximately equal widths across a large

frequency band, compared with the two-element array patterns of Figures 4 through 6, where the sum patterns are much narrower than the difference patterns. Secondary patterns for the three-spiral array in Figures 13 through 16 show no flattening of the sum pattern over a full 2.3:1 bandwidth ratio. Clearly, the three-element array extends the useful bandwidth of the monopulse reflector by making the "apparent" sum mode element spacing less than the physical spacing.

7.0 FOUR-ELEMENT FEED ARRAY.

In a monopulse system, the sum and difference beams should ideally point along the same boresight. Analysis of the triangular array in Figure 9 reveals that for the sum mode the overall phase center is located half way up the vertical centerline of the triangle, while the difference mode overall phase center is at the midpoint of the triangle base. This vertical phase center offset causes the reflector sum and difference pattern boresights to be slightly offset in the vertical plane. A solution to this problem is the four-element feed array shown in Figure 17. Note that the only difference from the three-element array is that the energy that went into element A is now split equally between elements A and D. While the phase center separations in the horizontal direction are still S/2 for the sum mode and S for the difference mode, the overall array phase centers are coincident with the array physical center for both sum and difference beams, thus producing colinear boresights.

Patterns of a four-element array are shown in Figures 18 through 20. The array elements are circular waveguide horns with dielectric phase plate polarizers. Note the similarity to the three-element array patterns of Figures 10 through 12. The reflector patterns in Figures 21 through 23 show that the four-element array produces uniform secondary patterns with no flattening of the sum pattern over a bandwidth ratio of at least 2.7:1.

Pictures of four-element feed array networks in both waveguide and coaxial configurations are shown in Figure 24. The waveguide network uses the "magic tee" as the circuit equivalent to the 180 degree hybrid.

8.0 ELEVATION PLANE CONSIDERATIONS.

In the foregoing examples, direction finding is performed in the azimuth plane only, and the elevation plane beamwidths are sufficiently broad to provide an adequate vertical field of view. Since signals may be incident from any angle in the elevation beam, the sum and difference patterns should ideally be independent of elevation angle. This implies equal sum and difference elevation beamwidths, so that both beams roll off at the same rate in elevation, thus providing a sum-difference amplitude ratio versus azimuth function that does not change with elevation. Equal sum and difference elevation beamwidths

are obtained by equal illumination tapers across the vertical dimension of the reflector.

Figure 25 illustrates illumination contours in decibels on a rectangular reflector, produced by the four-element feed array. Note that in Figure 17, elements A and D are effectively arrayed with combined elements B and C in the vertical plane for the sum mode (all four elements are excited equally), while for the difference mode the vertical plane sees only the equivalent of the single element pattern of B or C, with no arraying. As a result, difference pattern illumination is broader than sum pattern illumination in the elevation plane, thus producing narrower difference than sum pattern secondary beams.

A solution to the elevation illumination problem is shown in Figure 26. The proper absorber thickness is determined experimentally such that the difference pattern illumination taper is effectively increased to equal that of the sum. Figures 27 through 30 show patterns of this configuration at a fixed frequency for various angles in the elevation beam. The sum and difference pattern shapes are seen to be fairly constant over a 15 degree elevation sector.

9.0 AXIAL RATIO CONSIDERATIONS.

Careful design and fabrication of monopulse antennas to provide low axial ratios over the entire frequency band are critical to accurate DF

performance. The effect of axial ratio on DF accuracy is illustrated in Figure 31. Unlike other errors, the angular uncertainty induced by axial ratio cannot be calibrated out of the system.

10.0 SIDELOBE BLANKING.

CONTRACTOR STATES AND TOTAL MANAGERY SESSIONS BANGERY

In a typical monopulse system, signals strong enough to enter the sidelobes can trigger a sum-difference ratio response indistinguishable from that of the main beam. A common technique to remove such ambiguity is to use one or more omnidirectional antennas in a sidelobe blanking scheme as shown in Figure 32. The sidelobe blanking antenna or antennas must provide a level greater than the sum pattern sidelobes throughout all angular regions where unwanted signals may appear.

An omnidirectional antenna that provides good hemispherical coverage, optimized toward the horizon, is the four-arm conical spiral operated in the difference mode. Typical patterns are shown in Figures 33 and 34. Except for a narrow null directed toward the zenith, this antenna produces uniform azimuth patterns for elevation angles out to the horizon. Variations with frequency are minimal over a band at least as wide as that of the monopulse reflector described in paragraph 7.0.

11.0 TYPICAL WIDEBAND MONOPULSE ANTENNA SYSTEM.

Figures 35 through 37 show an integrated monopulse system that uses the four-element feed array described in paragraph 7.0, the absorber technique for elevation pattern control described in paragraph 8.0, and omnis for sidelobe blanking of the type described in paragraph 10.0. The large reflector has cavity-backed flat spiral feeds with a coaxial network, while the small reflector uses circular horn feeds with dielectric phase plate polarizers and a waveguide network. A four-arm conical spiral omni for each frequency band can be seen in the photographs. The absorber "shield" around the periphery of the small reflector is to block spillover that may exceed the sidelobe blanking levels. This antenna system provides performance similar to that described in paragraphs 7.0, 8.0 and 10.0 over two 2.7:1 frequency bands.

12.0 CONCLUSIONS.

While the theory of monopulse antennas is well established, the practical problems that the designer of a wideband monopulse antenna system must face include the wideband realization of efficient reflector illumination, high DF accuracy, adequate beamwidth control, low axial ratios, and sidelobe blanking. Solutions to these problems and resultant data have been presented which involve array feed configurations, absorber techniques, careful attention to antenna types and construction details for low axial ratios, and selection of a sidelobe blank-

ing system matched to the sidelobe characteristics of the DF antenna. Although each wideband monopulse system may have a unique set of requirements, the design considerations, trade-offs, and development processes bear a strong thread of commonality.

13.0 ACKNOWLEDGEMENTS.

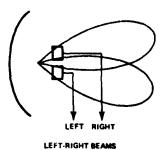
seeded to the terror of the seeded seeded to the seeded to the seeded to

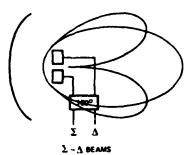
The author wishes to thank Mr. T. Carberry of MITRE Corporation and Mr. J. Hill of Watkins-Johnson Company for their discussions and ideas during the development of the antenna system.

14.0 REFERENCES.

- Silver, S., ed.(1965), <u>Microwave Antenna Theory and</u>
 <u>Design</u>, Dover Publications, Inc.
- Johnson, R.C., and Jasik, H., ed.(1984) <u>Antenna</u>
 Engineering Handbook, Second Edition, McGraw-Hill, New York.
- 3. Barton, D.K.(1977), Radars, Volume 1, Monopulse

 Radar, Artech House, Inc.
- Skolnik, M.I., ed.(1970), <u>Radar Handbook</u>,
 McGraw-Hill, New York.
- Love, A.W., ed.(1978), <u>Reflector Antennas</u>,
 IEEE Press, New York.
- 6. Schindall, J.E. (1984), ESM configuration for passive location and identification, <u>Proceedings of Watkins-Johnson Company Annual Technical Symposium</u>.





85 A.7016

ADVANTAGES

- DF ACCURACY IS ESSENTIALLY CONSTANT ACROSS FOV
- REFLECTOR ILLUMINATION IS SAME FOR LEFT AND RIGHT BEAMS
- . NO ARRAY FACTOR BANDWIDTH LIMITATION

DISADVANTAGES

- DF ACCURACY MAY NOT BE ADEQUATE FOR SOME APPLICATIONS
- DF ACCURACY DOES NOT INCREASE NEAR BORESIGHT FOR TRACKING APPLICATIONS

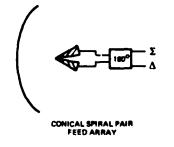
ADVANTAGES

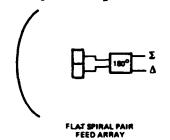
- HIGH DF ACCURACY IS ACHIEVED NEAR BORESIGHT
- INCREASED DF ACCURACY NEAR BORESIGHT IS IDEAL FOR TRACKING

DISADVANTAGES

- SUM PATTERN ILLUMINATION IS NARROWER THAN DIFFERENCE PATTERN
- ARRAY FACTOR LIMITS BANDWIDTH DUE TO NARROWING OF ILLUMINATION PATTERN AT HIGH END OF FREQUENCY BAND

Figure 1. Monopulse Feeds Excitation Techniques Comparison





85.A.7015

ADVANTAGES

- SPIRAL PHASE CENTER SEPARATION VARIES WITH FREQUENCY
- . LARGE BANDWIDTH POSSIBLE

DISADVANTAGES

- ARRAY PHASE CENTER MOTION CAUSES AXIAL DEFOCUSSING
- SPIRAL INTERACTION CAN CAUSE ARRAY PATTERN TO HAVE NULLS AT NUMEROUS FREQUENCIES THROUGHOUT THE BAND

ADVANTAGES

- ARRAY PHASE CENTER REMAINS AT FOCUS
 ACROSS FREQUENCY BAND
- . SPIRAL INTERACTION IS MINIMAL

DISADVANTAGES

- SPIRAL PHASE CENTER SEPARATION IS FIXED
- BANDWIDTH IS LIMITED DUE TO NARROWING OF ARRAY FACTOR BEAMWIDTH AT HIGH END OF BAND, CAUSING REFLECTOR UNDERILLUMINATION

Figure 2. Σ - Δ Monopulse Feed Array Types Comparison

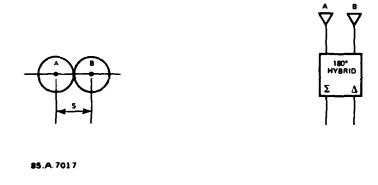


Figure 3. Two-Element Feed Array

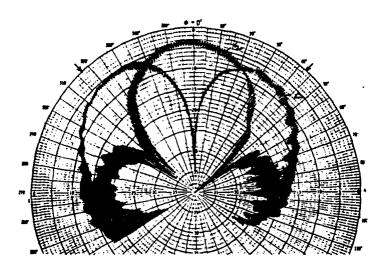
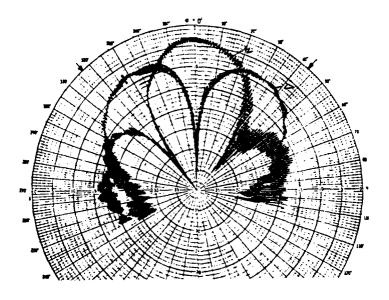


Figure 4. Two-Spiral Array Primary Patterns, 10 GHz



TO STATE OF THE PROPERTY OF TH

Figure 5. Two-Spiral Array Primary Patterns, 12 GHz

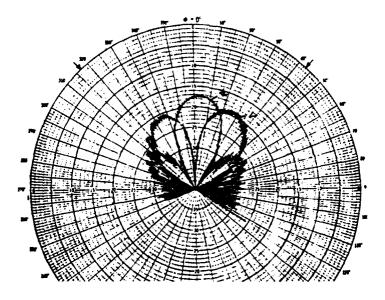


Figure 6. Two-Spiral Array Primary Patterns, 14 GHz

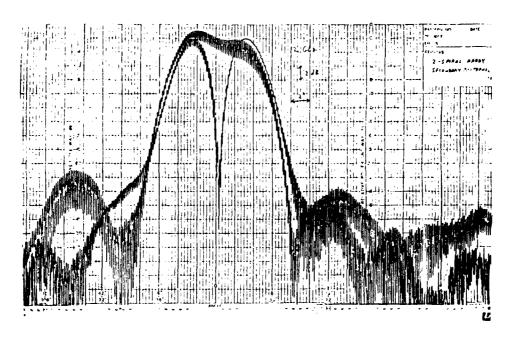


Figure 7. Two-Spiral Array Secondary Patterns, 12 GHz

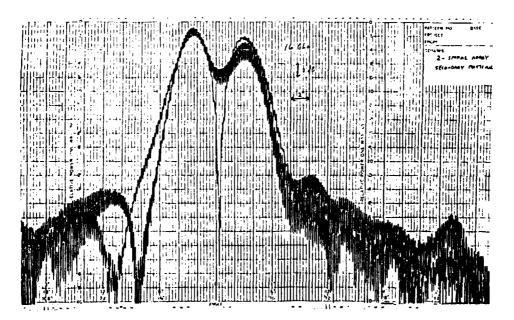


Figure 8. Two-Spiral Array Secondary Patterns, 16 GHz

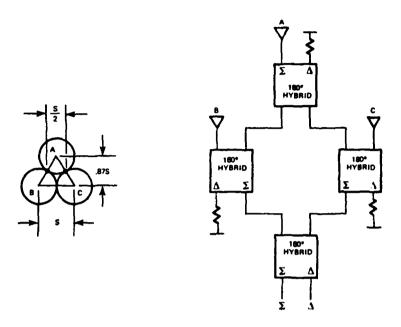


Figure 9. Three-Element Feed Array Concept

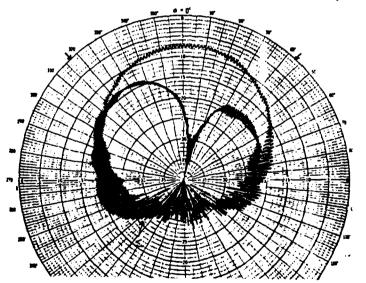


Figure 10. Three-Spiral Array Primary Patterns, Azimuth Cut, 8 GHz

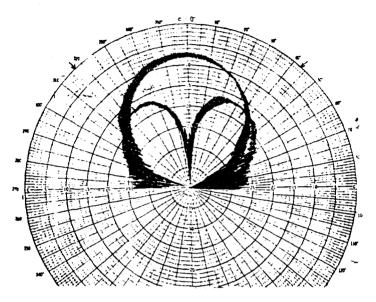


Figure 11. Three-Spiral Array Primary Patterns, Azimuth Cut, 12 GHz

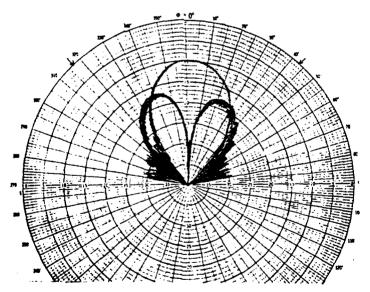


Figure 12. Three-Spiral Array Primary Patterns, Azimuth Cut, 18 GHz

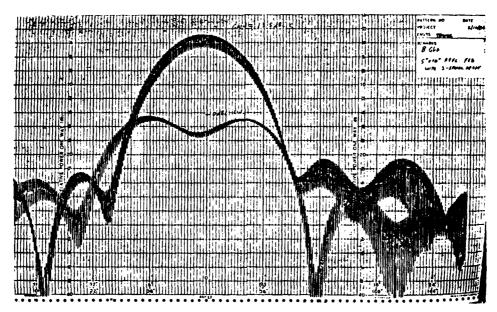


Figure 13. Three-Spiral Array Secondary Patterns, 8 GHz

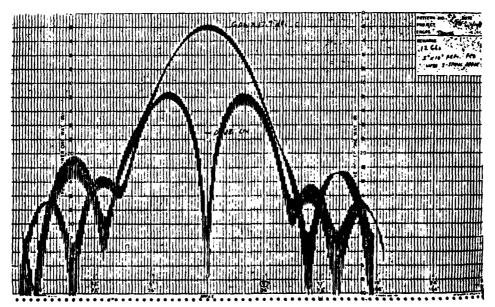


Figure 14. Three-Spiral Array Secondary Patterns, 12 GHz

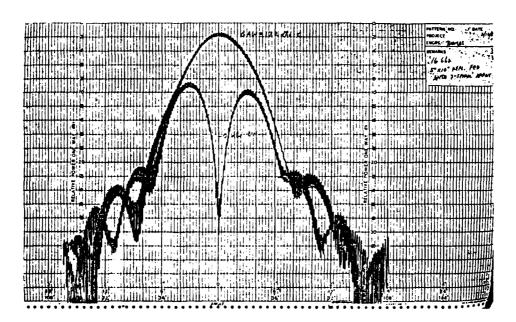


Figure 15. Three-Spiral Array Secondary Patterns, 16 GHz

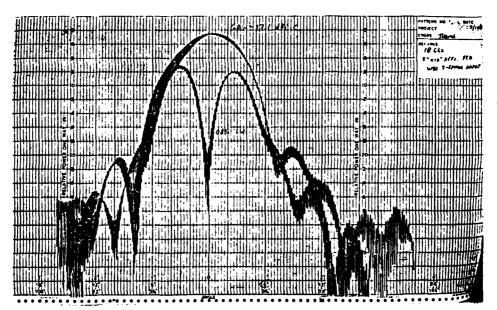


Figure 16. Three-Spiral Array Secondary Patterns, 18 GHz

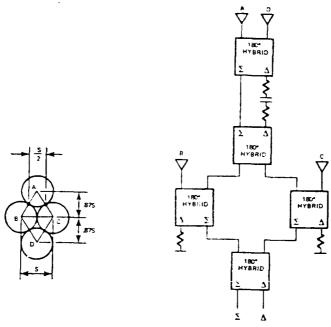


Figure 17. Four-Element Feed Array Concept

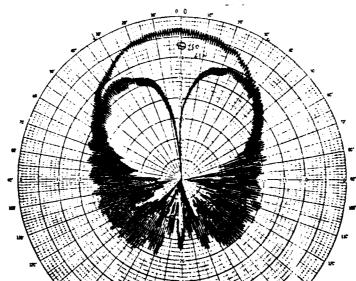


Figure 18. Four-Element Array Primary Patterns, Azimuth Cut, 7.5 GHz

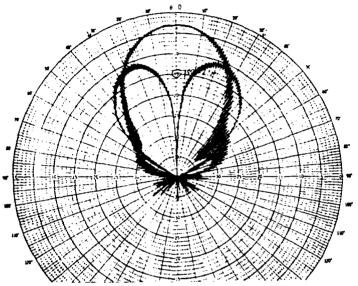


Figure 19. Four-Element Array Primary Patterns, Azimuth Cut, 11 GHz

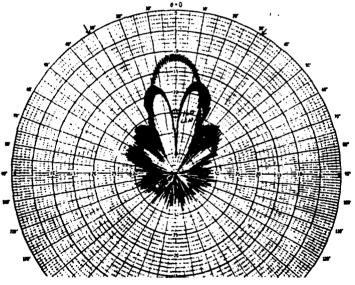
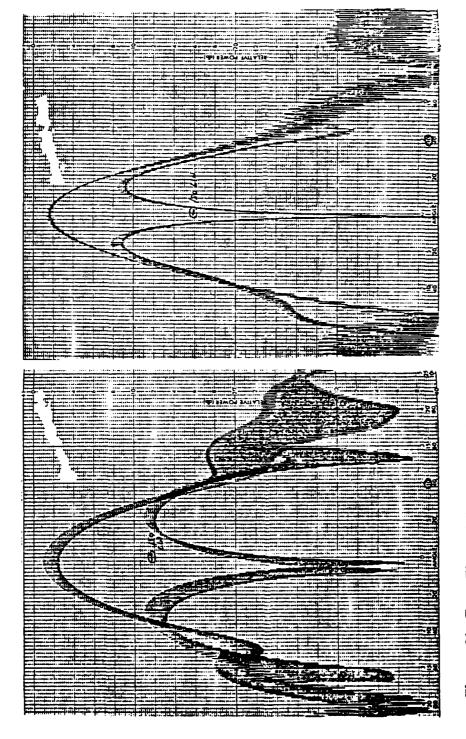


Figure 20. Four-Element Array Primary Patterns, Azimuth Cut, 17 GHz



PROPERTY INCOMENSATION OF PROPERTY OF THE PROPERTY OF THE

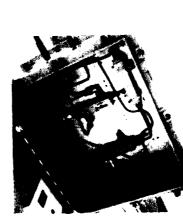
Figure 21. Four-Element Array Secondary Patterns, Frequency = F_{LO}

Figure 22. Four-Element Array Secondary Patterns, Frequency = $2.0 \times F_{LO}$



INCOME THE PROPERTY OF THE PRO

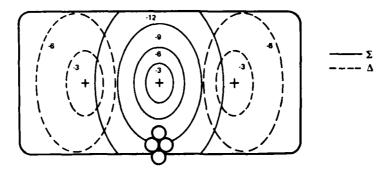
Waveguide



Coaxial

Figure 23. Four-Element Array Secondary Patterns, Frequency = $2.7 \times F_{LO}$

Figure 24. Four-Element Feed Array, Typical RF Distribution Network



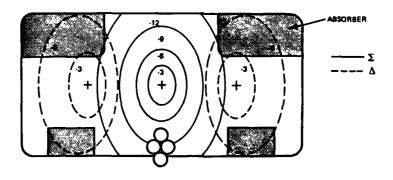
4 - ELEMENT FEED ARRAY PRODUCES:

SATISFACTORILY TAPERED SUM PATTERN ILLUMINATION DUE TO ARRAYING IN ELEVATION PLANE

OVER - ILLUMINATED DIFFERENCE PATTERN DUE TO NO ARRAYING IN ELEVATION PLANE

85.A.7011

Figure 25. Reflector Illumination



ABSORBER TECHNIQUE EFFECTIVELY TAPERS
THE DIFFERENCE MODE ELEVATION ILLUMINATION
WITH MINIMAL EFFECT ON SUM MODE ILLUMINATION

85 A.7012

Figure 26. Reflector Illumination, Showing Absorber

Figure 27. Four-Element Array Secondary Patterns, Azimuth Cut, 0° Elevation, Frequency = 1.7 x F_{LO}

Figure 28. Four-Element Array Secondary Patterns, Azimuth Cut, 5° Elevation, Frequency = 1.7 x $^{\rm F}$ LO

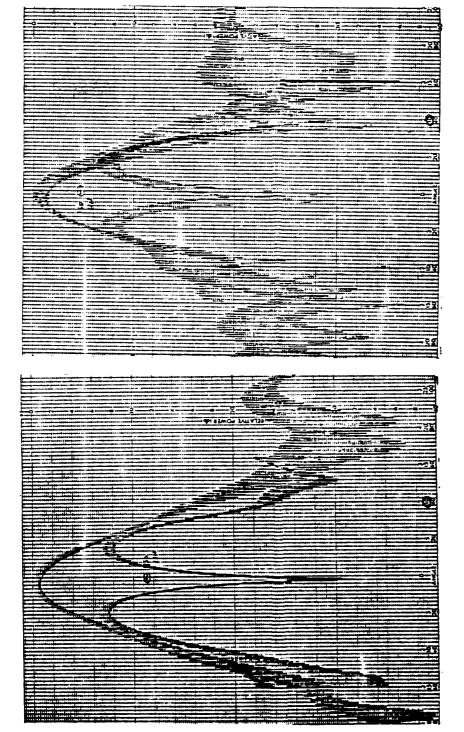


Figure 29. Four-Element Array Secondary Patterns, Azimuth Cut, 10° Elevation, Frequency = $1.7 \times F_{LO}$

Figure 30. Four-Element Array Secondary Patterns, Azimuth Cut, 15° Elevation, Frequency = 1.7 x $^{\rm F}_{\rm LO}$

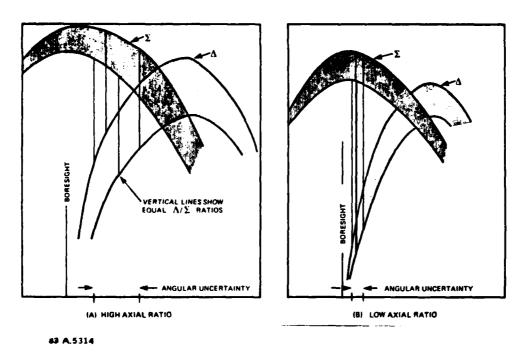
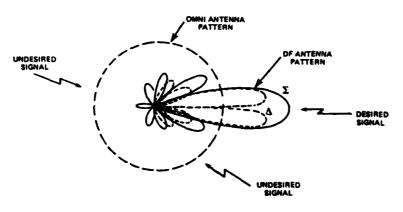


Figure 31. Effect of Axial Ratio on DF Accuracy

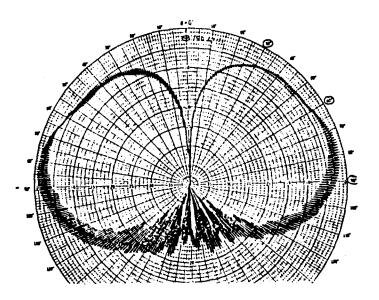


• SIGNAL IS PROCESSED IF Σ IS GREATER THAN OMNI

-signal is not processed if Σ is less than or equal to omni

85.A.7014

Figure 32. Sidelobe Blanking Technique



SASSESSED TO SOME DESCRIPTION OF THE PROPERTY OF THE PROPERTY

Figure 33. Four-Arm Conical Spiral Omni Patterns, Elevation Cut

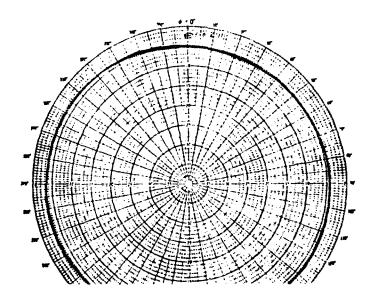
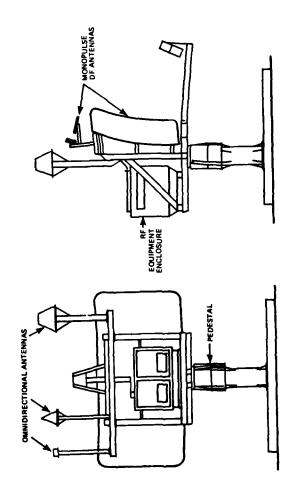


Figure 34. Four-Arm Conical Spiral Omni Patterns, Azimuth Cut, 60° Elevation



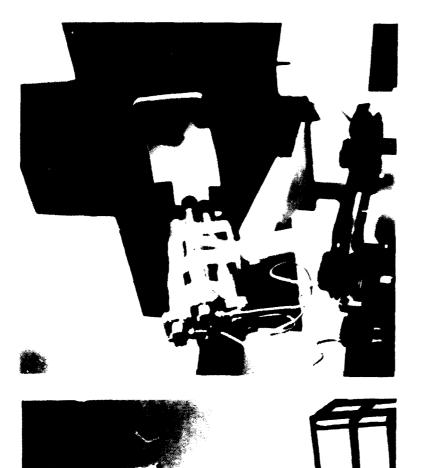
Ç

・・・ 1000 インスクラクの原理としてリングに、新聞した自然のものの問題にいっていない。 関目をあるからのでは、大学のなどのではないのである。

;; ;;,

Figure 35. Typical Direction Finding Antenna System

693



できるとのである。これは

■なられるのは

「なられる」というできます。

「いっと」

■なられる。

「いっと」

■なられる。

「いっと」

■なられる。

「いっと」

■なられる。

■なられる



.

12469-6

Figure 37. Direction Finding Antenna System Photograph, Close-up of High Frequency Reflector Figure 36. Direction Finding Antenna System Photograph

. چ

694

MISSION of

Rome Air Development Center

RADC plans and executes research, development, test and selected acquisition programs in support of Command, Control Communications and Intelligence (C^3I) activities. Technical and engineering support within areas of technical competence is provided to ESD Program Offices (POs) and other ESD elements. The principal technical mission areas are communications, electromagnetic guidance and control, surveillance of ground and aerospace objects, intelligence data collection and handling, information system technology, solid state sciences, electromagnetics and electronic reliability, maintainability and compatibility.

Printed by United States Air Force Hanscom AFB, Mass. 01731 F1/MED 4-86